FLOW STUDIES IN AN IN-LINE HIGH SHEAR MIXER

by

CYRUS JOHN UERA ESPINOZA

A thesis submitted to the
University of Birmingham
for the degree of
DOCTOR OF ENGINEERING

Centre for Doctoral Training in Formulation Engineering
School of Chemical Engineering
College of Engineering and Physical Sciences
University of Birmingham

March 2020

UNIVERSITY OF
BIRMINGHAM

University of Birmingham Research Archive

e-theses repository

This unpublished thesis/dissertation is copyright of the author and/or third parties. The intellectual property rights of the author or third parties in respect of this work are as defined by The Copyright Designs and Patents Act 1988 or as modified by any successor legislation.

Any use made of information contained in this thesis/dissertation must be in accordance with that legislation and must be properly acknowledged. Further distribution or reproduction in any format is prohibited without the permission of the copyright holder.

Abstract

Angle-resolved, 2-D Particle Image Velocimetry (PIV) was used to measure the influence of process parameters upon flow patterns and evaluate turbulence properties in an in-line Silverson mixer.

The main findings show that the dominant flow pattern in the mixing head can either be radial or tangential. The former is driven by the external pump while the latter by increasing the rotor speed. Increasing the back pressure through the outlet valve also promotes more tangential flows.

Areas of high ε, indicative of potential droplet break up locations, were found to exist within the jets emanating from the secondary stator and within the rotor swept volume. Moreover, it was also conveyed that different flow regimes (laminar, transitional and turbulent) could simultaneously occur at localised areas of the mixing head, implying important consideration of several droplet break up mechanisms.

Flow behaviour of selected Newtonian and non-Newtonian fluids were also investigated. The latter include generic transparent shampoo formulations representative of fluids processed by Unilever Port Sunlight. It was found that approximating local viscosity is important for the more viscous (salted) shampoo, which exhibited viscoelastic and shear-thinning behaviours. Furthermore, it was shown that highly shear-thinning areas had low Weissenberg numbers (low elasticity) and vice versa.

To my family and friends, this is for you

“The secret of getting ahead is getting started.”

– Mark Twain

“You never fail until you stop trying.”

– Albert Einstein

“It always seems impossible until it’s done.”

– Nelson Mandela

“To know, is to know that you know nothing.
That is the meaning of true knowledge.”

– Socrates

A Filipino proverb: “*Kapag may tiyaga, may nilaga.”*

“With perseverance, you will reap the fruits of your labour.”

Acknowledgements

I would like to express my sincerest gratitude to my academic supervisors: Prof. Mark Simmons and Dr. Federico Alberini, as well as my industrial supervisors: Prof. Adam Kowalski and Dr. Olga Mihailova for the opportunity to undertake the EngD programme and providing me their invaluable support, guidance and mentorship all throughout my journey. I would also like to thank the EPSRC and Unilever for sponsoring this project which gave me the privilege to learn many scientific techniques, share my findings at major conferences and grow as a person through the countless challenges I faced along the way. In light of this, I would also like to thank Dr. Richard Greenwood for coordinating such a life-changing programme.

My EngD experience will not have been as gratifying and memorable without all the caring friends I made. Special thanks to Toni, Ola, Gina and Zoe for always lending their helping hands and listening ears. I would also like to thank Lynn Draper and Christine Dickinson from reception for their kindness and constant reassurance. A big thank you also goes to David Boylin, Mala Patel, Sarah Fleming, Steve Brookes, Andy Tanner, Sailesh Pattni, Mark Taylor, Elaine Mitchell, Veronica Baglin, Kathleen Hynes and John Hooper for their great technical and administrative assistances. Also to David Rothman, Richard Berger and Steve Derx of Silverson Machines Ltd. for building the rig used in this project. To Jonathan O'Sullivan, Cha Casugbo and John Naughton of Unilever for their support whenever I was in Port Sunlight and finally, to Martin Hyde of TSI Inc. who was always patient and helpful.

Last but not the least, I would like to thank God for his never ending blessings, my family, especially to my parents Johnna and Edgardo for their relentless love, support and understanding and to Tessa, for always being there for me and keeping me motivated while being extremely patient. I will always aspire to make you all proud!

Table of Contents

List of Figures

List of Tables

Nomenclature

Symbols	*Description*
a	relaxation time pre-exponential factor in Equation 6.9, s^{b+1}
A	area or rotor blade area in Equation 2.31, m^2
A	arbitrary constant in Equation 2.7, Pa s^b
A	constant in Equation 2.76, dimensionless
b	power law exponent in Equations 2.7 and 6.9, dimensionless
B	rotor blade width, m
C	impeller clearance, m
$C_1, C_2 \ldots C_x$	dimensionless empirical constants, dimensionless
C_S	Smagorinsky constant, dimensionless
d_f	fringe spacing, m
d_{max}	maximum stable droplet diameter, m
D	rotor diameter throughout unless otherwise stated (see below), m
D	filled volume diameter in Figures 3.3 and 4.3 (2R), m
D_h	stator hole diameter, m
D_{inlet}	inlet pipe diameter, m
$D_{ps,inner}$	primary stator inner diameter, m
$D_{ps,outer}$	primary stator outer diameter, m
$D_{r,i}$	inner rotor diameter, m
$D_{r,o}$	outer rotor diameter, m
$D_{ss,inner}$	secondary stator inner diameter, m
$D_{ss,outer}$	secondary stator outer diameter, m
D_{volute}	hydraulic diameter between $D_{ss,\ outer}$ and filled volume diameter (2R), m
E_V	energy density, J m^{-3}
f_D	Doppler shift frequency, Hz or s^{-1}

F	force, N
g	acceleration due to gravity, m s^{-2}
G^*	complex shear modulus, Pa or kg m^{-1} s^{-2}
H	head, m
i, j	row (i) and column (j) grid position indices, dimensionless
I	image at time t, dimensionless
I'	image at time $t + \Delta t$, dimensionless
k	turbulent kinetic energy, m^2 s^{-2}
k_1	proportionality constant in Equation 2.24, dimensionless
k_s	Metzner-Otto constant, dimensionless
K	consistency index in Equation 2.5, Pa s^n
K	kinetic energy of the mean flow in Equation 6.5, m^2 s^{-2}
L	characteristic length, m
L_{IA}	side length of interrogation area, m
L_p	side length of interrogation area, pixels
$\dot{m}$	mass flow rate, kg hr^{-1}
M_{hole}	mass flow rate in a single stator hole, kg s^{-1}
M_P	external pump mass flow rate, kg s^{-1}
M_S	generated mass flow rate by Silverson, kg s^{-1}
M_T	total mass flow rate, kg s^{-1}
n	power law exponent, dimensionless
N	rotor speed, rps
N_1	first normal stress difference, Pa or kg m^{-1} s^{-2}
N_{P0}	shaft power draw constant in Equation 2.25, dimensionless
N_{P1}	shaft power draw constant in Equation 2.25, dimensionless
$< p >$	mean pressure, Pa or kg m^{-1} s^{-2}
P	power, W
P_{0Z}	'zero flow' power constant in Equation 2.24, dimensionless

P_1	point coordinates, (m, m)
P_2	point coordinates, (m, m)
P_{diss}	total turbulent dissipation power in Equation 2.25, W
P_F	power caused by the flow, W
$P_{Gearbox}$	power dissipated by the gearbox, W
$P_{Impeller}$	power dissipated by the impeller, W
P_{in}	mixer inlet pressure, bar
P_L	power loss, W
P_{Motor}	power dissipated by the motor, W
P_{out}	mixer outlet pressure, bar
P_{pump}	pumping power, W
P_T	power required to rotate the rotor blade against fluid resistance, W
$P_{thermal}$	total increase in fluid thermal energy, W
P_{Total}	total power dissipated, W
P_{Seal}	power dissipated by the seal, W
P_{shaft}	shaft power draw, W
$P_{shaft}^{'}$	loss-corrected shaft power draw ($P_{shaft} - P_L$), W
Q	volumetric flow rate, $m^3\ s^{-1}$
Q	Q criterion in §5.3.2, Figure 5.9, s^{-2}
$Q_{fit,integrated}$	calculated volumetric flow rate from a fitted function, $m^3\ s^{-1}$
$Q_{measured}$	measured volumetric flow rate using a flow meter, $m^3\ s^{-1}$
Q_{plug}	calculated volumetric flow rate using plug flow approximation, $m^3\ s^{-1}$
Q_T	total volumetric flow rate, $m^3\ s^{-1}$
r	arbitrary radial distance in cylindrical coordinates, m
r, θ, z	radial, tangential and axial directions in cylindrical coordinates, m
R	filled volume radius, m
R_{11}	normal Reynolds stresses in the x-direction, $m^2\ s^{-2}$

R_{12}	shear Reynolds stresses in the xy-plane, $m^2\ s^{-2}$
R_{22}	normal Reynolds stresses in the y-direction, $m^2\ s^{-2}$
Re	impeller Reynolds number, dimensionless
Re_{exit}	stator hole exit Reynolds number, dimensionless
S	magnification, dimensionless
$\lvert\bar{S}\rvert$	magnitude of the strain rate tensor $\sqrt{2\bar{S}_{ij}\bar{S}_{ij}}$, s^{-1}
$\bar{S}_{ij}$	resolved scale strain rate tensor, s^{-1}
S_r	row separation distance, m
S_{surf}	calculated surface flow rate, $m^2\ s^{-1}$
t	time, s
T	tank diameter, m
TI	turbulence intensity in Equation 6.6, dimensionless
u_p	velocity component in Equation 2.49, $m\ s^{-1}$
U	instantaneous velocity, $m\ s^{-1}$
U, V, W	x, y and z components of velocity in Cartesian coordinates, $m\ s^{-1}$
$\overline{U}$	mean velocity, $m\ s^{-1}$
$\overline{U}\lvert_\theta$	angle resolved mean velocity, $m\ s^{-1}$
U_θ	tangential component of velocity in cylindrical coordinates, $m\ s^{-1}$
U'	fluctuating quantity of instantaneous velocity from time-averaged data, $m\ s^{-1}$
U''	fluctuating quantity of instantaneous velocity from angle-resolved data, $m\ s^{-1}$
U_f	fluctuating velocity component, $m\ s^{-1}$
U_{hole}	stator hole velocity, $m\ s^{-1}$
U_{inlet}	inlet pipe velocity, $m\ s^{-1}$
U_{jet}	jet velocity, $m\ s^{-1}$
U_{max}	maximum velocity, $m\ s^{-1}$
U_p	periodic velocity component of the flow, $m\ s^{-1}$
U_r	radial component of velocity in cylindrical coordinates, $m\ s^{-1}$

U_{rms}	root mean square (RMS) of the fluctuating velocity, m s^{-1}
U_{tip}	rotor tip speed (πND), m s^{-1}
U_x	x-component of velocity in Cartesian coordinates, m s^{-1}
U_y	y-component of velocity in Cartesian coordinates, m s^{-1}
V	volume, m^3
V_δ	rotor-stator gap volume, m^3
V_{hole}	stator hole volume, m^3
V_{inlet}	entrance pipe volume, m^3
$V_{rotor\ swept}$	rotor swept volume, m^3
V_{volute}	volute volume, m^3
W	impeller width, m
x, y, z	directions in Cartesian coordinates, m
z	arbitrary axial distance in cylindrical coordinates, m
Z	stator thickness, m

Greek Symbols

β	rotor blade angle in Equation 2.31, radians
$\dot{\gamma}$	shear rate, s^{-1}
γ_a	strain amplitude, dimensionless or expressed as %
δ	rotor-stator gap, m
Δ	grid spacing or filter width, m
ΔH_P	head difference at the external pump, m
ΔH_S	head difference at the Silverson mixer, m
ΔH_T	total head difference, m
ΔP_P	pressure drop at the external pump, bar
ΔP_S	pressure drop at the Silverson mixer, bar
ΔP_T	total pressure drop, bar
Δt	time delay between image pairs, s

ε	local specific energy dissipation rate, $m^2\ s^{-3}$
ε^*	normalised local specific energy dissipation rate with N^2D^3, dimensionless
$\dot{\varepsilon}$	elongational strain rate, s^{-1}
$\bar{\varepsilon}$	mean specific energy dissipation rate, $m^2\ s^{-3}$
ε_{avg}	power per unit mass, W kg^{-1} ($m^2\ s^{-3}$)
ε_{DA}	calculated local energy dissipation rate using dimensional analysis, $m^2\ s^{-3}$
ε_{DE}	ε determined by the direct evaluation method, $m^2\ s^{-3}$
ε_{SGS}	ε determined by the sub-grid scale method, $m^2\ s^{-3}$
ε_T	local 'torque on shaft' energy dissipation rate per unit mass of fluid, W kg^{-1}
θ	tangential angle, radians
θ	angle of intersection of beams in Equation 2.48, radians
λ	wavelength, m
λ_{CI}	swirling strength, s^{-1}
λ_k	Kolmogorov length scale, m
λ_{RT}	relaxation time, s
Λ	macro integral length scale, m
μ	fluid viscosity, Pa s
μ_∞	infinite viscosity, Pa s
μ_A	apparent fluid viscosity, Pa s
μ_E	extensional viscosity, Pa s
ν	kinematic fluid viscosity, $m^2\ s^{-1}$
Π_{flow}	flow term in the shaft power draw expression in Equation 2.25, W
Π_L	loss term in the shaft power draw expression in Equation 2.25, W
Π_{rot}	rotation term in the shaft power draw expression in Equation 2.25, W
ρ	fluid density, kg m^{-3}
σ	surface or interfacial tension, N m^{-1}
σ_E	net tensile stress, Pa or kg $m^{-1}\ s^{-2}$
τ	shear stress, Pa or kg $m^{-1}\ s^{-2}$

τ_a	shear stress amplitude, Pa or kg m^{-1} s^{-2}
τ_c	cohesive stresses resisting droplet deformation, kg m^{-1} s^{-2}
τ_d	disruptive stresses acting on the droplet, kg m^{-1} s^{-2}
τ_R	residence times in Table 5.6, s
τ_s	cohesive surface tension stresses, kg m^{-1} s^{-2}
τ_v	cohesive viscous stresses, kg m^{-1} s^{-2}
τ_y	yield stress, Pa or kg m^{-1} s^{-2}
$\phi_{II'}$	cross-correlation function, dimensionless
ω	vorticity in §5.3.2, Figure 5.9, s^{-1}

Dimensionless Groups

$Ca = \frac{\rho_c U^2 L}{\sigma}$	Capillary number, dimensionless
$Fr = \frac{N^2 D}{g}$	Froude number, dimensionless
$N_Q = \frac{Q_T}{N D_{r,o}^3}$	Flow or pumping number, dimensionless
$Po\ or\ Ne = \frac{P}{\rho N^3 D^5}$	Power or Newton number, dimensionless
$Re = \frac{\rho N {D_{r,o}}^2}{\mu}$	Reynolds number at rotor swept area, dimensionless
$Re_{hole} = \frac{\rho U_{hole} D_h}{\mu_\infty}$	Reynolds number at stator holes, dimensionless
$Vi = \left(\frac{\rho_c}{\rho_d}\right)^{\frac{1}{2}} \left(\frac{\mu_d N D}{\sigma}\right)$	Viscosity group, dimensionless
$We = \frac{\rho_c N^2 D^3}{\sigma}$	Weber number, dimensionless
$Wi = \lambda_{RT} \dot{\gamma}$	Weissenberg number, dimensionless

Abbreviations

$CaBER$	capillary breakup exlongational rheometer
$CapB$	cocamidopropyl betaine
CFD	computational fluid dynamics

DE	direct evaluation
DRA	drag reducing agent
EIS	elongation induced structures
FIB	flow induced birefringence
FOV	field of view
HSM	high shear mixer
ILS	integral length scale
LDA	laser Doppler anemometry
LDV	laser Doppler velocimetry
LES	large eddy simulation
MHV	mixing head volume
MKE	mean (flow) kinetic energy
MRI	magnetic resonance imaging
NMR	nuclear magnetic resonance
$PEPT$	positron emission particle tracking
PIV	particle image velocimetry
$PLIF$	planar laser induced fluorescence
PO	pump only
PS	pump and Silverson
PTV	particle tracking velocimetry
QC	quality control
$R\&D$	research and development
$ROI\ A$	region of interest A
$ROI\ B$	region of interest B
RSM	rotor stator mixer
RSV	rotor swept volume
$SANS$	small angle neutron scattering
SGS	sub-grid scale

SIS	shear induced structures
$SLES$	sodium lauryl ether sulphate
SO	Silverson only
TEM	transmission electron microscopy
TKE	turbulent kinetic energy
VFO	valve fully open
VPC	valve partially closed
WLM	worm like micelles

Chapter 1 – Introduction

1.1 Background

'Rotor-stator' Mixers (RSM), or high shear mixers (HSM), are extensively used in industrial processes for liquid-liquid dispersion, emulsification and homogenisation due to their simplicity, flexibility and capability to produce high levels of shear and energy dissipation rates (three orders of magnitude greater than a mechanically stirred vessel) on a relatively small volume of fluid. They are used in the food, cosmetics, home and personal care as well as pharmaceutical industries for manufacturing products such as mayonnaise, detergents, shampoos and conditioners (Håkansson, 2018; Zhang et al., 2012) and can be operated in batch, semi-continuous or continuous (in-line single or multiple pass) modes. Moreover, they are often integrated as part of a unit operation for increasing process intensification and reducing processing times. They may also be classified as axial and radial discharge HSMs, toothed devices and colloid mills and they are manufactured by companies such as Ross, Chemineer, IKA work, Siefer, Rayneri and Silverson with a range of scales and geometries to suit a given application (Utomo, 2009).

In-line HSMs are deemed favourable by industry as, provided they are given the required process control to ensure consistent product quality, they deliver larger continuous throughput and offer the capability for real time process adjustments and rapid product changeover. In comparison, batch HSMs, albeit flexible, suffer from long equipment downtime (cleaning and changeover) and large volumes of waste when batches fail and are discarded (Paul et al., 2004; Qin et al., 2017). However, the lack of theoretical knowledge, even more than for batch operated HSMs, makes the design, scale-up and application of in-line HSMs very challenging

(Håkansson and Innings, 2017). This is mainly because such mixers are of pilot- or factory-scale which means that they are not built for research purposes. This poses difficulties in conducting continuous large- scale experiments which also require high operational costs (Hall, 2012). Moreover, additional complexities in the manufacturing process arise, as the fluids handled in HSMs and most that are processed in industry in general, often possess complex rheology (e.g. non-Newtonian) and thus, mixing time, order of ingredient addition, process parameters such as pressure, temperature and rotor speeds, as well as energy dissipation rates can influence the characteristics of the final product.

The focus of the research presented in this thesis is to understand and characterise the dynamics inside an in-line HSM, based upon the 150/250 in-line design by Silverson Machines Ltd., which are widely used in the food and home and personal care industries. Particle image velocimetry (PIV) is used to measure the flow within the mixer to examine ways of increased energy efficiency in operation and reduced waste material. As these mixers have complex geometries and are often constructed from opaque materials e.g. stainless steel, and rely on complex flow dynamics such as turbulence, the flow dynamics inside them are indeed difficult to characterise. In fact, the conventional way to study emulsification in HSMs is by analysing how droplet size distributions (DSD) and average drop sizes (such as $d_{3,2}$ and $d_{4,3}$ of emulsion systems at different sampling points in the process line) respond to changes in process parameters (Hall et al., 2011a; Qin et al., 2017; Thapar, 2004), or through Computational Fluid Dynamics (CFD) simulations (Ahmed et al., 2018; Jasińska et al., 2015; Utomo et al., 2008). Thus, to enable flow visualisation and study of the internal dynamics of these mixers using the PIV technique, a modified version of the 150/250 Silverson mixer was used. All of its internal components including the double emulsor screens and double concentric rotors were made out of transparent polymethyl methacrylate.

1.2 Business Case

Both batch and in-line HSMs such as the Silverson models, are an integral part of many of the processes run by the sponsoring company, Unilever, a global manufacturer of fast-moving consumer goods (FMCG) especially of formulated emulsion products with varying rheological complexities in its major divisions in the food and personal care sectors. Thus, it is essential for the company to gain as much insight on how these mixers operate to ensure that they run in the most efficient and cost-effective way to meet consumer demands in the fastest way possible, which is central to the sustainable growth strategy of Unilever.

Standardising the use of in-line Silverson mixers in manufacturing processes has been based on improving process scale-up from bench (laboratory) to factory scale (Hall, 2012), which remains to be very challenging due to the aforementioned complex rheological properties of handled products.

1.3 Context, Aims and Objectives

Although rotor-stator devices are used extensively in industry, fundamental research on their behaviour has only been focussed on for the last two decades. In 2004, Atiemo-Obeng and Calabrese (2004) concluded that: "*The current understanding of rotor-stator devices has almost no fundamental basis. There are few theories by which to predict, or systematic experimental protocols by which to assess, the performance of these mixers. In fact, there are very few archival publications on rotor-stator processing. Furthermore, the equipment is developed and manufactured by small, highly competitive and highly specialized companies in an environment that is not conducive to the development of a generalized knowledge base."* Thus, due to the lack of understanding of the underlying scientific and engineering principles of the process, previous optimisation of operating parameters has been heavily reliant on

operator experience and trial-and-error which is very costly and resource intensive (Mortensen et al., 2017). In a similar manner, experienced engineers have been dependent on established methods and using existing designs for similar products and processes (Casugbo and Baker, 2018). In light of these, the number of conducted experimental and numerical investigations to assess the performance of both batch and in-line rotor-stator mixers, has increased. In terms of emulsification processes, this spans from measuring mixer power consumption and performing flow visualisation techniques such as PIV to using CFD in modelling droplet break-up to determine the influence of process parameters such as rotor speed and flow rate on the final droplet size.

The overall aim of this study is to use PIV to characterise the fluid dynamics e.g. flow patterns and turbulence at different processing conditions in a modified in-line Silverson rotor-stator mixer to determine how they may influence droplet break up; and consequently identify regions and potential mechanisms of droplet break up, which may be useful for process optimisation of such mixers.

The main objectives of this study are as follows:

1. Assess the effects of changing process parameters such as rotor speed, externally driven flow rate and backpressure upon the flow field and pattern in the mixing head of the in-line HSM for Newtonian fluids (water) (Chapter 4).
2. Through the study of flow patterns, identify areas where droplet break up is likely to occur (Chapter 5).
3. Evaluate turbulence properties such as Reynolds stresses, turbulent kinetic energy and energy dissipation rates using velocity data to determine potential governing break up mechanism(s) (Chapter 5).

4. Assess the impact of changing fluid rheology (non-Newtonian fluids and higher viscosity Newtonian fluids) to ascertain its influence on flow patterns and turbulence and thus on potential mechanisms of droplet deformation (Chapter 6).

The findings made in this study were critically compared to the existing observations made in the literature to assess their contribution to knowledge. The results obtained from this research can also be used for the validation of both new and existing CFD models.

This research provides a conceptual framework for future studies that will eventually attain predictive capability of process performance e.g. resulting droplet size at various process conditions through the coupling of associated hydrodynamic effects and mechanisms of droplet deformation.

1.4 Thesis Outline

This thesis is comprised of 7 chapters:

- Chapter 1 provides the rationale for the research conducted.
- Chapter 2 contains fundamental theories on the topics of fluid mechanics, liquid-liquid mixing (emulsification), high shear mixers (including review of current literature) and velocimetry techniques.
- Chapter 3 details the materials and equipment used in the studies as well as the experimental arrangement and procedures.

- Chapter 4 presents the first results chapter on flow studies in an in-line high shear mixer using particle image velocimetry, investigating the effects of rotor speed, externally driven flow and back pressure.[1]
- Chapter 5 covers the second results chapter on characterising the flow, turbulence and potential droplet breakup mechanisms in an in-line high shear mixer.[2]
- Chapter 6 explores the third results chapter on the mean flow field and energy dissipation of fluids with complex rheology in an in-line high shear mixer.
- Chapter 7 summarises the conclusions and future recommendations for the work done in this thesis.

1.5 Publications and Presentations

Findings in this thesis have been published in the following journals and presented at the following conferences:

1.5.1 Publications

Espinoza, C.J.U., Simmons, M.J.H., Alberini, F., Mihailova, O., Kowalski A. J. and Rothman, D. (2018) Flow studies in an in-line Silverson 150/250 high shear mixer using PIV. **Chemical Engineering Research and Design**, 132: 989-1004.

Espinoza, C.J.U., Simmons, M.J.H., Alberini, F., Mihailova, O. and Kowalski A. J. (2020) Flow, turbulence and potential droplet break up mechanisms in an in-line Silverson 150/250 high shear mixer. **Chemical Engineering Science: X**, 6:100055.

[1] Part of this work has been published in: Espinoza, C.J.U., Simmons, M.J.H., Alberini, F., Mihailova, O., Kowalski A. J. and Rothman, D. (2018) Flow studies in an in-line Silverson 150/250 high shear mixer using PIV. **Chemical Engineering Research and Design**, 132: 989-1004

[2] Part of this work has been published in: Espinoza, C.J.U., Simmons, M.J.H., Alberini, F., Mihailova, O., Kowalski A. J. and Rothman, D. (2020) Flow, turbulence and potential droplet break up mechanisms in an in-line Silverson 150/250 high shear mixer. **Chemical Engineering Science: X**, 6:100055

1.5.2 Presentations

Oral

Espinoza, C.J.U., Simmons, M.J.H., Alberini, F., Mihailova, O. and Kowalski A. J. (2017) **A Study of Flow in an In-Line High Shear Mixer Using Angle-Resolved PIV**. Educational Visit at the Research Institutes of Sweden (RISE), Stockholm, Sweden.

Espinoza, C.J.U., Simmons, M.J.H., Alberini, F., Mihailova, O. and Kowalski A. J. (2017) **A Study of Flow in an In-Line High Shear Mixer Using Angle-Resolved PIV**. IChemE Student Competition Fluid Mixing Special Interest Group, Loughborough University, United Kingdom.

Espinoza, C.J.U., Simmons, M.J.H., Alberini, F., Mihailova, O. and Kowalski A.J. (2017) **Flow Studies in an In-Line High Shear Mixer Using Angle-Resolved PIV**. International Symposium on Mixing in Industrial Processes (ISMIP) IX, Birmingham, United Kingdom.

Espinoza, C.J.U., Simmons, M.J.H., Alberini, F., Mihailova, O. and Kowalski A.J. (2018) **Flow Studies in an In-Line High Shear Mixer Using Angle-Resolved PIV**. IChemE Student Competition Fluid Mixing Special Interest Group, University of Manchester, United Kingdom.

Espinoza, C.J.U., Simmons, M.J.H., Alberini, F., Mihailova, O. and Kowalski A.J. (2018) **Flow Studies in an In-Line High Shear Mixer Using Angle-Resolved PIV**. North American Mixing Forum (NAMF) Mixing XXVI, San Juan, Puerto Rico.

Poster

Espinoza, C.J.U., Simmons, M.J.H., Alberini, F. and Kowalski A.J. (2016) **Emulsification in High Shear Mixers**. North American Mixing Forum (NAMF) Mixing XXV, Quebec, Canada.

Espinoza, C.J.U., Simmons, M.J.H., Alberini, F., Mihailova, O. and Kowalski A.J. (2018) **Flow Studies in an In-Line High Shear Mixer Using Particle Image Velocimetry (PIV)**. SCI Formulation Forum, London, United Kingdom.

Chapter 2 – Literature Review

2.1 Introduction

This review begins by laying the foundations for the fundamentals of high shear mixers (HSM) by giving a description of relevant theories in fluid mechanics and liquid-liquid mixing. A section on HSM then follows, focusing on its design, working principles and applications. A literature survey giving the state-of-the-art in the understanding of the behaviour of HSM is then presented. Following this, relevant flow characterisation techniques are described, with particular focus on particle image velocimetry (PIV) and how data from it are used to quantify turbulence properties, followed by an overall summary.

2.2 Relevant Theories in Fluid Mechanics

2.2.1 Classification of Fluids

Newtonian

When a fluid is flowing and is subjected to external forces, it undergoes deformation via frictional effects due to the relative motion of liquid molecules. This effect is applicable to all fluids and manifests due to their viscosity (Chhabra and Shankar, 2018). Consider an infinitesimally small volume of fluid sheared between two parallel plates, separated by a distance *y* (Figure 2.1).

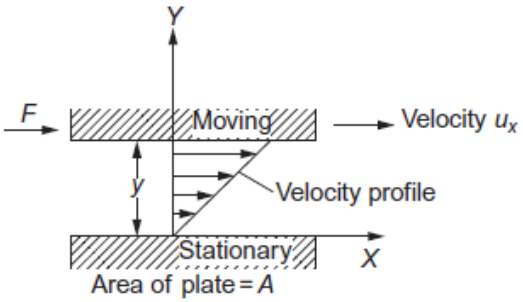

Figure 2.1: Unidirectional shearing flow (Chhabra and Shankar, 2018)

The bottom plate is stationary while the top plate is in motion at a velocity, u_x, in response to an applied force, F, which continuously deforms the fluid. At steady state conditions, the applied force is balanced by the internal force in the fluid, caused by its viscosity. The shear force per unit area, τ (Pa) is then proportional to the fluid velocity gradient (du_x/dy) or the shear rate, $\dot{\gamma}$ (s^{-1}):

$$\frac{F}{A} = \tau \propto \dot{\gamma} \tag{2.1}$$

The proportionality sign can be replaced by a proportionality factor, μ, also known as the coefficient of viscosity or the dynamic viscosity, which is a bulk property of the fluid:

$$\tau = \mu\dot{\gamma} \tag{2.2}$$

A Newtonian fluid is characterised by a constant dynamic viscosity (Newton's law of viscosity) provided that both pressure and temperature remain constant. This implies linear relationship between the applied shear stress and resulting shear rate.

In reality, all fluids show deviation from the perfect Newtonian behaviour e.g. they are non-Newtonian. However, fluids such as air, water, glycerol solutions and oil are commonly assumed Newtonian for simplicity of calculations since Newtonian fluids are the most basic mathematical models for fluids that take viscosity into account (Middleman, 1998).

Non-Newtonian

For non-Newtonian fluids (Figure 2.2), viscosity is not constant and is a function of shear rate and thus the term apparent viscosity is more appropriate and defined as:

$$\mu_A = \frac{\tau}{\dot{\gamma}} \tag{2.3}$$

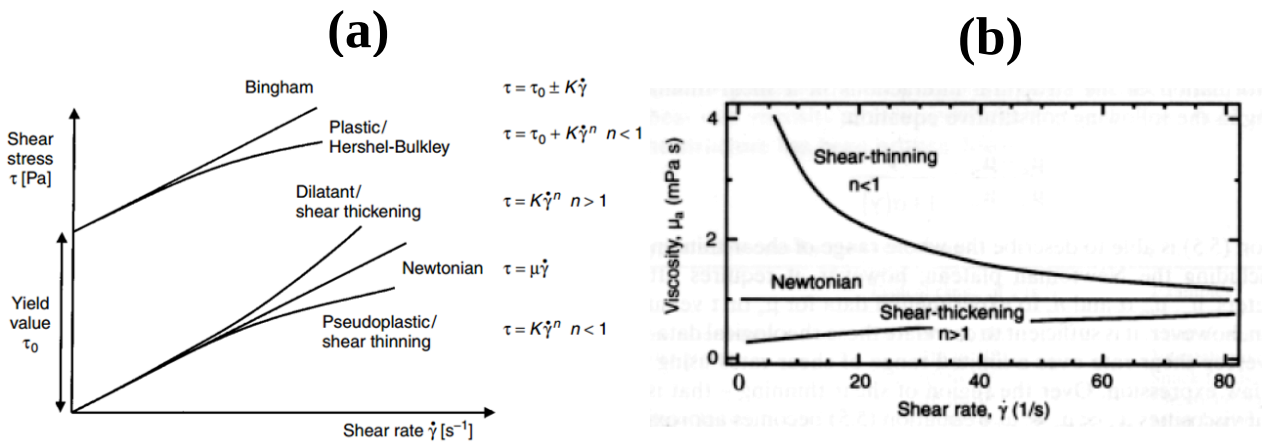

Figure 2.2: (a) Flow curves of Newtonian and non-Newtonian fluids (Brown et al., 2004) (b) Plot of apparent viscosities of Newtonian and non-Newtonian fluids against shear rate (Fryer et al., 1996)

Examples of non-Newtonian liquids in industrial practice include emulsions, paints, latex, liquid foods, mineral slurries, polymeric liquids and wastewater sludge (Brown et al., 2004). In most of these, the incorporation of solids and polymers (natural or synthetic) is responsible for the exhibited non-Newtonian behaviour. Non-Newtonian fluids can be classified into three main groups as shown in Table 2.1.

Table 2.1: Categories of non-Newtonian fluids (Brown et al., 2004)

Group	Description
Time independent fluids	Shear stress at a point depends solely on the instantaneous shear rate at that point.
Time dependent fluids	Shear stress and thus viscosity increases or decreases with shear duration. Such changes can be reversible or irreversible.
Viscoelastic fluids	The fluid possesses both viscous fluid and elastic solid characteristics. They demonstrate partial elastic recovery after the deforming shear stress is removed.

Time Independent Fluids

The viscosity of these fluids depends only on the applied shear rate and can be further sub-divided into three types: shear-thinning (pseudo-plastic), shear-thickening (dilatant) and viscoplastic materials. For shear-thinning and shear-thickening fluids, one of the most common

governing equation that describes their behaviour is the power law expression (Oswald de Waele power law model):

$$\tau = K\dot{\gamma}^n \tag{2.4}$$

where *K* and *n* are the consistency index and power law exponent respectively.

If $n = 1$, then the behaviour is Newtonian e.g. Equation 2.4 is analogous to Equation 2.2 and *K* is equal to μ. Thus the power law exponent provides an indication of the extent of how non-Newtonian a fluid is. For instance, if $n < 1$, the fluid is shear-thinning as the apparent viscosity decreases with increasing shear rate (Figure 2.2), examples include paint and polymer solutions. If $n > 1$, the fluid is shear-thickening as the apparent viscosity increases with increasing shear rate (Figure 2.2), examples include corn starch, starch slurries and whipped cream. Other models include Carreau, Ellis and Cross equations which are outside the scope of this section (Chhabra and Richardson, 1999).

In contrast to shear-thinning and shear-thickening fluids which readily deform when stress is applied, viscoplastic fluids such as Bingham plastic and Herschel-Bulkley fluids need to overcome a yield stress, τ_y, before they begin to flow (Brown et al., 2004). Examples of these fluids include tomato sauce, toothpaste, grease, mineral slurries and modern non-drip paints. The constitutive equation for Herschel-Bulkley fluids is:

$$\tau = \tau_y + K\dot{\gamma}^n \tag{2.5}$$

where for Bingham plastics, $n = 1$.

Time Dependent Fluids

This category includes rheopectic and thixotropic fluids. Rheopectic fluids exhibit a gradual increase in viscosity (thickens) while being sheared followed by a gradual recovery

after removing the shear inducing stress, examples are printer ink and gypsum paste. The opposite is true for thixotropic fluids where gradual decrease in viscosity (thins) is observed during shear which gradually recovers when the shear inducing stress is removed, examples are block co-polymers and self-assembling surfactant based systems (Brown et al., 2004).

Viscoelastic Fluids

Viscoelastic fluids simultaneously exhibit both viscous (e.g. like an ideal Newtonian fluid) and elastic (e.g. like an ideal elastic solid which obeys Hooke's law) properties. Thus, they possess some ability to flow like viscous fluids, as well as store and recover shear energy like elastic materials (Chhabra and Richardson, 1999). For instance, they temporarily store energy when the fluid is strained, which is released when the source of strain is removed. Normal forces/ stresses are generated under a simple shear flow of which magnitude varies with shear rate. It is common practice to use normal stress differences e.g. first normal stress difference, N_1 (Pa), instead of actual normal stresses with these materials (Brown et al., 2004):

$$N_1 = A\dot{\gamma}^b \tag{2.6}$$

When these fluids are mixed, the generated forces normal to the shear plane may result in rod-climbing phenomena (Weissenberg effect), flow reversal or die swell effect. Examples of viscoelastic fluids are flour dough, polymer solutions and shampoo formulations which have been investigated in this study (Brown et al., 2004; Chhabra and Richardson, 1999).

2.2.2 Rheological Measurements

Rheology is traditionally and ambiguously defined as the study of flow and deformation of matter (Malkin and Isayev, 2006; Rao, 2007). Its definition is close to continuum mechanics and is not about flow and deformation but of the properties of matter that define its behaviour (Malkin and Isayev, 2006). In addition, it is used to characterise materials that cannot be

described by the two extremes of viscous and elastic behaviours of Newtonian-Stokes fluids and Hookean solids respectively, but exhibit both viscous and elastic effects. Ultimately, it is the study of non-linear dependencies between structural changes imposed by applied forces (Rao, 2007). Rheometry is the set of standard measurement techniques used to experimentally identify the rheological properties of a material (solid or fluid). Its concept involves the realisation of flows where the applied strain and/or stress fields are known (pre-set) which permits the deduction of rheological properties from corresponding measurement of flow properties. It is vital to characterise the rheological properties of formulated products such as shampoo because (Abu-Jdayil et al., 2004; Dubey et al., 2014; Rounds, 2005): *(a)* Acceptance of final products depends on their flow properties because they influence storage stability, quality control, consumer sensory perception and efficiency of the manufacturing process. *(b)* Formulated products such as shampoos cover a wide range of the rheology spectrum from Newtonian fluids to semi-solid pastes. *(c)* Rheological measurements are important for the entire life cycle of formulated products from research and development (R&D) to quality control (QC) stages as rheology of raw materials, premixes, emulsions, dispersions and full formulations need to be established. In addition, benchmark data for product specification need to be met.

Shear Viscosity Measurement

A modern day rotational rheometer (Figure 2.3) is equipped with a motor/ engine that can exert a force (via torque) on a material (e.g. controlled shear stress, which is the most common type) and can also accurately measure the material's response with time. Alternatively, a strain rate can be imposed and torque measurements are taken (controlled shear rate) (Ancey, 2005). A suitable geometry is fitted onto the rheometer e.g. cone and plate or cup and bob (couette geometry). The sample is mounted onto a Peltier plate (a flat surface/ plate which uses

the ‘Peltier’ or ‘thermoelectric’ effect for temperature control of sample. This phenomenon works by generating or liberating heat when a current flows through a circuit junction that consists of two dissimilar conductors. The heating or cooling effect depends on the direction of current flow (Bakshi and Godse, 2007).) or filled into the geometry container e.g. for cup and bob. The standard operating procedure is setup using the rheometer software and the measurements take place automatically. Real-time response of the sample to known applied shear stress or strain rate are displayed on the computer monitor and obtained data can be further analysed. It is also noteworthy that the choice of geometry depends on the nature of the sample e.g. whether it is more on the solid (paste) or liquid (runny) consistency. Cone and plate (Figure 2.4a) and parallel plate (Figure 2.4b) geometries are most commonly ones used with the former more applicable for non-Newtonian fluids as it offers constant shear rate in the conical gap and can be used for all basic rheological tests such as creep, tension, relaxation, ramp and oscillatory tests. Parallel plates are more applicable for samples with suspended solids (Osswald and Rudolph, 2015). Other popular geometries include the capillary rheometer (Figure 2.4c) which

1. Motor assembly
2. Precision air bearing
3. Sensor assembly for accurate measurement of speed and absolute position
4. Collett-type chuck for attachment of upper measurement system
5. Leadscrew assembly for adjusting measurement sensor position
6. Linear bearing to support and guide air bearing and motor assembly
7. Integral normal face sensors situated within instrument mechanics
8. Temperature control unit
9. Universal clamping arrangement
10. Push button acrylic pad control unit and display
11. Integral electronics and power supply with the microprocessor and data communication links
12. Composite outer cover to protect the rheometer’s inner components

Figure 2.3: Anatomy of a modern day rotational rheometer (Ancey, 2005)

uses pressure-driven flow (Poiseuille device) and the concentric cylinder or Couette device (Figure 2.4d) which is used for fluids with low viscosity (Osswald and Menges, 2012).

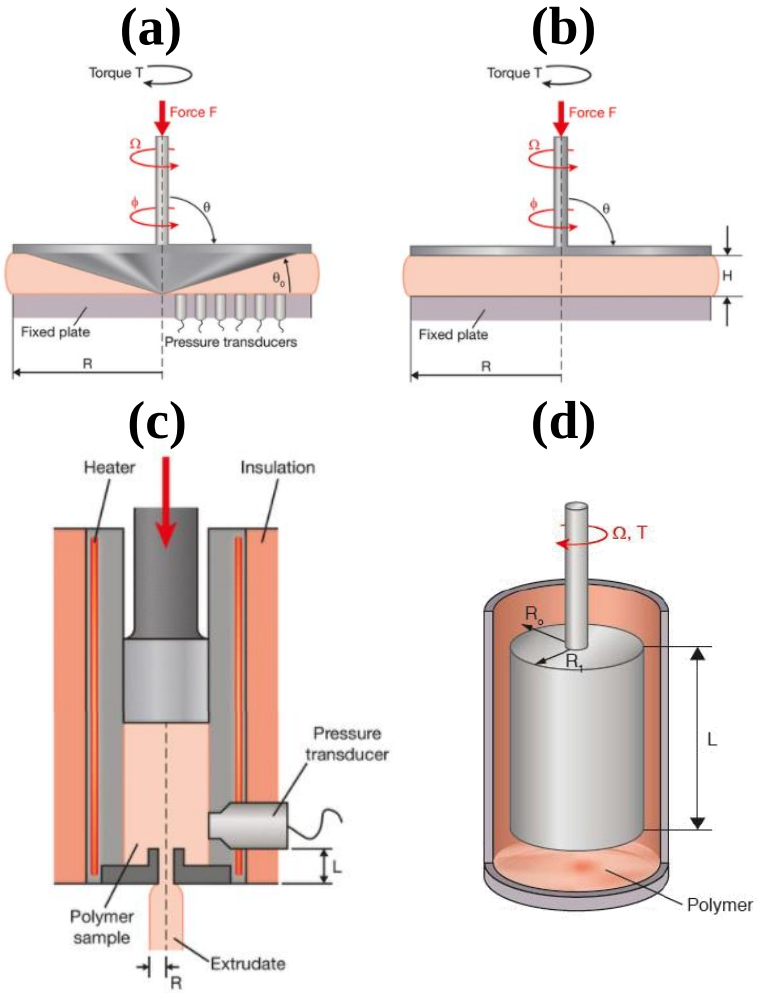

Figure 2.4: (a) Cone and plate geometry (b) Parallel plate geometry (c) Capillary rheometer (d) Couette rheometer (Osswald and Rudolph, 2015; Osswald and Menges, 2012)

Oscillatory Mode

In stationary mode rheometry, the shear stress or deformation rate is kept constant. In oscillatory mode, the moving plate goes back and forth and the torque variation is measured at adjusted values of amplitude and frequency of angular oscillation e.g. within the linear range of deformation to study the viscoelasticity of materials. This range is known as the 'Linear Viscoelastic' or 'LVE' region which indicates the span of values at which the sample structure is not destroyed (Figure 2.5). Viscoelastic materials exhibit a delayed response of deformation

under oscillatory stress e.g. a time lag or a phase shift, δ, between 0 and 90º. The two extremes are for ideal elastic deformation (pure solid) where δ = 0º and ideal viscous (fluid) flow behaviour where δ = 90º (Anton-Paar, 2019; Kutz, 2013). The complex shear modulus, G^* (Pa), describes the overall viscoelastic behaviour of a material (Anton-Paar, 2019):

$$G^* = \frac{\tau_a}{\gamma_a} \tag{2.7}$$

where τ_a is the shear-stress amplitude and γ_a is the strain amplitude (dimensionless or expressed as %). It also has two components: the storage modulus, *G'*, which represents the elastic response and the loss modulus, *G''*, which represents the viscous response (Figure 2.5).

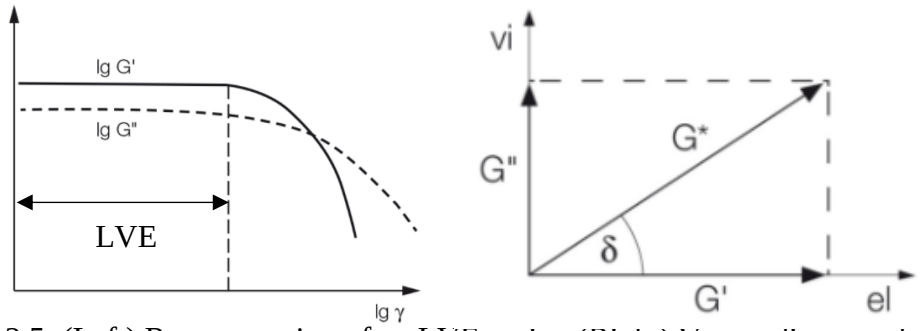

Figure 2.5: (Left) Representation of an LVE region (Right) Vector diagram showing components of the complex shear modulus (Anton-Paar, 2019)

Amplitude and frequency sweeps are the two main oscillatory tests. The former is used to determine the upper limit of the linear deformation region whereas the latter describes the time-dependent behaviour of the material within the linear deformation (non-destructive) range. For instance, low frequency simulates slow motion on long time scales while high frequency mimics fast motion on short time scales (Anton-Paar, 2019). The cone and plate geometry is usually used in oscillatory tests (Kutz, 2013; Osswald and Rudolph, 2015).

Extensional Viscosity Measurement

In addition to shear behaviour of materials, extensional or elongational properties are also important to be determined especially for polymeric processes (Osswald and Rudolph,

2015). Moreover, measuring extensional viscosity is also essential in the food industry as it is responsible for daily consumer activities such as spreading of butter, mouth-feel and swallowing of beverages and how well materials flow in process equipment such as in liquid sprayers where extensional viscosity effects retard the final jet breakup (Ahmed et al., 2017). The former can also be linked to the topic of tribology (science of interacting surfaces that are in relative motion from each other e.g. study of wear, friction and lubrication (Bhushan, 2013)) in terms of sensory perception, which is outside the scope of this thesis.

The most common modes of elongational deformation are portrayed in Figure 2.6. Meissner's extensional rheometer is shown in Figure 2.7 which uses a toothed rotary clamp system to grab the specimen while maintaining a constant specimen length. However, this design is limited to highly viscous rubbery liquids and soft polymeric materials e.g. polymer solutions (such as cellulose or polyvinyl alcohol (PVA)) used for film blowing, fibre spinning and extrusion, due to the difficulty associated with grabbing the sample ends as it is pulled apart (McKinley and Sridhar, 2002; Osswald and Rudolph, 2015).

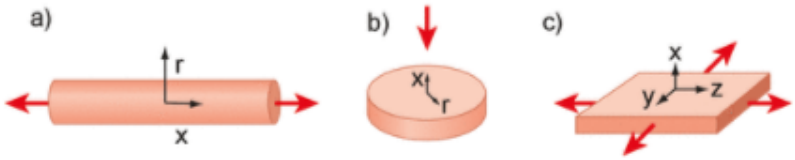

Figure 2.6: Geometries for pure extensional flow geometries: (a) simple extension (b) squeezing and (c) sheet stretching (Osswald and Rudolph, 2015)

Another method of determining extensional viscosity appropriate for both low- and high- viscosity liquids under extensional flow is by using a Capillary Breakup Extensional Rheometer (CaBER). A sample is situated between two plates of identical diameters and at t_0, one or both of the plates are set into rapid motion resulting in the elongation of the specimen at a relatively short distance. When the plate is then put into a halt, the change in diameter as a function of time of the filament, D_{min}, is measured at the midpoint between the two plates

(Figure 2.8). The measurement stops when the filament eventually breaks. The monitoring of the filament diameter is achieved using a laser or captured photographs with a high-speed camera (Ahmed et al., 2017).

The extensional viscosity, μ_E, is calculated by dividing the net tensile stress, σ_E with the velocity gradient in the direction of stretching (elongational strain rate), $\dot{\varepsilon}$ (Ahmed et al., 2017):

$$\mu_E = \frac{\sigma_E}{\dot{\varepsilon}} \tag{2.8}$$

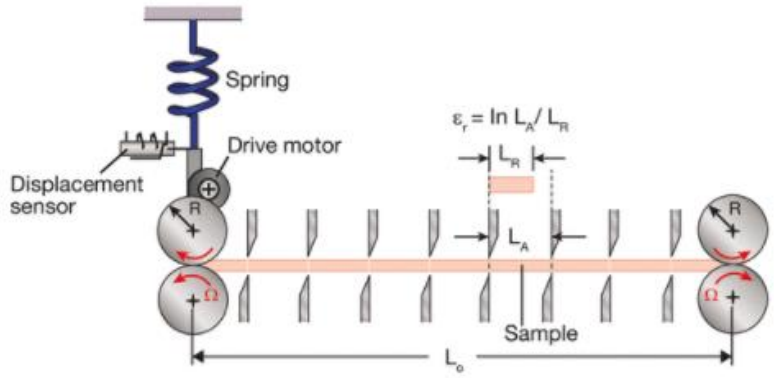

Figure 2.7: Schematic of Meissner's extensional rheometer (Osswald and Rudolph, 2015)

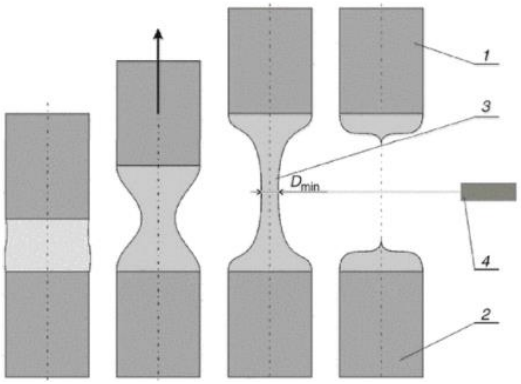

Figure 2.8: Liquid filament breakup: 1. Moving plate, 2. Stationary plate, 3. Filament stretching, 4. Laser system for measuring filament diameter (Ahmed et al., 2017)

2.2.3 Other Measurement Techniques

Fluid Physical Properties

Surface and Interfacial Tension (SFT and IFT)

Surface tension is the phenomenon observed that results from the short-range cohesive forces between liquid molecules at the molecular level. The molecules in the bulk interact

equally with each other in all directions whereas for those on the surface e.g. liquid-air interface, an unbalanced attractive force is apparent due to the absence of neighbouring molecules which results in a net inward pull (Shaw, 1992). Surface and interfacial tensions are essentially the same although the former is customarily used for liquid-air interface while the latter is used for liquid-liquid or liquid-solid interfaces. In addition, they are also dependent on temperature, pressure and presence of surfactants. SFT is essential in determining the critical micelle concentration (c. m. c.) of a surfactant system and IFT is an important parameter to consider in terms of emulsion formation e.g. by lowering interfacial energy through the use of surfactants, which may also influence emulsion stability via electrostatic or steric stabilisation, depending on the type used (Chang, 2016; Garti and Lutz, 2006). There is a variety of measurement techniques for SFT and IFT which are categorised as static, detachment and dynamic. Static measurement is considered to have greater accuracy especially if surfactants are involved and two popular methods are force and optical tensiometry (Laurén, 2019; Shaw, 1992). For the former, two most commonly used probes are the Du Noüy ring and Wilhelmy plate which are made up of platinum to ensure zero contact angle (Laurén, 2019) whereas the latter measures SFT and IFT through image analysis e.g. pendant (or sessile) drop shape analysis.

Droplet Size Analysis

Specifically for emulsion products, droplet size measurement is important because it is a valuable indicator of its quality and performance (Horiba, 2014). This is especially true for characterising its size distribution which gives information on its stability as well as providing information on manufacturing process efficiency (Dalgleish, 2001). Moreover, droplet size distribution (DSD) also determines the shelf life, appearance, texture/feel and scent of products (McClements, 2005). DSD measurement is also vital in defining characteristic drop diameters e.g. Sauter mean diameter ($d_{3,2}$) which serves as accurate descriptors of the size of the dispersed

phase. Nowadays, there are a number of advanced rapid particle size analysis techniques available such as laser diffraction, dynamic light scattering and image analysis (Horiba, 2014). The range of particle/droplet sizes of some of these techniques are shown in Figure 2.9 below.

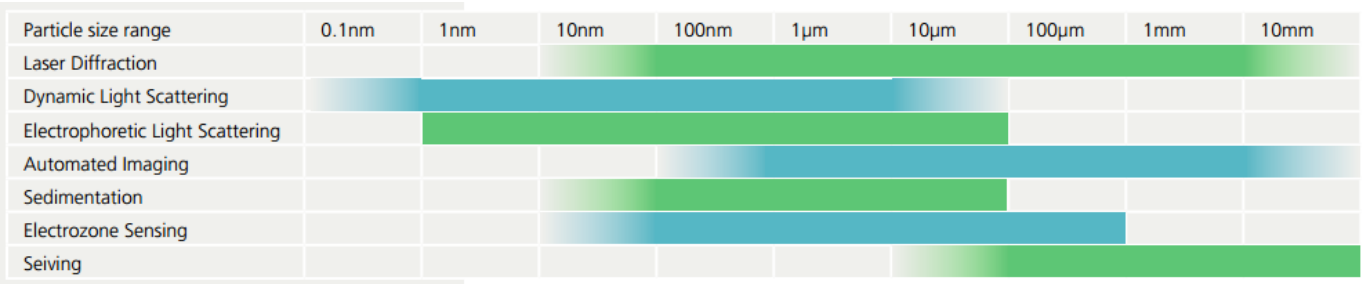

Figure 2.9: Available particle size analysing techniques (Malvern, 2012)

2.2.4 Classification of Fluid Flow

Fluid flow can be classified in a variety of ways in terms of: temporal and spatial effects, degree of fluid compressibility, viscous and inertial effects and many more as portrayed in Figure 2.10 (Khan, 2015). The most relevant categories are discussed in more detail below.

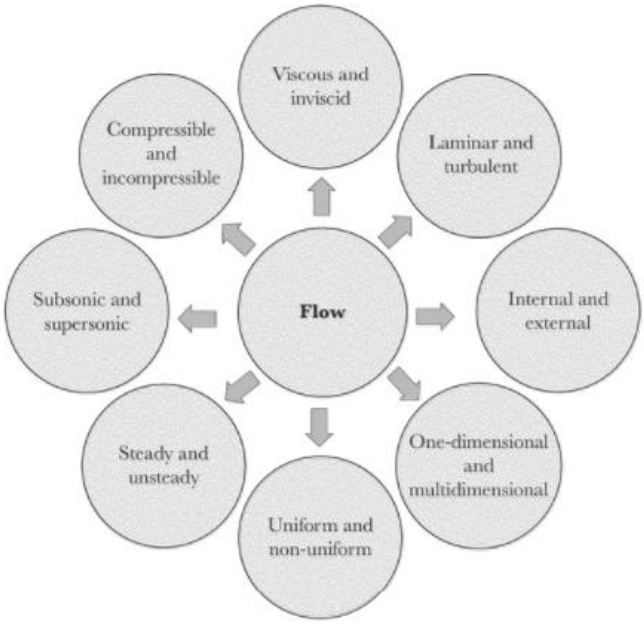

Figure 2.10: Classification of fluid flow (Khan, 2015)

Laminar and Turbulent Flows

This category is based on the ratio of inertial to viscous forces, defined by a non-dimensional Reynolds number, *Re*:

$$Re = \frac{inertial\ forces}{viscous\ forces} = \frac{\rho u L}{\mu} = \frac{uL}{\nu} \tag{2.9}$$

where ρ is the fluid density (kg m^{-3}), u is the characteristic velocity (m s^{-1}), L is the characteristic length (m), μ is the dynamic viscosity (Pa s) and υ is the kinematic viscosity (m^2 s^{-1}).

Laminar Flow

Laminar flow is considered the most ordered flow and is achieved at low velocities (given that geometry and fluid properties are fixed). The fluid flows in thin layers (laminae) over one another (Figure 2.11a) where linear viscous forces dominate (low Reynolds number). Fluid velocity at an arbitrary point also appears to stay constant over time (Figure 2.11b).

Turbulent Flow

In contrary for turbulent flow, the motion of individual fluid molecules is random (Figure 2.11a) as inertial effects cause instabilities to grow at higher Reynolds numbers. For a steady-on-average turbulent flow, the fluid velocity at an arbitrary point fluctuates around a steady mean value (Figure 2.11b).

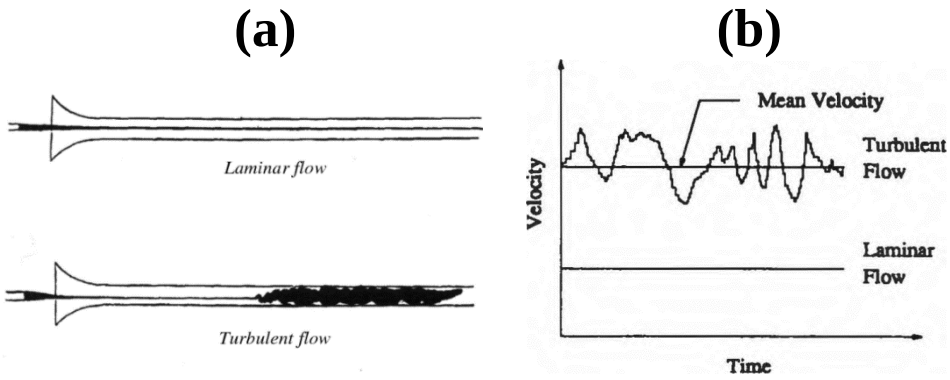

Figure 2.11: (a) Laminar and turbulent flow patterns in a pipe flow dye experiment by Osborne Reynolds (Reynolds, 1883) (b) Flow velocity fluctuation at an arbitrary point in a flow (Martin and McCutcheon, 1999)

Transitional Flow

Transitional flow is the intermediate zone between laminar and turbulent flows. At increasing Reynolds numbers, viscous effects mitigate the growth of instabilities caused by the

inertial effects up to a critical Reynolds number, Re_{crit}, above which the flow is considered fully turbulent and driven by inertial forces. The ranges of Reynolds numbers where the flow is considered laminar, transitional or turbulent depends on the geometry being considered e.g. for stirred vessels, the flow is fully turbulent at $Re \geq 10{,}000$.

Internal and External Flows

Internal flows occur in regions enclosed by solid surfaces e.g. flow inside pipes and ducts while external flows occur over solid objects e.g. flow over vehicles and aircraft.

One-dimensional and Multi-dimensional Flows

Dimensionality of flow describes the variation in fluid properties in terms of directions. A flow is one-dimensional (1-D) if it only takes place in one specific direction where a line represents the flow domain and points represent the boundaries. If the fluid properties vary significantly in various directions, then it is multi-dimensional. For a two-dimensional (2-D) flow, planes and lines represent the flow domain and boundaries respectively. For three-dimensional flows, where variations occur in all three directions, the flow domain is represented by a volume that is enclosed with planes or surfaces as boundaries.

Uniform and non-Uniform Flows

A flow is uniform if the magnitude and direction of fluid velocity in a flow field are constant at every point at a given instant of time. It is non-uniform if the velocity fluctuates at every point at a given instant of time.

Steady and Unsteady Flows

Motion of fluids is a function of both space and time. A flow is steady if it is time invariant e.g. fluid properties remain constant with time. In contrast, it is unsteady if the fluid properties vary considerably with time e.g. turbulent flows by definition are always unsteady.

Viscous and Inviscid Flows

An ideal fluid possesses zero viscosity and constant density. However, all real fluids are inherently viscous and thus exhibit both viscous and non-viscous (inviscid) flow phenomena. Viscous flows are confined within a very thin region near a solid surface, called the boundary layer, where viscous forces dominate and beyond which, the flow is considered inviscid. This is because according to Newton's law of viscosity (Equation 2.2), the effect of velocity gradient becomes increasingly small as the distance from the solid surface increases, to the point that it can be considered negligible above the boundary layer.

2.3 Liquid-Liquid Mixing

2.3.1 Emulsions Background

Emulsions are liquid-liquid systems with one immiscible liquid dispersed in droplet form, typically in the size range of 0.1 to 100 μm (dispersed phase) to another (continuous phase). Available liquid-liquid systems include the biphasic water-in-oil (W/O) and oil-in-water (O/W) systems or more complex systems such as double emulsions: oil-in-water-in-oil (O/W/O) and water-in-oil-in-water (W/O/W), and water-in-water (W/W) systems, also known as aqueous two-phase systems. The concentration of emulsion droplets is described as the dispersed phase volume fraction (Tadros, 2009).

Formulated emulsion products are usually manufactured by mechanical means e.g. by homogenisation and are either formed fresh from two separate immiscible liquids or by re-processing existing emulsions to reduce their current droplet sizes (McClements, 2005). Due to the thermodynamically unstable nature of these systems e.g. the two phases will coalesce and separate to reduce the system's free energy, a third component, namely an emulsifying agent (e.g. surfactants, proteins, polysaccharides), is required for their formation (lowering interfacial

tension) and stabilisation (prevent coalescence). The system, however, is only kinetically stable and long-term stability depends on the type of emulsifier used (Tadros, 2009; Walstra, 2005). Some breakdown processes of emulsions are shown in Figure 2.12.

Breakdown or instability (phase separation) of emulsions could be prevented by using emulsifiers which are surface active molecules that are normally amphiphilic and contain polar and non-polar regions or by using emulsion stabilisers such as viscosity modifiers. They adsorb onto droplet surface and alter the interfacial tension, aiding droplet break-up and preventing coalescence as described in §2.3.2. Moreover, additional ingredients such as texture modifers like thickeners may be added to the formulation to increase the viscosity of the continous phase and avoid phase separation through density differences (Hall, 2012).

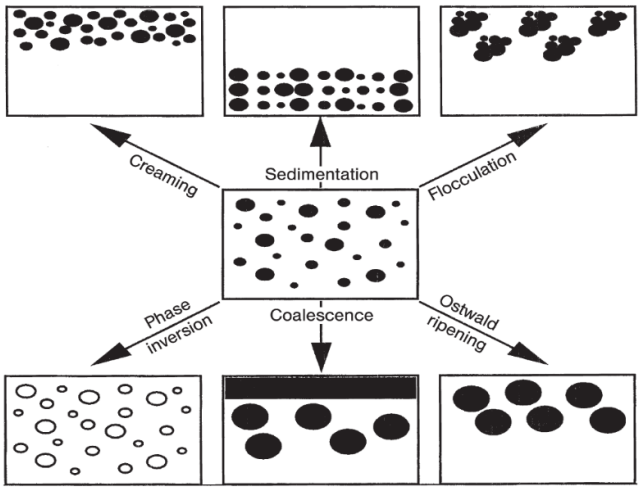

Figure 2.12: Different break-up processes in emulsion systems (Tadros, 2009)

2.3.2 Surfactants

Surface active molecules, known as 'surfactants' are amphiphilic in nature, meaning they consist of both hydrophilic and hydrophobic sections which have partial affinity towards both polar and non-polar phases (Figure 2.13). The hydrophilic regions of a surfactant molecule can either contain ionic functional groups e.g. ammonium and carboxylate or non-ionic polar groups e.g. a hydroxyl group. On the other hand, hydrophobic regions are made up of non-

polar moieties such as hydrocarbon chains (Free, 2008; Salager, 2002). The amphiphilicity of surfactants allow them to migrate to surfaces (gas-liquid or solid-liquid) or interfaces (liquid-liquid) with ease which is responsible for the lowering of the surface or interfacial tension (Salager, 2002). Classifications for surfactants include: anionic, cationic, non-ionic and zwitterionic (Free, 2008). Uses of such surfactants are summarised in Table 2.2.

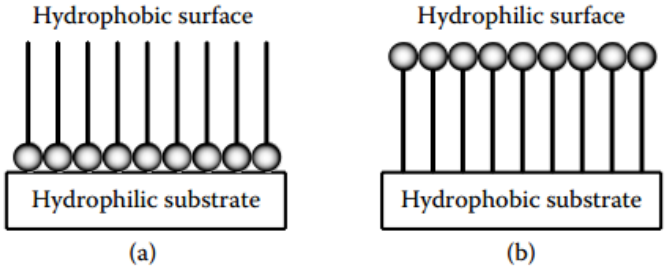

Figure 2.13: Representation of how amphiphilic surfactants arrange themselves when exposed in (a) Hydrophilic substrate and (b) Hydrophobic substrate. The polar head groups are the hydrophilic parts of the surfactants and the straight line chains represent their hydrophobic tails (Free, 2008).

Table 2.2: Summary of surfactant types (Free, 2008; Salager, 2002)

Surfactant	Use
Anionic	Most commonly used surfactants (account for about 50% of global production). Examples include lauryl sulphate (foaming agent), alkylbenzene sulfonates (detergents), fatty acids (soaps) etc.
Cationic	These are mainly used for: adsorbing negatively charged substances to induce a hydrophobic and or anti-static effect; corrosion management and bactericide. Examples include quaternary ammoniums and fatty amine salts. They are also more expensive than anionic surfactants because of the high pressure hydrogenation process involved in their production.
Non-ionic	Non-ionic surfactants are generally used as emulsifying agents and account for about 45% of the world production of surfactants. They are not found in salt forms and are available as alcohols, poly(ethylene oxide)s and polyglucosides.
Zwitterionic	Contains both anionic and cationic constituents. Examples include synthetic products such as sulfobetaines and betaines or natural substances like phospholipids and amino acids.

2.3.3 Equipment and Procedures Used in Emulsification Processes

The conventional method of emulsification (Figure 2.14) is through the application of high shear stresses upon the dispersed phase. A pre-emulsion is usually made first using high shear mixers such as Ultra Turrax (primary homogenisation) followed by the secondary homogenisation of the resulting coarse emulsion to form stable microdroplets (Earle, 1983; Herrera, 2012; Schramm, 2006; Weiss, 2008). Different types of homogenisers used in emulsification processes are summarised in Table 2.3. The focus of this thesis is on HSMs.

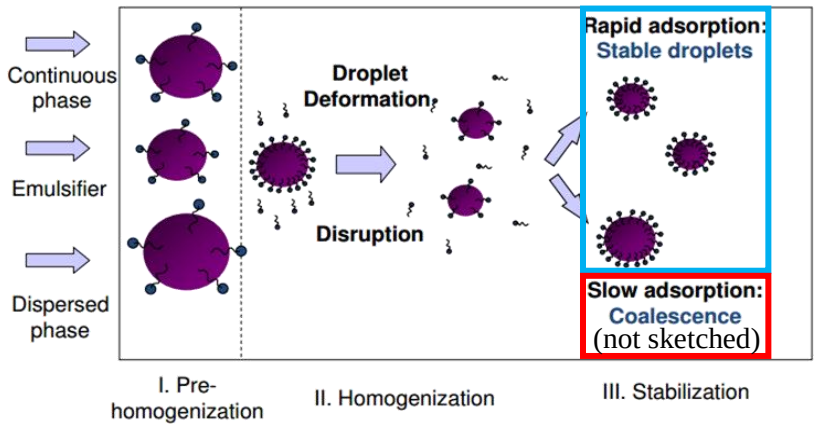

Figure 2.14: Physiochemical processes that occur during homogenisation (Weiss, 2008)

Table 2.3: A summary of homogeniser types used in producing emulsions by comminution adapted from Schramm (2006) and Weiss (2008)

Device	Mode	Mechanism	Energy Input	Use
High Speed Blender	Batch	Turbulence	Low	Premix production
High Pressure Homogenisers	Continuous	Turbulence/ cavitation	High	Homogeniser in food industry for milk, cream etc.
Colloid Mill	Continuous	Laminar flow	Moderate	Preparation of suspensions and emulsions
High Shear Mixer	Batch/ Continuous	Turbulence and high shear forces	High	Solid-liquid suspensions, emulsions, chemical reactions etc.
Ultrasonic Disruptor	Batch	Turbulence/ cavitation	High	Cosmetics, skin lotions, varnishes, ointments and tissue homogeniser
Membrane Homogenisers	Batch/ Continuous	Dynamic membrane/ pulsed flow	Moderate to High	Drug delivery systems

Unfortunately, as implied from Figure 2.15, mechanical mixers (red dash-dot (-.) line) can be very energy intensive especially when used to produce smaller droplets and thus are not very sustainable in terms of energy, raw material use and operating expenses (Hall, 2012). This is why optimisation studies that link control of process parameters to hydrodynamics and droplet break up mechanisms are very important.

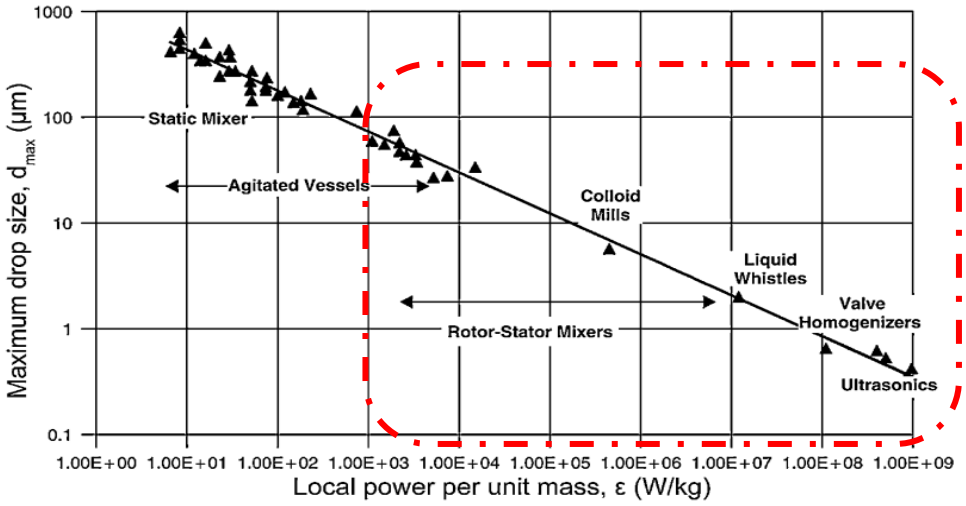

Figure 2.15: Maximum drop size against local power draw for dilute O/W dispersions (Davies, 1987; Paul et al., 2004; Zhang et al., 2012)

2.4 High Shear Mixers

HSM mixing heads consist of a high speed rotor (rotating mixing element with a typical tip speed range of 10 to 50 m s^{-1}) and a stator (fixed mixing element) which are in close proximity to each other (Atiemo-Obeng and Calabrese, 2004), with a rotor-stator (R-S) gap ranging from 100 to 3000 µm (Karbstein and Schubert, 1995). The operating principle (Figure 2.16), involves drawing the fluid axially into the R-S gap (stage 1 – suction); exposing it to high tangential velocity gradients and turbulence (equivalent shear rates from 20,000 to 100,000 s^{-1}) (stage 2 – acceleration); and eventually ejecting it radially in the form of jets through the stator holes (stage 3 – expulsion) (Silverson, 2016; Utomo et al., 2009; Zhang et al., 2012).

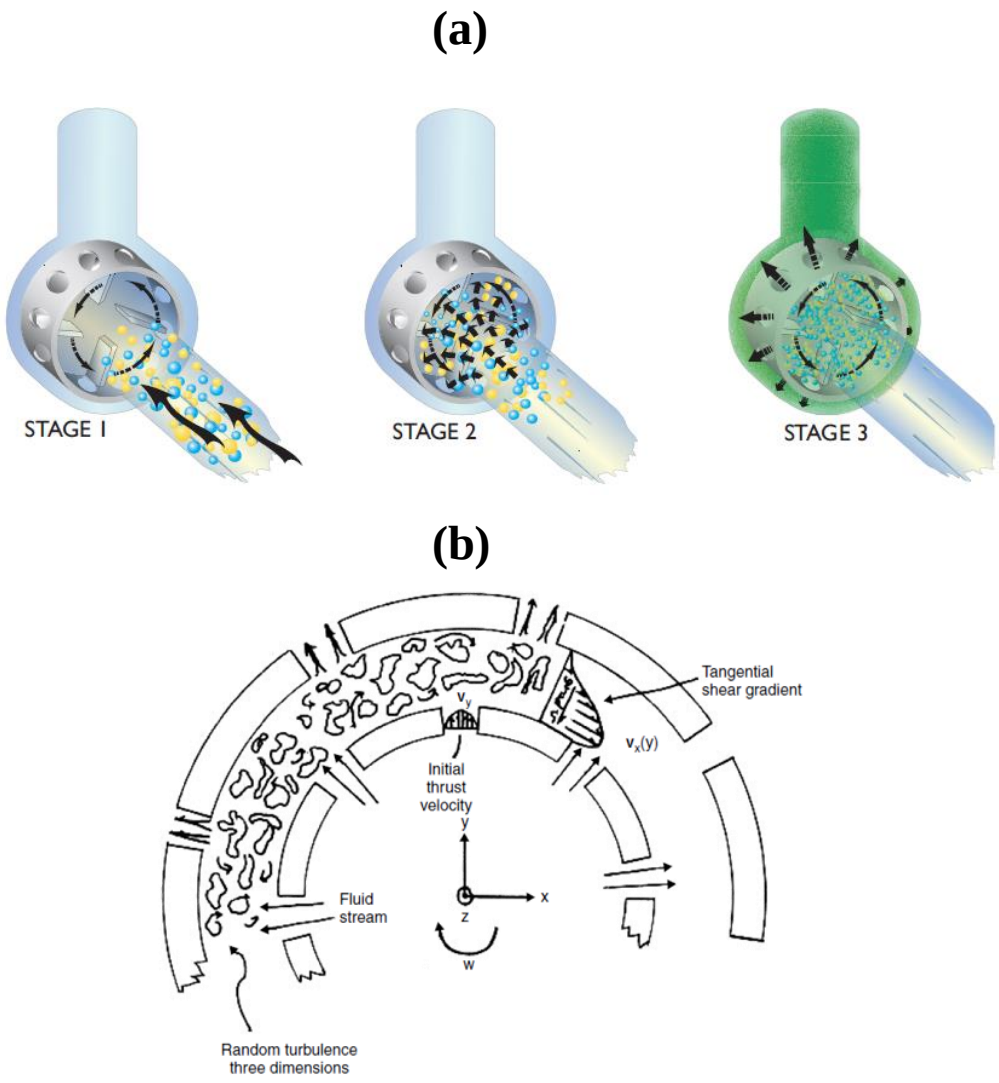

Figure 2.16: (a) Operation of in-line rotor-stator mixers (Silverson, 2016) (b) Schematic of hydrodynamics in a rotor-stator mixer (Atiemo-Obeng and Calabrese, 2004)

2.4.1 Designs, Types and Configuration

The main categories that encompass various designs of high shear mixers based on the dominating flow patterns in the mixing head include axial and radial discharge mixers, toothed devices and colloid mills (Atiemo-Obeng and Calabrese, 2004).

Axial Discharge Mixers

Axial discharge mixers consist of a rotor that directs the fluid axially through bored stator holes. The motion of the rotating impeller then generates tangential shear flow inside the stator. The rotor-stator clearance can be adjusted by combining various bushings and washers. They are also capable of delivering high throughputs if installed in-line (Atiemo-Obeng and Calabrese, 2004). Examples are those of Chemineer Greerco's designs shown in Figure 2.17.

Figure 2.17: (a) Single-stage and (b) Two-stage axial discharge mixer designs by Chemineer Greerco (Atiemo-Obeng and Calabrese, 2004)

Radial Discharge Mixers

In comparison to axial discharge mixers, the rotating radial impeller of these mixers pushes the fluid radially through the stator perforations (slots or holes) and has good pumping capacity. In addition to the radial flow, tangential shear flow also persists inside the stator (Atiemo-Obeng and Calabrese, 2004). They are robust, reliable and adaptable in manufacturing various products in commercial environments (Hall, 2012) and are available in several sizes (lab-, pilot- and factory- scale) and configurations (batch or in-line) to suit the intended application. Silverson Machines Ltd. and Ross Mixers are popular producers of these mixers.

A sub-section on the former, who manufactured the in-line Silverson 150/250 MS higher shear mixer model used in this study, is presented below.

Silverson High Shear Mixers

Silverson Machines Ltd. offers a variety of design, sizes and configurations of radial discharge mixers. Their mixing units are fitted with interchangeable assemblies, allowing for various stator designs (Figure 2.18) to be used in accordance with the process requirement.

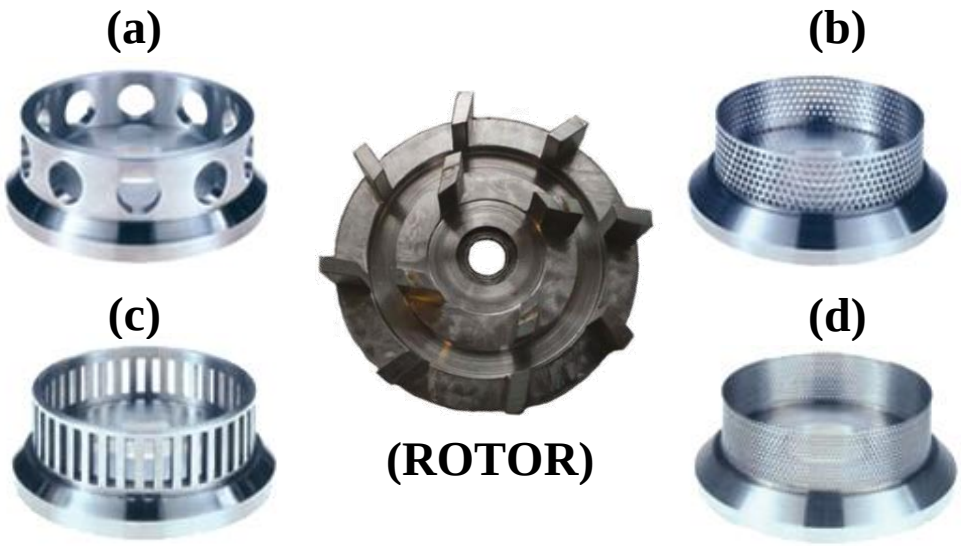

Figure 2.18: Images of the rotor (Cooke et al., 2012) and the stators: (a) General purpose disintegrating head (b) Square hole high shear screen^{TM} (c) Slotted disintegrating head (d) Emulsor screens (Silverson, 2019).

Their batch mixers include the laboratory scale L5 series (Figure 2.19a) which has the capacity to mix volumes of 1 mL up to 12 L and can be fitted with an in-line work head (pumping capacity of up to 20 L min^{-1}) or tubular mixing units (Silverson, 2019). The factory batch mixers (Figure 2.19b) can accommodate up to 30,000 L and are available as a bottom entry configuration (Figure 2.19c) for dispersing powders and processing highly viscous materials.

Silverson in-line mixers are self-pumping and are available in the laboratory scale e.g. the Verso model in Figure 2.20a, which can deliver a throughput of up to 1,500 L hr^{-1} and

factory scale (Figure 2.20b) which can process up to 300,000 L hr^{-1} depending on the selected model. They also come in specific designs to suit the process application. For instance, in sanitary processes that need to abide by strict manufacturing regulations, the ultra-hygienic design is an option or in powder dispersion, a hopper can be installed in its inlet for ease of incorporation. Finally, they can also be configured for single- or multiple-stage mixing (Silverson, 2019).

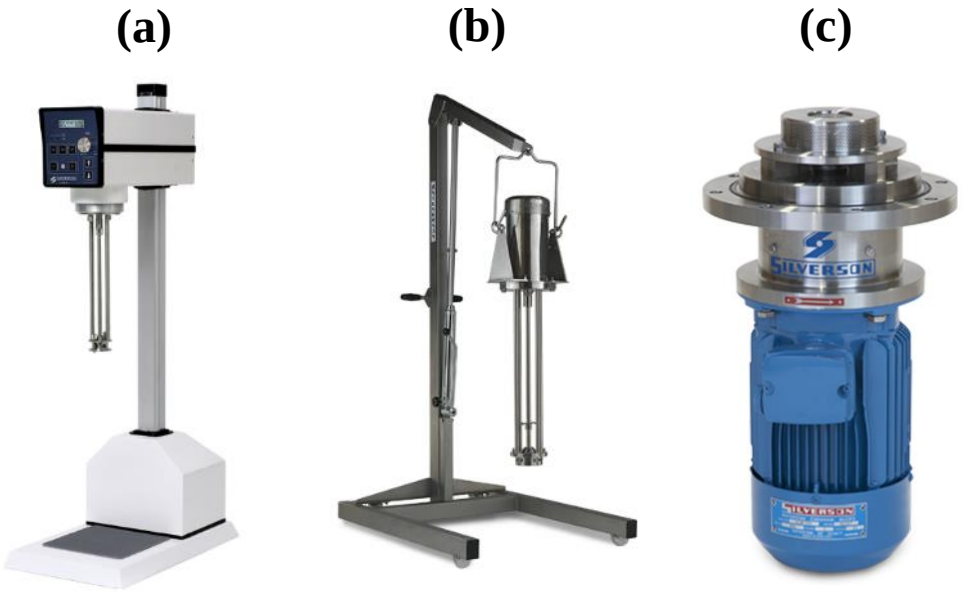

Figure 2.19: Batch Silverson mixers (a) Laboratory scale mixer (L5) (b) Factory scale mixer and (c) Bottom entry mixer (Silverson, 2019) *[Images are not to scale]

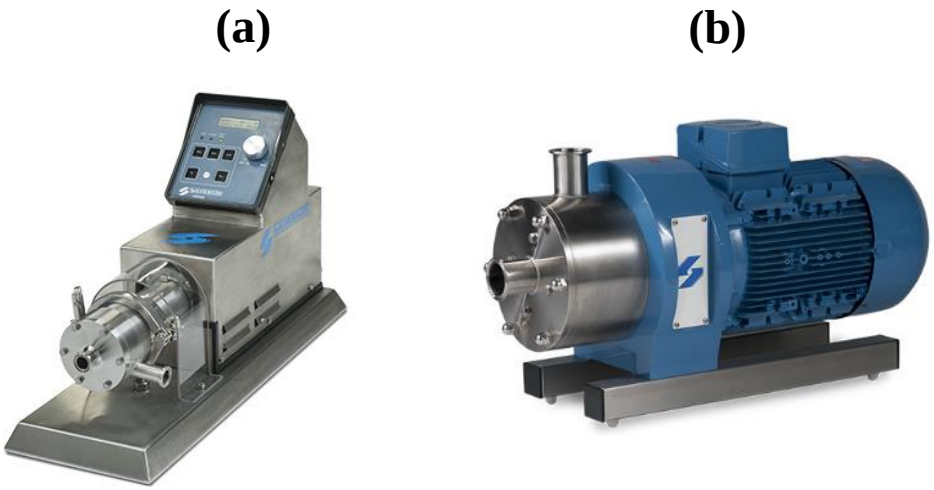

Figure 2.20: In-line Silverson mixers (a) Laboratory scale mixer (Verso) (b) Factory scale mixer (Silverson, 2019) *[Images are not to scale]

Toothed Devices

These devices have complex designs (Figure 2.21) where slots or teeth are present on both the rotor and stator. They also come as single or multiple stage assemblies to provide several paths for the fluid to flow into (Atiemo-Obeng and Calabrese, 2004).

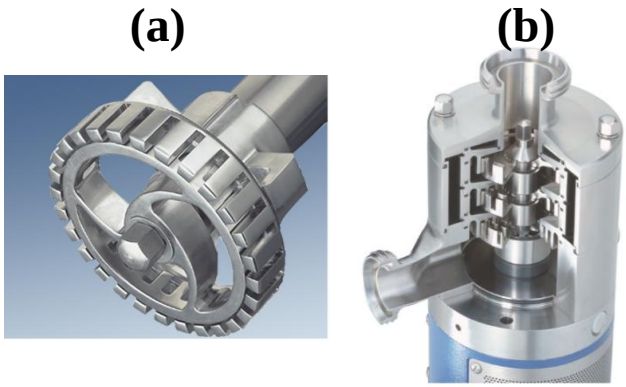

Figure 2.21: (a) Single-stage toothed device (b) Multi-stage assembly of toothed device (IKA, 2019)

Colloid Mills

Colloid mills (Figure 2.22) are wet milling devices that work by introducing a product premix in an adjustable narrow gap between a rotating surface (rotor) and stationary surface (stator) where it is subjected to high mechanical and hydraulic shear forces (Bematek, 2019). They are described as "a conical Couette device" by Atiemo-Obeng and Calabrese (2004). Surfaces used can either be smooth or grooved/serrated to promote laminar and turbulent flows respectively. They are often operated as in-line mixers in combination with an external pump as they possess poor pumping capabilities (Utomo, 2009).

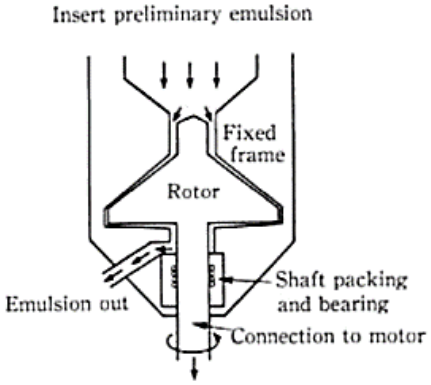

Figure 2.22: Colloid mill schematic diagram (Mitsui, 1997)

2.4.2 Configurations and Modes of Operation

Rotor-stator devices are classified as batch or in-line type. When the volume of materials required to be processed is relatively small, batch mixers is usually the option due to their simplicity and versatility (Hall, 2012). However, as the demand for capacity increases, batch devices are incapable of providing sufficient circulation flow because of the small mixing head in comparison to the vessel size and this leads to poor distributive mixing (Atiemo-Obeng and Calabrese, 2004). In such cases, it is more efficient to use an in-line mixer opposed to using a batch mixer with a larger rotor as power consumption rapidly increases with the rotor diameter e.g. $P \propto N^3 D^5$ which means a larger motor will be required and thus consume more energy (Pacek et al., 2013). For example, the rotor-stator device can be incorporated in the recycle loop with the primary purpose of delivering dispersive mixing (droplet break-up) while the distributive mixing (blending) is achieved in a mechanically agitated holding vessel (Baker, 1993; Kowalski et al., 2011). This is essential for the efficient mixing of materials with complex rheology e.g. highly viscous and non-Newtonian (Hall, 2012; Kowalski, 2009; Kowalski et al., 2011).

In-line devices can also be integrated in a continuous process in single- or multiple-pass modes (Figure 2.23). The former is a popular choice as they offer faster manufacturing times and are more energy efficient. However, in this set up, control of product quality is limited to the mixer rotor speed and process flow rate. Thus, multiple-pass systems are used where the number of passes controls the degree of homogenisation to achieve the desired product microstructure (Hall, 2012). Depending on what is feasible for the process, materials can be introduced directly into the mixing head or via injection in the upstream pipeline as shown in Figure 2.23a (Silverson, 2016). These configurations and operating modes emphasise the adaptability of in-line high shear mixers.

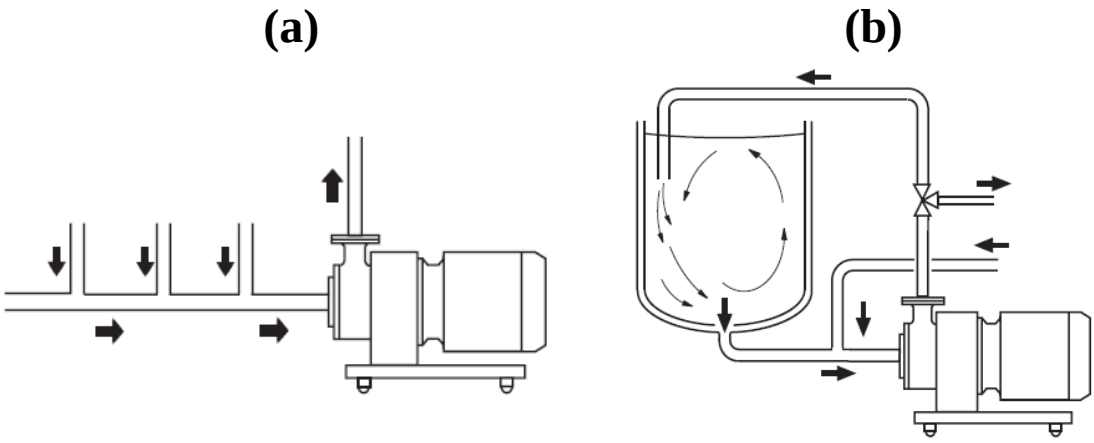

Figure 2.23: In-line mixer operating modes (a) Single-pass (b) Multiple-pass (Silverson, 2016)

2.4.3 Applications

Rotor-stator mixers are widely utilised in agricultural, biochemical & chemical, cosmetics, food, home and personal care as well as pharmaceutical industries to accomplish difficult and energy intensive mixing tasks. They are often employed in emulsification and dispersion processes to produce multiphase products such as shampoos, creams, deodorants, mayonnaise and salad dressings. In addition, they are also used in the de-agglomeration and solubilisation of solids, cell disruption etc. to make commodities such as adhesives, latex, chemical dispersions, pesticide formulations and many more (Atiemo-Obeng and Calabrese, 2004; Pacek et al., 2013; Utomo, 2009). Some of the specific applications of rotor-stator mixers are summarised in Table 2.4.

Table 2.4: Some of the specific applications of both batch and in-line rotor-stator devices (Atiemo-Obeng and Calabrese, 2004; Hall, 2012; Pacek et al., 2013; Utomo, 2009)

Phases	**Purpose**	**Examples**
Single Phase	Grinding/milling/ particle size reduction (solid)	De-agglomeration of powders.
	Accelerated dissolution/ blending (liquid)	Dilution of surfactant sodium lauryl ether sulphate (SLES) in water for making shampoos and shower gel.
Liquid-Solid	Powder wetting/ solid or polymer dispersion	Dispersion of silica and calcite on toothpastes. Pigment dispersion for inks and paints. Use of Carbopol/ CMC/ Xanthan gum to thicken shampoo/ dish-washing liquid/ toothpaste formulations with the absence of clumped material. Delamination of fibrous materials; cell disruption. Slurry Processing.
Liquid-Gas	Creating foams/ aerated products	Aeration of shower gels for aesthetic purposes.
Liquid-Liquid	Emulsification/ homogenisation/ surfactant mesophase	Making mayonnaise, ice cream, perfumes, body creams and lotions, hair conditioners and deodorants. Production of lamellar phase dispersions. Diesel formulation. Making primary emulsions for double emulsion microencapsulation techniques in pharmaceutical processes.

2.4.4 Mixer Power and Pumping Capacity

The power drawn or dissipated by a mixing impeller is an essential mixing process parameter used to assess its performance. It is defined as the amount of energy required to generate fluid motion by means of agitation and thus directly influences operating costs. Therefore, knowledge and accurate prediction of the power drawn is essential for optimising mixing processes e.g. in ensuring that adequate mixing is delivered to meet demands and that correct sizes of motors, gearboxes and shafts are installed. In addition, it also affects heat and mass transfer processes and is used as a scale up parameter for processes including emulsification (Hall, 2012).

The supplied power to a mixing system generates a circulating flow, *Q*, representing internal circulation and a velocity head, *H*, which provides the kinetic energy required to produce shear in mixing through pulsating motion of the fluid or jets and dissipated by turbulence (Hemrajani and Tatterson, 2004):

$$Q \propto ND^3 \tag{2.10}$$

$$H \propto N^2D^2 \tag{2.11}$$

where *N* is the rotor speed (rps) and *D* is the impeller diameter (m). Equation 2.10 can be re-written as:

$$N_Q = \frac{Q}{ND^3} \tag{2.12}$$

where N_Q is the pumping number, also known as the flow number and ranges between 0.30 – 0.76 for various impellers under turbulent flow. Moreover, it is dependent on the impeller type, impeller-to-tank diameter ratio (*D*/*T*) and a variant of the Reynolds number

defined in Equation 2.9 for stirred tanks e.g. the rotor tip speed ($U = U_{tip} = \pi ND$) and rotor outer diameter ($L = D$), are used as the characteristic velocity and length:

$$Re = \frac{\rho N D^2}{\mu} \tag{2.13}$$

The range of impeller Reynolds numbers at different flow regimes for stirred tanks can be used to predict (as an indication of) the flow regime in HSMs e.g. for laminar flow ($Re \leq 10$), for transitional flow ($10 < Re < 10^4$) and for turbulent flow ($Re \geq 10^4$) (James et al., 2017b).

Cooke et al. (2012) found that $N_Q \sim 0.050 – 0.070$ for a 150/250 Silverson mixer (similar as the one used in this study) which is much lower in comparison to that of stirred tanks as they have poorer pumping capabilities due to the additional flow restrictions in the equipment setup.

The total power dissipation in a system is defined as (Armenante, 2008):

$$P_{Total} = P_{Motor} + P_{Gearbox} + P_{Seal} + P_{Impeller} \tag{2.14}$$

In order to quantify $P_{Impeller}$, all the power sources in Equation 2.14 needs to be determined under dynamic conditions as well, which can be very challenging. Methods and equipment used in power draw investigation include: electric measurements, strain gauges, torque meters, dynamometers and calorimetric measurement (Armenante, 2008; Hall, 2012).

For cases where mixing parameters and a number of geometric variables have been defined, the overall power requirement can be determined through (Armenante, 2008; Simmons, 2012):

$$P = f(\rho, \mu, g, N, D, H, T, \frac{D}{T}, \frac{H}{T}, \frac{C}{T}, other\ geometric\ ratios) \tag{2.15}$$

By using dimensional analysis, Equation 2.15 can be re-written as:

$$Po = Ne = \frac{P}{\rho N^3 D^5} = f\left(\frac{\rho N D^2}{\mu}, \frac{N^2 D}{g}, \frac{W}{D}, \ldots\right) \tag{2.16}$$

where *Po* is the power number, also known as the Newton number, *Ne*, which is clearly a function of both the Reynolds number (Equation 2.13), as well as the Froude number, *Fr*, which is the ratio of inertial to gravitational forces:

$$Fr = \frac{N^2 D}{g} \tag{2.17}$$

The Froude number is only considered when extreme vortices are present and so can be treated negligible for baffled stirred vessels. In addition, if geometric similitude is met e.g. geometric ratios are constant (*D/T*, *H/T*, etc.), for single phase Newtonian fluids, Equation 2.16 can be simplified to (Hemrajani and Tatterson, 2004):

$$Po = f(Re) \tag{2.18}$$

where for laminar flow ($Re \leq 10$): $Po \propto Re^{-1}$, for transitional flow ($10 < Re < 10^4$): $Po = f(Re)$ and for turbulent flow ($Re \geq 10^4$): $Po = constant$ as shown in the power curves in Figure 2.24.

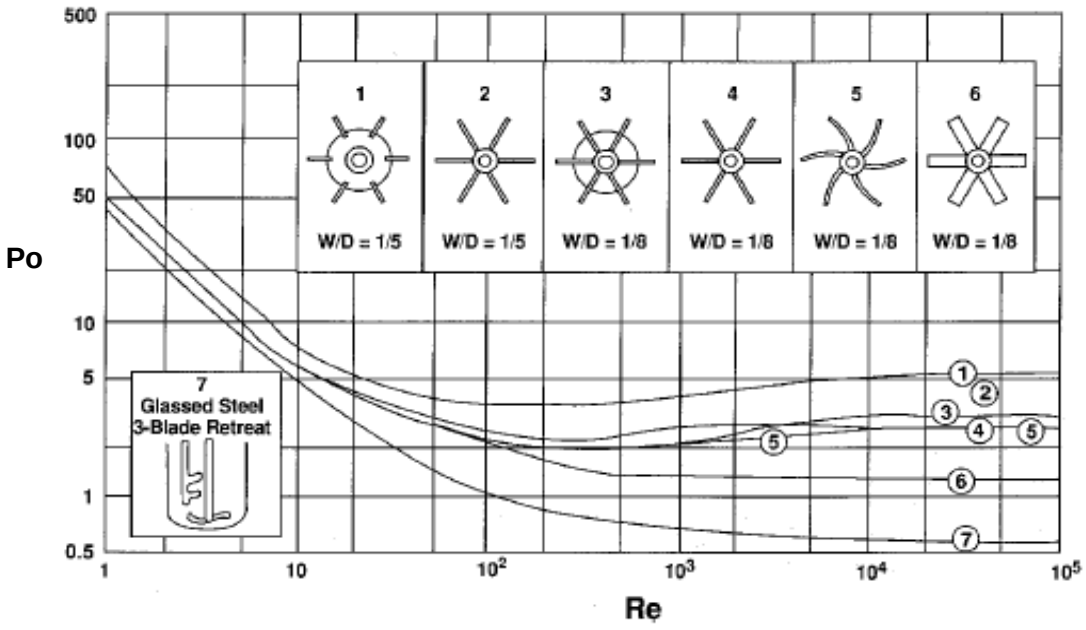

Figure 2.24: Power curves for various stirred tank impellers (Hemrajani and Tatterson, 2004)

For non-Newtonian fluids, in the laminar regime, power draw can be estimated using a correction using the Metzner-Otto equation (Metzner and Otto, 1957), which assumes that an average impeller shear rate, $\dot{\gamma}$ is proportional to the impeller speed, N:

$$\bar{\dot{\gamma}} = k_S N \tag{2.19}$$

where k_S is the Metzner-Otto constant which is a function of the impeller geometry and impeller flow number. For power law fluids, Equation 2.19 can be incorporated to the power law model to obtain:

$$\mu_A = K\bar{\dot{\gamma}}^{n-1} = K(k_s N)^{n-1} \tag{2.20}$$

which can then be substituted into Equation 2.13 to attain:

$$Re = \frac{\rho N D^2}{\mu_A} = \frac{\rho N^{2-n} D^2}{K k_S^{n-1}} \tag{2.21}$$

Power Draw in Batch Rotor-Stator Mixers

The power drawn of batch rotor-stator mixers can be measured and quantified in a similar way to that of stirred vessels e.g. using Equation 2.16 (Håkansson and Innings, 2017; Hall, 2012; Zhang et al., 2012). However, additional characteristic lengths need to be considered in rotor-stator mixers such as the rotor-stator clearance (shear gap width), δ, the nominal rotor diameter, D, and the hydraulic radius of the stator holes, R_h (Zhang et al., 2012). Padron (2001) acquired power draw data and quantified the power number of batch radial discharge mixers such as the Ross and Silverson mixing heads which are $Po \sim 2.4 – 3.0$ and $Po \sim 1.7 – 2.3$ respectively in the turbulent regime. Moreover, he found that turbulent power draw scaled with the rotor speed with an exponent ~2.84 – 3.45, which is close to the value of 3 as expected from Equation 2.16. In the laminar regime, he surmised that $Po \propto Re^{-1}$ and that it is somewhat independent of the stator geometry. Finally, he concluded that the most appropriate

correlation between *Re* and *Po* was achieved by using the rotor diameter, *D*, to calculate the Reynolds number (Equation 2.13).

Power Draw in In-Line Rotor-Stator Mixers

The approximation of power draw is more complicated for in-line rotor-stator mixers as the additional effect of the flow rate needs to be accounted for e.g. it is absent in Equation 2.16 (Hall, 2012). Thus, Kowalski (2009) proposed a multi-component expression for power draw of in-line rotor-stator mixers under turbulent conditions:

$$P = P_T + P_F + P_L \tag{2.22}$$

where P_T is the power required to rotate the rotor blade against fluid resistance in the gap: $Po_z \rho N^3 D^5$, analogous to Equation 2.16. P_F is power caused by the flow e.g. pumping action of the mixer which accelerates the fluid as well as actual pumping fluid away: $k_1 M N^2 D^2$. P_L are energy losses e.g. as sound and heat which can be neglected. The full expression is therefore:

$$P = Po_z \rho N^3 D^5 + k_1 M N^2 D^2 \tag{2.23}$$

where Po_z is the zero flow rate flow number and k_1 is the flow power constant.

Kowalski et al. (2011) conducted power draw measurements on a 150/250 in-line Silverson mixer (which is the same model used in this study, but with slightly different configuration; the rotor and stator geometries used are also similar but not exactly identical) where they used both torque measurement and calorimetric techniques. The values of Po_z and k_1 they obtained were 0.197 and 9.35 respectively for the torque method and 0.229 and 7.46 for the calorimetric procedure. Since the torque technique is considered as generally more accurate, the values used for Po_z and k_1 in in this study are 0.197 and 9.35 respectively.

Moreover, they fitted a power law on torque measured power versus the rotor speed and yielded an exponent ~ 2.5, which again is close to the value of 3 as in Equation 2.16. They attributed the discrepancy between the competing relationship between the power consumption under turbulent conditions ($\propto N^3D^5$) and the convection of energy from the mixer ($\propto N^2D^2$) (Kowalski et al., 2011; Zhang et al., 2012).

Håkansson and Innings (2017) also defined an analogous expression. They emphasise that the total energy or power dissipated, P_{diss}, or dissipated Turbulence Kinetic Energy (TKE) in the volume of fluid is not equal to the power input of an in-line mixer, P_{shaft}, defined in Equation 2.24. They argue that there is no consensus to how much of the power input is dissipated as turbulence.

$$P_{shaft} = \Pi_{rot} + \Pi_{flow} + \Pi_L = N_{P0}\rho N^3 D^5 + N_{P1}\rho Q N^2 D^2 + \Pi_L \tag{2.24}$$

The four main assumptions they identified in open literature are as follows:

1. $P_{diss} = \Pi_{flow}$, the total dissipative power is equivalent to the flow factor in Equation 2.24.
2. $P_{diss} = \Pi_{rot}$, the total dissipative power is equal to the rotational factor in Equation 2.24.
3. $P_{diss} = \Pi_{rot} + \Pi_{flow}$, assuming that all of the shaft power, excluding losses, is dissipated. This is the assumption made by (Kowalski et al., 2011).
4. $P_{diss} = \Pi_{rot} - \Pi_{flow}$, assuming that the dissipated energy is the difference between the rotational and flow terms in Equation 2.24.

In addition, they also identified the general disagreement on the effective region where dissipation occurs e.g. in the rotor-swept volume, rotor-stator clearance, stator hole, or a combination of these. Moreover, they acknowledged the difficulty of directly measuring the total turbulence dissipation, P_{diss}, and proposed to use measurable quantities to perform a differential energy balance over the mixer volume as portrayed in Figure 2.25:

$$P_{shaft} = P_{thermal} + P_{pump} + P_L \tag{2.25}$$

where $P_{thermal}$ is the thermal energy caused by the increase in fluid temperature. P_{pump} is the pumping energy caused by the increase of static and/or dynamic fluid pressure.

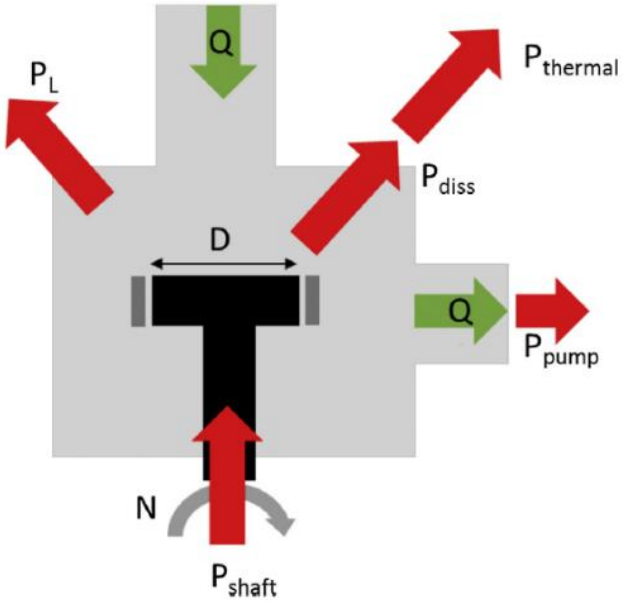

Figure 2.25: Illustration of energy balance in an in-line rotor-stator mixer (Håkansson and Innings, 2017)

They suggested that the increase in thermal energy may be due to both dissipation of TKE and laminar viscous heating. In the turbulent regime, the latter is small and can be neglected. Furthermore, at steady state conditions, it can be assumed that the resulting increase in thermal energy is equal to the rate of production and subsequent dissipation of TKE e.g. $P_{thermal} = P_{diss}$ and thus Equation 2.25 can be re-written as:

$$P_{shaft} = P_{diss} + P_{pump} + P_L \tag{2.26}$$

Or,

$$P'_{shaft} = P_{shaft} - P_L = P_{diss} + P_{Pump} \tag{2.27}$$

where P'_{shaft} is defined as the 'loss-free power draw'. Moreover, as the consequence of energy conservation and through substitution of Equation 2.27 into Equation 2.24, assuming $\Pi_L = P_L$, P_{diss} and P_{pump} are directly related as follows:

$$P_{diss} = \Pi_{rot} + \Pi_{flow} - P_{pump} \tag{2.28}$$

where P_{pump} is measured experimentally using pressure transducers and is defined as follows:

$$P_{pump} = P_{pump,static} + P_{pump,dynamic} = \Delta P_{static} Q + \Delta P_{dynamic} Q \tag{2.29}$$

where ΔP_{static} *and* $\Delta P_{dynamic}$ represent the static and dynamic pressure differences between the inlet and outlet of the in-line rotor-stator mixer. The former is usually used as the latter is normally assumed to be negligibly small. Finally, they also suggested an expression for P_{pump} through the use of ideal centrifugal pump theory and the conservation of angular momentum (all of the rotor blade torque is used for pumping e.g. converted to static pressure) to determine how pumping power depends on process parameters and design:

$$P_{pump} = \rho Q N^2 D^2 \left(\pi^2 - \frac{D^2}{\pi A tan(\beta)} N_Q\right) = \Pi_{flow} \left(\frac{\pi^2}{N_{P1}} - \frac{D^2}{\pi A N_{P1} tan(\beta)} N_Q\right) \tag{2.30}$$

where β is the blade angle (rad) and A, is the rotor blade area (m^2). For radial discharge mixers with radial blades (β = 90º), Equation 2.30 simplifies to:

$$P_{pump} = \Pi_{flow} \left(\frac{\pi^2}{N_{P1}}\right) \tag{2.31}$$

2.4.5 Droplet Break-Up in HSMs

A variety of parameters associated with product formulation and processing conditions influences droplet break-up mechanisms e.g. raw material properties and process variables such as temperature and rotor speed, has been investigated and described by authors using empirical and theoretical models. Furthermore, coalescence of droplets also affects their sizes but can be deemed negligible if the system is dilute e.g. very low phase volume fraction (Hall, 2012). Ultimately, it is the equilibrium between droplet break-up and coalescence mechanisms that determine the maximum stable drop size.

Cohesive and Disruptive Forces

The balance between cohesive and disruptive stresses acting on a drop determines whether it deforms or breaks. The latter occurs when sufficient energy is exerted to overcome the increase in surface energy imposed by the increase in total surface area. Cohesive stresses, which are assumed to be additive, arise from the interfacial tension between the dispersed and continuous phases (Equation 2.32) and/or the internal viscous stress (Equation 2.33). Disruptive stresses originate from external stresses acting on the droplet interface e.g. inertial and viscous stresses. An example of the former are pressure fluctuations in turbulent flows (Equation 2.34) and the latter due to a velocity gradient, *G*, manifested by the surrounding continuous phase (Equation 2.35). In laminar flow, *G* can be the shear rate ($\dot{\gamma}$) and in turbulent flow, it can be the velocity gradient of eddies (viscous shear) that are of similar size to the drops (Calabrese et al., 1986; Hinze, 1955; Kolmogorov, 1949; Zhou and Kresta, 1998). Coalescence is another phenomenon that affects droplet size, which is often neglected in very dilute dispersions or emulsion systems.

$$\tau_{cohesive,1} = \frac{4\gamma}{d} \tag{2.32}$$

$$\tau_{cohesive,2} = \frac{\mu_d}{d}\sqrt{\frac{\gamma}{\rho_d}} \tag{2.33}$$

$$\tau_{disruptive,1} = \overline{\rho_c U^2(d)} \tag{2.34}$$

$$\tau_{disruptive,2} = \mu_c G \tag{2.35}$$

Capillary and Weber Numbers

A useful indicator whether droplet break-up is likely to occur is the ratio of disruptive (acting on droplet surface) to cohesive (resisting droplet deformation) stresses ($\tau_{disruptive}/\tau_{cohesive}$) referred to as the Capillary number (*Ca*) (Equation 2.36a) and Weber (*We*) numbers (Equation 2.36b) for laminar and turbulent flows respectively. They are used to relate hydrodynamic conditions and physical properties of the continuous and dispersed phases to the maximum stable droplet size.

$$Ca = \frac{\mu_c U}{\sigma} \tag{2.36a}$$

$$We = \frac{\rho_c U^2 L}{\sigma} \tag{2.36b}$$

A variant of the Weber number (Equation 2.37) (Paul et al., 2004) can be derived if the rotor tip speed ($U = U_{tip} = \pi ND$) and rotor outer diameter ($L = D$) are used as the characteristic velocity and length respectively in Equation 2.36b:

$$We = \frac{\rho_c N^2 D^3}{\sigma} \tag{2.37}$$

The critical Capillary or Weber number (Ca_{cr} and We_{cr} respectively) corresponds to the conditions that yield the maximum stable drop size. When *Ca* or *We* is higher than this, the drop becomes unstable and breaks. On the other hand, if *Ca* or *We* is in the low to medium range, the drops experience some distortion but are stable and thus do not break (Peters, 1997).

Laminar droplet break-up

Laminar flow is distinguished by fluid moving in separate (parallel) layers or streamlines, where there is no cross flow between layers (but mixing can occur through molecular diffusion) and linear viscous forces dominate, opposed to the non-linear inertial forces in the turbulent flow. Steady laminar flow is encountered when the fluid viscosity is high or the fluid velocity is low (Szalai et al., 2004). Although the equipment name 'high shear mixer' may insinuate that the flow is turbulent inside the mixing head, it is not completely true as the complex nature of their geometry means that there are certain regions where the flow is laminar (Thapar, 2004). This flow is generally categorised into simple shear, plane hyperbolic and extensional (or elongational) flow as portrayed in Figure 2.26 (Walstra, 1983; Walstra and Smulders, 1998).

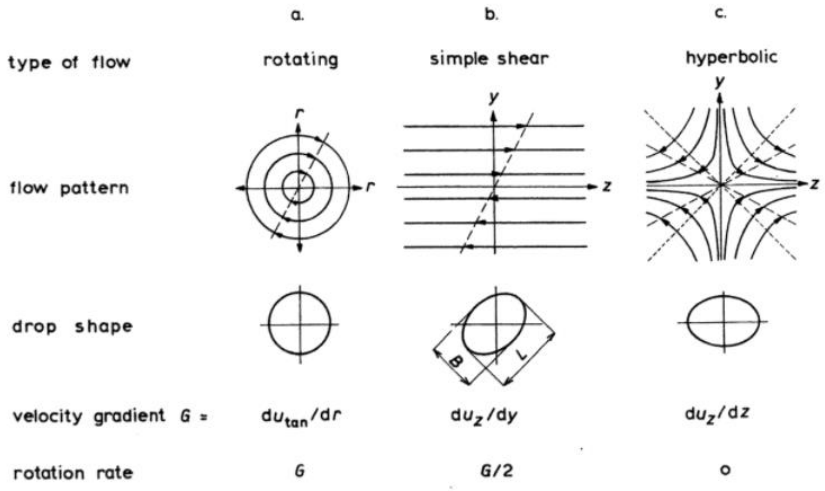

Figure 2.26: Classification of 2-D flow in laminar flow and their effects on droplet deformation (Walstra and Smulders, 1998)

Simple shear flow (also known as Couette flow) is a steady flow which manifests when a fluid is contained in a narrow gap between two parallel plates (Figure 2.1) or two concentric cylinders (Figure 2.4d) where one of the plates/cylinders is stationary and the other is moving/rotating or both moving in opposing directions. In radial HSMs, this most likely occurs in the rotor-stator (R-S) gap. Hyperbolic flow is used to model flow of viscous emulsions in

high pressure homogenisers and to estimate a jet of liquid impinging on a surface. Extensional flow occurs when a velocity gradient exists in the same direction as the flow and may occur in the stator holes of HSMs, where fluid is forced out in the radial direction (Hall, 2012). As established in the earlier section, drops are eventually deformed by disruptive shear stresses due to the velocity gradients acting on the drop. For laminar flow, the critical Capillary number, Ca_{Cr}, depends on the flow type and viscosity ratio of the dispersed to continuous phases as shown on the Grace curves in Figure 2.27 (Walstra, 1983).

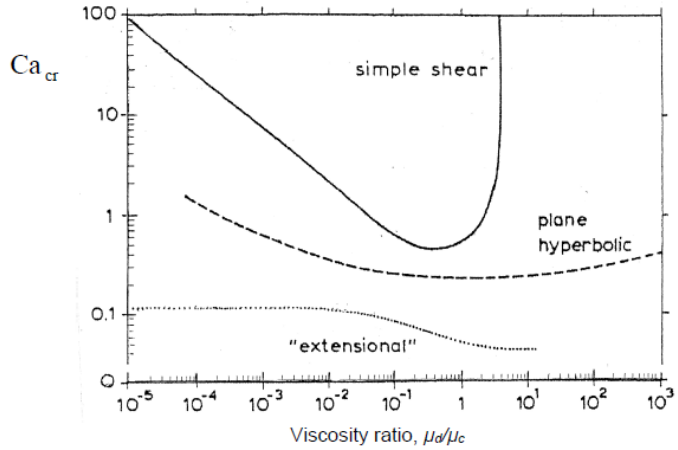

Figure 2.27: Critical Capillary number defining the maximum stable drop size in laminar flows (Walstra, 1983)

Turbulent Droplet Break-Up

In practice, emulsification processes are often performed in turbulent conditions (Peters, 1997). Provided that the Reynolds number (Equation 2.9) is high enough, Kolmogorov's theory regarding local isotropic turbulence (universal equilibrium range) can be used to simplify the complex analysis of a turbulent system (Nienow et al., 1997).

For mechanically agitated vessels, turbulent flow is treated as a superposition of velocity fluctuations and eddy sizes on an overall mean flow. Large and anisotropic primary eddies, of comparable sizes to the impeller diameter, contain the largest velocity fluctuations with low frequencies. Thus, they contain the majority of kinetic energy imparted by the impeller which is cascaded to smaller eddies, generated through the interaction of large eddies with slow

moving streams, until it finally dissipates to heat via viscous forces. The smaller eddies are considered to be independent of the bulk flow and are isotropic, given that the Reynolds number is sufficiently large (Nienow et al., 1997). These are illustrated in Figure 2.28. The Kolmogorov length scale, λ_k, is defined as follows:

$$\lambda_k = \left(\frac{\nu^3}{\varepsilon}\right)^{1/4} \tag{2.38}$$

where λ_k is the Kolmogorov length scale, ν is the fluid kinematic viscosity and ε is the local specific energy dissipation rate.

If the eddy size is larger than λ_k and the droplet's own diameter, it will merely convey the droplet. However, if the eddy becomes smaller in size e.g. the same magnitude as the droplet diameter or λ_k, it will cause droplet deformation. Schematics of these deformations are shown in Figure 2.28.

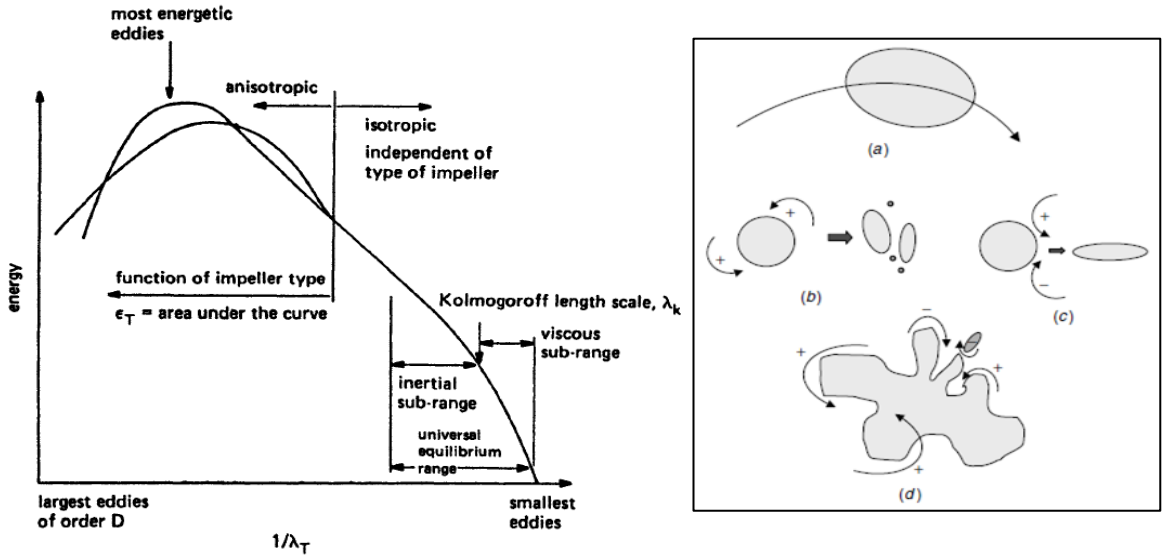

Figure 2.28: (Left) A range of eddy sizes and their corresponding energies in turbulent flow (Nienow et al., 1997) (Right) Scalar deformation of droplets by eddies in a turbulent field: (a) Convection by large eddies; (b) Erosion by co-rotating eddies; (c) Elongation by counter-rotating eddies; and (d) Multiple scales of deformation (Paul et al., 2004)

Droplet break-up models that apply the concept of cascading turbulent eddies above are then discussed in the following sections. Kolmogorov's universal equilibrium theory of local isotropic turbulence is classified into two regions as portrayed in Figure 2.28: inertial and

viscous sub-ranges where for the former, inertial forces dominate over the viscous forces and vice versa for the latter. The Kolmogorov length scale serves as the defining boundary between these regions e.g. where there are equivalent viscous and inertial stresses acting on the drop thus, the droplet break-up mechanism depends on whether the dispersed phase drop size is smaller or larger than λ_k. For rotor-stator devices that can produce droplet sizes in the order of λ_k or smaller, consideration of viscous forces becomes more essential and so analysis of breakage mechanisms is more complex (Hall et al., 2011a).

Turbulent Inertial Sub-range

For dilute liquid-liquid systems with low viscosity dispersed phase and droplet sizes larger than λ_k, drops are treated as inviscid and the interfacial tension is the only surface force that is making it stable. For such systems, a general relationship (Equation 2.39) relates the energy dissipation rate (based on rotor swept volume) to the maximum stable drop size (Hall, 2012; Hall et al., 2011a; Paul et al., 2004):

$$d_{max} = C_1 \left(\frac{\sigma}{\rho_c}\right)^{\frac{3}{5}} \varepsilon^{-\frac{2}{5}} \tag{2.39}$$

For geometrically similar systems with constant power numbers, the Weber number Equation 2.37 can be used in the correlation Equation 2.39:

$$\frac{d_{\max}}{D} = C_2 We^{-\frac{3}{5}} \tag{2.40}$$

If the drop sizes are larger than λ_k but the viscosity of the dispersed phase is high, internal viscous stresses which resist droplet instability dominate over the interfacial tension that also resists droplet deformation. Thus, a correlation Equation 2.41 which considers the dispersed phase viscosity can be used:

$$d_{max} = C_3 (\rho_c \rho_d)^{-\frac{3}{8}} \mu_d^{\frac{3}{4}} \varepsilon^{-\frac{1}{4}} \tag{2.41}$$

Again, for geometrically similar systems, keeping the power number constant, the Reynolds number Equation 2.13, can be applied to the correlation Equation 2.41:

$$\frac{d_{max}}{D} = C_4 \left(\frac{\rho_c}{\rho_d}\right)^{\frac{3}{8}} \left(\frac{\mu_d}{\mu_c}\right)^{\frac{3}{4}} Re^{-\frac{3}{4}} \tag{2.42}$$

Two similar approaches by Davies (1985) and Calabrese et al. (1986) for considering the effects of viscous stresses brought by the dispersed phase viscosity in stirred vessels, which may be applicable for high shear mixers can be found in the literature (Equation 2.43):

$$d_{max} = C_5 \left(\frac{\sigma}{\rho_c}\right)^{\frac{3}{5}} \varepsilon^{-\frac{2}{5}} \left[1 + C_6 \left(\frac{\mu_d}{\sigma}\right) \sqrt{\frac{\rho_c}{\rho_d}} \varepsilon^{\frac{1}{3}} d_{max}^{\frac{1}{3}}\right]^{3/5} \tag{2.43}$$

Once again, for a geometrically similar system with a constant power number, including the Weber number and viscosity group yields Equation 2.44 (Hall, 2012):

$$\frac{d_{max}}{D} = C_7 We^{-\frac{3}{5}} \left[1 + C_8 Vi \left(\frac{d_{max}}{D}\right)^{\frac{1}{3}}\right]^{\frac{3}{5}} \tag{2.44}$$

Where the viscosity group is defined as Equation 2.45:

$$Vi = \left(\frac{\rho_c}{\rho_d}\right)^{\frac{1}{2}} \left(\frac{\mu_d ND}{\sigma}\right) \tag{2.45}$$

Turbulent Viscous Sub-range

In isotropic turbulent flow, where droplet sizes are at or below the Kolmogorov length scale, the viscosity of the continuous phase also becomes influential thus either the inertial or viscous stress may dominate. For inviscid drops, Shinnar (1961) suggests using Equation 2.46 if the inertial stresses are considered more important and Equation 2.47 if viscous stresses are more dominant in the break-up mechanisms.

$$d_{max} = C_9 \left(\frac{\sigma \mu_c}{\rho_c^2}\right)^{\frac{1}{3}} \varepsilon^{-\frac{1}{3}} \tag{2.46}$$

$$d_{max} = C_{10} \sigma (\rho_c \mu_c)^{-\frac{1}{2}} \varepsilon^{-\frac{1}{2}} \tag{2.47}$$

Table 2.5 summarises the theoretical correlations discussed above.

Table 2.5: A summary of theoretical correlations found in literature for predicting mean droplet size (Hall, 2012)

Range	**Mechanism**	**Correlation in terms of ε**	**Correlation in terms of dimensionless groups (constant Po)**
$\mathbf{L \gg d \gg \lambda_k}$	Inertial stresses $\mu_d \to 0$ $\tau_{cohesive,1} \gg \tau_{cohesive,2}$	$d_{max} \propto \left(\frac{\sigma}{\rho_c}\right)^{\frac{3}{5}} \varepsilon^{-\frac{2}{5}}$	$\frac{d_{\max}}{D} \propto We^{-\frac{3}{5}}$
$\mathbf{L \gg d \gg \lambda_k}$	Inertial stresses $\mu_d \to \infty$ $\tau_{cohesive,2} \gg \tau_{cohesive,1}$	$d_{max} \propto (\rho_c \rho_d)^{-\frac{3}{8}} \mu_d^{\frac{3}{4}} \varepsilon^{-\frac{1}{4}}$	$\frac{d_{max}}{D} \propto \left(\frac{\rho_c}{\rho_d}\right)^{\frac{3}{8}} \left(\frac{\mu_d}{\mu_c}\right)^{\frac{3}{4}} Re^{-\frac{3}{4}}$
$\mathbf{\lambda_k > d}$	Inertial stresses $\mu_d \to 0$ $\tau_{cohesive,1} \gg \tau_{cohesive,2}$	$d_{max} \propto \left(\frac{\sigma \mu_c}{\rho_c^2}\right)^{\frac{1}{3}} \varepsilon^{-\frac{1}{3}}$	$\frac{d_{max}}{D} \propto (We\, Re)^{-\frac{1}{3}}$
$\mathbf{\lambda_k \gg d}$	Inertial stresses $\mu_d \to 0$ $\tau_{cohesive,1} \gg \tau_{cohesive,2}$	$d_{max} \propto \left(\frac{\sigma \mu_c^4}{\rho_c^5}\right)^{\frac{1}{7}} \varepsilon^{-\frac{2}{7}}$	$\frac{d_{max}}{D} \propto (We\, Re^4)^{-\frac{1}{7}}$
$\mathbf{\lambda_k > d}$	Viscous stresses $\mu_d \to 0$ $\tau_{cohesive,1} \gg \tau_{cohesive,2}$	$d_{max} \propto \sigma (\rho_c \mu_c)^{-\frac{1}{2}} \varepsilon^{-\frac{1}{2}}$	$\frac{d_{max}}{D} \propto We^{-1} Re^{\frac{1}{2}}$

A collection of existing theoretical, empirical or semi-empirical correlations for mean droplet diameters in HSM is summarised in Table 2.6. Most of the models presented are for very dilute emulsion systems e.g. negligible coalescence except for the newly developed correlation by Gingras et al. (2005) which contains an energy density term, $E_V = \left(\frac{P}{Q}\right)$ (Zhang et al., 2012). These models demonstrate how emulsion droplet size is a function of energy input e.g. whether indirectly by the Weber number or directly by the average energy dissipation rate per unit mass of fluid. Thus, it highlights the importance of understanding how process parameters such as the rotor speed and flow rate influence energy dissipation rate inside the mixing head, which is the focus of this thesis and is achieved by using the PIV technique.

Table 2.6: Summary of existing $d_{3,2}$ correlations for HSMs (Zhang et al., 2012)

Type	Mean droplet diameter correlations	Notes	Reference
Batch	$\frac{d_{3,2}}{D} = 0.038\, We^{-0.6} \quad (d > \lambda_k)$ $\frac{d_{3,2}}{D} = 0.0037 \left(We^{-1} Re^{-\frac{1}{2}}\right) \quad (d < \lambda_k)$	Surfactant free systems with low dispersed phase viscosity and concentration. Video probes were used for in-situ measurements.	(Calabrese et al., 2002; Calabrese et al., 2000)
Batch	$\frac{d_{3,2}}{D} = 0.055\, We^{-\frac{3}{5}} \left[1 + 2.06\, Vi \left(\frac{d_{3,2}}{D}\right)^{\frac{1}{3}}\right]^{\frac{3}{5}} \quad (d > \lambda_k)$ $\frac{d_{3,2}}{D} = 0.093\, (WeRe)^{-\frac{1}{3}} \left[1 + 24.44\, ViRe^{\frac{1}{2}} \left(\frac{d_{3,2}}{D}\right)\right]^{\frac{1}{3}} (d < \lambda_k)$	Surfactant-free and surfactant-laden systems were compared. Video microscopy and image analysis were used to measure DSD. The $d_{3,2}$ from both clean and surfactant-laden systems were correlated together through modification of physical properties.	(Padron, 2001)
In-line	$d_{3,2} \propto (1 + 20\Phi)(\mathrm{WeRe}^4)^{-\frac{1}{7}}$	Surfactant-free Kerosene-water system was confirmed as non-coalescing at moderate concentrations of Kerosene. Video probe as well as sampling and dilution techniques were used to measure DSDs.	(Thapar, 2004)
In-line	$d_{3,2} \propto \left(\frac{N^3}{Q}\right)^{-0.55} \Phi^{4.13} \left(\frac{\mu_d}{\mu_c}\right)^{-0.53}$	Highly concentrated, coalescing and temperature sensitive bitumen emulsions with cationic surfactants were prepared in pilot scale. Laser granulometer was used to measure DSD. The energy density term has also been included in a new correlation.	(Gingras et al., 2005)

Table 2.6: Summary of existing $d_{3,2}$ correlations for HSMs (Zhang et al., 2012) , Continued

In-line	$\frac{d_{3,2}}{D} = 0.250(1 + 0.459\Phi)We^{-0.58}$ $\frac{d_{3,2}}{D} = 0.201\left(\frac{\mu_d}{\mu_c}\right)^{0.066} We^{-0.6}$ $d_{3,2} \propto E_V^{-0.45}, d_{3,2} \propto E_V^{-0.39}$ $(at\ constant\ Q)$	Emulsions were prepared with added surfactants using a pilot-scale mixer with low to high dispersed phase viscosity and concentration. Sampling and dilution technique was used to measure DSDs. Correlations including the energy density term were also proposed.	(Hall et al., 2011a)
In-line	$\frac{d_{3,2}}{D} = 0.29We^{-0.58}$ $(high\ \mu_d)$ $\frac{d_{3,2}}{D} = 0.41We^{-0.66}$ $(low\ \mu_d)$	Laboratory and industrial size HSMs were used to make dilute emulsions with different dispersed phase viscosities. Constants for the Weber number model differ with dispersed phase viscosity but similar in both scales.	(Hall et al., 2011b)

2.5 HSM Literature

2.5.1 Overview

As established in §1.1, HSMs are extensively used in industrial processes for liquid-liquid dispersion, emulsification and homogenisation due to their capability to produce high levels of shear and energy dissipation rates on a relatively small volume of fluid. In spite of this, publications detailing aspects of their design and basis of operation have only surfaced over the last decade and therefore previous optimisation of operating parameters has been heavily reliant on operator experience and trial-and-error (Mortensen et al., 2017). Literature on both batch and in-line HSMs has focussed on the development of scaling rules and features of the turbulence within the mixing head.

The majority of studies have either been purely experimental, focussing on droplet break-up (Carrillo De Hert and Rodgers, 2017; Hall, 2012; Hall et al., 2011a; James et al., 2017a; Rodgers and Cooke, 2012; Rueger and Calabrese, 2013a; b; Shi et al., 2013; Thapar, 2004), measurement of power consumption (Cooke et al., 2012; James et al., 2017b; Kowalski et al., 2011; Padron, 2001; Sparks, 1993; Xu et al., 2013b), or flow visualisation studies using techniques such as Laser Doppler Anemometry (LDA), Particle Image Velocimetry (PIV) and high speed imaging (Ashar et al., 2018; Espinoza et al., 2018; Håkansson et al., 2017a; Håkansson et al., 2017c; Mortensen et al., 2011; Mortensen et al., 2017; 2018; Sparks, 1996; Utomo et al., 2008) to study the effects of process parameters such as rotor (and pump for in-line devices) settings as well as the influence of stator designs. Some published work on numerical simulations have employed computational fluid dynamics (CFD) to characterise turbulence in several in-line HSM models (Ahmed et al., 2018; Håkansson et al., 2017b; Håkansson and Innings, 2017; Minnick et al., 2018; Utomo et al., 2009). Most recent work published in the literature focuses on validating CFD simulations via experiments (Jasińska et

al., 2013; Jasińska et al., 2015; Kim, 2015; Qin et al., 2017; Utomo et al., 2008; Xu et al., 2013a; Zhang et al., 2017).

However, despite the above efforts and an increase in published articles on and around the topic, the number of studies remains relatively low compared to other well-established mixing equipment such as mechanically agitated vessels. This is because of the plethora of interacting factors that needs to be considered to fully characterise the fluid behaviour. These factors include, but are not limited to processing conditions such as flow rate, fluid properties, rotor and stator geometries, as well as mixing mechanisms and applications.

2.5.2 Complex Flow Patterns and Droplet Break-up in HSMs

HSMs possess inherently complex flow patterns which results in an inhomogeneous distribution of energy in the mixing head. Thus, although HSMs usually operate in fully turbulent conditions e.g. including the bulk region, it means that flow at certain locations in the mixing head can be laminar, transitional or turbulent, depending on the characteristic velocity and length scale in the location of interest. Laminar flows such as simple shear and elongational flows may occur in the R-S gap and in the fluid through the stator holes (or at locations with varying cross-sections) respectively (Hall, 2012; Sparks, 1996; Thapar, 2004).

In turbulent flow, turbulent pressure fluctuations dominate the viscous stresses and are responsible for droplet break up. Mechanistic models developed by Hinze (1955) and Kolmogorov (1949), which assume homogeneous isotropic turbulence (at very high Reynolds numbers), are often used as theoretical basis. This crude assumption rarely applies in practical situations since the flow, especially in close proximity to the rotor, is intermittently anisotropic, yet it is often the only option available to the practising engineer (Ashar et al., 2018; Håkansson et al., 2017c; Hall et al., 2011a; Thapar, 2004). Depending on whether the droplet size d, is

larger or smaller than the Kolmogorov length scale, λ_k, the droplet break up mechanisms in the universal equilibrium range can be sub-divided into inertial and viscous- subranges where inertial and viscous forces dominate respectively. A competing theory by Rodgers and Cooke (2012) proposes that agitator shear rate causes break-up, based on a force balance between the interfacial forces and the external viscous stresses generated by the agitator. They suggest that the equilibrium droplet size correlates with the maximum shear rate and thus the rotor tip speed and argue that without the stator screen, a HSM is practically a very small stirred vessel. Empirical equations based upon the energy density $E_V = \left(\frac{P}{Q}\right)$, can also be used for droplet size correlations. This parameter ignores the effects of re-coalescence and encompasses the effects of process parameters applied to a particular volume of emulsion, which takes into consideration the mean residence time acting on the drop (Hall et al., 2011a).

2.5.3 Effects of Configuration, Geometry and Mode of Operation

In industrial practice, an in-line mode of operation is more favourable due to the economic benefits in delivering larger continuous throughput (Qin et al., 2017). However, the lack of theoretical knowledge, even more than for batch operated HSMs, makes their design and application very challenging (Håkansson and Innings, 2017). Utomo et al. (2009) investigated the role of stator hole numbers, shapes and sizes and found that wider, far-spaced holes are more likely to develop stronger jets and recirculation which may be favourable for droplet break up. Espinoza et al. (2018) (covered in Chapter 4 of this thesis) showed that the flow behaviour in an in-line mixer equipped with an external pump was affected by the relative contribution of the mechanical energy inputted by both the mixing head and the pump, the former leading to a dominance of tangential flow and the latter leading to the creation of a strong radial flow component due to an increase of jetting through the stator holes. Additionally, Qin et al. (2017) found that having multiple rows of stator holes also results in a complex flow pattern due to jet-

to-jet interactions. Rodgers and Cooke (2012), together with Hall (2012), emphasised that the stator plays an essential role in reaching equilibrium droplet sizes faster in both single- and multi-pass emulsification. They also highlighted its importance at higher flow rates for droplet breakage where high velocities and pressure drop through the stator screens increase the shear through the holes. Moreover, Kowalski et al. (2011) highlighted that having multiple rows of small stator holes further increases the available surface area for shearing of the fluids. This is in line with the observations of Atiemo-Obeng and Calabrese (2004) that droplet break up occurs mainly from the stator walls and emanating jets from the stator holes due to the diversion and deceleration of the tangential flow imparted by the rotor (via the downstream face of the stator) to radial flow through the stator holes. The frequent and sudden acceleration (by the rotor) and deceleration (by the stator) is responsible for the main energy losses in the mixing head (Thapar, 2004). Finally, Håkansson et al. (2017c) and Ashar et al. (2018) further concluded that the probability of droplet break up due to collisions does not only depend on areas of intense turbulence but also on the local flow patterns which determine which areas are often visited by the drops.

2.5.4 Current Approach on Hydrodynamic Studies

The difference between the hydrodynamics of batch and in-line HSMs can influence droplet break up mechanisms (Håkansson et al., 2017b). Of the few studies on in-line HSMs, Sparks (1996) carried out flow visualisation experiments (through reactive mixing) and Thapar (2004) used these findings in combination with drop size analysis to determine the possible locations and potential mechanisms of droplet break up in turbulent flow, the results of which are summarised in Table 2.7. Furthermore, Thapar (2004) ordered these locations in terms of residence times: shear gap < stator < inlet pipe < rotor < volute which indicates that small areas

with high local energy dissipation rates are often bypassed by most drops and that most of them break by inertial and viscous stresses in the rotor region.

Table 2.7: Locations and proposed droplet breakup mechanisms under turbulent conditions in an in-line HSM (Sparks, 1996; Thapar, 2004)

Location	Breakup mechanism	Details
Inlet pipe	Inertial stresses	Inlet pipe flow is highly turbulent
Rotor region	Inertial and viscous stresses	Effective shear rates are very high; Re calculated indicative of turbulent condition; critical burst time << residence time, deeming breakup due to viscous stress possible
Shear gap	Inertial subrange eddies when Re is high enough (although mainly viscous stress at lower Re)	Drops similar to or below $d_{3,2}$ will break in the short time spent in the gap
Stator	Viscous stresses (laminar only as Re relatively low)	Drops from shear gap will break further in this region
Volute	Inertial stresses	Volute flow is turbulent and is responsible to break larger drops that bypassed regions of high energy and shear rates

The complexity presented in the above literature confirms the current status quo that generic scale-up rules do not exist for either batch or inline HSMs and indeed Mortensen et al. (2011) stated that: "a general characterisation of rotor-stator mixer performance by simple mechanistic models does not seem realistic". The implication is that robust and validated CFD based models are a necessary tool for the practising engineer. Studies by Xu et al. (2013a), Xu et al. (2013b) and Zhang et al. (2017) investigated the hydrodynamics (via LDA), power consumption (e.g. via torque measurements), residence time (pulse stimulus technique), strain and energy dissipation rate distributions (CFD) in a FLUKO® pilot-scale in-line HSM (model FDX1/60). However, these are single-phase experiments and thus no explicit links were made to emulsification processes. To date, performing visualisation experiments on emulsions (especially with PIV) is still very challenging or unachievable because of their inherent opacity. For techniques to work, emulsions have to be extremely dilute or alternatively, independent

visualisation and emulsification experiments, as done by Sparks (1996) and Thapar (2004) can be done. The latter evidently (Hall et al., 2011a; Qin et al., 2017; Thapar, 2004) remains as the conventional and convenient choice as it is easier to analyse how droplet size distributions (DSD) and average drop sizes such as $d_{3,2}$ and $d_{4,3}$ of emulsion systems respond to changes in process parameters. More recently, collaborative work by Håkansson et al. (2017c) and Ashar et al. (2018) investigated where, when and how droplets break in a bespoke batch HSM using results from CFD simulations, PIV and visualisation of single droplet break up with particular attention to disruptive stresses. Their approach, using a variety of techniques, is compelling, yet, it is necessary to be aware of the limitations of the methods used (e.g. PIV resolution) in the interpretation of the data.

2.6 Flow Characterisation Techniques

2.6.1 Laser Doppler Velocimetry (LDV)

Laser Doppler Velocimetry (LDV), also known as Laser Doppler Anemometry (LDA) for wind measurements, is a non-intrusive technique which involves measuring the velocity of suspended particles at a specific point in a flow. The particles used are small, of the order of micrometres in size, and are assumed good tracers if they faithfully follow the fluid motion e.g. their velocities correspond to the fluid velocity and they can be taken as true velocimeters (Brown et al., 2004; Zhang, 2010). LDA uses the Doppler effect as a means of measuring the instantaneous velocities. When the flow is illuminated by the laser beam, the frequency of the scattered (and/or refracted) light from the incident beam is fixed in the absence of particles and changes when particles are present in the flow. The resulting difference in frequency is referred to as the Doppler shift, which is linearly proportional to the particle velocities (Brown et al., 2004). A single laser light beam is split into two coherent and monochromatic beams which intersect at their waists in the measurement volume using a Bragg cell (Figure 2.29). The

intersection of these light beams results in their constructive and destructive interference/superposition which results in the formation of straight fringe patterns of maxima and minima intensities (bright and dark fringes respectively). The fringe spacing, d_f, is fixed and can be evaluated using the wavelength of the laser, λ and the angle of intersection of the beams, θ (Utomo, 2009):

$$d_f = \frac{\lambda}{2\sin\left(\frac{\theta}{2}\right)} \tag{2.48}$$

When the particles cross the fringe pattern, they generate oscillating signals of the reflected light intensity, which is captured by a photo detector and filtered by a signal processor to determine the Doppler shift frequency, f_D. The velocity component, u_P, perpendicular to the fringe pattern is then evaluated using:

$$u_P = d_f f_D \tag{2.49}$$

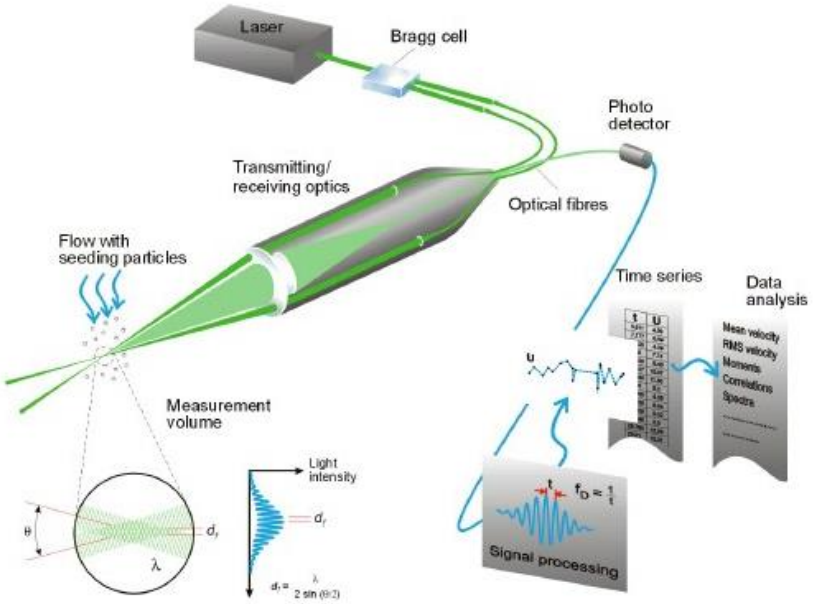

Figure 2.29: Principles of LDA (Dantec Dynamics, 2019a)

The advantages of using this technique according to Brown et al. (2004) are as follows: *(a)* It is non-intrusive, *(b)* It requires no calibration as the fringe spacing is set by the laser beam wavelength and the angle between the two laser beams, *(c)* It has well-defined directional

response and *(d)* It offers multi-component measurements of velocity as well as high spatial and temporal resolution. However, just like PIV, it requires transparent medium and optical access to the flow. It also only obtains measurements at a single point so a complex traverse system is needed to interrogate flows at more than one point. This technique has been used in the study of HSMs: Utomo (2009) compare LDA with Hot Wire Anemometry (HWA) and PIV measurements in batch rotor-stator mixers. Similarly, Xu et al. (2013a) compared LDA measurements with CFD simulations of in-line high shear mixers with ultrafine teeth.

2.6.2 Positron Emission Particle Tracking (PEPT)

Positron emission particle tracking (PEPT) is a Lagrangian flow visualisation and measurement technique, invented at the University of Birmingham (Figure 2.30a), which is based on a medical imaging technique, Positron Emission Tomography (PET) that can be used in enclosed and opaque systems (University of Birmingham, 2019). In essence, it uses PET technology to determine the location of a radioactive particle in motion. The tracer used is labelled with positron-emitting isotopes such as ^{11}C, ^{18}F, ^{68}Ga or ^{22}Na. The annihilation of positron with an electron within the vicinity of the tracer particle results in the emission of back-to-back coincident gamma, γ-rays, which are detected by an array of detectors (Figure 2.30a). Detection of back-to-back coincident γ-rays allows for a "line of response" (LOR) to be drawn between the two detection locations (positron camera). Multiple LORs or events (Figure 2.30b) can then be used to pinpoint the approximate location of the tracer particle using the process of triangulation (Govender et al., 2010; Langford et al., 2016). The PEPT algorithm is then used to discard invalid data e.g. random coincidence of two completely unrelated γ-rays, through the iterative calculation of the centroid of events. Gamma rays that pass through furthest from the centroid are discarded until a specified fraction of original events remains (Ingram et al., 2007).

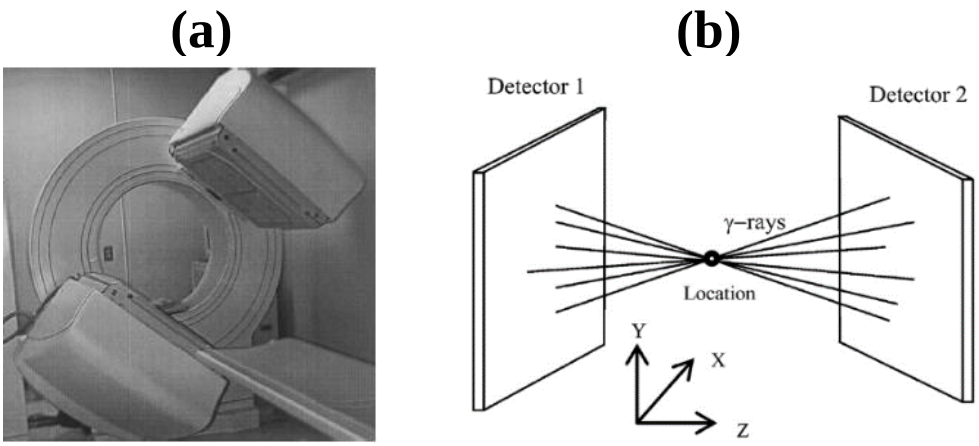

Figure 2.30: (a) PEPT camera at the University of Birmingham (Parker et al., 2002) (b) Schematic diagram of PEPT (Parker and Fan, 2008)

The 3-D data of tracer locations with respect to time can be used to evaluate local occupancies and concentrations, bulk dynamics, mixing efficiencies as well as local velocities and local shear rates in the system. This technique has been used in both solid and liquid media tracking applications e.g. in granulators, extruders, fluidised beds, static mixers, stirred tanks and many more (Mihailova, 2016). Some of the research works in a plethora of mixing studies using PEPT include: flow studies in static mixers (Mihailova et al., 2015; Mihailova et al., 2016; Rafiee et al., 2011; Rafiee et al., 2013), flow studies in stirred tanks (Chiti et al., 2011; Fishwick et al., 2005; Liu and Barigou, 2013), flow in fluidised beds (Chan et al., 2009; Stein et al., 2000; Van de Velden et al., 2007), flow in various mixers (Jones and Bridgwater, 1998; Laurent and Cleary, 2012; Marigo et al., 2013; Saito et al., 2011) as well as motion of textiles in a domestic washing machine (Mac Namara et al., 2012).

2.6.3 Magnetic Resonance Imaging (MRI)

Magnetic Resonance Imaging (MRI) is an imaging technique commonly used in the medical field for diagnostic purposes especially in cardiology. However, proton MRI which is the basis of many MRI measurements, can be utilised to quantify a range of parameters within a sample e.g. velocity, acceleration, relaxation time, diffusion coefficients as well as hydrogen

density. Moreover, if combined with Nuclear Magnetic Resonance (NMR) spectroscopy such as in specialised MRI facilities, detailed chemical information about the molecules can also be obtained. It is considered suited for fluid mechanics research due to the accuracy it offers on flow measurement e.g. displacement of less than 1 μm and velocities as slow as 10 μm s^{-1} and the possibility of working with opaque systems. It is also being increasingly used in the study of complex rheology of fluids such as those of polymer and surfactant solutions such as shear induced structures (SIS) or shear banding in surfactant systems (Bonn et al., 2008).

MRI uses the spin properties of atomic nuclei to gather spatially resolved information about the dynamics of the sample as well as its structure. Use of quantum mechanics is required to describe the NMR phenomenon in detail, however, a simplified description using the concept of proton NMR (NMR of hydrogen) will suffice. At the right conditions, any small group of hydrogen nuclei may develop a non-zero magnetic dipole and under the influence of a strong magnetic field, the magnetic dipole undergoes polarisation (at rest and in equilibrium in a strong static magnetic field), precession and relaxation (in out of equilibrium circumstances during radio frequency (RF) excitation). An MRI facility (Figure 2.31) is generally consisted of three parts: *(a)* Magnets that generates the magnetic field e.g. superconducting systems, *(b)* RF coils to surround the sample and emit and receive RF fields or initiates and detects the precession stage and *(c)* Gradient coils to detect and locate spatial motions of the sample. There are several ways to use MRI to investigate fluid velocity (Bonn et al., 2008):

1. *Time of flight (bolus)* – NMR excitation of the restricted part of the fluid, monitoring its position with time.
2. *Spin-tagging* – similar to *1* but tracks more complicated magnetic pattern drawn on the whole fluid and permits quantification of spatially resolved flow description (Figure 2.32a).

3. *Phase-shift or phase-contrast velocity mapping* – works in the same principle as *1* and *2* in terms of flow-induced changes in signal phase but also draws the phase map of the NMR signal throughout space (Figure 2.32b). Velocity information is determined through comparison of the measured phase with a zero-reference phase in each pixel.

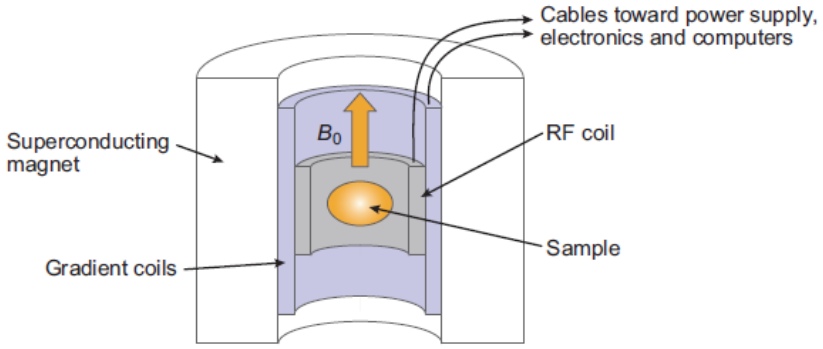

Figure 2.31: Structure of an MRI facility (Bonn et al., 2008)

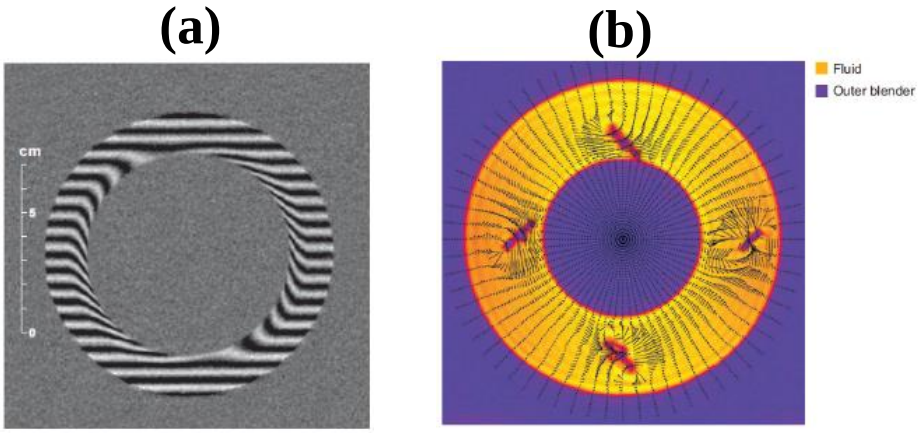

Figure 2.32: (a) 2-D flow of clay suspension in a Couette cell, bright lines correspond to tagged spins that were tagged as straight lines at time zero thus deformation of the lines demonstrate the flow e.g. shear locations near the moving inner cylinder. (b) 2-D section of a 3-D velocity map of Carbopol gel moving in an annular container; only in-plane motion is shown and orange represents the fluid (Bonn et al., 2008)

Although this technique is very versatile, the required use of superconducting magnets in traditional MRI facilities makes it unsuitable for commercial environments and unportable for laboratory studies. Moreover, the equipment being studied has to fit within the limited space of the scanner (Alberini, 2013).

2.6.4 Particle Image Velocimetry (PIV)

Background

Particle image velocimetry (PIV) is a term used to refer to optical visualisation techniques that measure the displacement of entrained seeding particles that accurately follow the fluid motion between two laser pulses, used to determine instantaneous velocity fields that characterise fluid behaviour and flow structures. It is used for qualitative flow visualisation and quantitative flow measurement in experimental fluid mechanics. The former is essential in gaining insight of the flow behaviour through visualising flow field patterns while the latter provides important information on flow statistics that support the visual observations (Adrian and Westerweel, 2011). A typical PIV set up is shown in Figure 2.33.

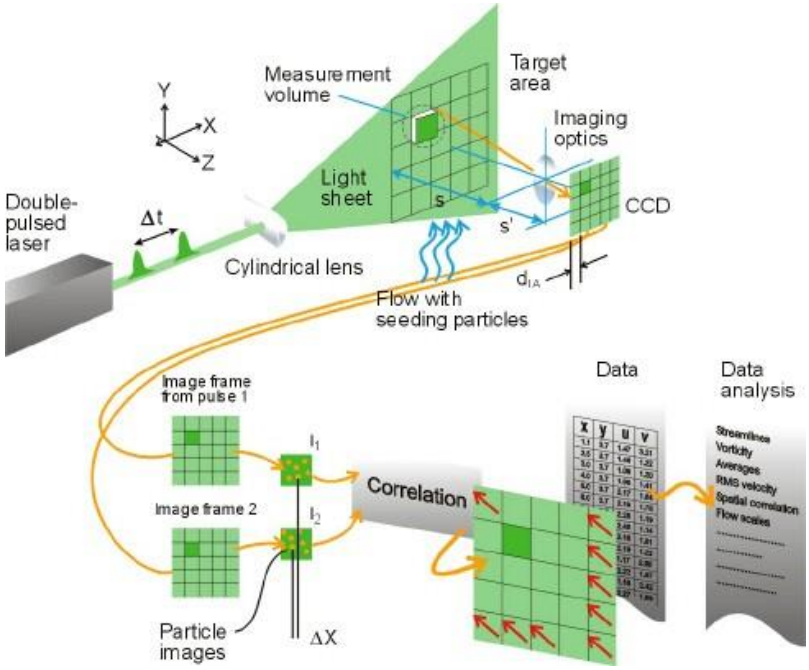

Figure 2.33: Schematic representation of the PIV experiment and data acquisition (Dantec Dynamics, 2019b)

Fundamentals of PIV

<u>Basic Planar 2-D System</u>

A standard planar PIV system (Figure 2.33) is comprised of a digital camera, seeding particles, a double-pulsed laser equipped with light sheet forming optics, an image digitisation

hardware and a computer for the storage and analysis of data (Adrian and Westerweel, 2011). In addition, a synchroniser, which is a programmable timing unit, is used to control the timing events of a complete PIV system (Intelligent Laser Applications, 2019).

Image Acquisition

Seeding Particles

The visibility of the particles under a given illumination is a prime selection criterion for the seeding particles. They must be large enough to sufficiently scatter light to enable capturing of bright images but small enough to faithfully follow fluid acceleration e.g. their sizes are of order 0.1 – 50 μm. They must also not deform so that they can act as substitutes for the small fluid element that they displace. In addition, differences in density and refractive indices between the fluid and particles, as well as the seeding concentration and polydispersity of the particles should also be considered (Adrian and Westerweel, 2011; Atkins, 2016). Spherical particles are preferred as they are independent of particle rotation and any camera aberrations as their centroid is their centre of mass. Examples of seeding particles used for liquid flow applications of PIV are made from borosilicate glass e.g. hollow glass spheres (HGS) and silver-coated hollow glass spheres (S-HGS) and polymers e.g. polyamide seeding particles (PSP) (Adrian and Westerweel, 2011; Dantec Dynamics, 2019c).

Laser and Optics

The area of interest is illuminated with a light sheet generated by a laser system. Double-pulsed systems are the primary choice as they are relatively cheaper than using multiple pulses (continuous laser systems). In addition, there are also dual (or twin) head lasers where each laser head can pulse independently of each other. The range of required emitted energy pulses from solid-state laser sources is between 5 – 500 mJ to ensure that sufficient illumination

intensity is achieved to attain clear images of micron-sized seeding particles. The certain energy required will depend upon the scattering properties of the particles. Neodymium-doped: Yttrium Aluminium Garnet (Nd:YAG) is a widely used source and emits at 532 nm via frequency doubling (emission is in the IR region at 1064 nm) which is green in the visible light spectrum (Adrian and Westerweel, 2011). To form a thin planar light sheet e.g. ~ 1 mm thickness, laser optics such as cylindrical and spherical lenses are used in series. The cylindrical lens diverges the light in one direction (makes a 'fan' in the vertical plane), dictating the measurement area whereas the spherical lens thins (makes a 'waist' in the horizontal plane) the light sheet and achieves the 2-D sheet as illustrated in Figure 2.34 (Hyde, 2015).

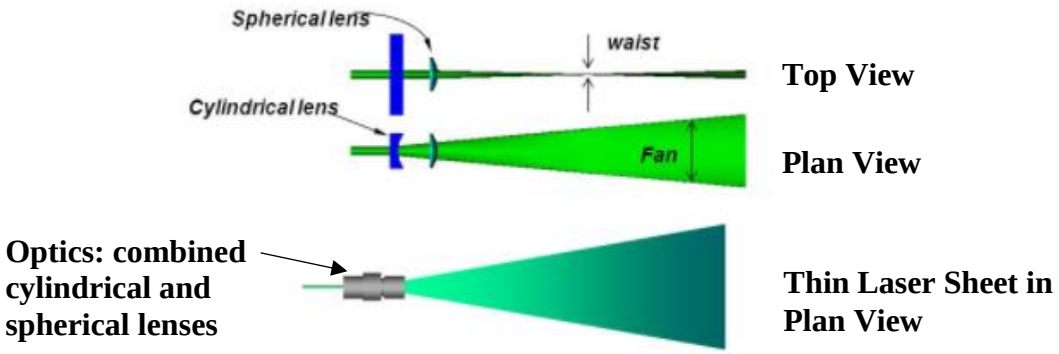

Figure 2.34: PIV laser optics (Hyde, 2015)

Camera and Imaging

High-speed digital cameras used in PIV are fitted either with complementary metal-oxide-semiconductor (CMOS) or charge-coupled device (CCD) sensors, which convert light energy to electrical energy/signals e.g. digitisation of light intensity into pixels. CMOS sensors are becoming more popular as although they are less sensitive and produce more noise in comparison to CCDs, they have significantly developed and are cheaper to manufacture (Teledyne Dalsa, 2019). The amount of images captured and duration of data acquisition are dependent on the internal storage of the camera and data transfer rate to the frame grabber installed on the computer (TSI, 2017).

Synchroniser

In order to perform PIV analysis, two successive exposures of the illuminated flow in the region of interest at a given time interval, Δt, are required. Thus, a computer-controlled digital synchroniser is used to control the timings between camera exposure and laser pulses in order to capture a specific event as accurately as possible. For instance, in a dual-frame PIV recording, the first laser pulse is captured in the first frame while the second laser pulse is captured in the second frame at a given Δt (Adrian and Westerweel, 2011).

External Trigger

Time-averaged velocity fields can be obtained by taking an ensemble average of the recorded instantaneous measurements over a long period of time (Atkins, 2016). However, if phase-locked or angle-resolved PIV measurements are desired e.g. only capturing images at a certain rotor blade angle/position, then an external trigger can be used. For example, an optical tachometer could be used in combination with an encoded mixer shaft at a fixed rotor blade position/angle. Time delays could then be set through the synchroniser to investigate the flow pattern at a different rotor blade position/angle (Espinoza et al., 2018).

Recording Techniques

The two main methods of implementing PIV are as follows (Atkins, 2016; Raffel et al., 2007):

1. ***Single frame/ double exposure***: images are recorded on the same frame and the displacement of particle is based on spatial auto-correlation (Figure 2.35a).
2. ***Double frame/ single exposure***: two images are captured on separate frames and the displacement of particle is based on spatial cross-correlation (Figure 2.35b).

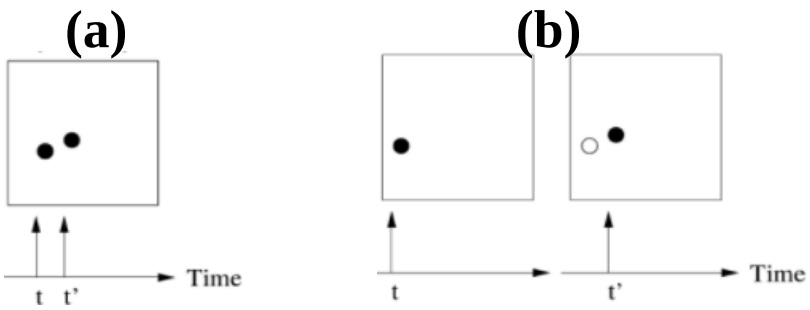

Figure 2.35: (a) Single frame/double exposure (b) Double frame/single exposure, open symbol represents the particle position in the previous frame (Raffel et al., 2007)

Frame Straddling

The second technique is more commonly used and requires that the two laser sheet pulses illuminating the particles (two exposures) are captured on two separate frames in close succession e.g. within a short time interval, Δt. This is achieved by utilising a dual-head laser system which consists of two isolated and independently firing laser cavities in addition to using modern CCD cameras with developed electronic architecture that are capable of acquiring image frames in the order of 200 ns apart (Atkins, 2016; Raffel et al., 2007). This process is limited by the frame transfer time which requires that $\Delta t \geq \Delta t_{transfer}$. To attain this, the illumination pulses are timed so that the first pulse occurs just before the event of frame transfer e.g. on frame *n*, and the second released immediately after e.g. on frame *n+1*, as portrayed in Figure 2.36. The timing of illumination pulses with respect to the periodic exposure cycles of the CCD sensor is known as frame straddling.

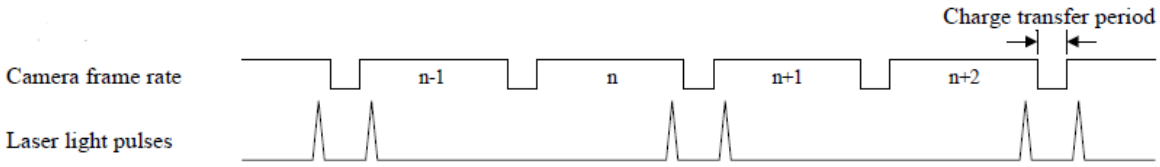

Figure 2.36: PIV frame-straddling timing diagram for a CCD sensor (Raffel et al., 2007)

Image Processing and Analysis

Captured image pairs are gridded into their interrogation windows (Figure 2.37a) e.g. 64 × 64 pixels where velocity vectors are determined by evaluating the average displacement

of the particles in that interrogation window between the two frames (Figure 2.37a) through spatial auto- or cross-correlation techniques (Figure 2.37b) and then dividing by the time interval, Δt. Cross-correlation is usually preferred as it does not suffer the 180º directional ambiguity that is inherent to auto-correlation which often requires an additional technique to identify the real sign (direction) of the displacement vector. It works by measuring the degree of similarity between the interrogation windows when they have been spatially shifted relative to one another. For instance, if an interrogation window was treated as a map of pixel intensities in frame A, the algorithm finds its closest match in frame B, which results in a displacement correlation peak (Figure 2.37b). This peak represents the numerical spatial shift e.g. the estimated coordinates of the new position and hence the average displacement of the group of particles in that interrogation window. For example in Figure 2.37b, the interrogation window has moved 8 pixels in the *x*-axis. Moreover, interrogation is usually performed in the frequency domain, using Fast Fourier Transforms (FFTs) as it simplifies and reduces the computational demands of using the discrete cross-correlation function:

$$\phi_{II'}(x,y) = \sum_{i=-\infty}^{\infty} \sum_{j=-\infty}^{\infty} [I(i,j)][I'(i+x,j+y)] \tag{2.50}$$

where i and j represent the grid position of the interrogation window where sub-sampling is carried out. Equation 2.50 is calculated by summing the products of the pixel gray values in the separate interrogation windows. The displacement correlation peak is yielded when the two frames match up.

The results are then converted back to the original variables by carrying out inverse FFT. Caution should still be taken as false correlations due to loss pairs may still occur which results in spurious/erroneous vectors (Atkins, 2016). The rules-of-thumb identified by TSI (2017) for PIV analysis to minimise loss pairs of particles are summarised in Table 2.8.

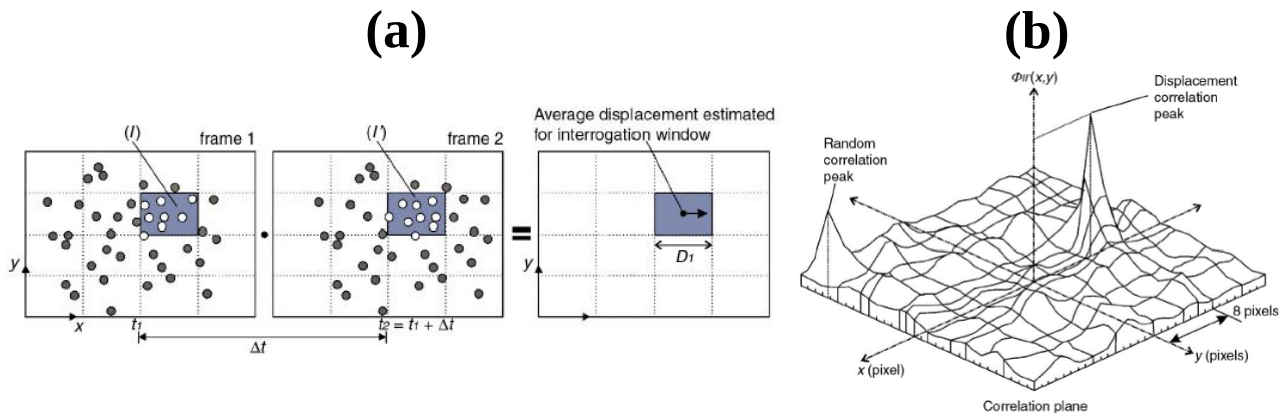

Figure 2.37: (a) Gridding of the image frames and subdivision into interrogation windows (I – frame 1, I' – frame 2) with the approximated single displacement vector (b) Displacement correlation peak in the cross-correlation plane (Atkins, 2016)

Table 2.8: PIV analysis rules-of-thumb (TSI, 2017)

Rule	Description
1	The interrogation window should be small enough so that the flow within it can be described by a single vector.
2	There should be at least 10 particles per interrogation window e.g. to achieve sufficient image density for a good signal-to-noise ratio (SNR).
3	Maximum in-plane displacement should not exceed ¼ of the interrogation window size.
4	Maximum out-of-plane displacements should not exceed ¼ of the light sheet thickness.
5	Minimum in-plane displacement should be at least two particle diameters.
6	Exposure should be long enough to ensure that particles are captured clearly.

Applications of PIV

PIV is employed in a plethora of flow characterisation experiments particularly in aerodynamic and hydrodynamic studies as well as turbulence research (Raffel et al., 2007). Existing studies include: air flow around cars and aircraft wings (wind tunnel experiments); flow around ship propellers; flow in ducts and pipes; flow in artificial heart valves (Lim et al., 1994); and fluid flow in process equipment such as fluidised beds (Müller et al., 2007), stirred tanks (Alberini et al., 2017; Aubin et al., 2004; Baldi et al., 2004; Delafosse et al., 2011;

Gabriele et al., 2009) and high shear mixers (Espinoza et al., 2018; Håkansson et al., 2017c; Mortensen et al., 2017).

Apart from planar (2-D) PIV, other systems include: stereoscopic (volume of single-plane flow cross section), multi-plane and scanning-plane arrangements to obtain *z*-displacements (3-D measurements) using multiple cameras at different viewing angles. In addition, specific applications lead to the development of microscopic (micro- or μ-PIV) systems where the high-speed camera is attached to a microscope, used in flow studies in microfluidic devices. Other systems allow 3-D reconstruction of particle position using multiple camera viewing angles such as photogrammetric and tomographic systems. Furthermore, holographic systems deal with focal depth limitation of standard PIV and multiphase systems allow the flow study of fluids containing both continuous and dispersed phases (Adrian and Westerweel, 2011).

The advantages and disadvantages of using the PIV technique are summarised in Table 2.9. In comparison to other techniques such as laser Doppler velocimetry and anemometry, which rely on indirect measurement of velocity inferred by Doppler shift or rate of heat transfer, PIV directly measures both displacement and time increment, which gives it an edge as these variables constitute the fundamental definition of velocity. Moreover, PIV produces whole velocity vector fields that describe the flow (Adrian and Westerweel, 2011). The main drawback of this technique is that both the process fluid and construction material of the vessel or at least the area of interest, must be transparent. This of course is rarely the case in real industrial systems and thus requires equipment modification e.g. use of poly(methyl methacrylate) or Perspex and preparation of mimic fluids with rheological properties that closely matches the original fluid.

Table 2.9: Advantages and Disadvantages of PIV

Advantages	Disadvantages
• Whole field measurement • Non-intrusive • High degree of accuracy and resolution • Flows in 3D can be measured	• High capital and operational costs • Can be time consuming during set-up and data processing • Safety as Class IV lasers are used • Limited to transparent fluids and vessels

2.6.5 Particle Tracking Velocimetry (PTV)

Particle Tracking Velocimetry (PTV) works in the same principle as PIV (§2.6.4). However, in comparison to PIV, which is an Eulerian method, PTV uses a Lagrangian approach, which involves tracking the motion and measuring the velocity of individual particles instead of the entire velocity field. The seeding/ image density required for this technique is much lower (Adrian and Westerweel, 2011). In this technique, it is important that within the time interval of captures (between frames A and B), the particles have only travelled small displacements e.g. the same particle is within the field of view to ensure correct results from the chosen correlation technique. Some of the interrogation algorithms used in this method include fixed-window search, nearest neighbour search, cost minimisation and neural nets and fuzzy logic (Adrian and Westerweel, 2011). Moreover, PTV can also be done in 3-D (3-D PTV) which requires the use of multiple cameras as discussed in §2.6.4 e.g. Alberini et al. (2017) compared 2-D PIV and 3-D PTV results to determine the hydrodynamics of complex fluids in a stirred vessel with a pitched blade turbine (PBT). They found that the latter is a comparable technique to PIV when acquiring flow fields in the *r-z* plane with additional 3-D information. However, the difference in seeding particle size (~10 μm for PIV and ~200 μm for PTV) affects the overall resolution of measurements and thus limits the capability of the technique to determine smaller turbulent scales.

2.7 Quantification of Turbulence Properties

2.7.1 Mean and root mean square (RMS) Velocities

Turbulent flow is characterised by temporal velocity fluctuations of the fluid at any point (Figure 2.38). For flows that are steady on average, the instantaneous velocity signal, for example, for the *x* component of velocity, U, can be decomposed to its mean, $\overline{U}$ and fluctuating, U' components (Reynolds decomposition):

$$U = \overline{U} + U' \tag{2.51}$$

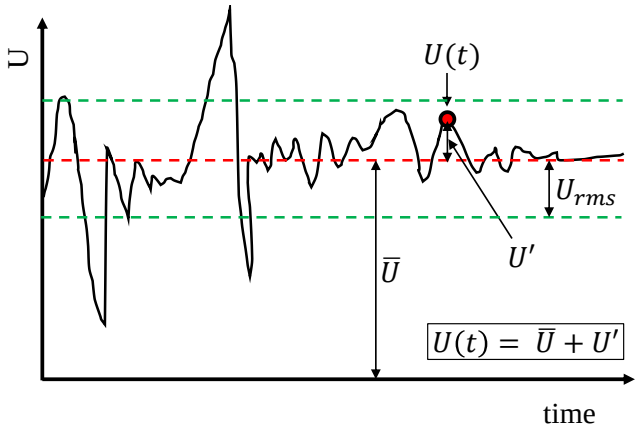

Figure 2.38: Variation of velocity at a point in a turbulent flow with respect to time and illustration of Reynolds decomposition

Since the PIV measurements conducted are angle-resolved, a similar decomposition proposed by Sharp and Adrian (2001) can be carried out:

$$U = U'' + \overline{U}|_{\theta} \tag{2.52}$$

where $\overline{U}|_{\theta}$ is the angle-resolved mean and the periodic fluctuations defined as:

$$U_p = \overline{U}|_{\theta} - \overline{U} \tag{2.53}$$

Thus,

$$U'' = U' - U_P \tag{2.54}$$

U'' is treated as the true fluctuating turbulent velocity component as it removes the periodic component U_p in U'. By definition, the fluctuating component should only consist of fluctuations that manifest purely from turbulence. Thus for the following equations, the angle resolved RMS values for the *x* and *y* components of velocity, *U* and *V* respectively e.g.

$$U_{rms} = \sqrt{\overline{U''^2}}, V_{rms} = \sqrt{\overline{V''^2}}$$

2.7.2 Reynolds Stresses and Turbulent Kinetic Energy (TKE)

The general form of the equation of conservation of momentum is given by Pope (2000):

$$\rho\left(\frac{\partial \overline{U}_j}{\partial t}\right) = \frac{\partial}{\partial x_i}\left[\underbrace{\mu\left(\frac{\partial \overline{U_\iota}}{\partial x_j} + \frac{\partial \overline{U_J}}{\partial x_i}\right)}_{I} \underbrace{-\langle p\rangle \delta_{ij}}_{II} \underbrace{-\rho\overline{U_\iota'' U_J''}}_{III}\right] \tag{2.55}$$

where $\overline{U}_\iota$ is the mean constituent of the i^{th} component of velocity, U'' is the fluctuating constituent of the i^{th} component of velocity, $\langle p\rangle$ is the mean pressure, ρ is the fluid density and μ is the fluid dynamic viscosity. The terms in the square brackets are as follows: I – viscous stresses, II – isotropic stress from the mean pressure field and III – Reynolds stresses which are stresses that arise due to momentum transfer by the fluctuating velocity field. It is normally defined as $R_{ij} = \overline{U_\iota'' U_J''}$which is a second order tensor:

$$R_{ij} = -\begin{pmatrix} \overline{U''U''} & \overline{U''V''} & \overline{U''W''} \\ \overline{V''U''} & \overline{V''V''} & \overline{V''W''} \\ \overline{W''U''} & \overline{W''V''} & \overline{W''W''} \end{pmatrix} \tag{2.56}$$

Since the measurements are 2-D, this can be reduced to:

$$R_{ij} = -\begin{pmatrix} \overline{U''U''} & \overline{U''V''} \\ \overline{V''U''} & \overline{V''V''} \end{pmatrix} \tag{2.57}$$

This tensor is also symmetric which means that $\overline{U''V''} = \overline{V''U''}$.

In high shear mixers, kinetic energy is transferred from the rotors to the fluid in the mixing head through the means of both the mean flow and fluctuating velocities in the flow. Turbulence kinetic energy or TKE (k), is the portion of the kinetic energy generated by eddies that manifest from velocity fluctuations due to turbulence. This provides a mixing mechanism via turbulent dispersion and can be evaluated using 3-D velocity data as:

$$k = \frac{1}{2}(U_{rms}^2 + V_{rms}^2 + W_{rms}^2) \tag{2.58}$$

However, since the measured velocity fields are only 2-D, the third fluctuating component W_{rms} has to be estimated using the isotropic approximation:

$$W_{rms}^2 = \frac{1}{2}(U_{rms}^2 + V_{rms}^2) \tag{2.59}$$

Hence,

$$k = \frac{3}{4}(U_{rms}^2 + V_{rms}^2) \tag{2.60}$$

This assumption was experimentally verified by Khan (2005) and the approach was used by Gabriele et al. (2009).

The energy cascade theory can be adopted to describe fluid behaviour at high Reynolds numbers. Larger anisotropic eddies are generated by the rotor with sizes comparable to that of the system's physical dimensions. These large eddies decay to smaller eddies with higher frequencies down to the Kolmogorov length scale where the ratio between viscous and inertial forces are equal to unity e.g. *Re* = 1, in which dimensionless analysis yields Equation 2.38 (Leng and Calabrese, 2004).

The average λ_k can be estimated using Equation 2.38 by using the average value for ε (Equation 2.61) e.g. power per unit mass:

$$\varepsilon_{avg} = \frac{P}{\rho V} \tag{2.61}$$

where ρ is the fluid density, V is the filled volume of the mixing head (4.47 x 10^{-4} m^3) (opposed to conventional rotor-swept volume) and P is the power, which for a standard 150/250 Silverson in-line high shear mixer is defined as (Cooke et al., 2012):

$$P = Po_Z \rho N^3 {D_{r,o}}^5 + k_1 M_T N^2 {D_{r,o}}^2 \quad (2.62)$$

where Po_Z is the 'zero flow' power constant (0.197), ρ is the fluid density, $N$is the rotor speed, $D_{r,o}$ is the outer rotor diameter, k_1 is a proportionality constant (9.35) and M_T is the total mass flow rate.

2.7.3 Estimation of Local Specific Energy Dissipation rate, ε

As established earlier, due to the dissipative nature of turbulent flows, the kinetic energy supplied by the rotor is eventually converted into heat through viscous dissipation. It occurs as viscous shear stresses act on the fluid to increase its internal energy at the expense of TKE. The amount of energy available for conversion is known as the TKE budget and its conversion into heat is the physical representation of dissipation at the smallest scale of turbulent eddies, λ_k. The rate of dissipation of energy per unit mass, ε, is one of the most important ways to characterise turbulence as it drives bubble and droplet segregation and breakup in gas- liquid- and solid-liquid mixing as well as chemical reactions (Khan, 2005). There are several ways to approximate ε, with governing assumptions such as local isotropy but in this thesis, the direct evaluation (DE) and large eddy PIV with Smagorinsky sub-grid scale (SGS) closure model are the main focus. The former uses the raw velocity data from 2-D PIV measurements whereas the latter addresses the resolution limitation of the DE method by modelling the small scale structures that are of the order of λ_k.

Direct Evaluation (DE)

The local specific energy dissipation rate may be determined from rate of viscous dissipation of the mechanical energy (Equation 2.63) (Hinze, 1975) and assuming isotropic turbulence; for 2-D data this reduces to (Equation 2.68) (Sharp and Adrian, 2001).

$$\varepsilon = \nu \overline{\left(\frac{\partial U_i''}{\partial x_j} + \frac{\partial U_j''}{\partial x_i}\right)\frac{\partial U_j''}{\partial x_i}} \tag{2.63}$$

The step-by-step derivation is as follows:

Equation 2.63 expansion yields:

$$\varepsilon = \nu \begin{bmatrix} 2\overline{\left(\frac{\partial U''}{\partial x}\right)^2} + \overline{\left(\frac{\partial V''}{\partial x}\right)^2} + \overline{\left(\frac{\partial W''}{\partial x}\right)^2} + \overline{\left(\frac{\partial U''}{\partial y}\right)^2} \\ +2\overline{\left(\frac{\partial V''}{\partial y}\right)^2} + \overline{\left(\frac{\partial W''}{\partial y}\right)^2} + \overline{\left(\frac{\partial U''}{\partial z}\right)^2} + \overline{\left(\frac{\partial V''}{\partial z}\right)^2} \\ +2\overline{\left(\frac{\partial W''}{\partial z}\right)^2} + 2\left(\overline{\left(\frac{\partial U''}{\partial y}\right)\cdot\left(\frac{\partial V''}{\partial x}\right)} + \overline{\left(\frac{\partial U''}{\partial z}\right)\cdot\left(\frac{\partial W''}{\partial x}\right)} + \overline{\left(\frac{\partial V''}{\partial z}\right)\cdot\left(\frac{\partial W''}{\partial y}\right)}\right) \end{bmatrix} \tag{2.64}$$

Through isotropic assumptions, other gradients can be estimated as (Sharp and Adrian, 2001):

$$\overline{\left(\frac{\partial W''}{\partial z}\right)^2} = \frac{1}{2}\left[\overline{\left(\frac{\partial U''}{\partial x}\right)^2} + \overline{\left(\frac{\partial V''}{\partial y}\right)^2}\right] \tag{2.65}$$

$$\overline{\left(\frac{\partial U''}{\partial z}\right)^2} = \overline{\left(\frac{\partial W''}{\partial x}\right)^2} = \overline{\left(\frac{\partial V''}{\partial z}\right)^2} = \overline{\left(\frac{\partial W''}{\partial y}\right)^2} = \frac{1}{2}\left[\overline{\left(\frac{\partial U''}{\partial y}\right)^2} + \overline{\left(\frac{\partial V''}{\partial x}\right)^2}\right] \tag{2.66}$$

$$\overline{\left(\frac{\partial U''}{\partial z}\right)\cdot\left(\frac{\partial W''}{\partial x}\right)} = \overline{\left(\frac{\partial V''}{\partial z}\right)\cdot\left(\frac{\partial W''}{\partial y}\right)} = -\frac{1}{2}\left[\overline{\left(\frac{\partial U''}{\partial x}\right)^2} + \overline{\left(\frac{\partial V''}{\partial y}\right)^2}\right] \tag{2.67}$$

Substituting these into Equation 2.64 then results to:

$$\varepsilon_{DE} = \nu\left[2\overline{\left(\frac{\partial U''}{\partial x}\right)^2} + 2\overline{\left(\frac{\partial V''}{\partial y}\right)^2} + 3\overline{\left(\frac{\partial V''}{\partial x}\right)^2} + 3\overline{\left(\frac{\partial U''}{\partial y}\right)^2} + 2\overline{\frac{\partial U''}{\partial y}\cdot\frac{\partial V''}{\partial x}}\right] \tag{2.68}$$

This method was applied at the best achievable spatial resolution (~14 λ_k) using the velocity data from the PIV measurements. However, as Saarenrinne et al. (2001) demonstrated, the spatial resolution has to be $9\lambda_k$ and $2\lambda_k$, to resolve 65% and 90% of the dissipation rate

with sufficient accuracy, respectively. Ideally, higher resolution measurements of velocity and its gradients will address this issue. However, it is currently difficult to achieve this and hence, an alternative approach which is to model the unresolved scales as in the large eddy PIV method with SGS closure was explored.

Large Eddy PIV with Smagorinsky sub-grid closure model (SGS)

Large eddy simulation (LES) approach exploits the assumption that within a turbulent flow in dynamic equilibrium, the structures of the largest scales where TKE is generated, are flow dependent whereas the smallest scales, where TKE is dissipated, are more uniform. In effect, it subjects the Navier Stokes equation, solved for the larger scales, to a low pass filter. The sub-grid scale (SGS) stress τ_{ij}, which arise from the filtering process is then found from a model for the smaller scales. This is beneficial as computation times are massively reduced, opposed to methods used in CFD packages. Sheng et al. (2000) adopted the SGS models to calculate the contribution of the unresolved scales to the total energy dissipation rate. The most suitable closure model chosen is that by Smagorinsky (1963), which is the eddy viscosity model. Using the Smagorinsky model, the SGS stress tensor is:

$$\tau_{ij} = -(C_S\Delta)^2|\bar{S}|\bar{S}_{ij}, \tag{2.69}$$

where C_S is the Smagorinsky constant (0.17 was used in this work), Δ is the filtering scale, the grid size (L_{IA}), $|\bar{S}|$is the characteristic filtered rate of strain (Equation 2.70), $\bar{S}_{ij}$ is the resolved scale strain rate tensor (Equation 2.71), and $(C_S\Delta)^2|\bar{S}|$ is the eddy viscosity (Khan, 2005).

$$|\bar{S}| = \sqrt{2\bar{S}_{ij}\bar{S}_{ij}}\,, \tag{2.70}$$

$$\bar{S}_{ij} = \frac{1}{2}\left(\frac{\partial\overline{U_i''}}{\partial x_j} + \frac{\partial\overline{U_j''}}{\partial x_i}\right), \tag{2.71}$$

The local specific energy dissipation rate can then be approximated as:

$$\varepsilon \approx \varepsilon_{SGS} = -2\langle \tau_{ij} \bar{S}_{ij} \rangle, \tag{2.72}$$

Expansion of Equation 2.72, for Cartesian coordinates using 2-D PIV data, yields:

$$\varepsilon = (C_S\Delta)^2 \left[\begin{array}{c} 2\overline{\left(\frac{\partial U''}{\partial x}\right)^2} + \overline{\left(\frac{\partial V''}{\partial x}\right)^2} + \overline{\left(\frac{\partial W''}{\partial x}\right)^2} + \overline{\left(\frac{\partial U''}{\partial y}\right)^2} \\ +2\overline{\left(\frac{\partial V''}{\partial y}\right)^2} + \overline{\left(\frac{\partial W''}{\partial y}\right)^2} + \overline{\left(\frac{\partial U''}{\partial z}\right)^2} + \overline{\left(\frac{\partial V''}{\partial z}\right)^2} \\ +2\overline{\left(\frac{\partial W''}{\partial z}\right)^2} + 2\left(\overline{\left(\frac{\partial U''}{\partial y}\right)\cdot\left(\frac{\partial V''}{\partial x}\right)} + \overline{\left(\frac{\partial U''}{\partial z}\right)\cdot\left(\frac{\partial W''}{\partial x}\right)} + \overline{\left(\frac{\partial V''}{\partial z}\right)\cdot\left(\frac{\partial W''}{\partial y}\right)}\right) \end{array} \right]^{\frac{3}{2}} \tag{2.73}$$

which can be simplified to Equation 2.74 by also applying isotropic assumptions to estimate the missing *z* components:

$$\varepsilon_{SGS} = (C_S\Delta)^2 \left[4\overline{\left(\frac{\partial U''}{\partial x}\right)^2} + 4\overline{\left(\frac{\partial V''}{\partial y}\right)^2} + 2\overline{\left(\frac{\partial V''}{\partial x}\right)^2} + 2\overline{\left(\frac{\partial U''}{\partial y}\right)^2} \right]^{\frac{3}{2}} \tag{2.74}$$

Dimensional Analysis

This method uses Equation 2.75, through dimensional relations proposed by Wu and Patterson (1989), which assumes isotropic turbulence to compute the local energy dissipation from the TKE, *k*:

$$\varepsilon_{DA} = A\frac{k^{\frac{3}{2}}}{\Lambda} \tag{2.75}$$

where *A* is a constant of the order of 1, taken as 0.85 by Wu and Patterson (1989) and Λ is a resultant macro integral length scale (ILS) defined as: $\Lambda = (\Lambda_x^2 + \Lambda_y^2 + \Lambda_z^2)^{\frac{1}{2}}$, which for 2-D PIV reduces to: $\Lambda = (\Lambda_x^2 + \Lambda_y^2 + \Lambda_x\Lambda_y)^{\frac{1}{2}}$. Λ_x and Λ_y are evaluated from 2-D spatial autocorrelation of the fluctuating velocity components (Gabriele et al., 2009).

Governing assumptions using this method include: *(a)* the majority of energy enters the turbulent flow at the largest scales of motion (ILS, Λ) and is contained in the larger eddies and

(b) this energy is transferred to the smaller scales without dissipative loss e.g. the flow is in local equilibrium. In order to use this method, the ILS has to be defined e.g. for RDT and PBT impellers, the reported vortex length scale was *W*/2 or *D*/10. A limitation of this method is that Λ is treated constant when in reality, it is non-uniformly distributed in the vessel (Khan, 2005).

Total Energy Input per Unit Mass

This is the simplest of methods where the energy dissipation is approximated using the total energy input per unit mass (Equation 2.61). This should yield a value equivalent to the volume-average of the local energy dissipation rates integrated throughout the entire vessel, which is often used as a scale-up parameter for stirred vessels. The issue with using this quantity is that the distribution of ε in the vessel is very inhomogeneous e.g. the maximum ε can be much greater than ε_{avg} (Khan, 2005).

2.8 Conclusions

As established in §1.1, although in-line rotor-stator mixers are widely used in many industrial processes due to their simplicity, flexibility and reliability, they still present a very challenging feat towards being fully characterised due to their inherent complexity e.g. mixing head geometries and number of process parameters to be considered. For instance, they are often constructed from opaque materials e.g. stainless steel (challenging in terms of flow visualisation) and rely on complex flow dynamics such as turbulence, hence why their operations are still reliant on trial and error and operator experience.

In terms of studying emulsification in HSMs, the conventional method is to analyse how droplet size distributions (DSD) and average drop sizes (such as $d_{3,2}$ and $d_{4,3}$) respond to changes in process parameters or through Computational Fluid Dynamics (CFD) simulations. In this thesis, the aim is to use PIV to characterise the fluid dynamics in a pilot scale in-line

Silverson mixer to investigate the influence of process parameters and liquid formulations upon flow field patterns and evaluated turbulence properties to determine potential areas and mechanisms of droplet break up. A modified version of the 150/250 Silverson mixer was used to achieve this e.g. all of its internal components were made out of transparent polymethyl methacrylate, including the double emulsor screens and double concentric rotors. The results discussed in the succeeding chapters aim to contribute in advancing the research area on in-line high shear mixers and suggest recommendations for future work.

Topics in fluid mechanics, liquid-liquid mixing, turbulence, fundamentals of PIV and how measurement data from it are used to quantify turbulence properties have been presented in this chapter to supplement the understanding of surveyed literature on HSMs as well as the results presented in the following chapters.

Chapter 3 – Materials and Methods

3.1 Equipment

The schematic of the experimental rig is shown in Figure 3.1. It consists of a 100 L vessel (1) fitted with a ball valve (2) at the outlet (DN25 PN25, NTC); a positive displacement pump (3) (DW1/007/7, SPX Flow); a Coriolis mass flow meter (4) (Optimass 7000C, Krohne) and a pilot scale in-line 150/250 MS Silverson rotor-stator mixer (5) (Silverson Machines Ltd) equipped with pressure (Cerebar M PMP51, Endress+ Hauser Ltd) and temperature (PT100, Thermosense) sensors at the inlet and outlet as well as a proportional relief valve (6) (SS-RL4M8F8-SET, Swagelok). A needle valve (7) (SS-16GUF16, Swagelok) was used to control the backpressure at the mixer outlet. All units are connected with 1" flexible braided pipes. A vortex breaker is also present at the bottom of the vessel (1) to prevent air entrainment. Photographs of the rig and pilot plant scale 150/250 mixer used in this work are shown in Figures 3.2a and 3.2b respectively. A raw PIV image of the mixing head and its parts is also portrayed in Figure 3.3.

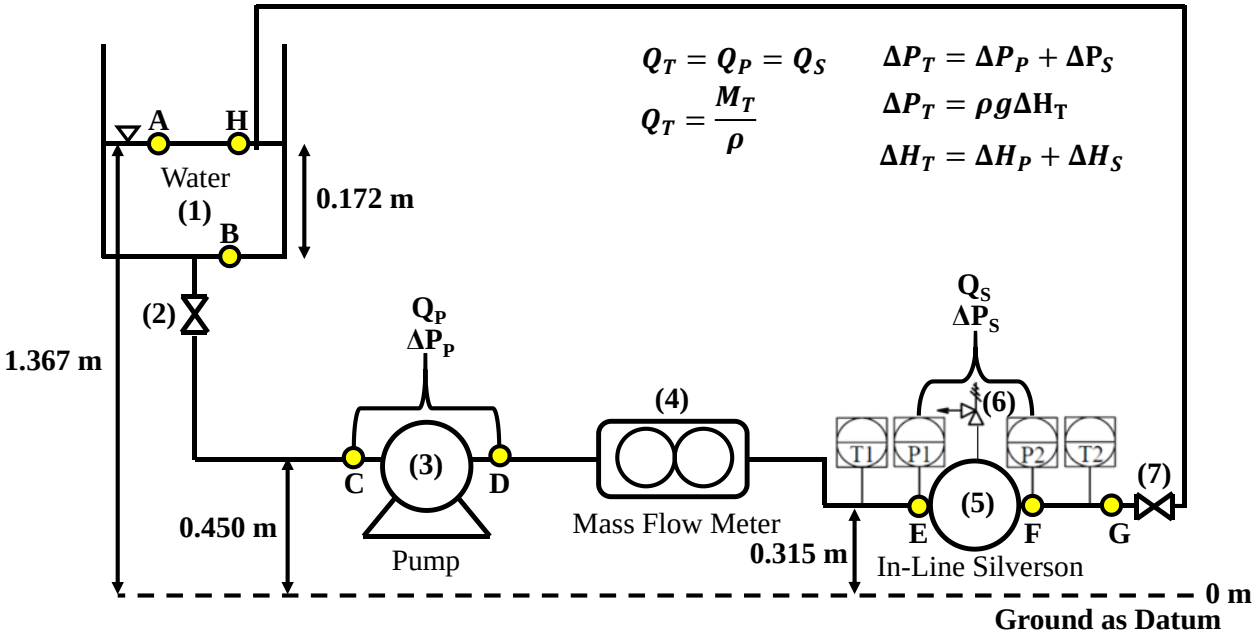

Figure 3.1: Schematic of the experimental setup. Annotations A to H represent pressure head measurements points in the system (discussed further in §5.3, Figure 5.5). A (and H): Fluid free surface, B: Tank bottom, C: Pump inlet, D: Pump outlet, E: Silverson inlet, F: Silverson outlet and G: Point before the needle valve (treated equal to F)

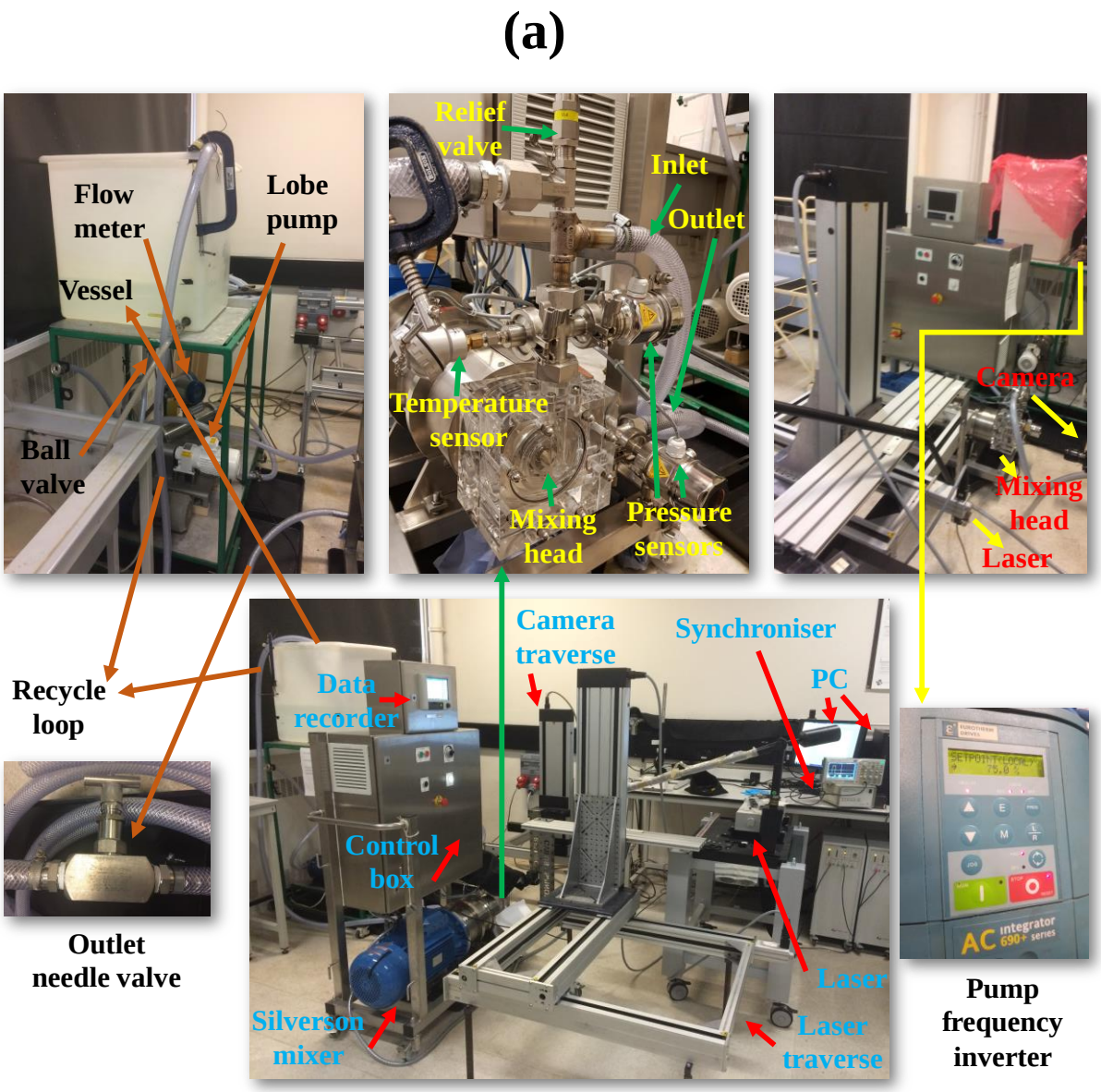

Figure 3.2: Photographs of (a) Experimental rig (b) The modified in-line Silverson 150/250 mixer

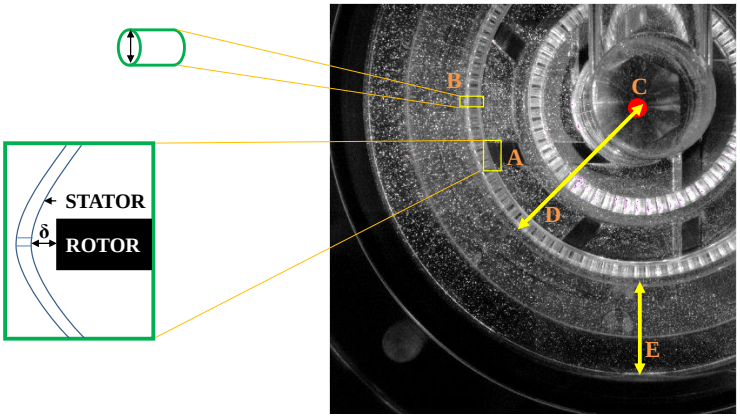

Letter	Location
A	R-S gap
B	Stator hole
C	Inlet
D	Rotor
E	Volute

Figure 3.3: Raw PIV image showing parts of the mixing head and/or identified potential droplet breakup locations in Chapter 5

The schematics of the mixing head geometry is shown in Figure 3.4 with the front view of the mixing head illustrated in Figure 3.4a. All internal components including the double emulsor screens and double concentric rotors were made out of transparent polymethyl methacrylate to enable flow visualisation. The internal space within the head has a diameter D = 108 mm and the other dimensions illustrated in Figure 3.4 are provided in Table 3.1. The rotor-stator gap is 0.23 mm and the stator thickness, Z is 15.875 mm. The physical alignment of the mixer, laser sheet and CCD camera was made as consistent as possible my marking the positions of the mixer and computer controlled traverses on the ground. In addition, the traverses were always reset 'home' positions (0, 0, 0) prior to setting the same x, y and z coordinates for a given field of view.

Table 3.1: Dimensions and details of the rotor-stator

Item	**Inner diameter (mm)**	**Outer diameter (mm)**	**Details**
Inner rotor, $D_{r,i}$	38.10	-	4 blades Blade width, B = 3.17 mm
Outer rotor, $D_{r,o}$	63.50	-	8 blades Blade width, B = 3.17 mm
Primary stator (inner screen), D_{ps}	38.56	42.55	- 5 rows of 30 x D_h = 1.59 mm circular holes, 150 holes - Separation distance between aligned rows, S_r = 4.75 mm
Secondary stator (outer screen), D_{ss}	63.96	68.33	- 6 rows of 48 x D_h = 1.59 mm circular holes, 288 holes - Separation distance between aligned rows, S_r = 4.75 mm

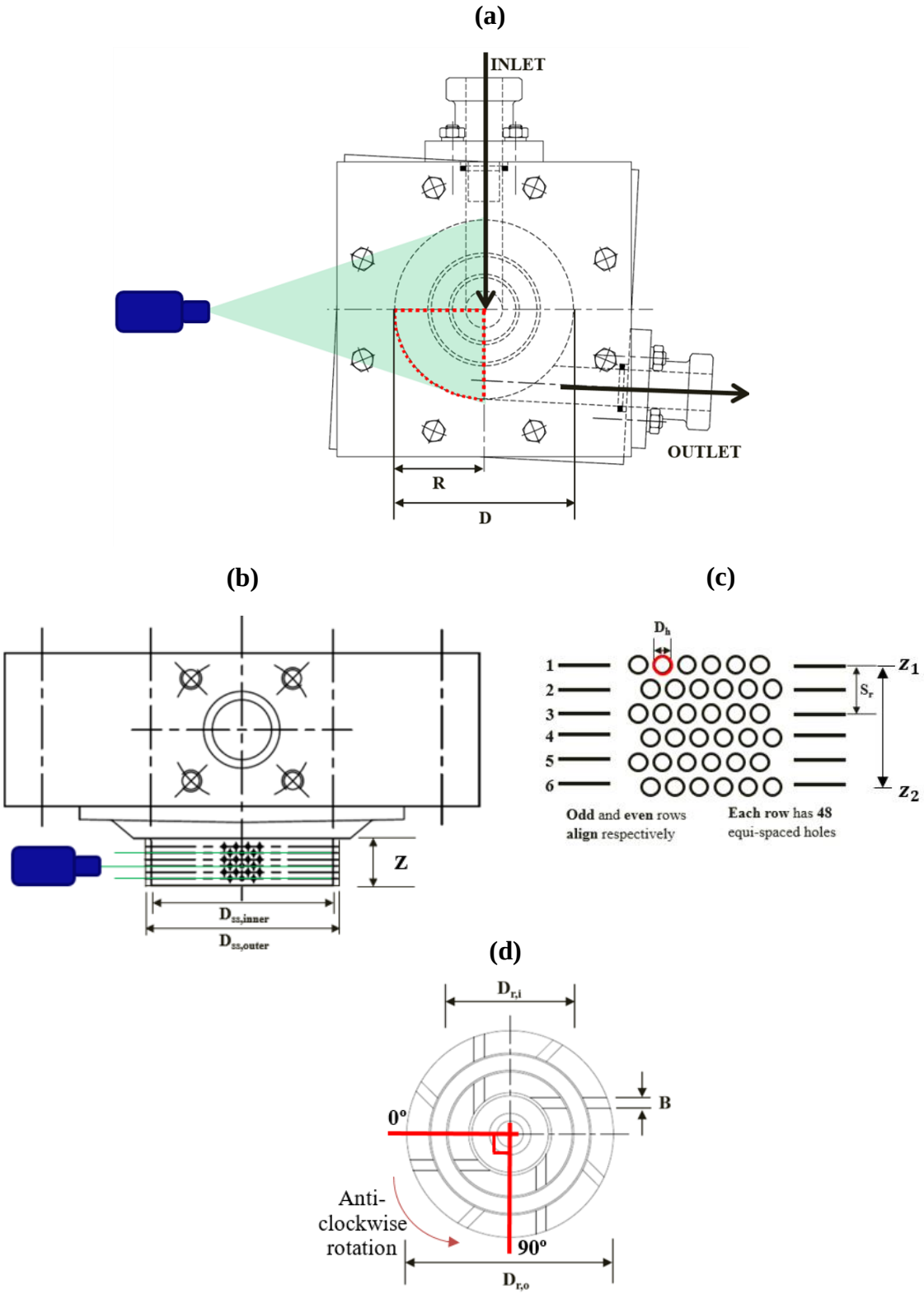

Figure 3.4: (a) Mixing head inlet, outlet, laser sheet and region of interest at the front view (b) Mixing head showing laser sheet positions from top view (c) Secondary stator details (d) Rotors schematic at 0º position

3.2 Particle Image Velocimetry Experiments

The core technique used in this thesis is particle image velocimetry (PIV) as described in §2.6.4. The 2-D PIV measurements taken were obtained using the frame straddling technique and were angle resolved to the rotor position defined in Figure 3.4d. The PIV system (Figure 3.5) consists of a dual head 532 nm Nd:YAG laser (Litron Nano PIV) pulsing from 10 to 100 Hz, a 4 megapixel (2048 x 2048 pixels^2) single frame-straddling 12 bit CCD camera (630091, TSI Inc., USA), a synchroniser (610036, TSI Inc., USA) and a personal computer running TSI Insight 4G software. The outlet of the laser light arm and camera were mounted on a computer controlled traverse which has a precision of 0.2 mm. An optical tachometer is attached onto the mixer shaft to enable encoding of the rotor angle by sending a signal to the synchroniser at the 0^o position. Other angles can then be set by inputting the necessary time delay into the Insight 4G software. The seeding particles used were silver coated hollow glass 10 µm diameter spheres with a density of 1400 kg m^{-3} (Dantec Inc., DK). They have been shown previously to have a short relaxation time and can be assumed to faithfully follow the fluid motion (Gabriele et al. 2009).

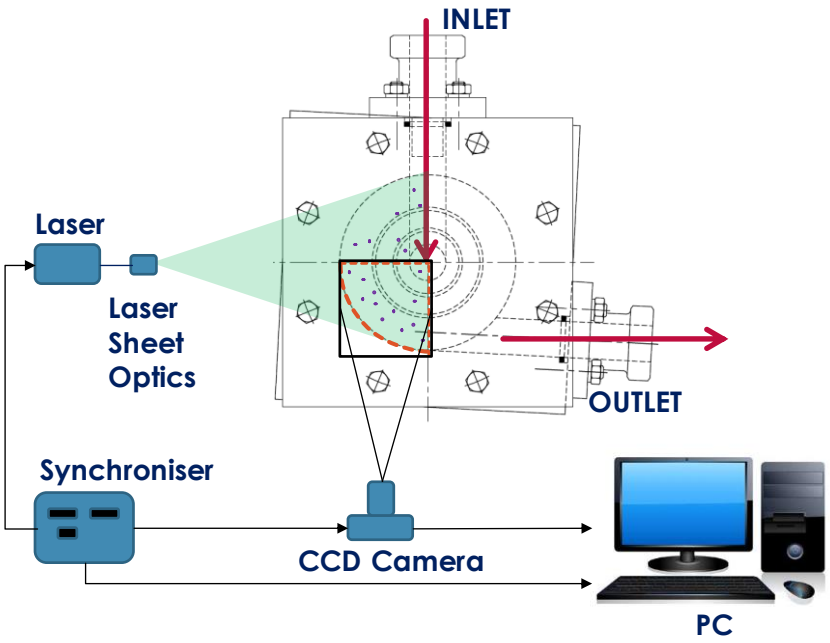

Figure 3.5: PIV setup

500 image pairs, and thus instantaneous velocity fields, were obtained for each experiment (the camera frame rate is 32 frames per second). Figure 3.6 shows that both mean, $\overline{U}$, and rms velocity, U_{rms}, values stabilise after 150 image pairs both in high shear (P_1) and bulk regions (P_2) (Figure 3.7), thus a sample of 500 is more than sufficient to ensure the turbulent features of the flow are captured (Gabriele et al. (2009). These data were used to calculate average velocity fields as well as Reynolds stresses, turbulent kinetic energy and energy dissipation rate in Chapters 4, 5 and 6. The images were processed using a recursive Nyquist grid algorithm using interrogation areas (IA) defined in the respective chapters. The Gaussian peak method by Westerweel (1997) was used to identify individual particles in the image.

The resolution of the PIV measurement depends upon the length scale of the IA, $L_{IA,}$ which acts as a filter below which length scales are not resolved. Thus, there is a compromise between resolution and field of view (FOV) and is discussed in Chapter 5. The time delay between each image in an image pair was calculated in terms of the recommended maximum displacement travelled by a particle within an interrogation area, 0.25 L_{IA} (Adrian, 1986) using:

$$\Delta t < \frac{0.25\, L_{IA}}{U_{tip}} \tag{3.1}$$

where $L_{IA} = S \times L_p$; where S is the magnification factor, L_p is the length of the IA in pixels and rotor tip speed, $U_{tip} = \pi ND$. In post-processing, velocities greater than U_{tip} as well as the vectors that failed the validation stage using the median test (5 × 5 neighbourhood size) were filtered out and replaced with interpolated values from the same grid size.

Despite numerous contributing factors to PIV data uncertainty, PIV system measurements have an accuracy of ~ 1-2% of the full-scale displacement range (Westerweel et al., 2013). The square outer section of the mixing head also ensured that reflections and optical distortions were minimised.

Velocity, turbulent kinetic energy, Reynolds stress and energy dissipation rate plots as well as some 2-D plots of dependent versus independent variables were drawn using bespoke MATLAB® codes. Microsoft® Office Excel 2016 was also used for other 2-D plots.

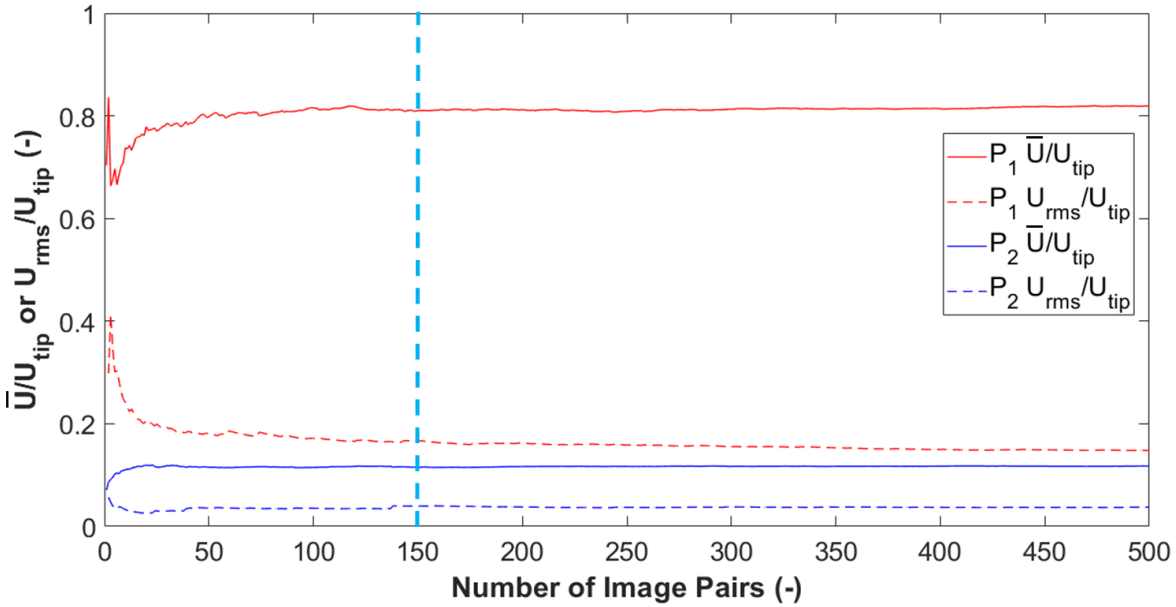

Figure 3.6: Plot of normalised mean velocities ($\bar{U}/U_{tip}$) and root mean square velocities (U_{rms}/U_{tip}) at high shear (P_1) and bulk regions (P_2) indicated in Figure 3.7 for the process condition 60.0 rps; 0.278 kg s^{-1} VFO – row 4 (z = 8.573 mm)

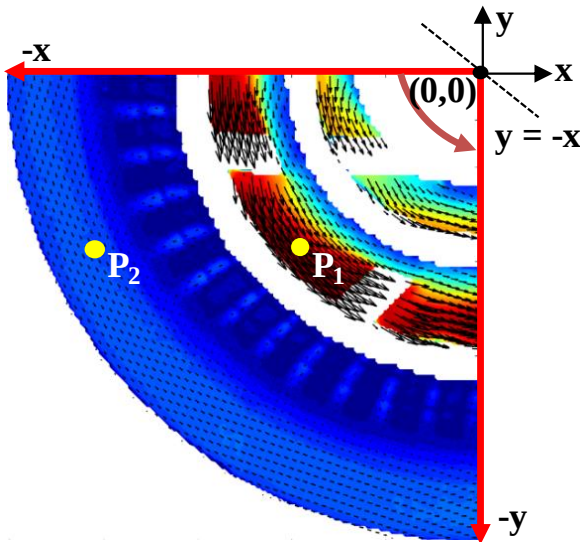

Figure 3.7: Test points in high shear (P_1) and bulk regions (P_2)

3.3 Process Conditions

Experimental/process conditions e.g. combination of rotor speed, external pump flow rate and degree of valve opening are discussed in the following results Chapters 4-6.

3.4 Working Fluids

Water was used as the working fluid in the studies presented in Chapters 4 and 5. For the studies in Chapter 6, fluids were formulated using a bench-scale laboratory mixer (Heidolph Instruments, model: RZR-2102). A dilute polymer solution (PAA) was formulated, consisting of polyacrylamide (Sigma Aldrich, UK) in aqueous glycerol (ReAgent, UK), water and sodium chloride (Sigma Aldrich, UK), to aid polymer dissolution. Shampoo solutions were also formulated with surfactants commonly used in personal care products such as sodium lauryl ether sulphate (SLES), 'Texapon N70 NA' (BASF, Germany) and cocamidopropyl betaine, 'CapB' (Stepan Company, USA), both supplied by Unilever. The former is an anionic surfactant supplied as a viscous yellow fluid with 70 wt% active ingredient at a commercial grade containing impurities. The latter is an amphoteric surfactant supplied as a clear yellowish fluid with 30 wt% active ingredient. Sodium benzoate (Sigma Aldrich, UK) was added as a preservative and citric acid (Sigma Aldrich, UK) as a pH modifier. Deionised water makes up the remainder of the shampoo. Sodium chloride (Sigma Aldrich, UK), was also added as brine to act as a viscosity modifier for shampoo B. These are common ingredients that can be found on shampoo labels (Gubitosa et al., 2019; Inolex, 2019).

3.4.1 Shear Viscosity Measurements

The principles of shear viscosity measurements are covered in §2.2.2. The viscosity, μ, and apparent viscosities, μ_A, of the fluids: glycerol and polyacrylamide solutions and the shampoo formulations, were measured at 23 ºC using a 60 mm 2º cone and plate stainless steel

geometry in a Discovery Hybrid Rheometer (DHR-2, TA Instruments, Inc). The shear profile was increased from 0.1 to 1400 s^{-1}. The rheology of shampoo formulation B was shear-thinning and follow the power law viscosity relationship (Equation 2.5). It also did not change over time as measurement of pre- and post- shear sample flow curves did not reveal any significant differences. A viscometric material property, normal stress differences, N_1, which manifest due to the differences in the normal components of the stress tensor (Phan-Thien, 2002), were also simultaneously attained via axial force measurements during the acquisition of shear stress versus shear rate data on the same instrument. It revealed that shampoo B exhibited viscoelastic traits e.g. fluid relaxation time (Equation 6.9). Detailed rheological parameters are presented in §6.2.1.

3.4.2 Density Measurements

The densities of the fluids were estimated by taking an average of triplicate measurements of weighed 10 mL volume of each fluid using a micropipette and a weighing scale (data shown in §6.2.2).

3.5 Conclusions

The equipment and experimental setups used for the PIV experiments performed to investigate the flow behaviour in an in-line 150/250 Silverson high shear mixer have been described in this chapter. Furthermore, measurement of the viscometric properties of the working fluids were discussed. Finally, the process conditions used for specific studies are detailed in their respective chapters.

Chapter 4 – Flow Studies in an In-Line Silverson 150/250 High Shear Mixer Using PIV[3]

4.1 Introduction

Studies on the hydrodynamics of in-line high shear mixers are still limited, thus in this chapter, angle resolved 2-D PIV measurements were carried out to increase the understanding of and characterise the flow field inside a custom built, pilot-scale, in-line Silverson 150/250 HSM, using water as the working fluid (single phase flow). The effects of process parameters such as rotor speed, external pump flow rate and back pressure on the overall flow field were investigated. The velocity fields were also analysed to determine overall flow structures, in particular flows near the stator holes and also to evaluate the mixer flow number.

4.2 Materials and Methods

4.2.1 Process Conditions

Water was used as the working fluid for measurements made in the turbulent regime (Re > 10,000), where 120,000 < Re < 420,000, calculated using:

$$Re = \frac{\rho N {D_{r,o}}^2}{\mu} \tag{4.1}$$

where ρ is the density, μ is the viscosity at a fixed temperature, N is the rotor speed and $D_{r,o}$ is the outer rotor diameter.

[3] Part of this work has been published in: Espinoza, C.J.U., Simmons, M.J.H., Alberini, F., Mihailova, O., Kowalski A. J. and Rothman, D. (2018) Flow studies in an in-line Silverson 150/250 high shear mixer using PIV. **Chemical Engineering Research and Design**, 132: 989-1004

The pump was used to provide a flowrate, $\dot{m}$ in the mixing head (0.208 – 0.347 kg s^{-1}) and the rotor speed, was controlled independently (30.0 – 103.3 rps); both were controlled using frequency inverters. The needle valve was also used to control the flow rate and back pressure, with the relief valve set at 5 bar (below the pressure rating of the mixing head of 7 bar). A data recorder (Memograph RSG45, Endress+Hauser) was used to log the mass flow rate, rotor speed, as well as the pressure and temperature at the mixer inlet and outlet. Flow meters were calibrated using the bucket and timer method and were found to be accurate within 1.3% in all experiments.

The parameters used for each experiment are summarised in Table 4.1. Runs 1-3 were carried out using the external pump only (PO), whereas runs 4-5 were carried out using the Silverson mixing head only with the pump switched off (SO). Runs 6-8 and 9-11 were carried out with both pump and Silverson operating but with the outlet back pressure valve set either fully open (VFO) or partially closed (VPC) respectively. For VPC conditions, the needle valve was set to achieve the (PO) flowrate prior to switching the Silverson on so that the external pump controls the overall process flow rate e.g. to prevent the Silverson from acting as a pump.

Table 4.1: Summary of the experimental runs

Run (-)	**External pump flow rate, $\dot{m}$ (kg s^{-1})**	**Rotor speed, N (rps)**	**Flow class (-)**
1	0.208	0	PO
2	0.278	0	PO
3	0.347	0	PO
4	0.000	30.0	SO
5	0.000	60.0	SO
6	0.278	30.0	VFO
7	0.278	60.0	VFO
8	0.278	103.3	VFO
9	0.278	30.0	VPC
10	0.278	60.0	VPC
11	0.278	103.3	VPC

4.2.2 PIV Experiments

The images were processed using a recursive Nyquist grid algorithm using interrogation areas (IA) of 32 × 32 and 16 × 16 pixels for the first and second passes respectively. For the experiments performed, the spatial resolution is 38.58 μm pixel^{-1} which equates to a resolution of 0.62 mm for a 16 x 16 pixel IA, with vectors spaced 0.31 mm apart allowing for 50% overlap of IAs. The time delay between each image in an image pair was calculated in terms of the recommended maximum displacement travelled by a particle within an interrogation area, 0.25 L_{IA} (Adrian, 1986) using Equation 3.1. These spatial and temporal resolutions are compliant to the rules of thumb of PIV measurements described in Table 2.8.

Velocity vectors obtained in Cartesian coordinates are defined as U_x and U_y. Due to the geometry of the filled volume, these values are also converted to cylindrical coordinates as illustrated in Figure 4.1, to ease visualisation. The data is first reflected over the line $y = -x$ as shown in Figure 4.1a to 4.1b (axes re-labelled in cylindrical coordinates), which is then transformed into tangential and radial velocity components in the plane of interest (θ, r), defined as U_θ and U_r respectively as portrayed in Figure 4.1c. Finally, a section of the field corresponding to the jets emerging from the stator holes is examined in detail, Figure 4.1d. Triangular interpolation was also performed using '*gridfit*', a MATLAB® function developed by D'Errico (2005) to evaluate velocity components at a fixed radius across all tangential positions e.g. 3 mm above the outer stator radius, r = 37.2 mm. The result of this process is shown in Figure 4.2, where it is demonstrated that the interpolated values track the sparse raw data for r = 37.2 mm +/- 0.2 mm. Most of the results, were the ones evaluated for the 4th row of holes in the stator at z = 8.573 mm, Figure 3.4c.

Four-fold symmetry is assumed as shown in Figure 4.3. It is noteworthy that this assumption is subject to some limitations, for instance, the exit pipe is only present in one

quadrant of the mixing head and unfortunately, one that is not suitable for laser access hence its effects on the overall flow pattern were indeterminable

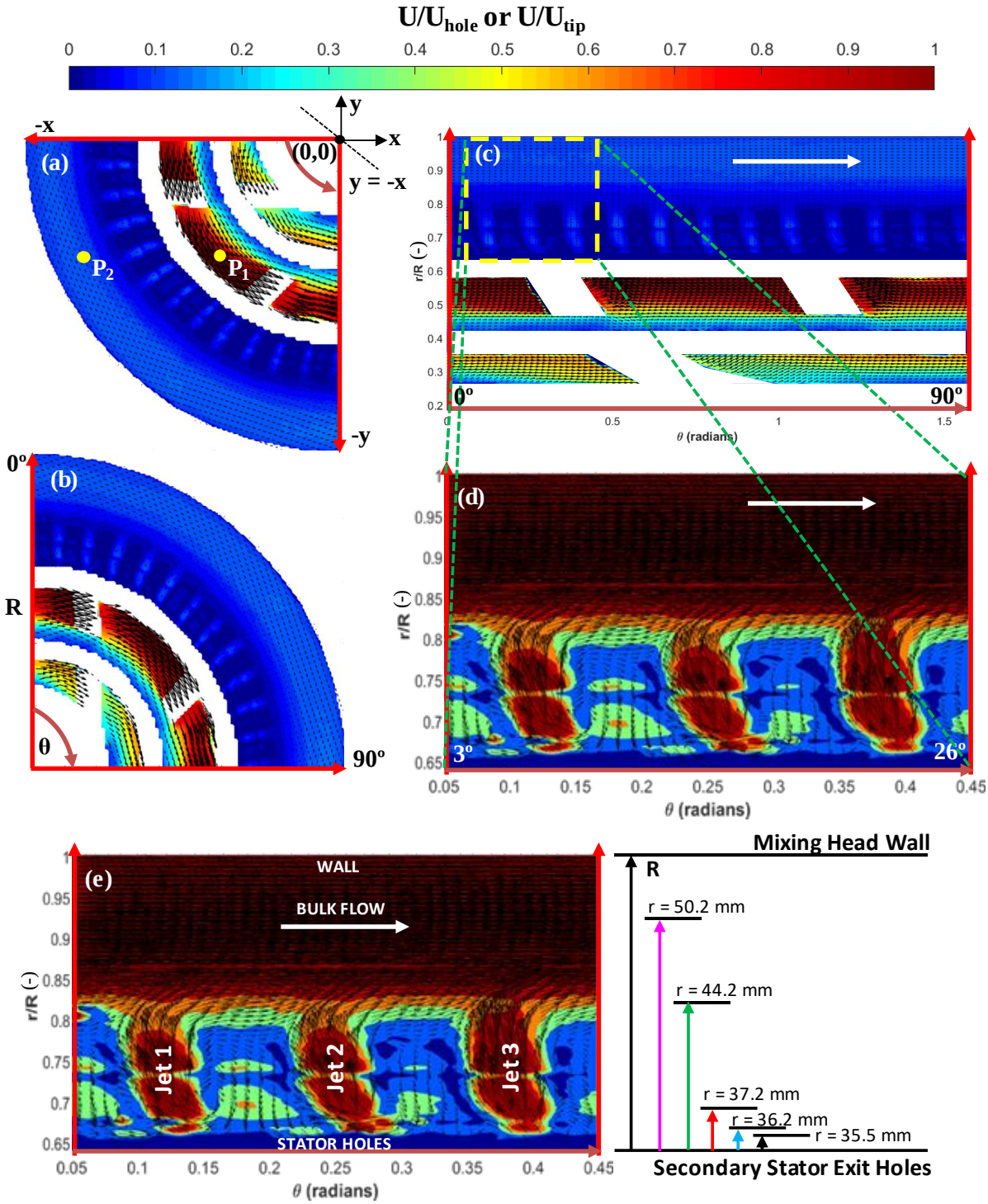

Figure 4.1: Schematic to show how different contour plots were created for the process condition 60.0 rps; 0.278 kg s^{-1} VFO – row 4 (z = 8.573 mm) (a) Contour plot of raw PIV velocity data in Cartesian coordinates, normalised with U_{tip} (b) Reflection of (a) over the $y = -x$ line (axes re-labelled in cylindrical coordinates) (c) PIV velocity data in cylindrical coordinates, normalised with U_{tip} (d) Zoomed contour plots for better visualisation of jets emerging from the stator holes, normalised with U_{hole} (e) Location details of the zoomed contour plots including the radii in Figure 4.7. P_1 and P_2 in (a) are high shear and bulk regions respectively at which average velocities and rms velocities were monitored (Figure 3.7).

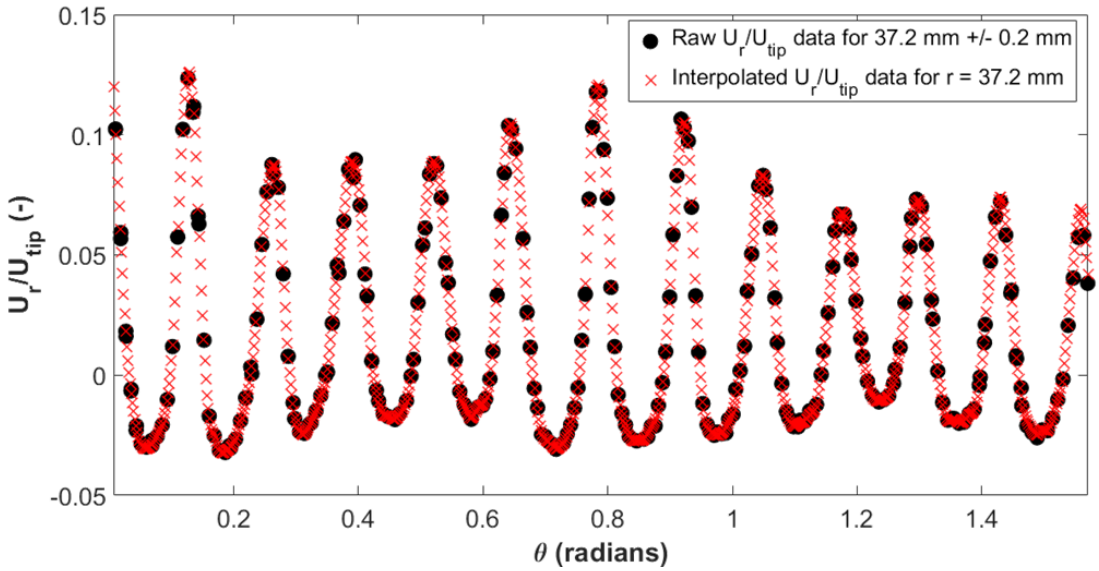

Figure 4.3: Raw data and interpolated values for condition 60.0 rps; 0.278 kg s^{-1} PS VFO at *r* = 37.2 mm – row 4 (z = 8.573 mm)

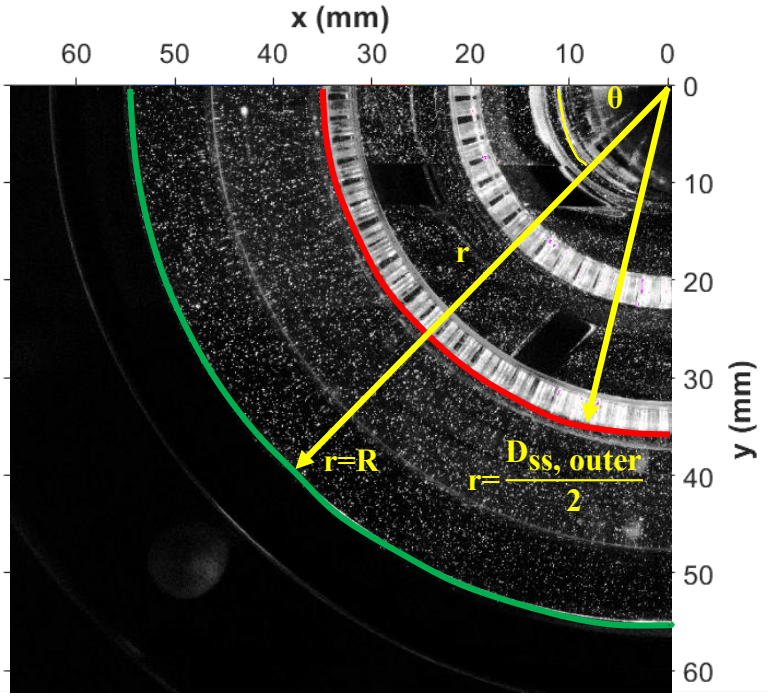

Figure 4.2: Raw image example

4.2.3 Flow Number

Flow number, N_Q, is a measure of the capability of a mixer to deliver flow, defined as the ratio between the volumetric flow rate, Q_T ($m^3\ s^{-1}$) and a hypothetical flow rate imposed by the rotor:

$$N_Q = \frac{Q_T}{N{D_{r,o}}^3} \tag{4.2}$$

Volumetric flow rate, Q_T is calculated as the net flow through a control surface set normal to the radial flow coming out of the secondary stator. In these experiments this was set as an arc close to the outer secondary stator (red line in Figure 4.3) where the radius of the arc could be varied. The minimum distance taken from the outer stator was 1.00 mm to prevent reflections from the rotor which can cause interference in the data. With the symmetry assumption of every 90º or π/2 radians (Figure 3.4d), Q_T can thus be calculated from angle resolved PIV measurements using:

$$Q_T = 4\int_{z_1}^{z_2}\int_0^{\frac{\pi}{2}} r\,U_r d\theta dz = 4r\sum_{z=z_1}^{z=z_2}\sum_{\theta=0}^{\theta=\frac{\pi}{2}} U_r d\theta dz \tag{4.3}$$

where U_r is the radial velocity component, r is the radial distance from the centre of the rotor shaft, z is the axial distance from the middle of the first row of stator holes, z_1 to the middle of the last row of stator holes, z_2 e.g. $z_2 - z_1$ = 9.6 mm (Figure 3.4c) and θ is the tangential angle.

Net flow rates were initially calculated using the plug flow approximation. Equation 4.3 was simplified to calculate the surface flow rate per unit width ($m^2\ s^{-1}$) from the 2-D data:

$$S_{surf} = 4r\sum_{\theta=0}^{\theta=\frac{\pi}{2}} U_r d\theta, \tag{4.4}$$

The resulting value was then multiplied by $6D_h$ (effective stator thickness with fluid flowing out is comprised of the six rows of holes of diameter D_h) to evaluate a plug flow approximation of net flow rate, Q_{plug} ($m^3\ s^{-1}$):

$$Q_{plug} = 6D_h S_{surf}, \tag{4.5}$$

The flow number, N_Q of the rotor may also be calculated directly from the relationship between the volumetric flow rate and the set rotor speed e.g. by plotting Q vs N, when the outlet valve is fully open and the external pump is switched off. Since the relationship is linear, the gradient was used to calculate N_Q from Equation 4.2. The value obtained, $N_Q = 0.010$, is of similar magnitude to that obtained by Cooke et al. (2012) ($N_Q = 0.050 – 0.070$) for a similar mixing head. The smaller value obtained in this work is most likely due to differences in the piping system which influence the flow. Moreover, these flow numbers are very small in comparison with impellers used in stirred vessels which are an order of magnitude higher e.g. 0.7 for a Rushton disk turbine (Hemrajani and Tatterson, 2004). This implies that the rotor has low pumping capability. This is thought to be due to additional flow restrictions in the equipment setup that are not present in conventional stirred vessels e.g. walls of the mixing chamber; presence of flow control elements, pipe fittings and bends; and most importantly the geometry of the double screen stator. The narrow holes within the stator allow for better transfer of tangential momentum from the rotor to the surrounding fluid hence the fluid moves in the tangential direction as opposed to being ‘pumped out’ in the radial direction (Utomo, 2009).

4.3 Results and Discussion

4.3.1 Average Flow Fields

Flow patterns of water in the mixing head generated by either the external pump (PO) or Silverson alone (SO) are given in Figure 4.4. The corresponding figures for flows with both the pump and Silverson operating (defined as PS) with either VFO or VPC are given in Figure 4.5. The velocities shown are either normalised by the calculated hole velocity from the secondary stator, U_{hole} (0.36 – 0.60 m s^{-1}) or rotor tip speed, U_{tip} (5.98 – 20.61 m s^{-1}) for ease of illustration. The coordinates (Cartesian: x, y; cylindrical polar: r) are normalised by the inner radius of the mixer head ($D/2$ = 54 mm).

Figure 4.4 shows that the normalized velocity fields for both PO and SO conditions are self-similar as would be expected given that the flow is well within the turbulent regime. Moreover, it can also be observed that for PO (Figure 4.4a), the flow pattern is dominated by radial discharge jets through the stator holes. This is as expected since there is no mechanism for tangential flow as the rotor is stationary. For SO (Figure 4.4b), the flow is dominated by tangential motion due to the motion of the rotor and the highest velocities (0.8-0.9 U_{tip}) are present close to the rotor and in the R-S gap. For PS conditions, a combination of both radial and tangential flows are present as shown in Figure 4.5. Due to the possibility of cavitation in the mixer head when the outlet was set at ambient (atmospheric) pressure (e.g. at N > 4200 rpm SO), even with the presence of the external pump, it is necessary to set a back pressure at the outlet to alleviate this. The needle valve installed restricts flow due to its small orifice even when fully open (VFO); the impact of an additional flow restriction through partially closing this valve (VPC), was also investigated.

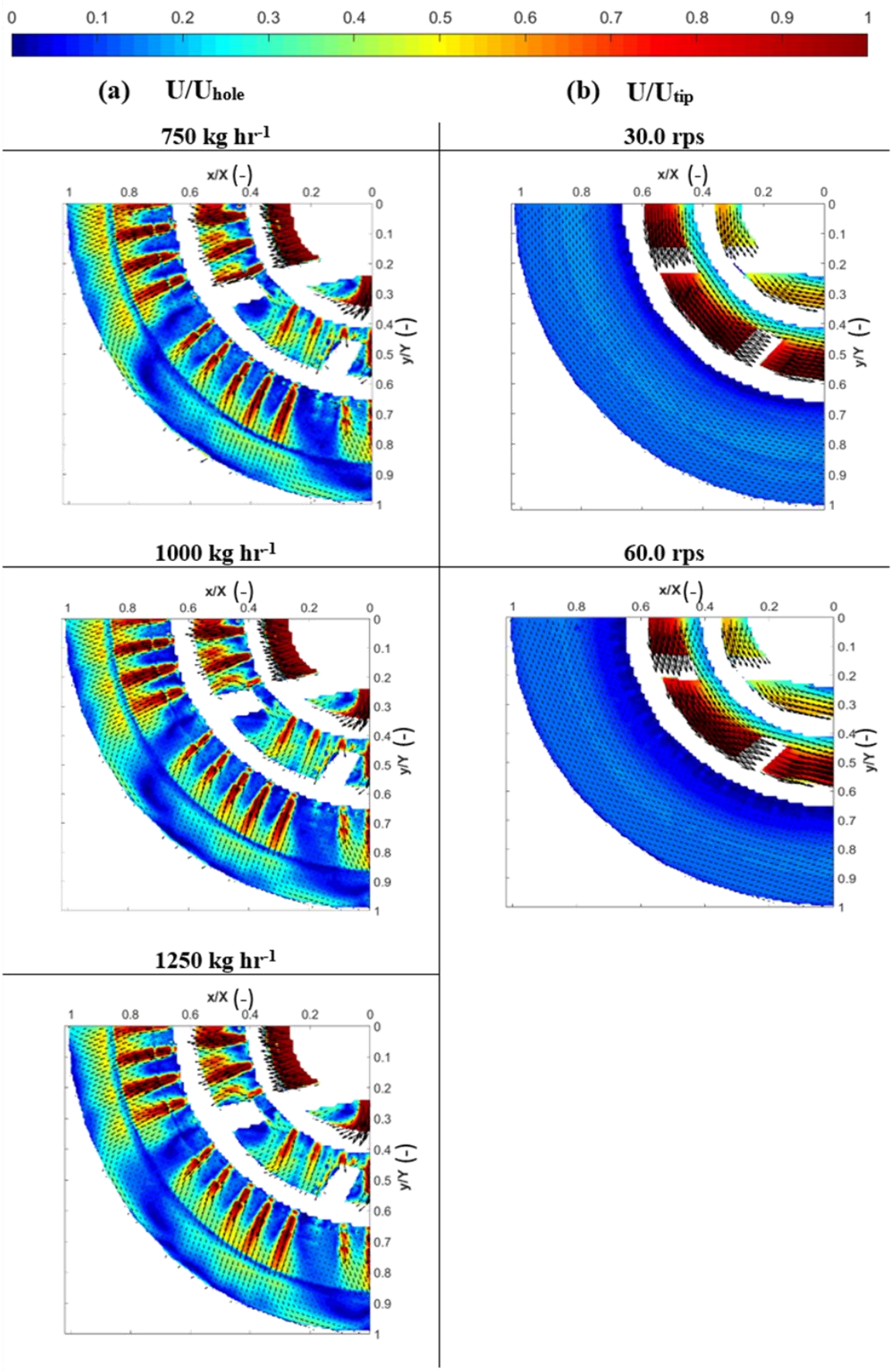

Figure 4.4: Flow patterns generated by (a) Pump only (PO) and (b) Mixer/Silverson only (SO) – row 4 (z = 8.573 mm)

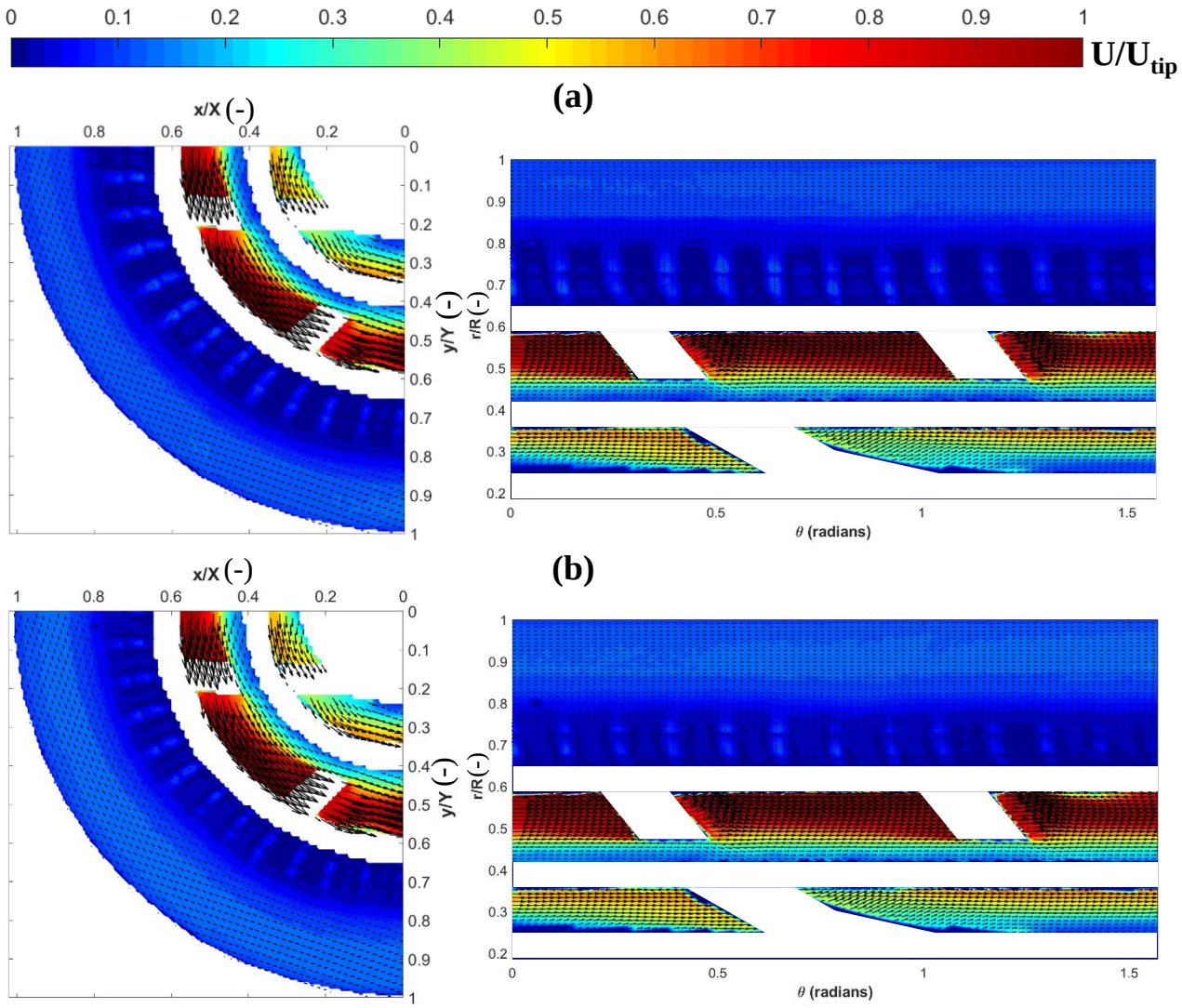

Figure 4.5: Flow patterns generated by both the pump and Silverson mixer (PS) at 60.0 rps; 0.278 kg s^{-1} – row 4 (z = 8.573 mm) with (a) valve fully open (VFO) and (b) valve partially closed (VPC). The images on the left and right are in Cartesian and Cylindrical coordinates respectively.

Figure 4.5 shows very subtle differences between VFO and VPC flow fields despite the same pump flow rate (0.278 kg s^{-1}) and rotor speed being set (N = 60.0 rps). Examining the flows in Cartesian coordinates on the left of the figure, the jet penetration distance is slightly larger for the VFO case than the VPC case, and the velocity magnitudes are slightly larger. It might be expected that partially closing the valve has the effect of increasing the amount of bulk fluid moving tangentially which in effect, decreases the depth of jet penetration.

Detailed analysis of the normalised average radial (U_r) and tangential (U_θ) velocity components are presented in Figure 4.6 to quantify the above findings at fixed r = 37.2 mm. Figure 4.6a confirms the earlier observation that the flow is primarily radial when the flow is delivered by an external pump only (PO), the data for radial velocities are stacked on top of each other and the corresponding tangential velocities are practically zero. This is expected as there is no rotational flow generated by the rotor. Conversely in Figure 4.6b, when the flow is generated by the Silverson mixer only (SO), both radial and tangential components exist as when the rotor rotates, it pushes the fluid towards the direction of rotation e.g. tangentially anti-clockwise. In addition, due to the stator geometry, jets are also produced when the fluid escapes the volume enclosed by the rotor and the stator. Figure 4.6b shows that, at 30.0 rps for SO, the radial and tangential velocities are weakest and strongest respectively, suggesting that the Silverson mixer has poor pumping capability at low rotor speeds and thus the flow is predominantly tangential. As the rotor speed is increased e.g. at 60.0 rps, the balance between radial and tangential components become apparent e.g. the radial velocity increases at the expense of decreased tangential velocity, implying improved pumping capability.

This effect may also be illustrated by examining the effect of introducing a pump flow rate of 0.278 kg s^{-1} at 30.0 rps; the governing flow switches from tangential to radial entailing that the external pump has more impact on the overall flow. However, beyond a certain rotor speed e.g. 60.0 rps, there is no discernible differences in the flow patterns and the tangential flow pattern dominates. This general trend is true for all pump external flow rates examined, but the value of the mixer speed at transition increases with pump flow rate.

In terms of whether the valve is fully open or partially closed (Figure 4.6c and 4.6d), the radial velocity components are similar whereas, it is evident that the tangential flow significantly increases with rotor speed for VPC conditions (Figure 4.6d). This suggests that

increasing flow restriction at the outlet results in decreased radial and increased tangential velocities.

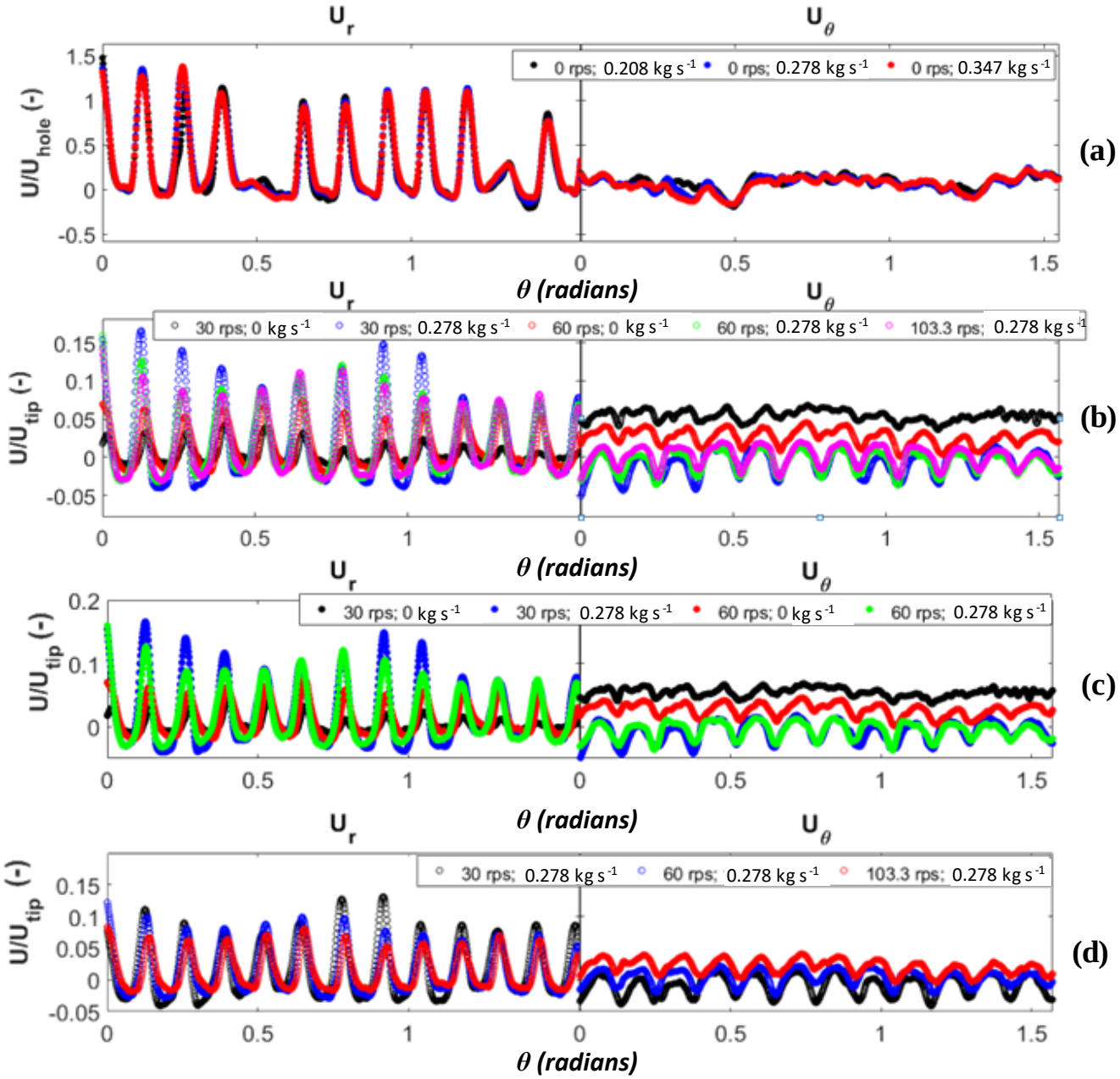

Figure 4.6: Trends of radial and tangential average velocities at varying process conditions at a fixed r = 37.2 mm – row 4 (z = 8.573 mm) (a) PO only conditions, VFO (b) SO and PS conditions, VFO (c) SO and PS conditions, VFO only (d) PS conditions, VPC only

4.3.2 Effect of Radial Distance Upon the Flow Fields

Figure 4.7 demonstrates that radial flow velocities dissipate dramatically with increasing radial distance from the outer secondary stator (Figures 4.1e and/or 4.3). A region of high radial velocities is found a few mm above the secondary stator ($D_{SS,outer}/2 = 34.16$) e.g. at r = 37.2 mm and lowest near the inner wall of the mixer head e.g. r = 50.2 mm. This is because the stator jets do not penetrate far enough into the bulk fluid. However, the contrary can be observed with tangential velocities; they are strongest near the inner wall because the bulk fluid follows the tangential motion of the rotor, and with increasing radial distance, the bulk flow becomes increasingly free of penetrating jets. Through this, an indication of how far the jet can penetrate the bulk fluid can be obtained e.g. between 44.2 and 50.2 mm.

It was noted above that if the valve is partially closed (VPC), jet penetration distance is decreased and tangential flow is increased as can be observed by comparison of the profiles at r = 44.2 mm between Figure 4.7a and Figure 4.7b. Another observation is the decreased difference in tangential velocity values between r = 44.2 and 50.2 mm along with their increased magnitudes. These convey that more of the bulk fluid flow tangentially when the valve is partially closed. Since the magnitude of radial velocities are similar when the valve is fully open, it is implied that the energy of the jets is conserved. Thus, this phenomenon can be treated analogous to a short nozzle-to-wall distance configuration for impinging jets.

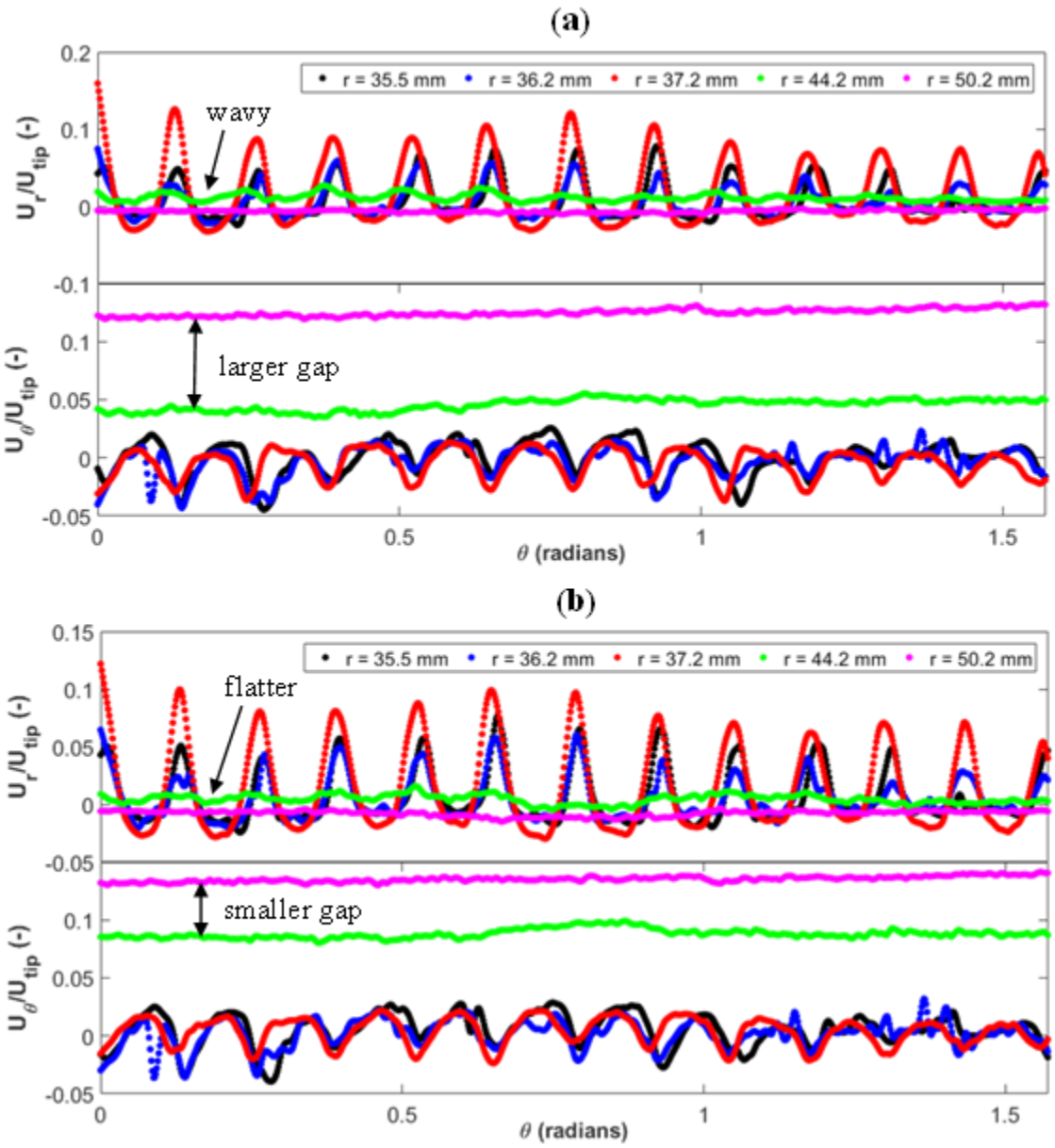

Figure 4.7: Trends of radial and tangential average velocities at varying radii defined in Figure 4.1e for 60.0 rps; 0.278 kg s^{-1}– row 4 (z = 8.573 mm) (a) VFO (b) VPC

4.3.3 Jet and Recirculating Flow Patterns

Jets are generated as the fluid flows through the stator holes. Their penetrating distance is greatest when the flow is solely delivered by an external pump as the flow is predominantly radial (Figure 4.4a); least when the flow is generated by the Silverson mixer only as the flow is predominantly tangential (Figure 4.4b); and governed by selected process conditions in

combined flows. Contour plots of average radial and tangential velocities are useful in distinguishing differences between PO and SO conditions because they were normalised with U_{hole} and U_{tip} respectively. However, since PS conditions were also normalised with U_{tip}, the difference between VFO (Figure 4.5a) and VPC (Figure 4.5b) conditions appeared subtle as jet velocities are much lower in magnitude.

Zoomed contour plots of the jets (between ~ 3 to 26º or 0.05 to 0.45 radians as demonstrated in Figure 4.2) are shown in Figure 4.8, normalised with U_{hole} of the combined flow rate (VFO) to emphasise the nature of jet and recirculation flows. From this, it is evident that the length of jet penetration (where the radial flow from the stator holes turns into tangential flow in the bulk e.g. when the vertical radial vectors out of the stator hole translate to horizontal tangential vectors in the bulk) decreases as rotor speed increases (observe the distance of the broken yellow line from the wall where this occurs in Figure 4.8 c,e,g for VFO conditions), which is much more prominent in VPC conditions (Figure 4.8 d,f,h). The presence of high velocity jets induce recirculation loops as can be seen from the observed negative radial and tangential velocities e.g. encircled in Figure 4.8d. This phenomenon, with the absence of an external pump in the system, was also observed both numerically and experimentally by Utomo et al. (2008, 2009) and Mortensen et al. (2011, 2017) respectively in batch rotor-stator systems. It was found in these studies that regardless of the blade position, jets were centred towards the leading edge of the stator hole while the backflow occurred at the trailing edge. Furthermore, as the jets exit the stator hole, they bend in the opposite direction to the rotor rotation. These are consistent with the results presented in Figure 4.8. It is thought that the jets are formed when the leading edge of the rotor blade expels fluid out of the stator hole (momentum flux changes direction from tangential to radial as the fluid hits the surface of the stator's leading edge) while its trailing edge generates a negative pressure that pulls the fluid back in.

Since there are two sources of flow and additional flow control elements e.g. valves are included in the current setup, the flow is very complex. For PO conditions, the jets are comparatively more uniform: straighter and stronger, penetrating closer to the inner wall of the mixer head (Figure 4.8a). Recirculation occurs due to jet-to-jet interaction (encircled in Figure 4.8a), similar to that observed in multiple impinging jet studies. For SO conditions, hardly any jetting occurs (Figure 4.8b). The reason behind this can be attributed to the stator geometry: Utomo et al. (2009) concluded that for geometries with narrower holes, jets decay within a few millimetres from the holes. This is because these jets are small and have large surface areas, allowing them to efficiently transfer momentum to the surrounding bulk fluid. This also implies that the geometry used has poor pumping capabilities and thus the jets are primarily generated by the external pump.

For combined flows (PS conditions), partially closing the outlet valve also has a significant effect on the recirculation loop pattern. At low rotor speeds, the effect is practically negligible as can be seen when comparing Figure 4.8c with Figure 4.8d. At a higher rotor speed, recirculation is weaker and the fluid tends to accelerate down to the next stator hole (comparing Figure 4.8e with 4.8f); more of the fluid flows tangentially in the same direction (positive values) as the rotor rotation and jet penetration length is also reduced. These results are shown in 2-D in Figure 4.9 for a fixed r = 37.2 mm. At an even higher rotor speed (comparing Figure 4.8g with 4.8h), the overall flow pattern begins to resemble a SO condition. With the valve fully open, the same transition is also observed but occurs at a slower rate; partially closing the valve accelerates this occurrence as portrayed by Figure 4.9b where for 103.3 rps VPC, tangential velocities are almost always positive.

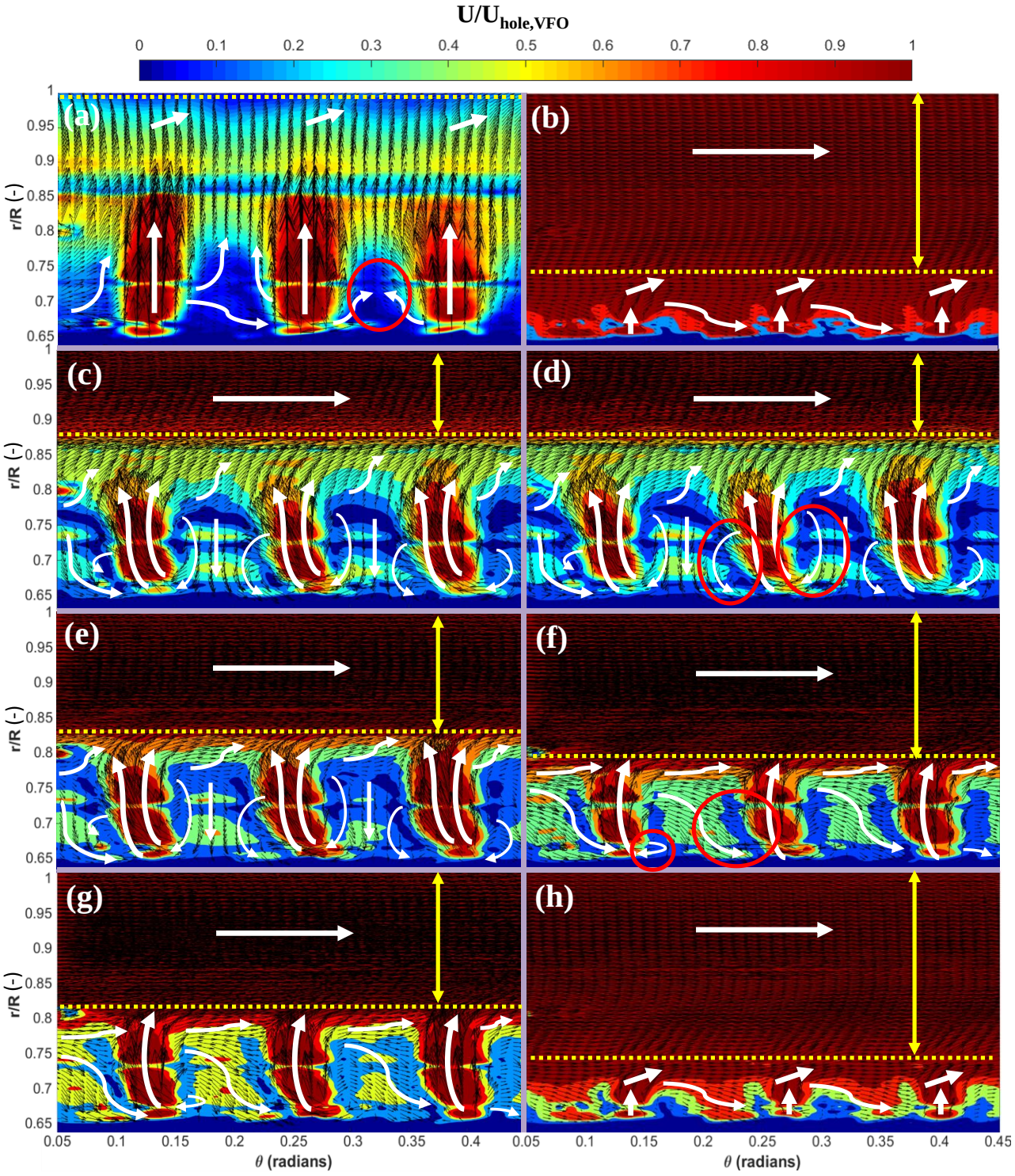

Figure 4.8: Zoomed in velocity fields and contour plots in cylindrical coordinates between 0.05 and 0.45 radians, all normalised with U_{hole} to highlight jet and recirculation flow patterns – row 4 (z = 8.573 mm) for (a) 0.278 kg s^{-1} PO (b) 60.0 rps SO (c) 30.0 rps; 0.278 kg s^{-1} VFO (d) 30.0 rps; 0.278 kg s^{-1} VPC (e) 60.0 rps; 0.278 kg s^{-1} VFO (f) 60.0 rps; 0.278 kg s^{-1} VPC (g) 103.3 rps; 0.278 kg s^{-1} VFO (h) 103.3 rps; 0.278 kg s^{-1} VPC

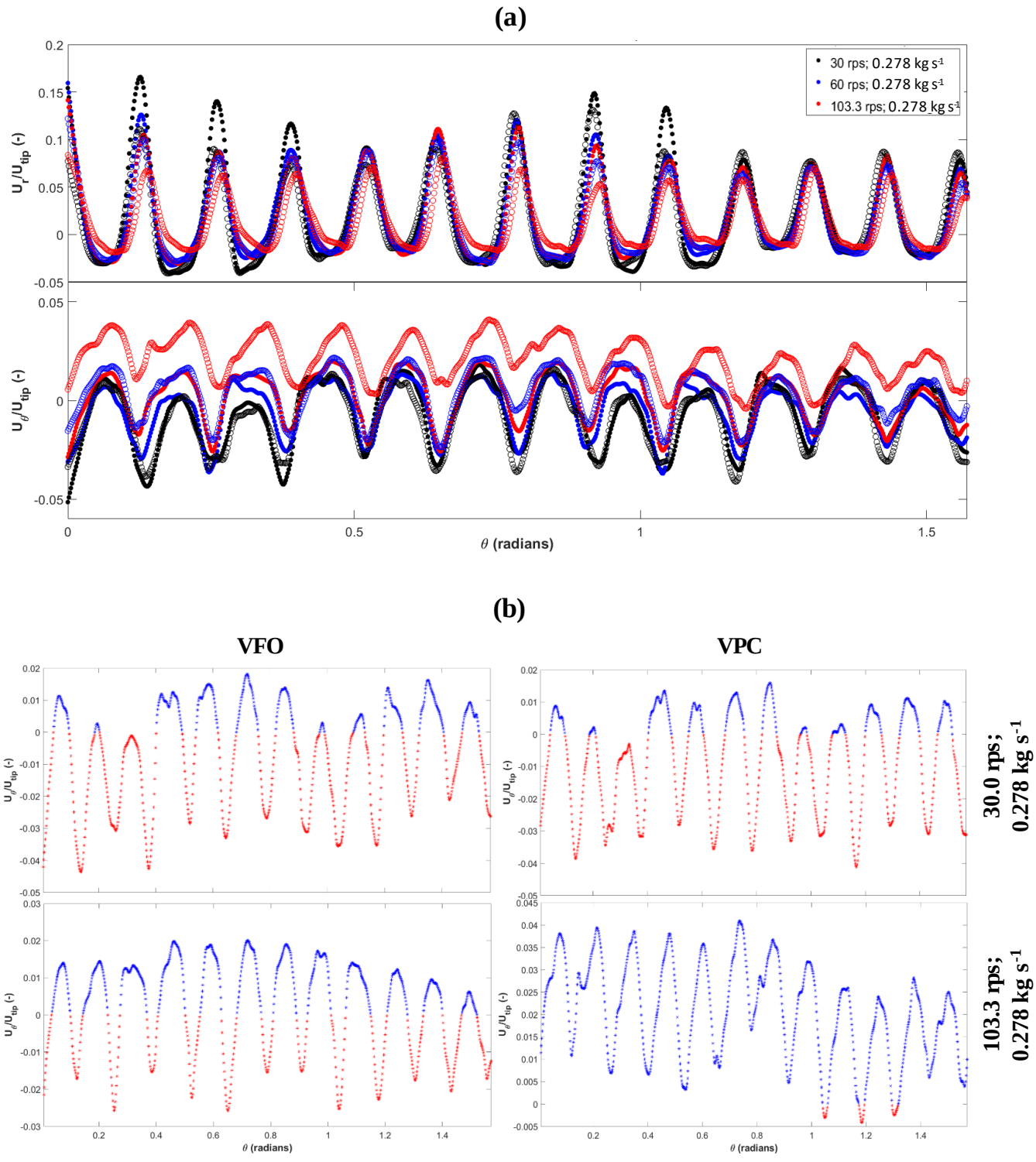

Figure 4.9: VFO vs VPC for 60.0 rps; 0.278 kg s^{-1} at fixed r = 37.2 mm – row 4 (z = 8.573 mm) (a) Radial (top) and tangential (bottom) velocity trends: filled symbols for VFO, empty symbols for VPC (b) Individual tangential velocity trends where blue and red represent positive and negative velocities respectively

4.3.4 Flow Rate and Flow Number Calculations

Figure 4.10a shows an example of the radial flow components calculated at a fixed r = 37.2 mm on row 4 to calculate S_{surf} while Figure 4.10b summarises the results of the flow rates obtained using the plug flow approximation (Equation 4.5) versus the flow rates measured by the flow meter. This plug flow assumption is found to be acceptable when the flow is delivered by the external pump only e.g. values are within confidence intervals of +/- 20% (in Table 4.2, errors were calculated as +/- % error from the Q_{plug} (or $Q_{fit,integrated}$) = $Q_{measured}$ line). This is because the flow pattern is more uniform in the radial direction as seen in Figure 4.8a. Overestimation is expected with this method as the velocity profile is expected to be constrained to zero at the mixer head walls due to the no-slip condition. Since for a fully developed turbulent pipe flow, the maximum centre line velocity, $U_{max} = 1.2\overline{U}$ (Lowe, 1979) and since row 4 can effectively be treated as the centre of the stator, an overestimation of about 20% is expected (hence the confidence interval of +/- 20%).

Table 4.2: Summary of results for different methods of evaluation of flow rates from PIV data

Run (-)	**$Q_{measured}$ x 10^{-4}, (m^3 s^{-1})**	**Q_{plug} x 10^{-4}, (m^3 s^{-1})**	**Q_{plug} error, (%)**	**$Q_{fit,\ integrated}$ x 10^{-4}, (m^3 s^{-1})**	**$Q_{fit,\ integrated}$ error, (%)**	**Calc. Flow number, N_Q (-)**
1	2.08	2.09	+ 0.38	-	-	-
2	2.78	3.04	+ 9.31	3.34	+ 20.1	N/A
3	3.47	3.90	+ 12.2	-	-	-
4	0.64	0.50	- 21.9	-	-	-
5	1.58	3.13	+ 98.2	1.59	+ 0.63	0.0103
6	2.95	2.81	- 4.92	2.49	- 15.6	0.0324
7	3.55	4.87	+ 37.2	3.64	+ 2.54	0.0237
8	5.10	7.68	+ 50.6	5.15	+ 0.98	0.0195
9	2.78	2.20	- 20.7	2.24	- 19.4	0.0292
10	2.78	3.96	+ 42.7	2.69	- 3.24	0.0175
11	2.78	5.88	+ 112	3.28	+ 18.0	0.0124

Furthermore, significant overestimation is apparent at high rotor speeds but this is due to the increased tangential flow which results in the reduction of fluid recirculation and directing the fluid onto the following jet for both VFO and VPC conditions (Figure 4.8). The underprediction for 30.0 rps conditions could be due to the increased recirculation of fluid in comparison with PO conditions as shown in Figure 4.8a,c.

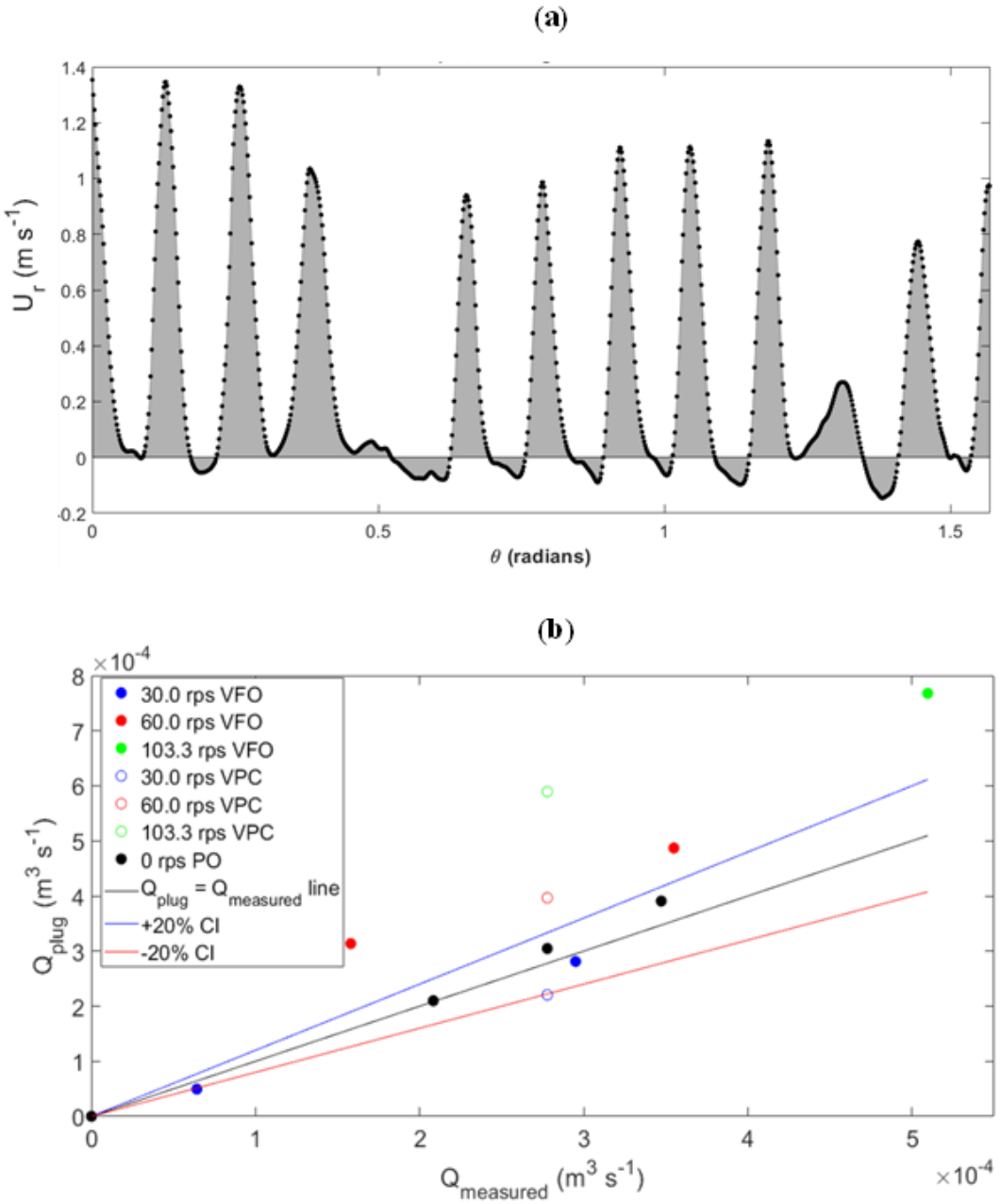

Figure 4.10: Flow rate calculation by plug flow approximation (a) Surface area integral for 0.278 kg s^{-1} VFO at fixed r = 37.2 mm – row 4 (z = 8.573 mm) (b) Results for varying rotor speeds with 0.278 kg s^{-1} external flow rate

More detailed PIV measurements at different z positions enabled S_{surf} to be calculated from individual stator rows for the same condition e.g. 0.278 kg s^{-1} PO; the fitting process is shown in Figure 4.11a. The overestimation inherent in a plug flow assumption using the result from row 4 is evident on Figure 4.11a. The results of this improved estimation method for $S_{surf,}$ are shown in Figure 4.11b. The flow numbers calculated using this method are given in Table 4.2. The value of flow number calculated for 60.0 rps SO is consistent with the calculated N_Q of 0.010. It is not surprising to see that flow numbers increase with additional flow from the external pump at each respective rotor speed as it enhances the pumping capability of the rotor. The values in Table 4.2 are at a maximum at VFO conditions while the values for VPC conditions are found between SO and VFO conditions. This, again suggests that more of the fluids flow tangentially as the rotor speed begins to control the overall flow pattern inside the mixing head. Moreover, the rate at which flow numbers decrease back to the original SO values increases with rotor speed.

Overall, although the flow rates for both VFO and VPC conditions are better approximated with this method, since it still does not account for all the effects imposed by the complex flow within the vicinity of the outer stator where interacting multiple jets of fluid are present, which is also simulated by Qin et al. (2017), better accuracy is still required to calculate the flow numbers.

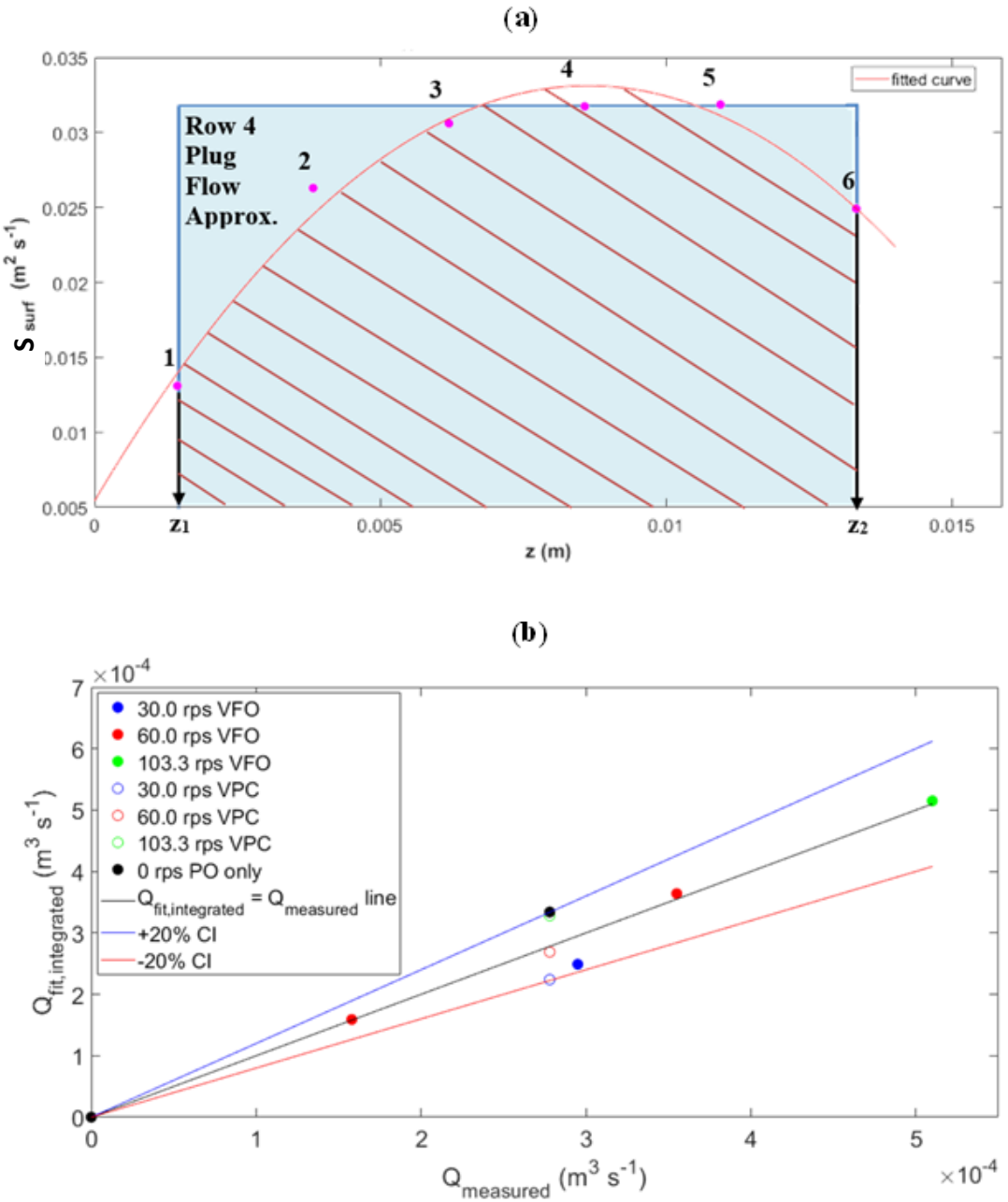

Figure 4.11: Flow rate calculation by evaluating S_{surf} at all rows at fixed r = 37.2 mm (a) Integration of fitted curve for 0.278 kg s^{-1} VFO across all rows (red hashed area), plug flow approximation for row 4 shown for comparison (shaded light blue area) (b) Results for varying rotor speeds 0.278 kg s^{-1} external flow rate across all rows

4.3.5 Implications on Emulsification Processes for Practitioners

A way to use the information acquired from this study is to explain previously observed trends in recent experimental studies that investigated the effects of process parameters in HSMs upon droplet size distributions. The velocity field data presented can provide a physical

insight on the types of dispersion/ droplet breakup mechanism that occur in the mixing head. This is important since the flow in Silverson is highly irregular due to different breakup mechanisms that occur simultaneously. For instance, turbulence may not fully develop in the high shear region at short residence times hence simple shear flow may be more important (Hall et al., 2011a). In relation to existing experimental results on the same Silverson model obtained by Hall et al. (2011a), in terms of:

(a) Rotor Speed at Constant Flow Rate

Droplet size decreases with increasing rotor speed regardless of dispersed phase viscosity. This suggests that increased tangential flow favours droplet breakup (as found in this study) and implies that the predominant dispersion mechanism is caused by the impingement of fluid on the stator surface (Padron, 2001).

(b) Flow Rate at Constant Rotor Speed

Hall et al. (2011a) also controlled the flowrate using an outlet valve and they found that droplet size was generally independent of flow rate. At high rotor speeds (11,000 rpm), they observed that as expected, droplet size has decreased. However, drops of lower viscosity (μ_d = 9.4 mPa s) exhibited a dependence on flow rate at lower flow rates e.g. smaller drops were produced at lower flow rates. They attributed this to the effects of breakup mechanisms and residence times. For instance, they deduced that low viscosity droplets have shorter deformation times hence, they can break to a greater degree under simple shear flow under prolonged residence times. This highlights the importance of investigating the effects of varying the external pump flow rate for some emulsion systems e.g. longer residence times allow more time for droplet breakup. Thus, the analysis of PIV data can provide both qualitative and quantitative supporting evidence for observed experimental results.

4.4 Conclusions

2-D angle-resolved PIV measurements were carried out to investigate flow patterns on a 150/250 in-line Silverson high shear mixer. Particular attention was given to the overall flow pattern across the whole mixing head as opposed to existing studies that focus on flow within the stator hole as well as on the effects of varying the external pump flow rate to the overall flow pattern. With the current equipment setup, it was found that the overall flow is comprised of both radial and tangential flows. The former is primarily provided by the external pump while the latter is induced by rotor rotation. The dominating flow depends on the combination of external pump flow rate and rotor speed. In general, the higher the rotor speed, the more tangential the flow becomes and vice versa. Furthermore, the addition of an outlet valve was also found to promote a more tangential flow.

Flow rates evaluated by calculating surface flow rates across all rows and fitting a function that is integrated over the effective stator thickness yielded results with better accuracy opposed to plug flow approximation and was used to calculate flow numbers which are of similar magnitude to those found in literature for a similar mixing head.

Finally, based on the experimental study by Hall et al. (2011a), analysis of such results can be attributed to their implication on emulsification processes: a more tangential flow may be attributed to generating smaller droplet sizes due to the dominating breakup mechanism caused by fluid impingement on the stator and the role of the stator becomes more important at higher flow rates.

Chapter 5 – Flow, Turbulence and Potential Droplet Break Up Mechanisms in an In-Line Silverson 150/250 High Shear Mixer[4]

5.1 Introduction

This chapter follows on from the hydrodynamic studies conducted in Chapter 4 and presents an analysis of the turbulent properties of the flow fields obtained, namely by determination of Reynolds stresses, turbulent kinetic energy (TKE) and energy dissipation rates from the PIV data (with due consideration to the resolution of the measurements). These data were used to identify where in the mixing head droplet break up is most likely to occur (e.g. in areas of high energy dissipation) and to propose possible break-up mechanisms. The chapter begins with an investigation of the influence of PIV resolution on estimated energy dissipation rates using both the direct evaluation (DE) and Smagorinsky closure sub-grid scale (SGS) methods. A quantification of when radial (via external pump) or tangential (via rotor) flow dominates inside the mixing head was made, followed by the evaluation of ε, TKE and Reynolds stresses. Practical implications of the findings are also discussed.

[4] Part of this work has been published in: Espinoza, C.J.U., Simmons, M.J.H., Alberini, F., Mihailova, O., Kowalski A. J. and Rothman, D. (2020) Flow, turbulence and potential droplet break up mechanisms in an in-line Silverson 150/250 high shear mixer. **Chemical Engineering Science: X**, 6: 100055

5.2 Materials and Methods

5.2.1 Process Conditions

Water was used as the working fluid and the measurements were performed in the turbulent regime over a range of Reynolds number, *Re* from 120,000 – 420,000, calculated using

$$Re = \frac{\rho N {D_{r,o}}^2}{\mu}, \tag{5.1}$$

where ρ is the density, μ is the viscosity at a fixed temperature, N is the rotor speed and $D_{r,o}$ is the outer rotor diameter.

The pump was used to provide an externally driven flow rate, M_P in the mixing head (0.208 – 0.347 kg s^{-1}) and the rotor speed was controlled independently (30.0 – 103.3 rps); both were controlled using separate frequency inverters. The needle valve was also used to control the flow rate and backpressure in the mixing head, with the relief valve set at 5 bar (lower than the pressure rating of the mixing head of 7 bar). A data recorder (Memograph RSG45, Endress+Hauser) was used to log the mass flow rate, rotor speed, pressure and temperature at the mixer inlet and outlet. The flow meter was calibrated using the bucket and timer method and was found to be accurate within 1.3% in all experiments.

The parameters set for each experimental run are summarised in Table 5.1. Runs 1–3 were carried out using the external pump only (PO), whereas runs 4 and 11 were carried out using the Silverson mixing head only with the pump switched off (SO). The remaining runs were carried out with both the pump and Silverson operating but with the outlet back pressure valve set either fully open (VFO), with mixer outlet pressure (P_{OUT}) ranging from 0.259 – 1.094 bar, or partially closed (VPC), P_{OUT} = 0.259 – 1.777 bar respectively. The total flow rate, M_T is the combined flow rates of the external pump (M_P) and the Silverson mixer (M_S). However,

it is important to note that these are not additive e.g. $M_T \neq M_P + M_S$. For VPC conditions, the needle valve was partially closed after both the external pump and Silverson are in operation. This is done to match the initially set flow rate, M_P before the Silverson was switched on (the pump is always switched on first). This is done to allow the external pump to control the overall process flow rate and thus the fluid residence time in the mixer and also to prevent the Silverson from acting as a pump; and instead, focus on inputting energy and imposing shear on the fluid (Casugbo and Baker, 2018). This also throttles the discharge from the Silverson, which delays the onset of cavitation by reducing the net positive suction head (NPSH) required.

5.2.2 PIV Experiments

The images were processed using a recursive Nyquist grid algorithm using interrogation areas (IA) of 64 × 64 and 32 × 32 pixels for the first and second passes respectively. The resolution of the PIV measurement depends upon the length scale of the IA, $L_{IA,}$ which acts as a filter below which length scales are not resolved. Thus, there is a compromise between resolution and field of view (FOV). For the conducted experiments, the FOVs and spatial resolutions used are portrayed and summarised in Figure 5.1 and Table 5.1 respectively. These FOVs represent the optimal viewing area with the best resolution attained using the available camera lens at the given rotor blade position (0º) in Figure 3.4d, which was selected for symmetry purposes. In these FOVs, two regions of interest (ROI): A (jet region) and B (high shear region), where droplet breakup may occur, were studied (Figure 5.1a). FOV 3 was used for the majority of the results obtained with a spatial resolution of 6.6 µm pixel^{-1} which equates to a resolution of 210 µm for a 32 × 32 pixel IA, with vectors spaced 105 µm apart allowing for 50% overlap of IAs. The time delays between each image in an image pair were calculated in terms of the recommended maximum displacement travelled by a particle within an interrogation area, 0.25 L_{IA} (Adrian, 1986) using Equation 3.1 and are summarised in Table 5.1.

Table 5.1: Experimental runs and their corresponding power (calculated using Equation 5.4), power per unit mass (ε_{avg}), Kolmogorov length scales (λ_k) as well as the image acquisition parameters and spatial resolutions. *Calculated using $P_{Pump} = (M_P/\rho)\, P_{in}$

								FOV 1			FOV 2			FOV 3		
Run (-)	**Rotor speed, N (rps)**	**External pump flow rate, M_P (kg s^{-1})**	**Flow class (-)**	**Measured total pump flow rate, M_T (kg s^{-1})**	**P (kg m^2 s^{-3})**	**ε_{avg} (m^2 s^{-3})**	**λ_k (µm)**	**Δ (µm)**	**Δt (µs)**	**Δ/ λ_k (-)**	**Δ (µm)**	**Δt (µs)**	**Δ/ λ_k (-)**	**Δ (µm)**	**Δt (µs)**	**Δ/ λ_k (-)**
1	**0.0**	0.208	VFO (PO)	0.208	*5.22	-	-	1273.6	106.40	-	352.64	29.46	-	211.2	17.64	-
2	**0.0**	0.278	VFO (PO)	0.278	*10.47	-	-			-			-			-
3	**0.0**	0.347	VFO (PO)	0.347	*18.59	-	-			-			-			-
4	**30.0**	0.000	VFO (SO)	0.066	7.74	17.31	15.50			82.15			22.75			13.62
5	**30.0**	0.208	VFO	0.231	13.35	29.88	13.53			94.16			26.07			15.61
6	**30.0**	0.278	VFO	0.295	15.51	34.69	13.03			97.75			27.06			16.21
7	**30.0**	0.347	VFO	0.361	17.75	39.70	12.60			101.10			27.99			16.77
8	**30.0**	0.208	VPC	0.208	12.56	28.10	13.73			92.73			25.67			15.38
9	**30.0**	0.278	VPC	0.278	14.92	33.37	13.16			96.80			26.80			16.05
10	**30.0**	0.347	VPC	0.347	17.27	38.64	12.68			100.42			27.80			16.65
11	**60.0**	0.000	VFO (SO)	0.159	65.53	146.60	9.09		53.20	140.14		14.73	38.80		8.82	23.24
12	**60.0**	0.208	VFO	0.309	85.90	192.18	8.49			149.95			41.52			24.87
13	**60.0**	0.278	VFO	0.355	92.15	206.15	8.35			152.61			42.25			25.31
14	**60.0**	0.347	VFO	0.410	99.55	222.71	8.19			155.59			43.08			25.80
15	**60.0**	0.208	VPC	0.208	72.21	161.54	8.87			143.58			39.76			23.81
16	**60.0**	0.278	VPC	0.278	81.63	182.63	8.60			148.06			40.99			24.55
17	**60.0**	0.347	VPC	0.347	91.06	203.71	8.37			152.16			42.13			25.23
18	**103.3**	0.208	VFO	0.473	415.12	928.68	5.73		30.89	222.33		8.55	61.56		5.12	36.87
19	**103.3**	0.278	VFO	0.510	429.66	961.21	5.68			224.25			62.09			37.19
20	**103.3**	0.347	VFO	0.539	441.40	987.48	5.64			225.77			62.51			37.44
21	**103.3**	0.208	VPC	0.208	308.29	689.68	6.17			206.39			57.15			34.23
22	**103.3**	0.278	VPC	0.278	336.24	752.22	6.04			210.92			58.40			34.98
23	**103.3**	0.347	VPC	0.347	364.20	814.76	5.92			215.17			59.58			35.68

5.2.3 Analysis of PIV Data

There is a compromise between the desired FOV and spatial resolution as the calculation of turbulence properties requires in principle full resolution of the flow field down to the Kolmogorov length scale, λ_k. This is challenging in terms of optics and seeding levels and would require multiple measurements to be taken of adjacent regions to adequately cover the area to be imaged, see for example (Khan et al., 2004). The method chosen in this work was to take three FOVs at different resolutions, a similar approach taken for dissipation rate studies in mechanically agitated vessels (Baldi and Yianneskis, 2003; Delafosse et al., 2011; Hoque et al., 2015; Xu and Chen, 2013). The fields of view selected in this work are shown in Figure 5.1.

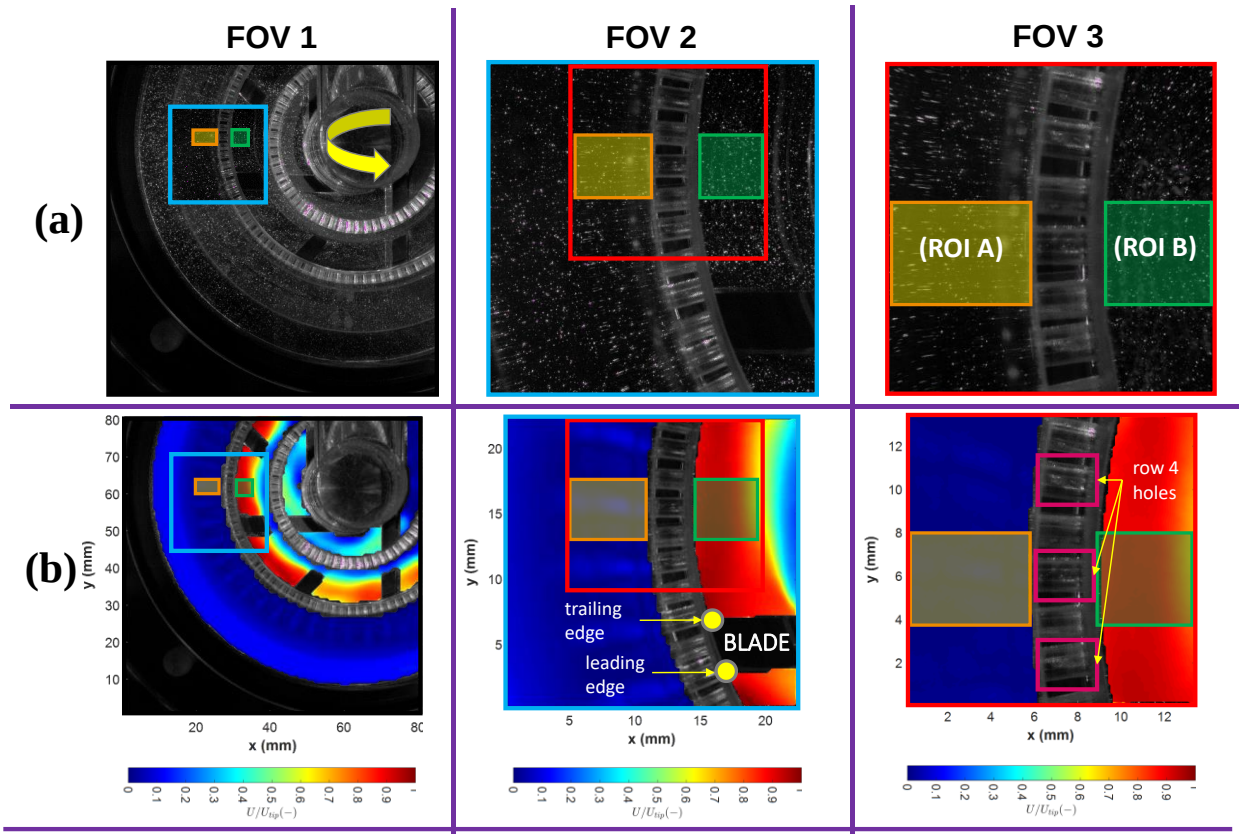

Figure 5.1: Regions of interest at selected field of views FOV 1, FOV 2 and FOV 3 in: (a) Raw images and (b) Velocity field plots

Saarenrinne et al. (2001) showed that, for example, to resolve 65% and 90% of the dissipation rate with sufficient accuracy, the spatial resolution has to be $9\lambda_k$ and $2\lambda_k$ respectively, where:

$$\lambda_k = \left(\frac{\nu^3}{\varepsilon}\right)^{1/4} \tag{5.2}$$

and ν is the fluid kinematic viscosity and ε is the local specific energy dissipation rate. An average value for ε (power per unit mass) can be calculated using:

$$\varepsilon_{avg} = \frac{P}{\rho V} \tag{5.3}$$

where ρ is the fluid density, V is the filled volume of the mixing head (4.47×10^{-4} m^3) (opposed to conventional rotor-swept volume) and P is the power, which for a standard 150/250 Silverson in-line high shear mixer is defined as (Cooke et al., 2012):

$$P = Po_Z \rho N^3 {D_{r,o}}^5 + k_1 M_T N^2 {D_{r,o}}^2 \tag{5.4}$$

where Po_Z is the 'zero flow' power constant (0.197), ρ is the fluid density, $N$is the rotor speed, $D_{r,o}$ is the outer rotor diameter, k_1 is a proportionality constant (9.35) and M_T is the total mass flow rate.

Calculated values of λ_k are summarised in Table 5.1 which shows that the highest PIV resolution achieved in the experiments at FOV 3 is ~14 λ_k which implies that < 65% of the energy dissipated is resolved.

The turbulent flow properties can be obtained by carrying out a Reynolds decomposition of the angle resolved velocity as proposed by Sharp and Adrian (2001). This is carried out below, for example, for the *x* component of velocity, *U*,

$$U = U'' + \bar{U}|_\theta, \tag{5.5}$$

where $\bar{U}|_\theta$ is the angle-resolved mean and U'' is the true fluctuating turbulent velocity component since the periodic component U_p is removed by using angle-resolved

measurements. Thus, for the following equations, the angle resolved RMS values for the *x* and *y* components of velocity, *U* and *V* respectively are

$$U_{rms} = \sqrt{\overline{U''^2}}, V_{rms} = \sqrt{\overline{V''^2}}, \tag{5.6}$$

The turbulent kinetic energy or TKE (*k*), is the portion of the kinetic energy generated by eddies that manifest from velocity fluctuations due to turbulence. This provides a mixing mechanism via turbulent dispersion and can be evaluated from 2-D velocity using the isotropic approximation:

$$k = \frac{3}{4}(U_{rms}^2 + V_{rms}^2), \tag{5.7}$$

Reynolds stresses arise due to momentum transfer by the fluctuating velocity field and are normally defined as $R_{ij} = \overline{U_i'' U_j''}$which in 2-D, can be reduced to the following symmetric tensor:

$$R_{ij} = -\begin{pmatrix} \overline{U''U''} & \overline{U''V''} \\ \overline{V''U''} & \overline{V''V''} \end{pmatrix}, \tag{5.8}$$

The local specific energy dissipation rate may be determined from rate of viscous dissipation of the mechanical energy (Hinze, 1975) and assuming isotropic turbulence, for 2-D data this reduces to (Sharp and Adrian, 2001):

$$\varepsilon_{DE} = \nu \left[2\overline{\left(\frac{\partial U''}{\partial x}\right)^2} + 2\overline{\left(\frac{\partial V''}{\partial y}\right)^2} + 3\overline{\left(\frac{\partial V''}{\partial x}\right)^2} + 3\overline{\left(\frac{\partial U''}{\partial y}\right)^2} + 2\overline{\frac{\partial U''}{\partial y} \cdot \frac{\partial V''}{\partial x}} \right], \tag{5.9}$$

This method was applied at the best achievable spatial resolution (~14 λ_K) using the velocity data from the PIV measurements. Since this is still relatively coarse, the Smagorinsky closure sub-grid scale (SGS) model was also used to enable estimation of the unresolved scales (see Gabriele et al. 2009; Sheng et al. 2000).

$$\varepsilon_{SGS} = (C_S\Delta)^2\left[4\overline{\left(\frac{\partial U''}{\partial x}\right)^2} + 4\overline{\left(\frac{\partial V''}{\partial y}\right)^2} + 2\overline{\left(\frac{\partial V''}{\partial x}\right)^2} + 2\overline{\left(\frac{\partial U''}{\partial y}\right)^2}\right]^{\frac{3}{2}}, \quad (5.10)$$

The link between the dimensionless spatial resolution and the calculated mean specific energy dissipation rates for both ROIs using the DE method, portrayed in Figure 5.2 are very similar and follow a power-law relationship e.g. $\overline{\varepsilon_{DE}^*} \propto \left(\frac{\Delta}{\lambda_k}\right)^{\sim -2}$ with coefficient of determinations, $R^2 > 0.986$ (see Table 5.2). This approach is the same as that of Delafosse et al. (2011) and also takes into account an important consideration that the evaluated coefficients and exponents (Table 5.2) are only valid for the energy dissipation rates averaged over the selected ROI. The results using SGS also follow the same general trend but also emphasise the difference (larger gap) between ROIs A and B as well as between VFO and VPC conditions. In both methods, ROI B and VFO lines are consistently higher than ROI A and VPC lines respectively. This is because higher energy dissipation is expected in regions that are subject to higher shear e.g. within the rotor swept volume (ROI B) while partially closing the valve (VPC conditions) has a dampening effect on overall energy dissipation by imposing solid body rotation (discussed in detail in §5.3).

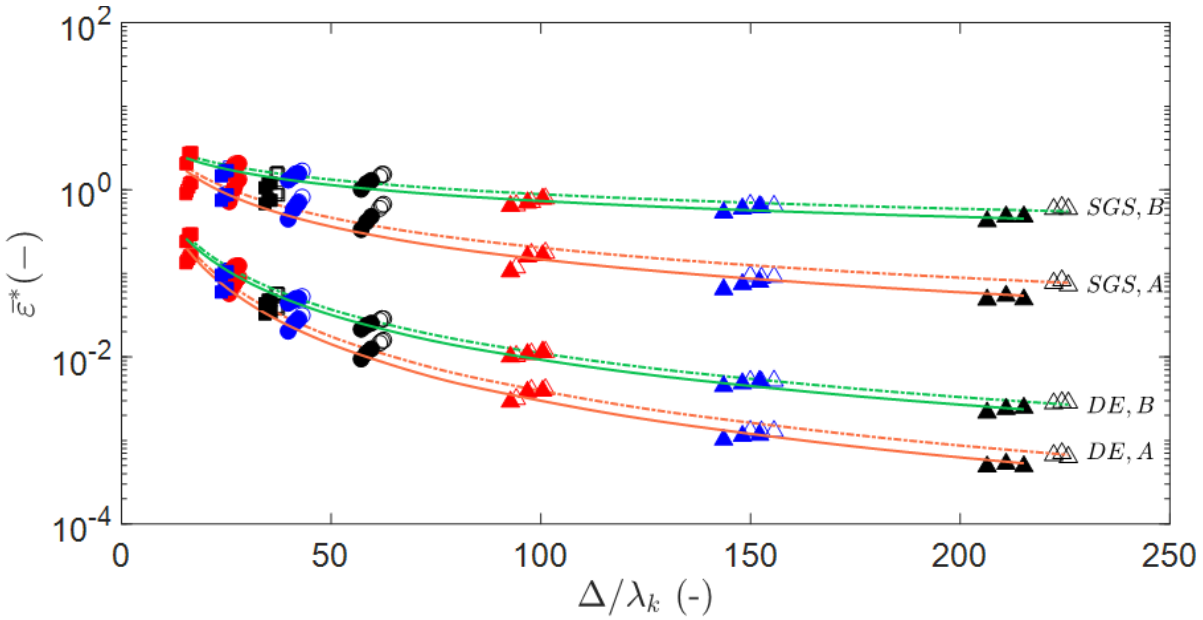

Figure 5.2: Effect of the dimensionless spatial resolution on the mean specific energy dissipation rates (non-dimensionalised with N^3D^2) calculated using Direct Evaluation, DE and Sub-grid Scale, SGS methods at the regions of interest: A (presence of jet), in orange lines and B (presence of high shear), in green lines. The combination of dash-dot (-.) lines and open symbols represent VFO conditions while solid (–) lines and filled symbols represent VPC conditions. For the symbols, colours denote rotor speeds: N = 30.0 rps (red), N = 60.0 rps (blue) and N = 103.3 rps (black) whereas shapes denote field of view: FOV 1 (Δ), FOV 2 (○) and FOV 3 (□)

Table 5.2: Summary of constants and exponents for $\overline{\varepsilon^*_{DE}} = A\left(\frac{\Delta}{\lambda_k}\right)^b$ (Figure 5.2)

ROI (-)	Flow class (-)	Method (-)	constant A (-)	exponent b (-)	R^2 (-)
A	VFO	DE	86.01	-2.19	0.987
A	VPC	DE	95.37	-2.25	0.987
B	VFO	DE	33.66	-1.76	0.994
B	VPC	DE	34.32	-1.78	0.986
A	VFO	SGS	50.65	-1.21	0.901
A	VPC	SGS	59.99	-1.31	0.926
B	VFO	SGS	12.96	-0.59	0.922
B	VPC	SGS	13.60	-0.63	0.917

Although SGS method results in higher values of energy dissipation rates, the results using the DE method are used in the discussions. This is to ensure homogeneity in the methodology used to evaluate other turbulence properties such as Reynolds stresses and turbulent kinetic energy (TKE), which do not model for the unresolved scales. In addition, the distributions generated using both the SGS and DE methods were very similar.

5.3 Results

5.3.1 Fluid Dynamics

The total mass flow rates for all experimental runs (Table 5.1) are plotted in Figure 5.3a. The black, blue, red and green dash-dot (-.) lines indicate the M_Ps set in the runs: 0, 0.208, 0.278 and 0.347 kg s^{-1} respectively. The open symbols represent the total mass flow rates achieved for VFO conditions and the closed symbols are for VPC conditions. When the external pump is switched off (M_P = 0 kg s^{-1}), the Silverson mixer can self-pump (SO conditions) up to 60.0 rps (a tip speed of 11.97 m s^{-1}) and generate a flow rate (M_S), shown by the black open symbols. This is over twice the 5 m s^{-1} tip speed achieved by Casugbo and Baker (2018) for the same mixer with similar setup and experimental condition. The pumping by the Silverson alone was possible as water can pass through the clearances between the lobes and housing in the external pump. Air entrainment occurred for rotor speeds higher than 60.0 rps as the external pump acts as a flow restriction in the suction line. This may occur for a number of reasons. One possibility is that the pressure in the Silverson drop below the vapour pressure, another may be leakage of air from the atmosphere into the low pressure zone in the mixing head via the mechanical seals. Calculation of the net positive suction head (NPSH) revealed that notwithstanding the restriction imposed, the NPSH at the highest flow rate at the external pump was 10.97 m which exceeds the required NPSH of 2.0 m. At the mixer, the NPSH was 9.44 m which suggests leakage rather than cavitation as the mechanism, but no definitive cause was identified. However, no air entrainment was observed across the experimental runs when the external pump was used in addition to the Silverson. Furthermore, system curves for VFO and VPC conditions, superimposed with the measured heads delivered by the pump and Silverson showed that the NPSH requirements were met in all experimental runs.

It is evident through Figure 5.3a that higher flow rates are attained as M_P and N are increased, as expected. Espinoza et al. (2018) observed that the flows were predominantly radial at high pump flow rates (M_P) and tangential at high Silverson rotor speeds, N. Since the pump and Silverson are arranged in series (Figure 3.1), $M_T = M_P = M_S$ and the relative contributions of the Silverson and external pump which drive the overall flow regime are a function of total head profile through the pipework (Figure 5.3b). The total head is the sum of the total dynamic heads (static head + dynamic head) generated by the pump and Silverson: $\Delta H_T = \Delta H_P + \Delta H_S$. In addition, volumetric flow rate, Q_T (M_T/ρ) was used to follow conventions in plotting system and pump performance curves.

It is clear from Figure 5.3b that when the external pump is used solely (PO, N = 0 rps), the total head delivered (green bars) is generated mostly by the external pump (orange bars) thus, the flow in the mixing head is predominantly radial (Figure 5.4a). When the Silverson is used alone (SO), unsurprisingly it provides the majority of the total head for SO conditions (purple bars) hence the flow is predominantly tangential and there is hardly any jetting (Figure 5.4h). Moreover, Figure 5.3b shows that negative head occurs when the external pump is switched off and it acts as a flow restriction. For VFO and VPC conditions, it can be seen that the relative contributions by the external pump and Silverson vary according to the process parameters set. At constant M_P, for both VFO (bars with dashed (--) line border) and VPC (bars with solid (-) line border) conditions, the Silverson mixer contributes more head as N is increased. However, the contribution by the external pump at VFO conditions decreases down to a negative value, showing that it still acts as a flow restriction when the external pump flow rate is exceeded by the pumping capacity of the Silverson. The rate of decline decreases when M_P is increased (compare decline of orange bars at constant 0.208 kg s^{-1} and 0.347 kg s^{-1}). Finally, for VFO and VPC conditions that have similar M_T, e.g. for VFO: N = 60.0 rps; M_P =

0.278 kg s^{-1} (red open symbol in Figure 5.3a) and for VPC: N = 60.0 rps; M_P = 0.347 kg s^{-1} (green closed symbol in Figure 5.3a), the pressure drop across the Silverson mixer (purple bars for corresponding conditions in Figure 5.3b) is more or less the same. This implies that the flow patterns are also very similar (compare Figures 5.7 and 5.8 for the corresponding conditions). This suggests that pressure drop across the mixing head governs the local flow patterns inside it.

The influence of changing N at constant M_P and vice versa is shown in Figure 5.4. Figures 5.4b and 5.4c show that when N was increased at constant M_P, the region of higher velocities (red) in the rotor swept volume increased (top right of each plot with green arrows) and the jets get weaker (in terms of penetrating the bulk as although the jet exit hole velocity has increased, it does not penetrate the bulk as effectively as in PO conditions (Figure 5.4a) because it moves more in the tangential direction), whereas the opposite is true when M_P was increased at constant N (compare Figure 5.4c and d). The weakening effect on the jet is also more apparent at VPC conditions especially at low M_P and higher rotor speeds (compare Figure 5.4f and g).

For VPC conditions, the contribution of the external pump is shown as constant and positive at constant M_P and gradually increases as M_P was increased (compare orange bars of equal heights to the M_P set (PO bars) in Figure 5.3b). This was expected as the increased backpressure ensured that the positive displacement pump delivered a constant flow rate at a certain head and pump speed. This also suggests that the radial flow profile is fixed at constant M_P thus the strength of jets depended on the rotor speed. For instance, by comparing Figure 5.4e and g, jets significantly diminish to a point where the flow pattern resembles that for a SO condition (Figure 5.4h) although it is important to note that the outlet valve opening (number of turns open) differs with varying rotor speeds for a constant M_P. Finally, it is noteworthy that

the values of total head delivered at VPC conditions are consistently higher than the corresponding VFO conditions which implies that energy is lost when overcoming additional resistance imparted by the valve. This is emphasised in Figure 5.5 which portrays the system head profiles for varying process conditions at locations defined in Figure 3.1. It shows that the gap between VFO (open symbols, dashed lines) and VPC conditions (closed symbols, solid lines) is more significant at higher rotor speeds. It is also noteworthy that after the Silverson e.g. between locations E and F, there is an increase in head due to back pressure losses imposed by the pipework of the recycle loop (1" diameter, 4.55 m flexible braided pipe).

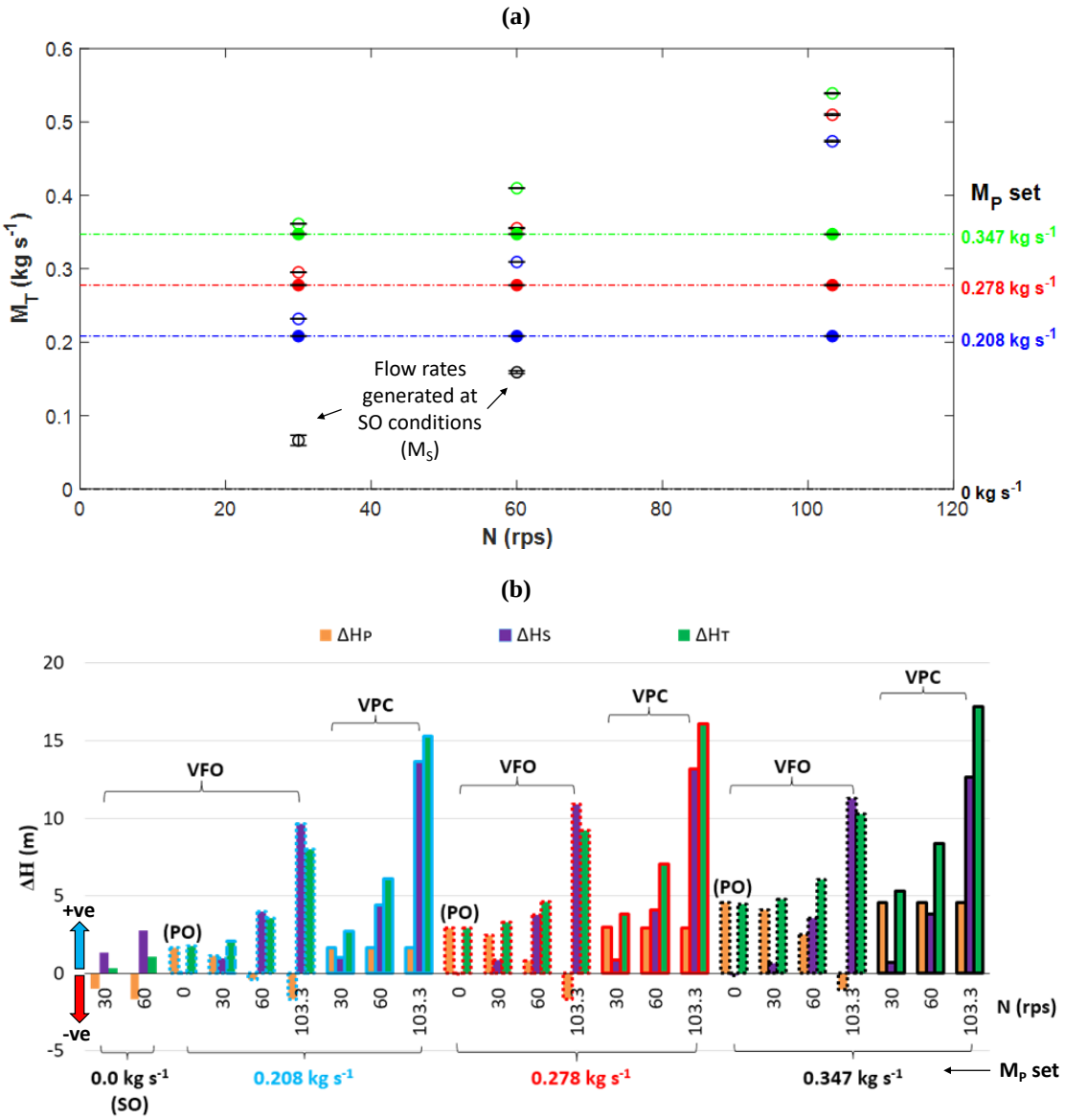

Figure 5.3: (a) Total mass flow rates achieved in experimental runs. Open and closed symbols indicate data points for VFO and VPC conditions respectively. Blue, red and green horizontal dash-dot (-.) lines are drawn to emphasise that at VPC conditions, $M_T = M_P$ (b) Total head delivered by the external pump and Silverson in all experimental runs

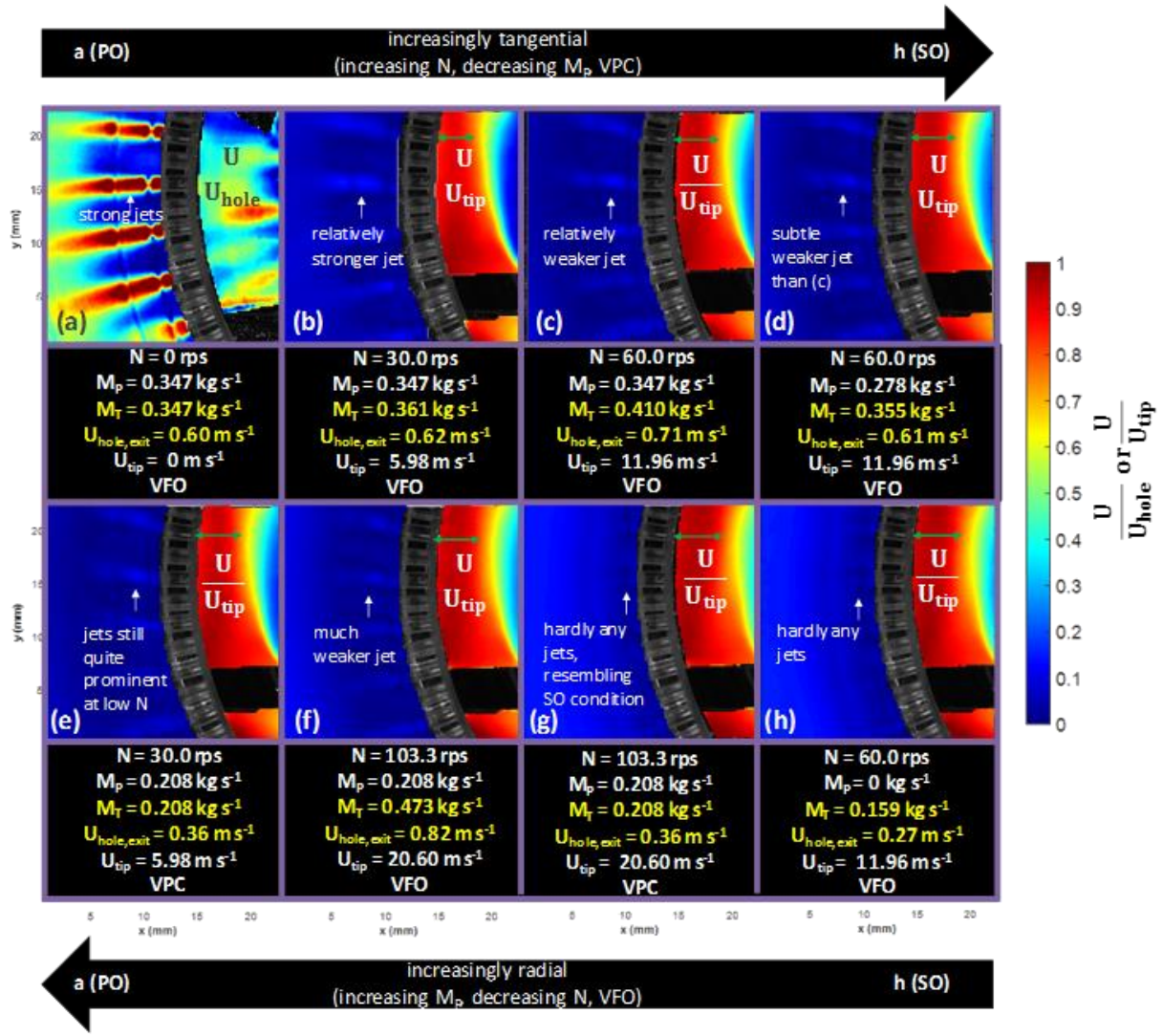

Figure 5.4: Velocity field plots at different experimental runs

Figure 5.6 shows the relative contributions of the external pump ($\Delta H_P/\ \Delta H_T$ – circles and orange lines) and Silverson mixer ($\Delta H_S/\ \Delta H_T$ – squares and purple lines) to the total head delivered in VFO (Figure 5.6a) and VPC (Figure 5.6b) conditions at varying rotor speeds and M_P set (symbol colours). The orange and purple lines were drawn to guide the eyes where the crossover of overall flow control is between the pump and the Silverson mixer at the 0.5 line (red dash-dot (.-) line) at constant M_P (same symbol colours). For instance, once $\Delta H_S/\ \Delta H_T >$ 0.5, it is presumed that the Silverson dominates and generates a more tangential flow while the contrary is true when $\Delta H_P/\ \Delta H_T >$ 0.5. It is evident that in both VFO and VPC conditions, the

external pump only dominates the process flow rate and hence flow patterns at really low rotor speeds e.g. at N = 0 (PO conditions in Figure 5.6a) and 30.0 rps (Figures 5.6a and b) (all the circle symbols are above 0.5). At intermediate rotor speeds, the Silverson mixer influences the flow strongly and completely dominates at very high rotor speeds (all the square symbols are above 0.5). Looking at the VFO data points in Figure 5.6a, the point of crossover (**X** symbols) occurs at higher rotor speeds at increasing M_P set e.g. from ~32 rps at 0.208 kg s^{-1} to ~54 rps at 0.347 kg s^{-1}. This demonstrates the relative competition between the pump and the Silverson mixer at varying process conditions. Partially closing the valves (Figure 5.6b) pushes these boundaries further to the right e.g. ~38 rps at 0.208 kg s^{-1} to ~66 rps at 0.347 kg s^{-1} and ensures that the contribution of both the pump and Silverson mixer are positive. For example at N = 103.3 rps, the Silverson mixer does not have to work harder in overcoming the restriction imposed by the pump at VFO conditions (square symbols > 1 and circle symbols < 0). However, this is not necessarily an advantage as although throttling the valve lowers the NPSH, energy is wasted in trying to overcome the additional resistance. Moreover, this promotes fluid recirculation (solid body rotation) and leads to an increase of temperature in the mixing head. At PO conditions, the Silverson mixer also acts as a restriction but not as significantly. These plots can be useful in applications where essential knowledge of how much the pump and Silverson mixer influence the flow is required. For instance, depending on the application and rheology of the handled fluid, if a certain breakup mechanism may be favourable e.g. via extensional (pump driven) or shear (Silverson driven) stresses, knowing the point at which the pump or Silverson dominates the flow will be useful i.e. the pump flow rate and rotor speed can be optimally set.

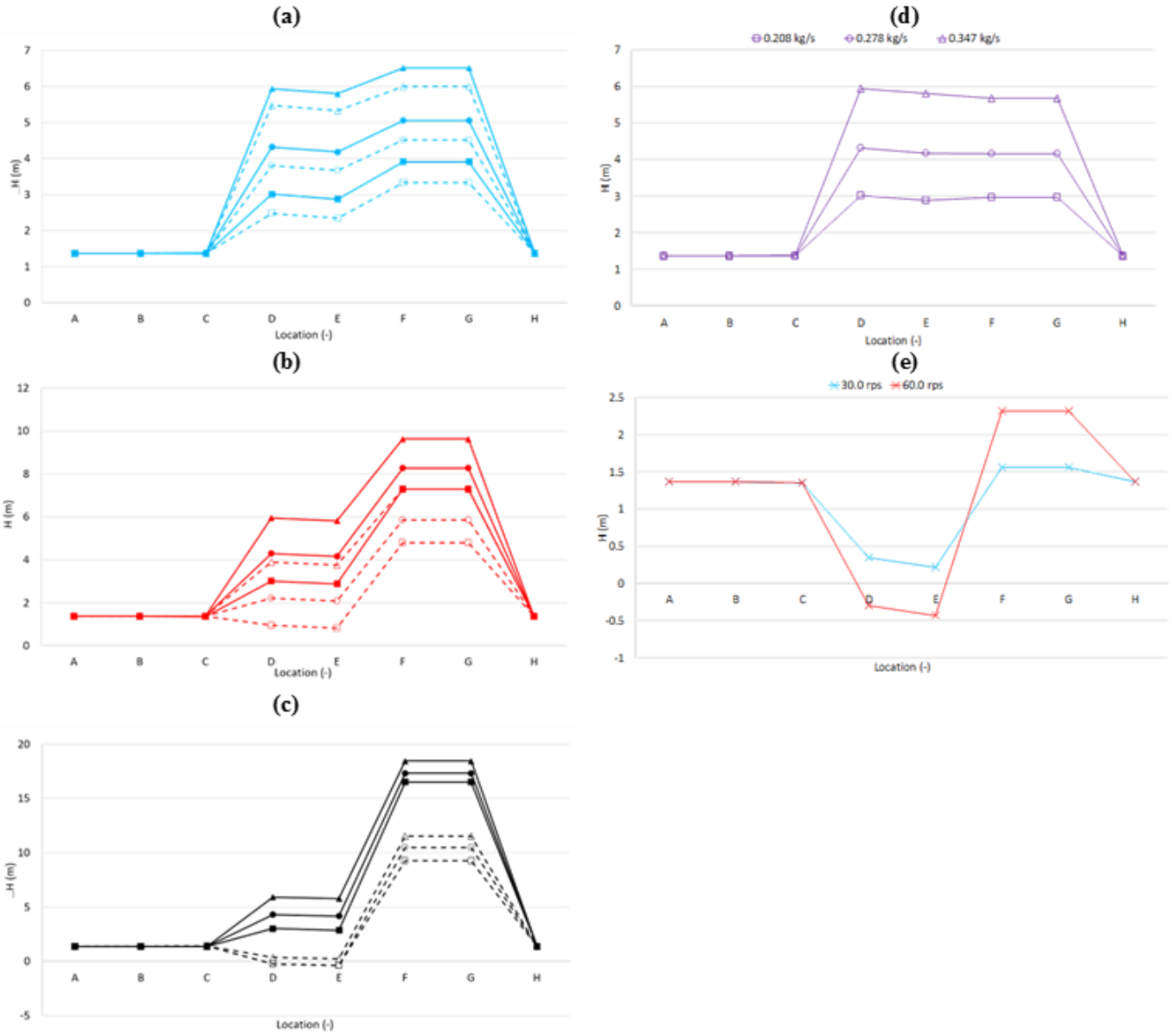

Figure 5.5: Head profiles at locations defined in Figure 3.1 for VFO and VPC conditions at fixed rotor speeds (a) 30.0 rps (b) 60.0 rps and (c) 103.3 rps. Symbols colours denote rotor speeds: N = 30.0 rps (blue), N = 60.0 rps (red) and N = 103.3 rps (black). Shapes denote external pump flow rate set, M_P = 0.208 kg s^{-1} (□), M_P = 0.278 kg s^{-1} (○), M_P = 0.347 kg s^{-1} (Δ). Open and closed symbols as well as dashed (--) and solid (-) lines indicate data points for VFO and VPC conditions respectively. Head profiles for PO and SO conditions are shown in (d) and (e) respectively.

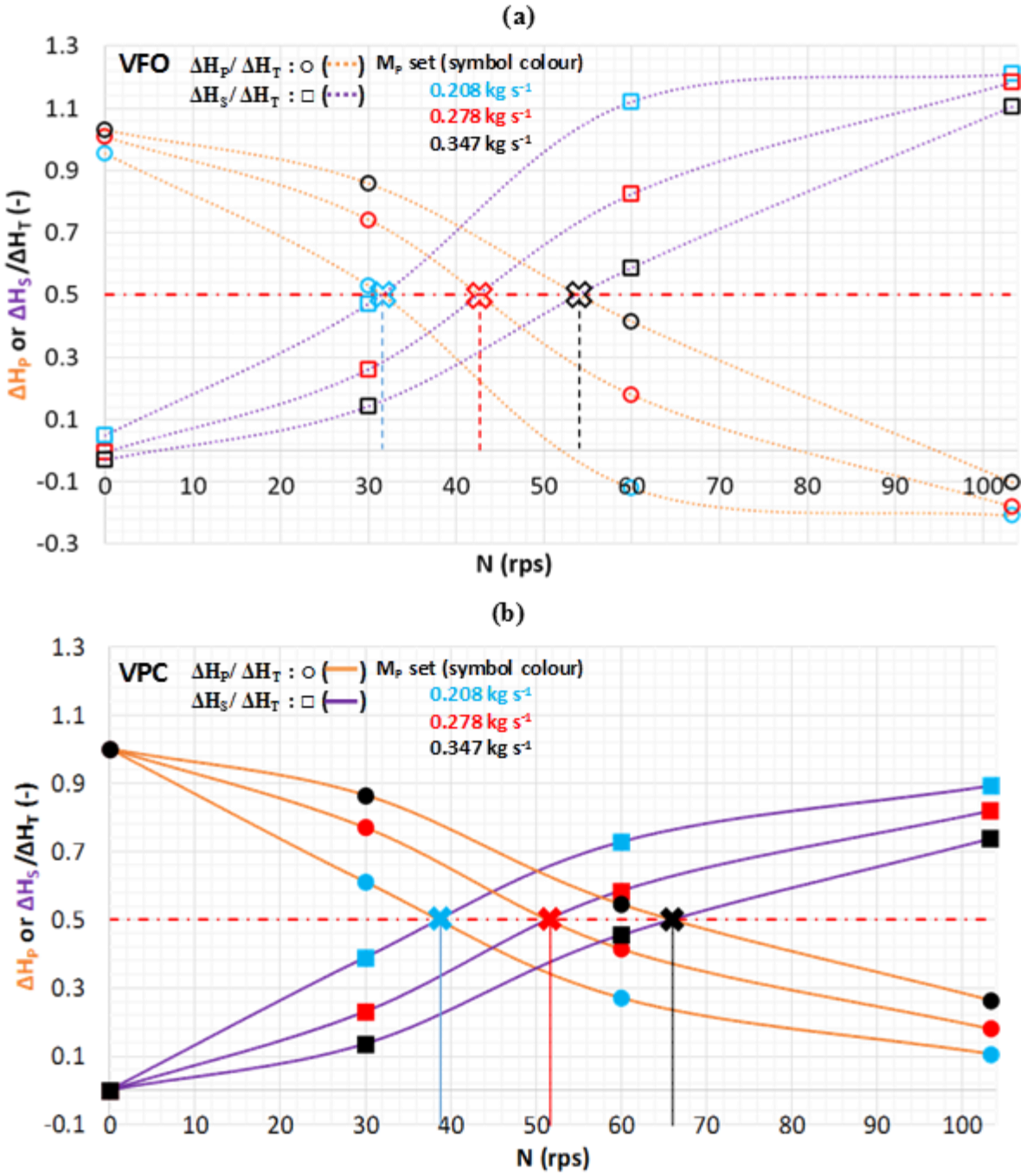

Figure 5.6: Contribution of pump and Silverson on the total head delivered at (a) VFO and (b) VPC conditions. Colours denote external pump flow rates: M_P = 0.208 kg s^{-1} (blue), M_P = 0.278 kg s^{-1} (red), M_P = 0.347 kg s^{-1} (black). Shapes and lines denote head contribution by the pump: ΔH_P (○, orange line) and Silverson, ΔH_S (□, purple line). Lines are to guide the eyes only to give an indication where the change of dominance occurs, denoted by (X) symbols at the 0.5 red dash-dot (-.) line

5.3.2 Energy Dissipation

Effect of N and M_T on Regions of Maximum ε

Energy dissipation plots calculated from the highest resolution measurements made (FOV 3) are shown in Figures 5.7 and 5.8 for VFO and VPC conditions respectively. The figures are designed to show the effect of increasing M_P at constant N (rows) and vice versa (columns). The maximum value of ε in the colour bar for each row in the figures (e.g. at constant N) is set to the maximum value in ROI A.

The figures show that, unsurprisingly, energy dissipation rate increases with N at constant M_P. As the rotor rotates anticlockwise, as N increases it can be observed that the angle of the jets emanating through the stator holes changes in the direction of rotation (purple arrows). This effect is more significant at lower M_P (first column in Figure 5.7) and when the valve is partially closed (Figure 5.8). Additionally, the intensity of energy dissipation in the jets are lower at VPC conditions, implying that the tangential motion of the fluid causes the energy to be re-distributed to the surrounding fluid more uniformly (or moves as a solid body, losing energy as heat). In ROI B, the distribution of energy dissipation in the area near the primary stator appears to be dependent on N for both VFO and VPC conditions.

Another interesting observation is the presence of low energy dissipation behind the rotor blade (blue boxes in Figures 5.7 and 5.8) and high-energy dissipation near the outer primary stator (right edge of the plots in Figures 5.7 and 5.8). The latter could be attributed to the interaction of fluid behind the blade with the jets emanating from the primary stator, whilst, the former could be due to the fluid attaching onto the upstream face of the rotor blade, as observed by Sparks (1996). This observation is also apparent in the work by Jasińska et al. (2015). Since the PIV measurements are angle resolved, it can be seen that this low energy

dissipation region extends with increasing rotor speed and occurs more rapidly at VPC conditions (blue boxes in Figures 5.7 and 5.8), which, again, implies the onset of solid body rotation which is not desired in mixing/ emulsification. Moreover, this also reveals that there are sweet spots of high energy dissipation rate at the inner wall of the secondary stator (magenta circles in Figures 5.7 and 5.8) which also recede with increasing *N*.

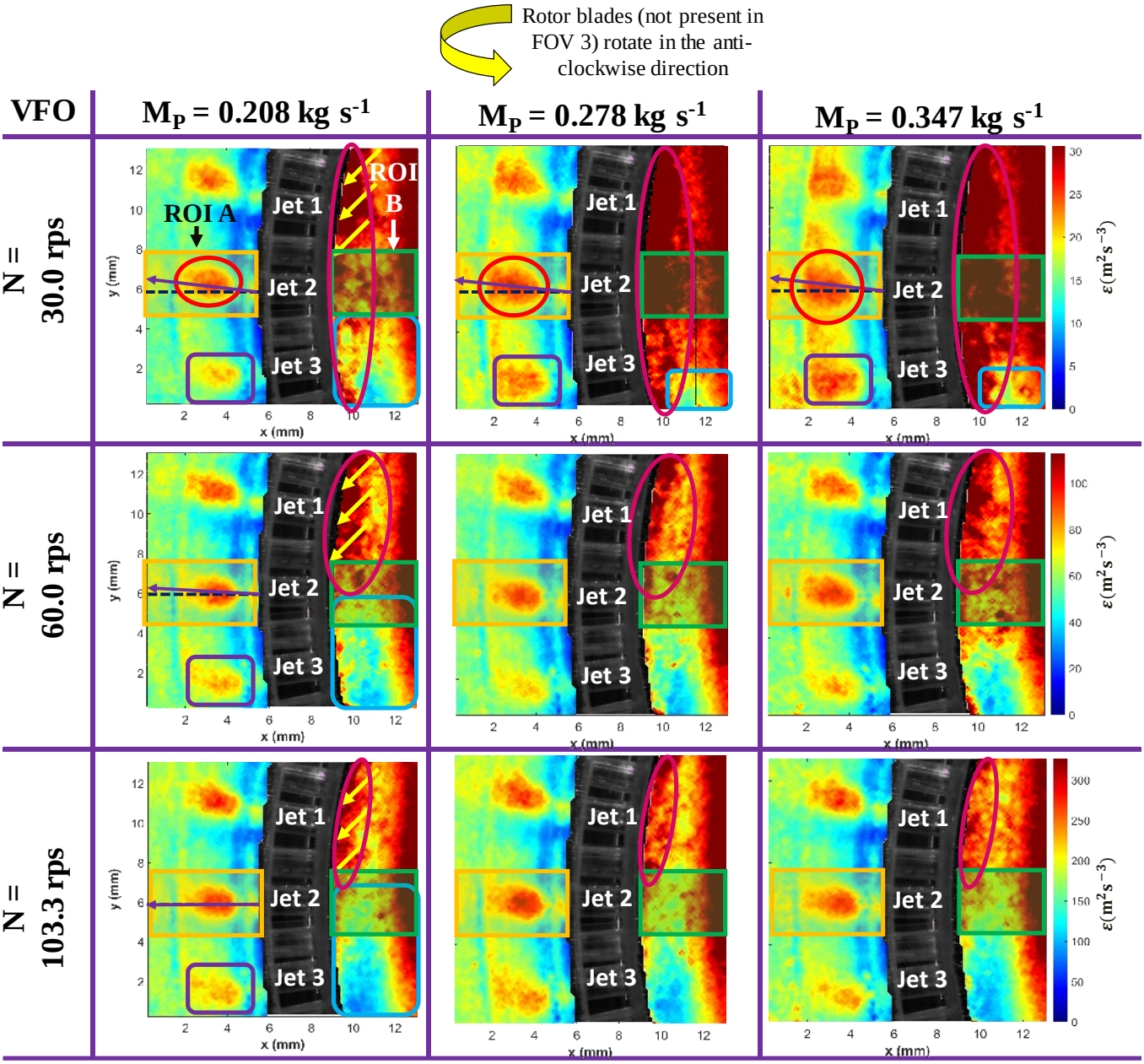

Figure 5.7: Local specific energy dissipation rate distributions calculated by the direct evaluation (DE) method for VFO conditions in FOV 3

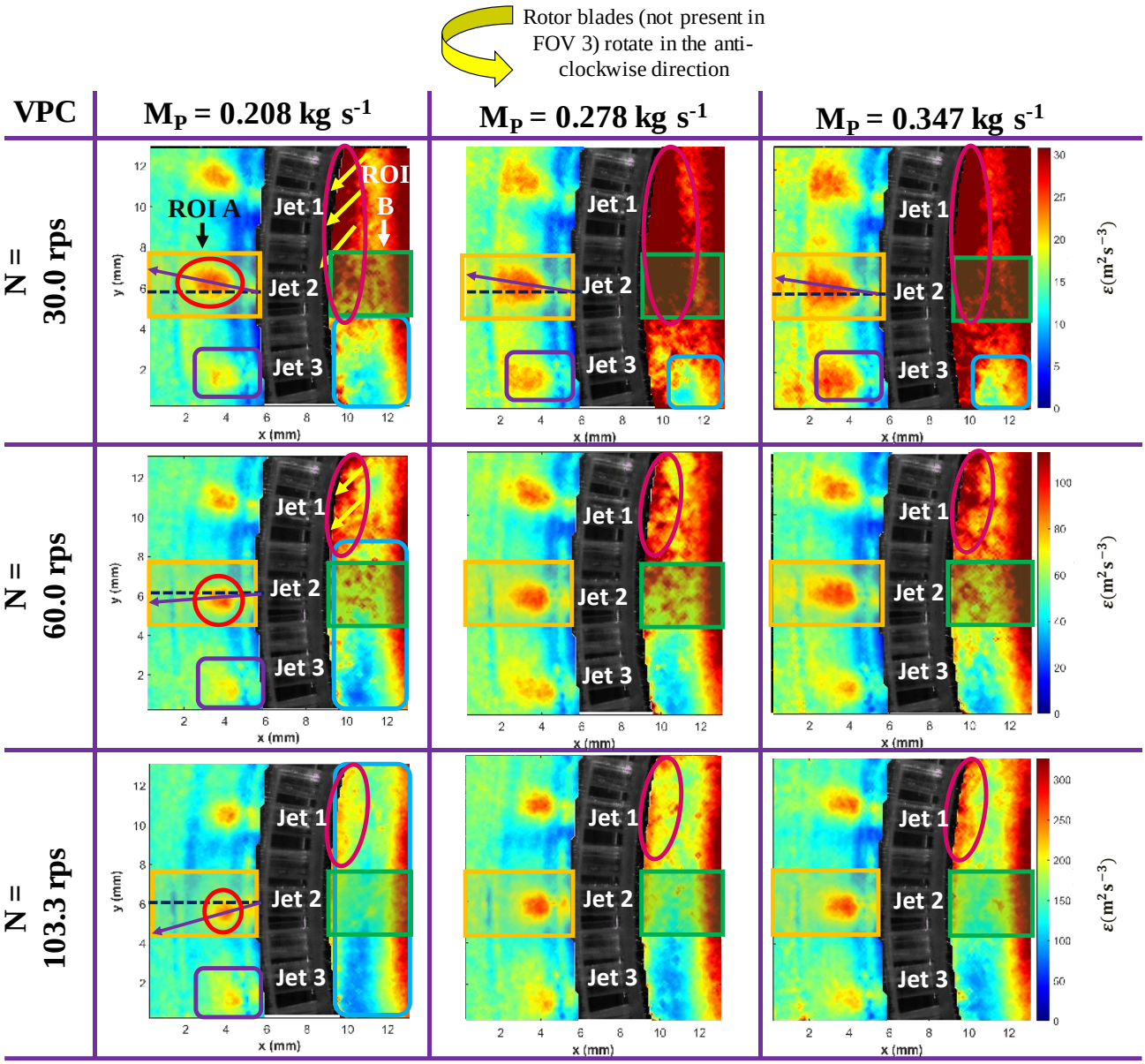

Figure 5.8: Local specific energy dissipation rate distributions calculated by the direct evaluation (DE) method for VPC conditions in FOV 3

A hypothesis that trailing vortices form behind the rotor blade (on either side), similar to that in Rushton Disk Turbines in stirred vessels, is also considered. This is confirmed by the vorticity, *Q* criterion and swirl strength (λ_{CI}) plots in Figure 5.9. The vortex near the inner wall of the outer stator is dissipated by the perforated stator wall (otherwise, a phenomenon called tip leakage vortex similar to those in turbomachinery and centrifugal pump with solid wall casings will manifest), which is supported by weak energy dissipation in the adjacent stator

hole (purple boxes in Figures 5.7 and 5.8). The vortex on the other side of the blade then interacts with the jets emanating from the primary stator. This phenomenon is not fully understood but may be important for potential break up mechanisms.

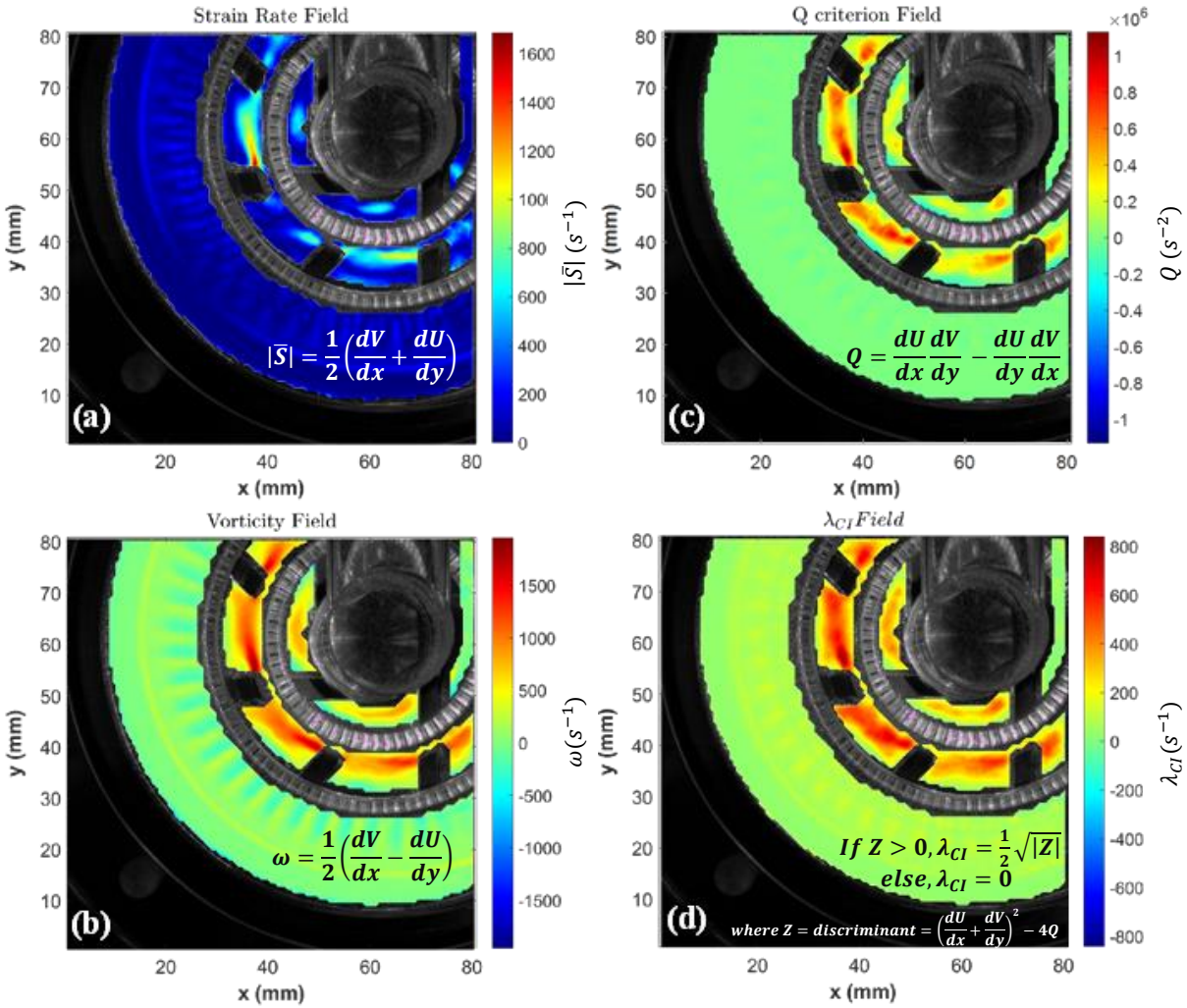

Figure 5.9: Contour plots of (a) Rate-of-Strain (RoS) (b) Vorticity (c) Q criterion (vortex core identifier) and (d) λ_{CI} (swirling strength, another vortex core identifier) criterion for process condition combination of N = 60.0 rps; M_P = 0.278 kg s^{-1}; VFO at FOV 1

In Figure 5.7, it is evident in ROI A that at constant N, increasing M_P intensifies and spreads the maximum energy dissipated through the jets (red circles in Figure 5.7). Additionally, doing so drives the jet angle towards the clockwise direction (purple arrows). The flow becomes more radial for both VFO and VPC conditions since the contribution of the pump to the total head also increases with M_P (Figure 5.3b). As for ROI B, the areas of high energy

dissipation e.g. in close proximity to the primary stator and in the inner wall of the secondary stator, bridge together to a greater degree with increasing M_P especially for VFO conditions at lower N (green box in Figure 5.7). These results suggest that an optimal match between N and M_P has to be found to maximise areas of high energy dissipation rates within the mixing head.

Close-up plots of energy dissipation within ROIs A and B are shown in Figure 5.10. These respective areas corresponding to the emanating jets and high shear region have been identified by Ashar et al. (2018), Atiemo-Obeng and Calabrese (2004),Håkansson (2018) and Thapar (2004), as areas where break up of droplets is most likely to occur. The following observations apply to all runs that have both the Silverson mixer and external pump in operation. Run 13 (with N = 60.0 rps and M_P = 0.278 kg s^{-1}) is used as a reference to illustrate flow patterns in the ROIs in Figure 5.10 as a function of whether the outlet flow is unrestricted (VFO) or restricted (VPC). The velocity vectors show that fluid recirculation occurs in ROI A and is stronger under VFO conditions, which is also reflected by the stronger dissipation rate. The jets in VFO conditions are stronger and more uniform, resembling those for PO conditions (see Figure 5.4a) and are weaker in VPC condition as the flow inside the mixing head becomes more tangential, similar to SO conditions (see Figure 5.4h). In ROI B, the fluid flows in the direction of rotation as it is within the rotor swept region. These results are consistent with the findings of Espinoza et al. (2018) (covered in Chapter 4 of this thesis). There are three distinct levels of energy dissipation in this region shown in the figure: I – intermediate dissipation near the inner wall of the secondary stator, II – lower dissipation in between regions I and III, and III – higher dissipation further to the right near to the emanating jets from the primary stator. The difference between VFO and VPC conditions for this particular run is small but becomes dramatic at higher rotor speeds. This could be due to a more uniform dissipation of energy across the whole mixing head promoted by increased tangential motion of the fluid which

results in better transfer of momentum or it could be perceived as poor mixing due to the onset of solid body rotation. The latter is supported by the increased head at VPC conditions (Figures 5.3b and 5.8) and suggests that energy is lost to heat due to the recirculation of the fluid caused by the increased resistance at the outlet. Either way, increasing the rotor speed and partially closing the outlet valve results in lower ε in localised areas.

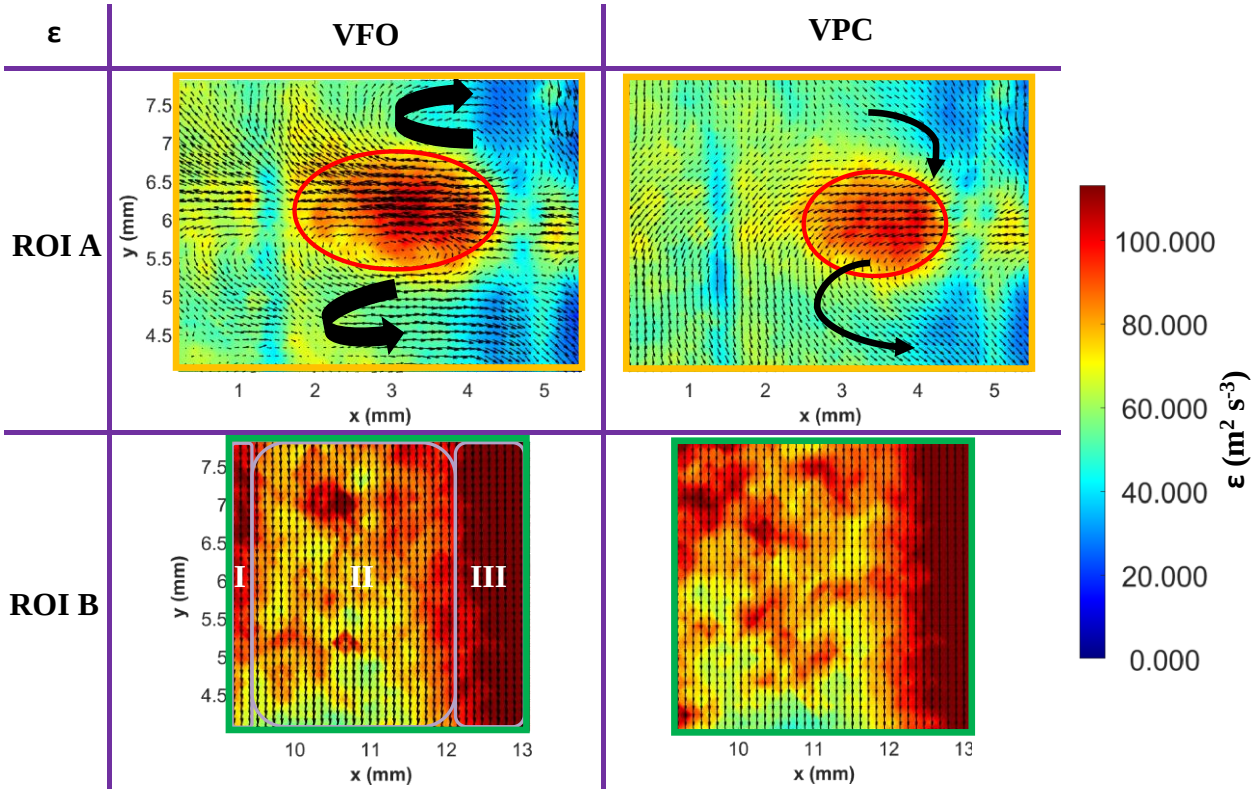

Figure 5.10: Local specific energy dissipation rates calculated by direct evaluation (DE) method with accompanying vectors for the process condition combination of N = 60.0 rps; M_P = 0.278 kg s^{-1} at ROIs A and B in FOV 3 (left column: VFO; right column: VPC)

Dependencies on N and M_T

Table 5.3 and Figure 5.11a imply that $\overline{\varepsilon_{DE,A}} \propto N^{\sim 1.77-1.90}$ and $\overline{\varepsilon_{DE,B}} \propto N^{\sim 1.59-1.72}$ do not follow the conventional $\varepsilon \propto N^3$ as established in the literature, mainly because only a fraction of the total energy dissipation has been resolved. The same was found with the SGS results which exhibited very similar trends, suggesting that the trends are correct but not the absolute values. The exponents are $\overline{\varepsilon_{SGS,A}} \propto N^{\sim 2.66-2.84}$ and $\overline{\varepsilon_{SGS,B}} \propto N^{\sim 2.42-2.61}$ but still do

not equal 3. The only main difference between the DE and SGS distribution plots is that the relative values are higher for SGS as this method models the unresolved scales. This can be attributed to the fact that the measurements were made in 2-D and so the third component of velocity had to be calculated using the isotropy assumption. In addition, the finest spatial resolution used with the DE method of ~$14\lambda_k$ is >>$2\lambda_k$ and considering that high shear mixers can generate droplet sizes lower than λ_k, it is inevitable that the exponents will be underestimated (Saarenrinne et al., 2001). Moreover, as the turbulence intensity increases e.g. at higher ε, the length scales get smaller hence more is missed by the DE method (lower exponents than SGS). The same applies for SGS as it is also very sensitive to the PIV resolution e.g. it models more effectively with better measurements (Håkansson et al., 2017c). This analogy also explains why the exponents in ROI B are less than that in ROI A as the flow in the former is more turbulent. Furthermore, it also has to be taken into account that these exponents apply to their respective ROIs only e.g. it does not take into account the entire mixing head volume or area. These suggest that the relationship between ε and N is not the same across the whole mixing head, supporting the claims by Thapar (2004) and Sparks (1996) that different locations in the mixing head may be locally laminar or turbulent due to the complex geometry within the mixer.

Table 5.3: Summary of constants and exponents for $\bar{\varepsilon} = AN^b$ (Figure 5.11a)

ROI (-)	**External pump flow rate, M_P (kg s^{-1})**	**Method (-)**	**constant A (-)**	**exponent b (-)**	**R^2 (-)**
A	0.208	DE	0.023	1.90	0.996
A	0.278	DE	0.032	1.84	0.997
A	0.347	DE	0.043	1.77	0.998
B	0.208	DE	0.075	1.72	0.990
B	0.278	DE	0.129	1.61	0.993
B	0.347	DE	0.141	1.59	0.996

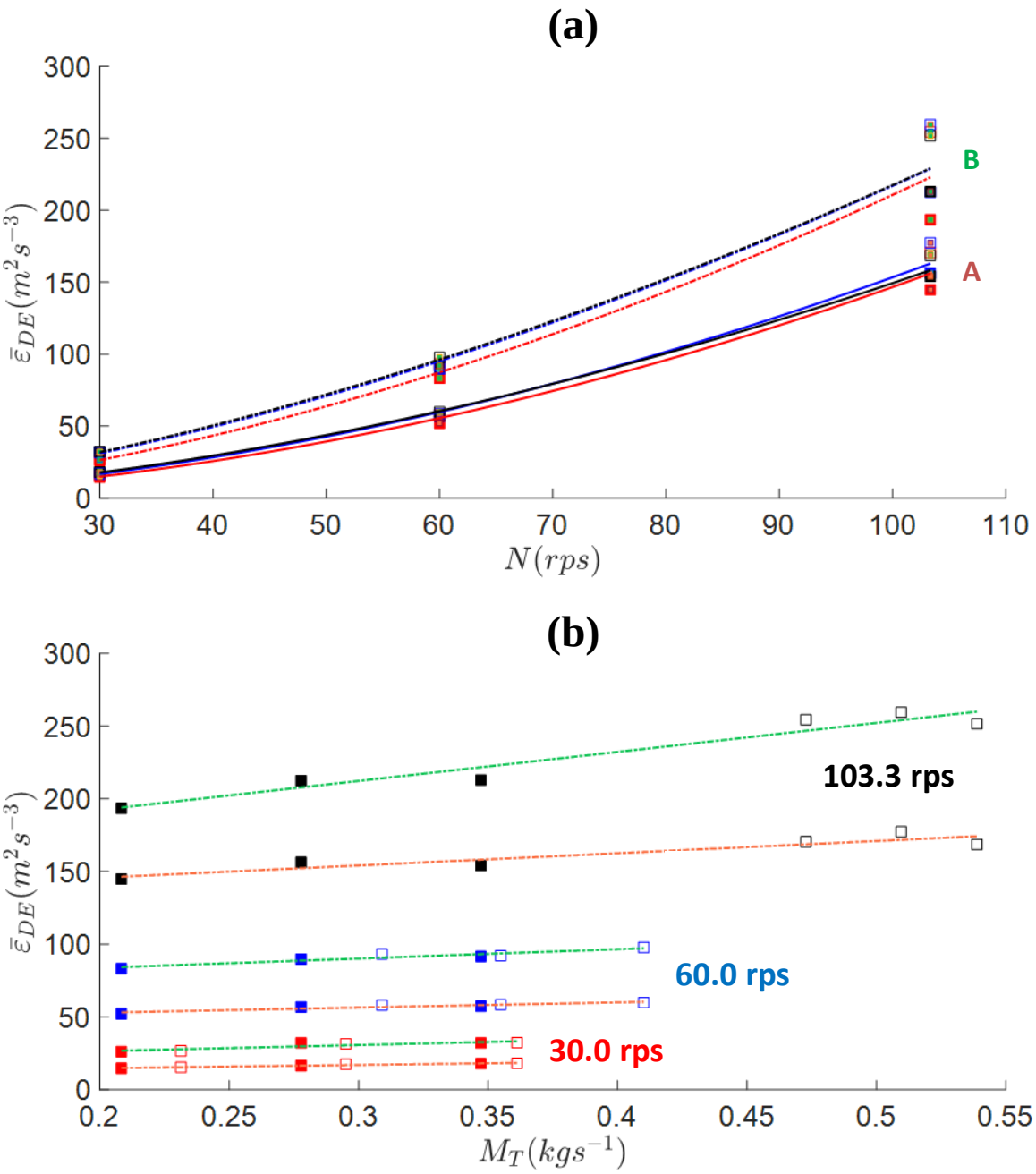

Figure 5.11: Influence of (a) Rotor speed, N and (b) Total mass flow rate, M_T on the mean local specific energy dissipation rates calculated using the Direct Evaluation (DE) method at the regions of interest: A (presence of jet), in solid (–) lines and B (presence of high shear), in dash-dot (-.) lines in FOV 3. Open and closed symbols represent VFO and VPC conditions respectively. Symbol colours denote external pump flow rate: M_P = 0.208 kg s^{-1} (red), M_P = 0.278 kg s^{-1} (blue) and M_P = 0.347 kg s^{-1} (black). For (b), orange and green lines represent ROIs A and B respectively.

The maximum values of energy dissipation obtained in this study (in the hundreds for DE, or thousands for SGS) are comparable to the lower end of the range of simulated values obtained in an existing CFD study (k-ε model) by Jasińska et al. (2015) for the same Silverson model (Case III). In a similar region, the simulated values of energy dissipation at a constant rotor speed of N = 100 rps and a range of total mass flowrate (of water) M_T = 0.167 to 0.667 kg s^{-1} ranges from ~152 to 124,000 m^2 s^{-3}. To the best knowledge of the authors, these results have not been validated with experimental measurements which would have been useful as a comparison for this work. However, it is important to note the differences between the experimental setup as the modelled system in the CFD study did not have an external pump in the loop and thus not accounted for. In addition, the Silverson mixer was gravity fed and its flow rate was solely regulated by an outlet valve.

Another point of view regarding the $\varepsilon \propto N^a$ relationship is through the relationship $P \propto N^b$ which is relevant as $\varepsilon \propto P$. Thapar (2004) stated that determination of the flow regime can be done by investigating the dependency of the unit's power draw on rotational speed e.g. if exponent b is 3, turbulent conditions apply otherwise if it is 2 then laminar conditions apply. This implies that energy dissipation rate at different locations in the mixing head will have a different dependency on the rotor speed depending on whether the flow is laminar or turbulent. On the other hand, Hall (2012) attributes the difference in b values to the different terms in the power draw equation for the same mixer (Equation 5.4). The first term on the right hand side is due to fluid resistance which is analogous to a stirred vessel and is proportional to N^3 whereas the second term is due to fluid acceleration inside the mixing head, which is proportional to N^2D^2. The b values he evaluated are between 2.26 and 2.67 which he compared to that of Bourne and Studer (1992) ~2.5. He then concluded that the resulting values are due to the combined effects of the first and second terms in Equation 5.4. Furthermore, his b values

decreased with increasing flow rate indicating the greater impact of the squared flow rate term on the total power draw at increased M_T. The b values determined in this work (Table 5.3) e.g. 1.59 to 1.90 for DE and 2.42 to 2.84 for SGS, reflect the same trend and are in the same range and magnitude.

Finally, the effect of the total mass flow rate, M_T on energy dissipation rates in ROIs A and B calculated using the DE method is portrayed in Figure 5.11b. At constant N, M_T is always higher in VFO conditions as the combined flow rate was not restricted to the initially set M_P as in the VPC conditions. Nevertheless, all data points fall on the same line and display a linear relationship (see Table 5.4 for exponents). The values for ROI B are always higher than in ROI A, e.g. in the high shear region. The gap between ROI A and ROI B lines increases with N as there is more energy input into the system thus more energy is dissipated and more so in ROI B. Furthermore, the lines have low gradients at lower rotor speeds, meaning that dissipation values can be treated constant and indicates that M_T is only influential at very high rotor speeds which agrees with the findings of Hall et al. (2011a). The dip at higher N from VFO to VPC, again, suggests that partially closing the valve results in overall lower energy dissipation (most likely due to heat loss by fluid recirculation/ solid body rotation) e.g. by a factor of ~0.20 (250 to 200 $m^2\ s^{-3}$) in ROI B and ~0.14 (175 to 150 $m^2\ s^{-3}$) in ROI A at N = 103.3 rps and thus affecting ROI B more significantly (compare Figure 5.7 with Figure 5.8).

Table 5.4: Summary of constants and exponents for $\bar{\varepsilon} = AM_T + c$ (Figure 5.11b)

ROI (-)	**Rotor speed, N (rps)**	**Method (-)**	**constant A (-)**	**constant c (-)**	**R^2 (-)**
A	30.0	DE	22.61	10.14	0.936
A	60.0	DE	35.39	45.77	0.852
A	103.3	DE	84.12	128.87	0.863
B	30.0	DE	42.07	18.00	0.772
B	60.0	DE	64.12	70.87	0.878
B	103.3	DE	199.48	152.41	0.934

5.3.3 Reynolds stresses and TKE

It is expected that areas of high energy dissipation rates are also areas of high TKE and Reynolds stresses (Figure 5.12). Knowing where stresses are localised is vital in determining potential droplet break up mechanisms. In ROI A, the highest value of R_{11} is in the core of the jets for both VFO and VPC conditions (orange box in Figure 5.12), caused by the presence of dominant *x*-velocity components emanating from the stator hole. The area of higher values is larger for VFO ($2 < x < 4$ mm; $5.75 < y < 6.5$ mm) in comparison with that for VPC ($3 < x < 4$ mm; $6 < y < 6.25$ mm). Away from the jets, the values approach zero. For R_{22}, the highest values are still in the core of the jets for both VFO and VPC conditions but are lower in magnitude by about half the maximum of R_{11}. The *y*-velocity components from the jets are lower than the *x*-velocity components. The magnitude of the maximum R_{12} is much lower for both VFO and VPC conditions e.g. about a tenth of the maximum of R_{11}, suggesting that the shear is negligible. It is, however, interesting to see that shear stresses are higher in VPC conditions as the tangential motion of the fluid is increased, suggesting increased interaction between the bulk fluid and the emanating jet. Moreover, the fluid from the preceding jet directly enters the core of the succeeding jet, as opposed to going around the recirculation zones prior to reaching the jet core as in the VFO condition (Figure 5.10).

In ROI B, areas of high R_{11} (green box in Figure 5.12) have similar magnitude as in ROI A and resemble the regions defined in Figure 5.10. Region I has higher ε due to the *x*-velocity component of the fluid impinging on the inner wall of the secondary stator. Region II has lower ε as it is within the area behind the blade while Region III also has higher ε due to the *x*-velocity components of the jets from the primary stator interacting with the fluid within the area between the primary and secondary stators. R_{11} values are slightly higher in VFO conditions especially in the area near the primary stator as the jet flows are less affected by relatively weaker

tangential flow. Areas of high R_{22} are an order of magnitude higher than both the maximum values of corresponding R_{11} and R_{12}, which means that it dominates in ROI B. This makes sense as it is within the rotor swept volume, meaning that the majority of the fluid flows in the direction of rotation i.e. *y*-velocity components in the downwards direction. Finally, as with ROI A, R_{12} has very little influence in this region.

From these observations, it can be deduced that R_{11} and R_{22} dominate in ROIs A (squares in Figure 5.13a) and B (circles in Figure 5.13b) respectively (although their values are of the same magnitude and do not differ significantly, conveying some validity of the isotropic assumptions) especially at higher N and M_P. R_{12} can be treated negligible in both regions. In addition, they also influence the ε values in these regions (Figures 5.13c and d). Furthermore, they also dictate the TKE values in ROIs A and B (Figure 5.12) since $k = \frac{3}{4}\,(U_{rms}^2 + V_{rms}^2)$ which is equivalent to $k = \frac{3}{4}(R_{11} + R_{22})$. It then follows that high TKE results in high ε (Figure 5.14b). TKE is always higher in ROI B and at increasing N (Figure 5.14a) as the flow in this region is turbulent e.g. it is within the rotor swept volume where Re ≥ 120,000.

Figure 5.14a shows the relationships between N and TKE in ROIs A and B. For ROI A, it was deduced that $k \propto N^{\sim 1.8}$ (Table 5.5) which is as expected as $k \propto N^2$ (Equation 5.4). Conversely, it is more complicated for ROI B e.g. a second order polynomial (which is expected) and a linear fit were used for VFO and VPC conditions respectively (Table 5.5). This can be explained by referring to ε plots in Figures 5.7 and 5.8 for the process conditions where the differences are greatest e.g. at N = 103.3 rps and at constant M_P. For the VFO conditions in ROI B, at constant N = 103.3 rps, the distributions of ε (and hence TKE) look very similar hence why the data points (encircled red) in Figure 5.14a are clustered together.

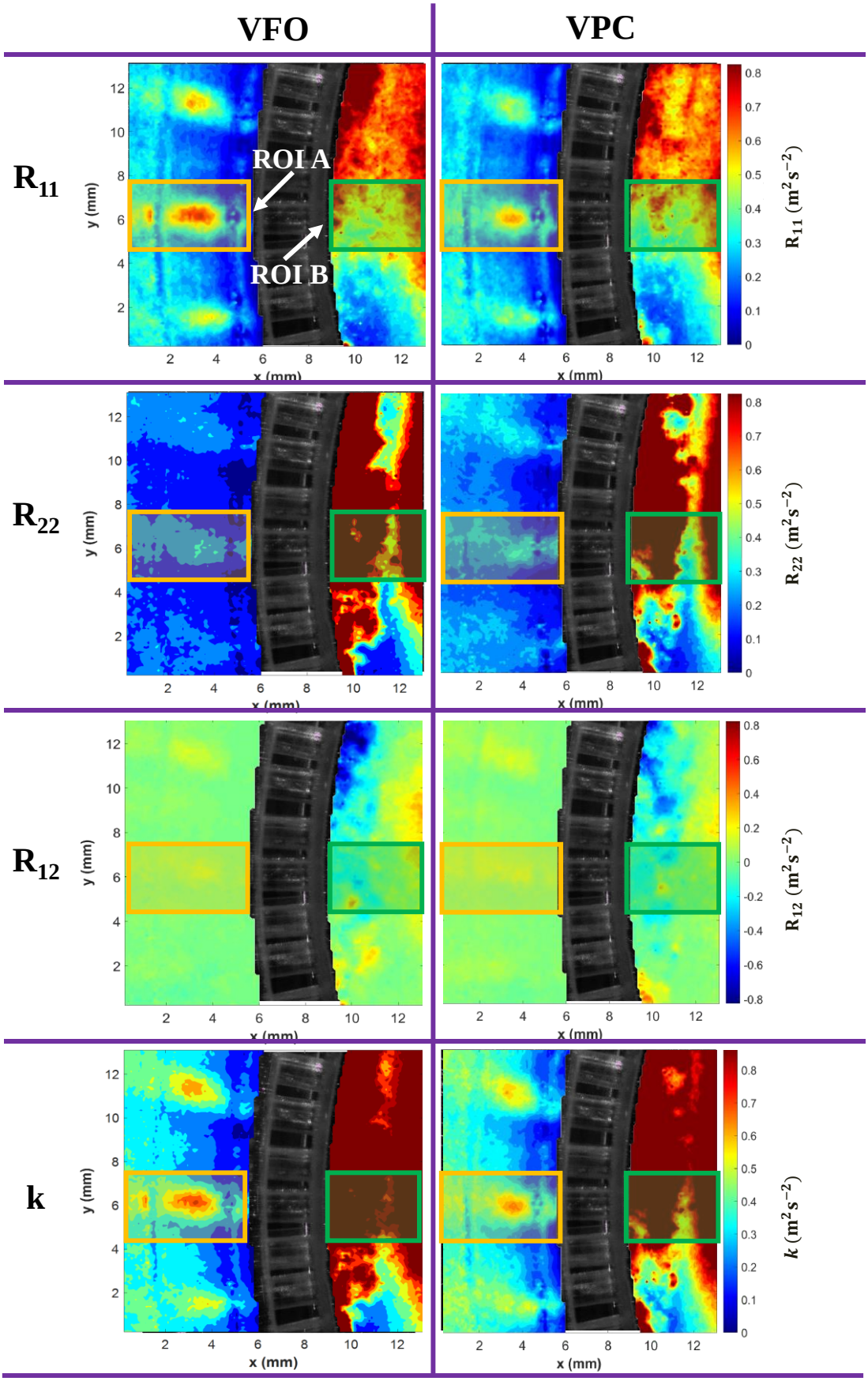

Figure 5.12: Reynolds stresses (R_{11}, R_{22} and R_{12}) and turbulent kinetic energy, k plots in FOV 3 for the process condition combination of N = 60.0 rps; M_P = 0.278 kg s^{-1}

For VPC, the distributions are also very similar but are weaker in magnitude. As for constant M_P at 0.278 kg s^{-1} (blue line in Figure 5.14a), for VFO conditions, as N increases, areas of high ε diminish as low ε extends behind the blade which is more dramatic for VPC conditions. This is why the data points for VFO and VPC are very different at N = 103.3 rps (black arrow, Figure 5.14a). The same trend applies for all other conditions with constant M_P. Ultimately, the relationship (equation of the curve) depends on what is captured in the ROI e.g. for ROI B, the distribution of high ε will depend on N, the higher it is, the lower ε is due to solid body rotation.

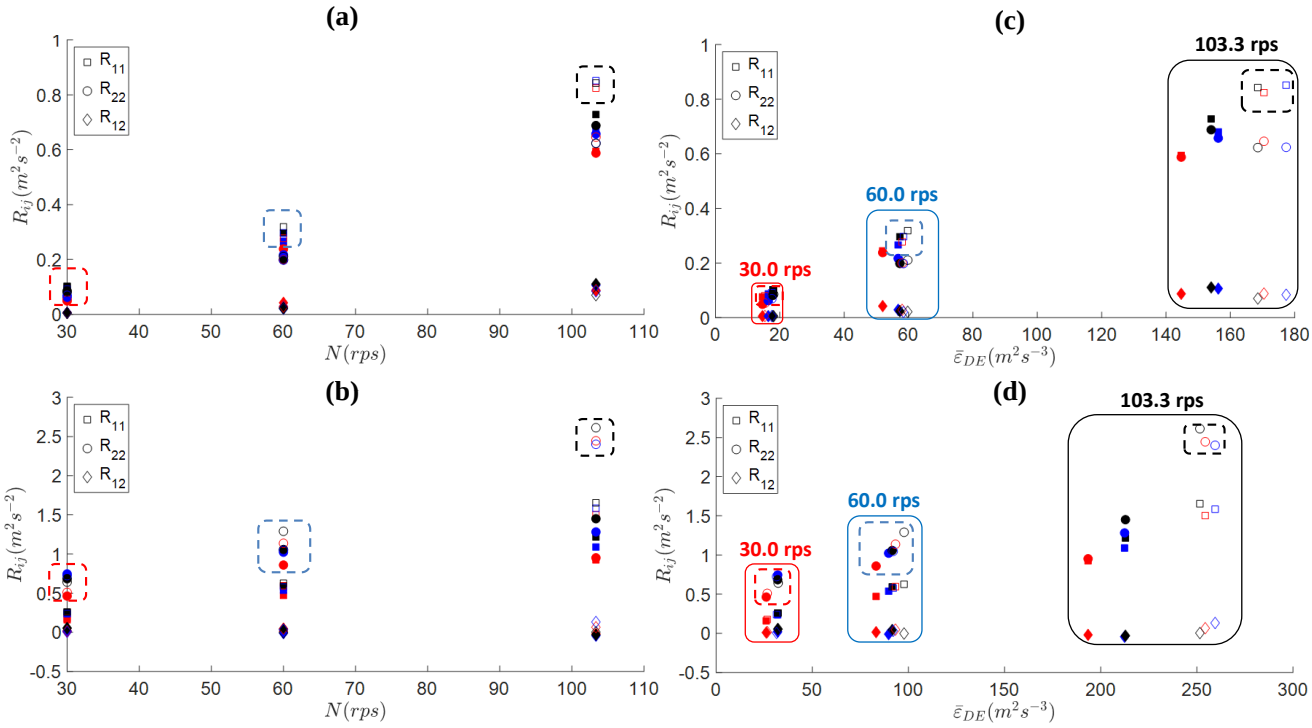

Figure 5.13: (a) Influence of rotor speed on Reynolds stresses (R_{11}, R_{22} and R_{12}) in ROI A, (b) Influence of rotor speed on Reynolds stresses in ROI B. Corresponding plots of the relationship between local specific energy dissipation rates and Reynold stress components in (c) ROI A and (d) ROI B. In all plots, open and closed symbols represent VFO and VPC conditions respectively and symbol colours denote external pump flow rate: M_P = 0.208 kg s^{-1} (red), M_P = 0.278 kg s^{-1} (blue) and M_P = 0.347 kg s^{-1} (black)

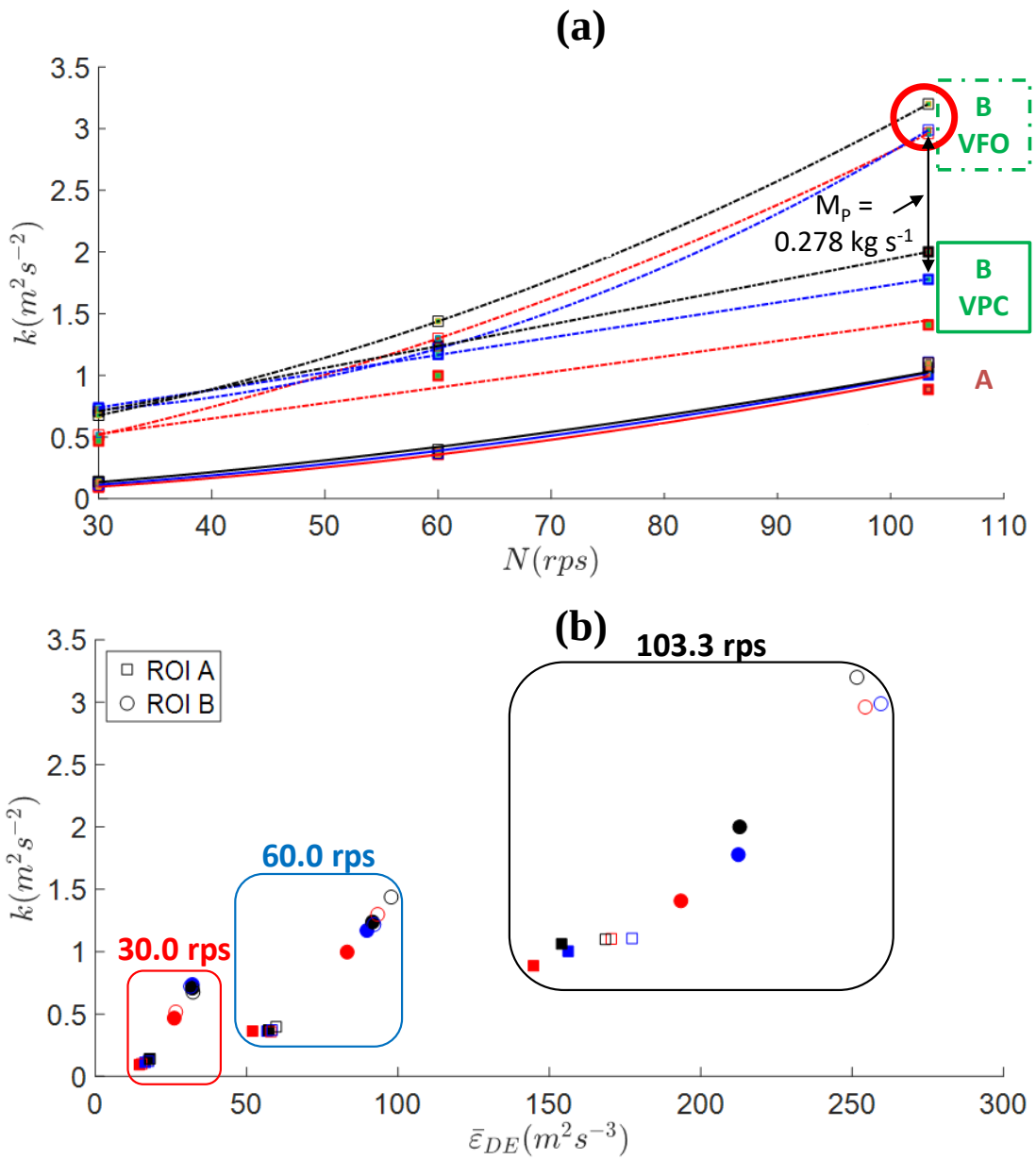

Figure 5.14: (a) Influence of rotor speed on turbulent kinetic energy at ROIs A (presence of jet), in solid (–) and B (presence of high shear), in dash-dot (-.) lines in FOV 3 and; (b) Relationship between local mean specific energy dissipation rates (calculated using DE method) and turbulent kinetic energy. In both plots, open and closed symbols represent VFO and VPC conditions respectively and symbol colours denote external pump flow rate: M_P = 0.208 kg s^{-1} (red), M_P = 0.278 kg s^{-1} (blue) and M_P = 0.347 kg s^{-1} (black)

Table 5.5: Summary of constants and exponents for $k = AN^b + C$ or $k = AN^2 + DN + E$ (Figure 5.14a)

ROI (-)	**External pump flow rate, M_P (kg s^{-1})**	**Method (-)**	**Flow class (-)**	**constant A (-)**	**exponent b (-) *constant C (-) ˣconstant D (-)**	**^constant E (-)**	**R^2 (-)**
A	0.208	DE	VFO + VPC	0.0002	1.88	-	0.995
A	0.278	DE	VFO + VPC	0.0003	1.78	-	0.996
A	0.347	DE	VFO + VPC	0.0005	1.65	-	0.994
B	0.208	DE	VFO	0.0002	*0.011	^0.036	1.000
B	0.278	DE	VFO	0.0003	*-0.013	^0.823	1.000
B	0.347	DE	VFO	0.0002	*0.007	^0.289	1.000
B	0.208	DE	VPC	0.0126	ˣ0.146	-	0.969
B	0.278	DE	VPC	0.0142	ˣ0.314	-	1.000
B	0.347	DE	VPC	0.0176	ˣ0.180	-	1.000

5.4 Discussion

With the current knowledge of Reynolds stress, TKE and ε distributions, as well as calculated *Re* and nominal residence times (τ_R), defined in Table 5.6 at probable locations (Figure 3.3), it can be deduced that droplet break up locations and potential break up mechanisms in the mixing head are similar to those identified by Thapar (2004).

In the stator hole and R-S gap, simple shear and elongational stresses may apply as the flow is laminar due to the small length scale. The τ_R of droplets in the R-S gap is very short which implies that it is bypassed by many droplets which break further in the stator hole. However, τ_R in the stator hole is also very short thus the drops have insufficient time to be sheared/ elongated and split (deformation time > τ_R). In the turbulent regions such as in the inlet pipe, rotor and volute, the drops break due to the dissipation of TKE, primarily in the inertial subrange. This is a reasonable assumption as it was found that ε is proportional to at least the square of *N*, approaching N^3, which convey that the dominating disruptive stress is the

inertial stress (Ashar et al., 2018). Furthermore, the residence times of the droplets are longer in these regions, providing the drops greater probability to break.

Table 5.6: Ranges of Reynolds numbers and residence times at different locations in the mixing head

	L (m)	U (m s^{-1})	Re Range	τ_R (s)
Inlet pipe	D_{inlet} = 0.01905	U_{inlet} = 0.73 – 0.89	$\frac{\rho U_{inlet} D_{inlet}}{\mu}$ = 14,000 – 36,000	$\frac{V_{inlet}}{M_T/\rho} = 0.029 - 0.075$
Rotor	$D_{ss,outer}$ = 0.0635	U_{tip} = 5.98 – 20.61	$\frac{\rho N D^2}{\mu} = 120{,}000 - 420{,}000$	$\frac{V_{rotor\ swept}}{M_T/\rho} = 0.271 - 0.701$
Stator hole	D_h = 0.00159	U_{hole} = 0.36 – 0.94	$\frac{\rho U_{hole} D_h}{\mu}$ = 600 – 1,500	$\frac{V_{hole}}{M_{hole}/\rho} = 0.004 - 0.011$
R-S gap	δ = 0.00024	U_{tip} = 5.98 – 20.61	$\frac{\rho N \delta}{\mu}$ = 7,200 – 25,000	$\frac{V_\delta}{M_T/\rho} = 0.001 - 0.004$
Volute (jets)	*Distance from outer wall of secondary stator to the inner wall of the mixing head = 0.019835	$U_{jet} = U_{hole}$ = 0.36 – 0.94	$\frac{\rho U_{hole} D_{volute}}{\mu}$ = 7,200 – 19,000	$\frac{V_{volute}}{M_T/\rho}$ = 0.721 – 1.866 *The jet penetration length e.g. as shown in Figure 4.8 would also be a good alternative as a characteristic length to calculate V_{volute} as that would be where the greatest interaction between the jet and the bulk will occur.

From the above observations, it can be concluded that dissipation of TKE is the main driving force for droplet break up in in-line HSMs. The proposed break up sequence can be described by considering the streamlines (velocity vectors) that the drops may follow and comparing areas of high ε in the mixing head. The droplet may be conveyed into the bulk flow induced by the rotor within the area bounded by the secondary stator via the inlet pipe; it may then collide with the inner stator wall and subsequently sheared in the stator holes. Eventually, they emanate from the holes and are subjected to deformation stresses within the jets that interact with the bulk flow in the volute. This also occurs between the primary and secondary

stators. Therefore, in relation to the findings on how the process parameters affected *Re* stress, TKE and ε distributions, their possible effects on droplet break up, are identified as follows:

- The maximum value of ε, especially in ROI B will increase with *N*, but at the expense of more confined regions of 'sweet spots' (high ε). This means that droplets may be subject to greater disruptive forces in these regions but are less likely to visit them. This therefore emphasises the importance of simultaneously considering both the hydrodynamics and distribution of disruptive forces in the mixing head (Ashar et al., 2018). Furthermore, partially closing the outlet valve impose the same effects at an accelerated rate as it induces a greater tangential motion, promoting solid body rotation (wasted energy) which results in larger areas of the mixing head with medium ε. This is evident in Figure 5.8.

- Increasing M_P yields stronger jets and promotes interaction with the surrounding fluid (improved turbulence). However, caution must be taken as suggested by Sparks (1996) not to end up with a 'drowned suction'. A mismatch between the process flow rate (M_P) and Silverson flow rate (M_S) must be avoided (Casugbo and Baker, 2018).

Finally, agitator shear rate also has a contribution, as shown in the RoS plot in Figure 5.9, but as expected, high levels are concentrated within the rotor swept volume. Finally, results support the claim that the R-S gap does not significantly influence droplet break up (Atiemo-Obeng and Calabrese, 2004).

5.5 Conclusions

2-D PIV data were used to study the turbulence characteristics in a 150/250 in-line Silverson high shear mixer. Influence of process variables on turbulence parameters such as Reynolds stresses, TKE and energy dissipation rates have been investigated. A method of quantifying external pump and Silverson mixer contribution on driving the overall system flow

and thus the mixing head, as well as identifying potential droplet break up mechanisms have been proposed.

Two main regions of interest: jet region (ROI A) and high shear region (ROI B) were investigated. In ROI A, radial flow dominates due to the emanating jets from the secondary stator (driven by the external pump) hence most of the energy is dissipated through the jet cores. In contrary for ROI B, tangential flow dominates as it is in the rotor swept volume. As the flow in this region is highly turbulent, droplet break up occurs due to turbulent stresses in the inertial sub-range. Areas of high ε or 'sweet spots' manifest due to the proposed phenomena: *(a)* fluid impaction on the inner wall of the secondary stator and *(b)* interactions between the undisturbed vortex that forms behind the rotor blade and the jets emanating from the primary stator. Energy dissipation rates were found to be proportional to $N^{\sim 1.59-1.90}$ and $N^{\sim 2.42-2.84}$ using DE and SGS methods respectively at the best attained spatial resolution ($\sim 14\lambda_K$). Both methods yielded exponents that are approaching the value of, but do not equal 3 that is well established in the literature e.g. between 2.26 and 2.67 for in-line HSMs (Bourne and Studer, 1992; Hall, 2012).

Finally, the recommended operating zones are highly dependent on the process application. In general, operating at higher flow rates is preferable as at constant rotor speed, higher flow rates have the lowest energy density which means that the mixer requires lower energies to achieve a desired droplet size. In light of this, VFO conditions may be deemed favourable over VPC conditions as long as ΔP_T in the mixing head is the same (similar flow patterns achieved) as the latter promotes unnecessary increase in outlet temperature and residence times which leads to wasted energy. However, it still has its uses e.g. in throttling the Silverson discharge along with increasing the set pump flow rate to prevent the onset of cavitation. These implications in practice are covered in more detail in §7.2.

Chapter 6 – Mean Flow Field and Energy Dissipation for Fluids with Complex Rheology in an Inline High Shear Mixer

6.1 Introduction

Newtonian fluids such as water and aqueous solutions of glycerol are often used as mimics for process fluids enabling flow field studies to be made on mechanically agitated vessels including HSMs (Baldi et al., 2004; Mortensen et al., 2017; Utomo, 2009; Wang et al., 2014). However, many fluids that are handled in process industries are non-Newtonian in nature e.g. the apparent viscosity is a function of time, shear rate, elasticity and other factors (Wang et al., 2014). This means that the rheological properties of processed fluids and how they affect the flow when the fluids interact with fast rotating rotor blades and stators, are essential considerations in optimising the operating conditions of HSMs. As established by Thapar (2004), this results in the presence of localised flow regimes in the mixing head, depending on the area of concern. Laminar, transitional and turbulent conditions may persist depending on the considered characteristic velocity and characteristic length.

The aim of this chapter is to examine the behaviour of selected Newtonian and non-Newtonian fluids in an in-line 150/250 Silverson mixer. The fluids chosen comprise of two Newtonian fluids of different viscosity (water and glycerol) to provide a base/control case and two generic transparent shampoo formulations (SA, Newtonian, and SB, shear thinning) representative of fluids processed by Unilever Port Sunlight. Some preliminary studies using a Polyacrylamide (PAA) solution (which exhibits some behaviour that could be attributed to viscoelastic properties) are described in Appendix A.

The rationale for fluid choice and flow conditions is given in §6.2 with optimisation of the PIV settings and energy dissipation calculations described in §6.3. The rest of the chapter describes the comparison of mean flow fields in §6.4, kinetic energy and energy dissipation rate distributions for water, glycerol and shampoo formulations in §6.5 and 6.6. In addition, the effect of kinematic viscosity used in energy dissipation rate calculations was also discussed in §6.6. Turbulence intensity is discussed in §6.7 for all fluids. Shear rates and Weissenberg numbers for SB have also been covered in §6.8. The study is concluded in §6.9.

6.2 Materials and Methods

6.2.1 Working Fluids

The formulations are given in Table 6.1.

Table 6.1: Formulation of fluids used in the HSM.

Fluid	Composition
Water (WATER)	- 100 wt% tap water
Glycerol solution (GLY)	- 40 wt% glycerol - 60 wt% deionised water
Shampoo A (unsalted) (SA)	- Individual components of the shampoo formulations are described in §3.4. However, exact levels are confidential. Relevant rheological data are available in Table 6.2.
Shampoo B (salted – 0.71 wt%) (SB)	

Table 6.2, gives the rheological properties, measured using a 60 mm 2º cone and plate stainless steel geometry in a Discovery Hybrid Rheometer (DHR-2, TA Instruments, Inc). As the HSM can generate very high shear rates, temperature increase in the mixing head is inevitable thus, the amount of glycerol was limited to 40 wt%, when its viscosity is not significantly dependent on temperature e.g. $\mu = 3.72 – 2.72$ Pa s between 20 to 30 ºC (Segur and Oberstar, 1951). During the experimental runs, the glycerol solution temperature varied from 23 to 30 ºC. It would also have been ideal to control the mixing head temperature directly

using a cooling circuit but any design would have been incompatible with the optical PIV measurements.

Table 6.2: Rheological properties of fluids used in the HSM.

Fluid	**K (Pa s^n)**	**n (-)**	**Relaxation time pre-exponential factor a (s $^{b+1}$) Equation 6.9**	**Relaxation time power law exponent b (-) Equation 6.9**
WATER	0.00100	1.00	-	-
GLY	0.00334	1.00	-	-
SA	0.01200	1.00	-	-
SB	9.46	0.349	113.33	-2.282
SB μ_∞ at ~1400 s^{-1}	0.0638	1.00	-	-

The shampoo formulations, SA and SB, are simplified versions of full formulations, the latter are generally opaque and are therefore not suitable for PIV studies. Shampoo A (SA) is the less viscous base whereas Shampoo B (SB), contains additional salt (introduced as brine) to raise its viscosity closer to that of a consumer product. The flow curves for SB are given in Figure 6.1. Comparing results between SA and SB will be interesting to see the effects of salt/ surfactant interaction which leads to its viscoelastic behaviour. To avoid over-pressurising the mixing head, which has a pressure limit of 7 barg, the zero viscosity, μ_0 was limited to ~ 1.5 Pa s (Figure 6.1a). Figure 6.1b shows that the first normal stress difference, N_1 for SB is positive, which means that the sample pushes the geometry upwards and reflects traits of a viscoelastic fluid e.g. increased elasticity at high shear (Phan-Thien, 2002). Ideally, extensional and oscillatory rheological measurements should also be conducted for the shampoo formulations. However, previous attempts on similar formulations e.g. containing 1 wt% NaCl (comparable to 0.71 wt% in SB) (data in Appendix B), show that doing the latter was generally unsuccessful as the results are irreproducible especially at lower salt content e.g. lower viscosity. As for the former, the equipment required was unavailable. The densities of the fluids in Table 6.3 were

estimated by taking an average of triplicate measurements of weighed 10 mL volume of each fluid using a micropipette and a weighing scale.

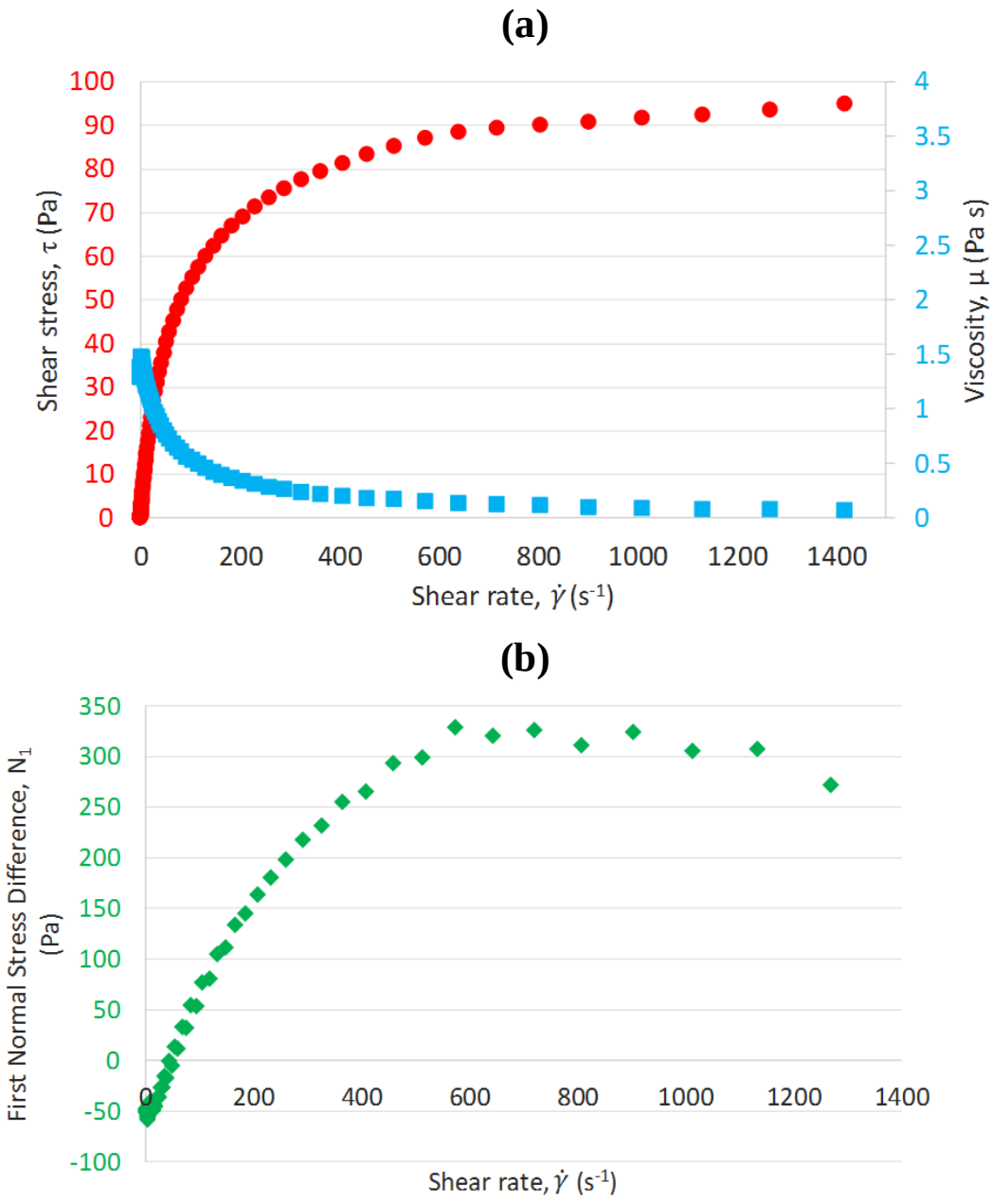

Figure 6.1: (a) Shear stress, τ and viscosity μ versus shear rate for Shampoo B (b) First normal stress difference, N_1 versus shear rate for Shampoo B.

6.2.2 Flow Conditions in the HSM

For calculation of flow regime, the viscosity of shampoo B was initially approximated as its infinite viscosity, μ_∞ according to the rheometer measurement (0.0638 Pa s) at a maximum shear rate, $\dot{\gamma}$, of ~1400 s^{-1}. The Newtonian viscosity was assumed for all other fluids. Calculations of the values of Reynolds number show that the flow conditions are all turbulent in the rotor swept volume for all fluids e.g. Re > 10,000, except for SB at a rotor speed, N = 60.0 rps (SB1) and external pump flow rate, M_P = 0.347 kg s^{-1} (Table 6.3). This is because of its higher viscosity and thus, the rotor speed was increased to 133.3 rps (SB2) while keeping M_P constant at 0.347 kg s^{-1}. However, it is evident through Table 6.3 that this is still in the transitional regime. Hence, to develop a fully turbulent flow, at least within the rotor swept region, the rotor speed was further increased to 183.3 rps (SB3) with the consequence of having to increase M_P = 0.403 kg s^{-1} (maximum capability of the external pump) to prevent the onset of cavitation. When SB results were compared with water and SA, its kinematic viscosity, υ, was initially treated as constant for simplification e.g. equal to (μ_∞/ρ). However, the importance of approximating local υ for SB is covered in §6.6.1.

Table 6.3: Reynolds number calculations for all fluids in the rotor swept volume. M_T presented is for VFO conditions, for VPC conditions, $M_T = M_P$

Fluid	**N (rps)**	**M_P (kg s^{-1})**	***M_T (kg s^{-1})**	**μ_∞ (Pa s)**	**ρ (kg m^{-3})**	**Re = $\frac{\rho N D^2}{\mu_\infty}$ (-)**
WATER	60.0	0.347	0.410	0.00100	1000	242,000
GLY			0.407	0.00334	1098	79,500
SA			0.391	0.01200	1030	20,800
SB (SB1)			0.386	0.06380	1068	4,050
(SB2)	133.3		0.521			9,000
(SB3)	183.3	0.403	0.672			12,400

6.3 PIV Acquisition and Data Processing

6.3.1 Calculation of Local Specific Energy Dissipation Rate, ε

The method for calculation of ε for the Newtonian fluids was the same as used in Chapter 5.2.3. Given that SB is clearly a shear thinning fluid (Figure 6.1a), in the calculation of ε, local viscosities were also evaluated and compared to the results obtained when the kinematic viscosity was treated as a constant. Velocity data was used to estimate the local shear rates, $\dot{\gamma}$, in a similar manner to Wang et al. (2014):

$$\dot{\gamma} = \sqrt{2\,\overline{S_{ij} : S_{ij}}} \tag{6.1}$$

where S_{ij} is the resolved scale strain rate tensor:

$$S_{ij} = \frac{1}{2}\left[\frac{\partial U_i}{\partial x_j} + \frac{\partial U_j}{\partial x_i}\right] \tag{6.2}$$

Since the kinematic viscosity can be written as:

$$\nu = \frac{\mu_{apparent}}{\rho} = \frac{K}{\rho}\dot{\gamma}^{(n-1)} \tag{6.3}$$

then Equation 5.9, becomes

$$\varepsilon_{DE} = \frac{K}{\rho}\left[2\overline{\left(\frac{\partial U}{dx}\right)^2} + 2\overline{\left(\frac{\partial V}{dy}\right)^2} + 3\overline{\left(\frac{\partial V}{dx}\right)^2} + \overline{3\left(\frac{\partial U}{dy}\right)^2} + 2\overline{\frac{\partial U}{\partial y}\cdot\frac{\partial V}{\partial x}}\right]^{\frac{n-1}{2}}\left[2\overline{\left(\frac{\partial U''}{\partial x}\right)^2} + 2\overline{\left(\frac{\partial V''}{\partial y}\right)^2} + 3\overline{\left(\frac{\partial V''}{\partial x}\right)^2} + 3\overline{\left(\frac{\partial U''}{\partial y}\right)^2} + 2\overline{\frac{\partial U''}{\partial y}\cdot\frac{\partial V''}{\partial x}}\right] \tag{6.4}$$

6.3.2 Optimisation of PIV Data Processing

During the analysis, artefacts were observed using the PIV processing settings used in Chapter 5. Spurious results included slow moving fluids and higher dissipation rates that

persisted by the inner wall of the secondary stator (encircled in magenta in Figure 6.2). This observation was more prominent with shampoo and so was initially incorrectly attributed to its non-Newtonian behaviour e.g. possibility of shear banding. However, this cannot be proven without conducting experimental techniques such as flow-induced birefringence measurement which was not performed in this study.

The underlying cause was identified as the particles moving faster by the inner wall of the secondary stator, beyond the allowable movement ($0.25 \times L_{IA}$) set by the PIV recursive Nyquist algorithm at the resolved grid size (64×64 pixels). This led to the generation of spurious vectors that were then erroneously used for interpolating vectors and this effect worsened as the second pass was done in a smaller grid size of 32×32 pixels.

The solution was to re-process the images, still using the recursive Nyquist grid but instead starting and ending with 128×128 and 64×64 pixel grids for the first and second passes respectively. This resulted in the disappearance of slow moving fluids and high energy dissipation rates as well as an almost negligible % of interpolated vectors (yellow arrows in the raw image) by the inner wall of the secondary stator (compare before and after columns in Figure 6.2). Although this improved the number of good vectors (green arrows in the raw image in Figure 6.2 and as summarised in Table 6.4), it compromised the measurement resolution e.g. the total number of vectors reduced by ~ 76%. Data for all the fluids used was thus reprocessed at this resolution to enable fair comparison to be made. It should be noted that Figure 6.3 shows that data for water also suffered slightly from these same issues and was resolved by the reprocessing. This is also reflected in Table 6.4 where it shows that the % of good and interpolated vectors also improved. According to the Insight 4G manual, 95% of good vectors is ideal but is not always practicable.

Seeding density, focus, aperture, size of particles and quality of Perspex are also key factors in optimising and validating these statistics. The magnification factor of the raw images is ~ 11.02 μm/pixel and the mean seeding particle size of the silver coated hollow glass spheres (S-HGS) is 10 μm thus technically, a particle should occupy just over a pixel. The size distribution of S-HGS by Dantec Dantec Dynamics (2019c) ranges from 2 – 20 μm, thus a 20 μm particle will take up ~ 2 pixels which is considered acceptable. However, the number of occupied pixels also depends on the camera focus and intensity of reflection (which also depends on the motion of the particle in or out of plane when the image was taken) e.g. a particle can easily occupy over 2 pixels. This becomes increasingly problematic as the interrogation window reduces in size as the algorithm is more prone to generate false vectors especially if a particle occupies almost the whole of the interrogation window e.g. false correlations will be made. Furthermore, details of the captured image of the mixing head including the stator walls and imperfections e.g. scratches are also correlated and may lead to artefacts. It was unexpected that water has lower % of good vectors in comparison to SB e.g. ~ 87% vs ~ 97% after re-processing. As the locations of the interpolated vectors more or less stay the same e.g. by the inner wall of the secondary stator and within the jets, the discrepancy may be attributed to the difference in refractive indices, in addition to the identified sources of errors above.

The time interval set, Δt between frames A and B for all fluids were the same for runs with the same rotor speed set as it was calculated using Equation 3.1.

Table 6.4: Vector statistics for velocity fields that underwent re-processing to optimise the number of good vectors and minimise artefacts. The processing conditions used were: N = 60.0 rps and M_P = 0.347 kg s^{-1}

	Average number of total vectors (-)		**Average percentage of good vectors (%)**		**Average percentage of interpolated vectors (%)**	
Fluid	**Before**	**After**	**Before**	**After**	**Before**	**After**
SB	12,480	3,022	92.59	96.95	7.41	3.05
WATER	12,565	3,006	83.69	86.91	16.31	13.09

SHAMPOO B (SB1)	BEFORE	AFTER
Velocity Distribution	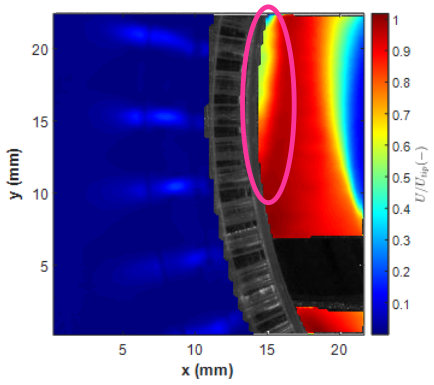	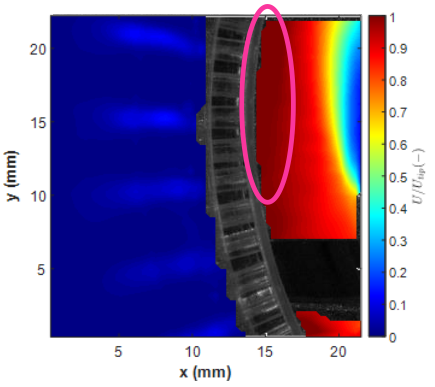
ε Distribution	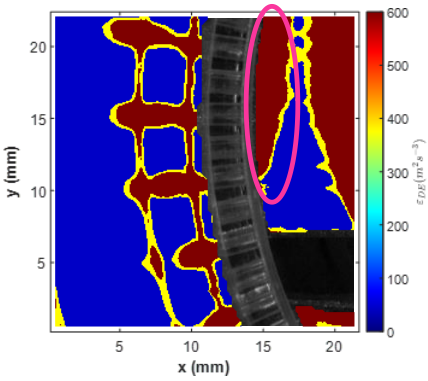	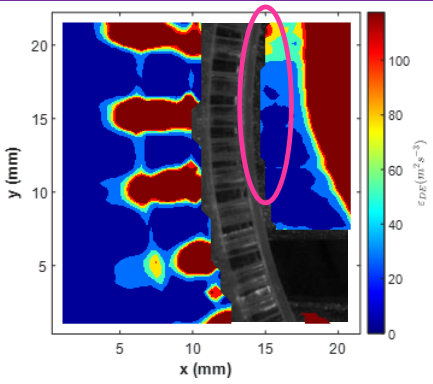
% Interpolated Vectors Distribution	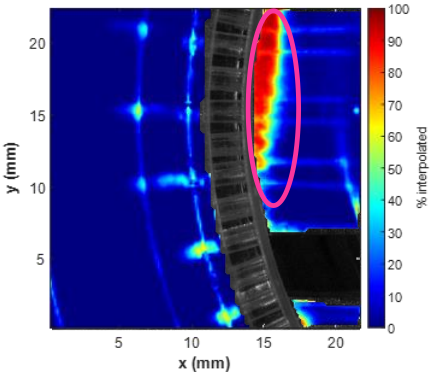	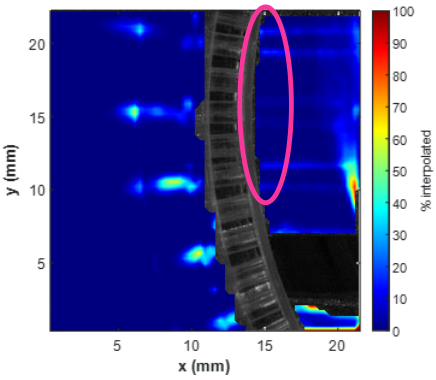
Vector Distribution	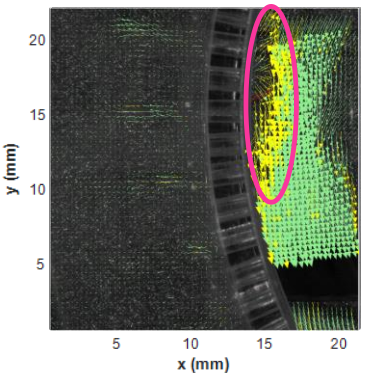	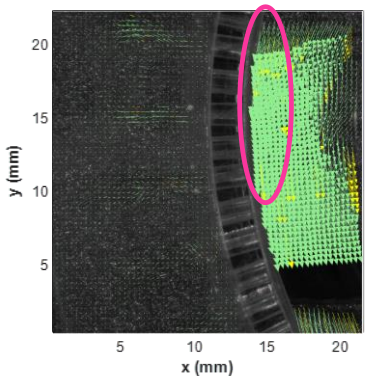

Figure 6.2: Field plots before and after optimising PIV processing of data for shampoo B. Example shown is for the VFO condition when N = 60.0 rps and M_P = 0.347 kg s^{-1}. For the 'BEFORE' vector distribution, only half of the vectors are displayed

WATER	BEFORE	AFTER
Velocity Distribution	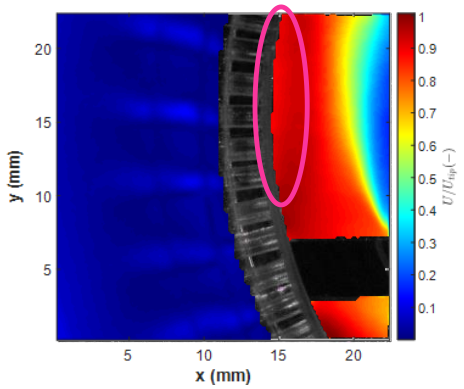	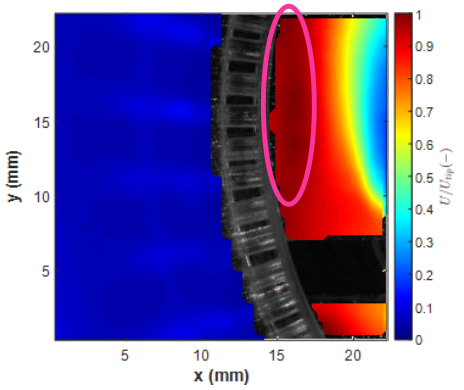
ε Distribution	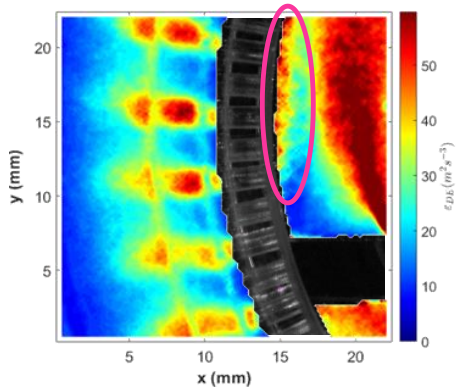	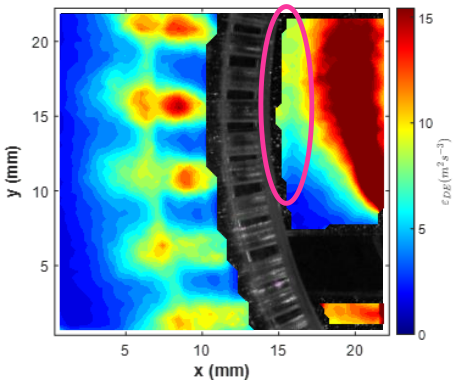
% Interpolated Vectors Distribution	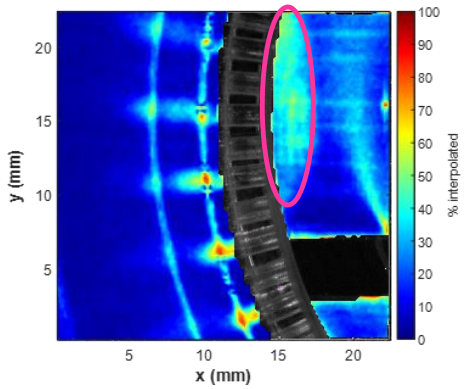	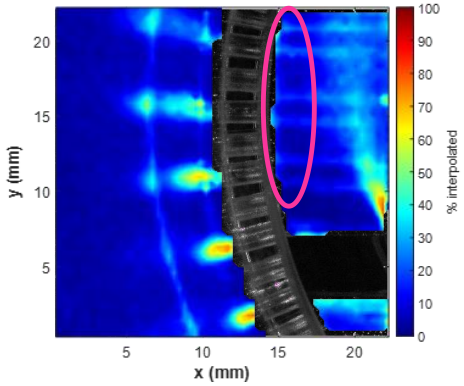
Vector Distribution	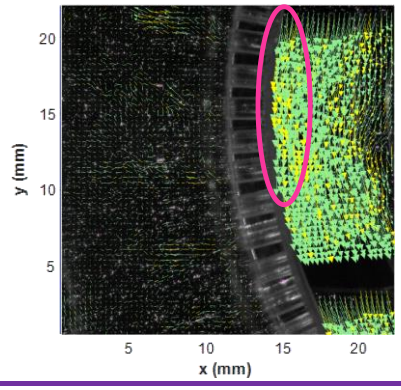	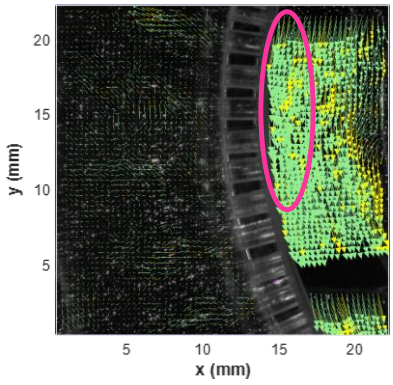

Figure 6.3: Field plots before and after optimising PIV processing of data for water. Example shown is for the VFO condition when N = 60.0 rps and M_P = 0.347 kg s^{-1}. For the 'BEFORE' vector distribution, only half of the vectors are displayed

The succeeding sections focus on the comparison of mean flow fields, kinetic energy and at VFO and VPC conditions when N = 60.0 rps and M_P = 0.347 kg s^{-1}, which for water and glycerol, the flow is fully turbulent, at least within the high shear region (rotor swept volume).

6.4 Mean Flow Fields

It is evident from Figure 6.4 that in the high shear region, there are no discernible differences across the flow fields of water and glycerol e.g. they are self-similar, suggesting that the flow within this region is fully turbulent. On the other hand, there are significant differences in the bulk jet region. For water, there are asymmetrical recirculating flow patterns that rotate in opposite directions on either sides of the jets (blue arrows) as observed by Espinoza et al. (2018). The smaller vortex seems to feed the preceding jet which is then opposed by the larger vortex on that jet. The remaining flow from a jet is then directed into the bulk.

For glycerol, there are no fully developed recirculation patterns, rather, some of the flow from a jet feeds the preceding jet (black arrows), similar to water while the rest of the flow rejoins the bulk (yellow arrows). The reason for this could be attributed to the local flow regimes in the bulk region which is dependent on fluid rheology. For instance with water, the viscosity is much lower than that of glycerol (~ 3x smaller, see Table 6.3) thus, higher Reynolds numbers are reached around the stator holes (Table 6.5) which results in larger and stronger vortices. Although turbulent regime is not reached for all fluids at the stator hole, e.g. Re_{exit} is less than ~ 2,000, above which, the jet is considered to be turbulent (Lee and Chu, 2003), since water has the lowest viscosity, any manifestation of flow instabilities due to turbulence would be expected with it first. This is evident around the tips and edges of the jets in the turbulent kinetic energy dissipation plots (Figure 6.15) where there seems to be a shedding (dissipative) effect, which is least obvious in SA and SB (Figure 6.16). This makes sense as for free turbulent

jets, there exists a 'shear layer' (Figure 6.5) where vortices can form due to the presence of large velocity gradients between the relatively quiescent bulk and the jet (Abdel-Rahman, 2010). For glycerol, higher viscosity delays the onset of turbulence (lower Reynolds numbers) and hence, there are no recirculation patterns observed. As for the effect of partially closing the valves (VPC conditions), the same flow structures are sustained but the amount of fluid rotating tangentially in the bulk increases (yellow double headed arrows), which results in a confinement effect on the jets (orange double headed arrows). This effect is more noticeable with glycerol. These will become much clearer when mean and root mean square profiles of the velocity components *U* (radial component) and *V* (tangential component) at constant *x*- and *y*- values are examined in regions of interest (ROIs A (bulk jet region) and B (high shear region)) (Figure 6.7).

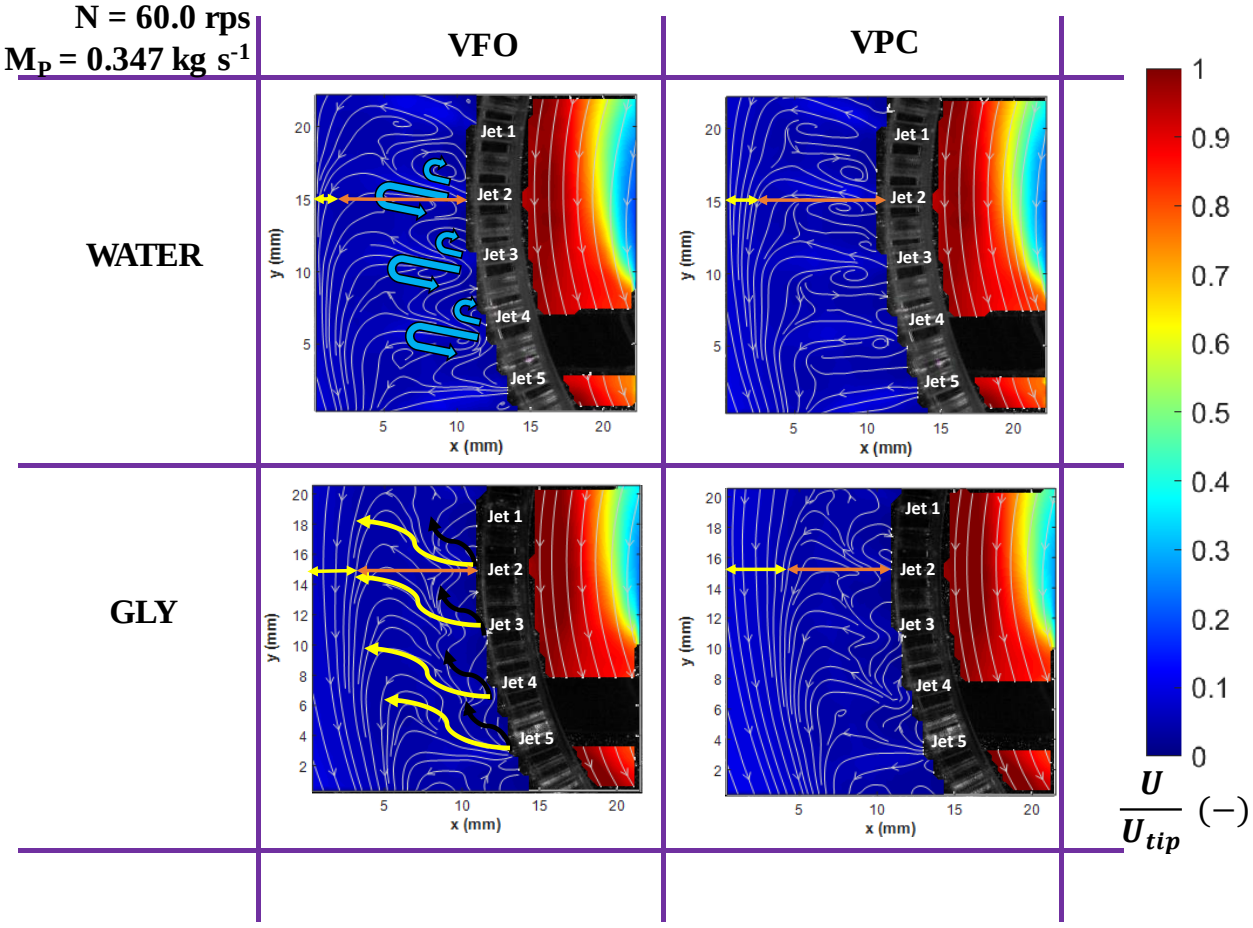

Figure 6.4: Mean velocity field plots and accompanying streamlines at VFO and VPC conditions for water and glycerol when N = 60.0 rps and M_P = 0.347 kg s^{-1}

Table 6.5: Hole velocity and corresponding Reynolds numbers at the hole exit for each fluid at N = 60.0 rps; M_P = 0.347 kg s^{-1}. If $M_T = M_P$, U_{hole} = 0.60 m s^{-1}

Fluid (-)	**M_T (kg s^{-1})**	**U_{hole} (m s^{-1})**	**$Re_{hole} = \frac{\rho U_{hole} D_{hole}}{\mu_\infty}$ (-)**	**Regime (-)**	**Laminar length (m)**
WATER	0.410	0.708	1130	Transitional	0.001
GLY	0.407	0.702	369	Transitional	0.004
SA	0.391	0.675	93	Laminar	0.017
SB1	0.386	0.670	18	Laminar	0.089
SB2	0.521	0.900	24	Laminar	0.067
SB3	0.672	1.161	31	Laminar	0.052

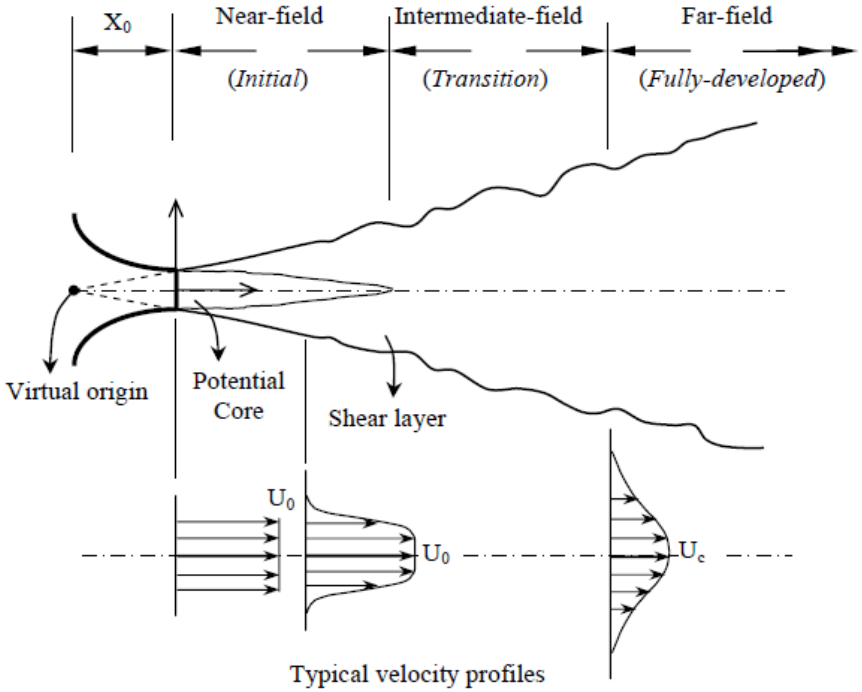

Figure 6.5: Schematic of a free turbulent jet (Abdel-Rahman, 2010)

Figure 6.6 shows the mean velocity fields for shampoos SA and SB. SA, which is in the turbulent regime, shares the same field characteristics as glycerol (Figure 6.4) e.g. there are no fully developed recirculation patterns and some of the flow from a jet feeds the preceding jet (black arrows) while the rest rejoins the bulk (yellow arrows). Partially closing the valve has the effect of confining the flow from the stator holes due to an increased tangential bulk

flow. One noticeable difference, however, is that the streamlines of SA in the bulk jet region are more uniform and orderly, which could be due to the drag reducing effect of the surfactants e.g. attributed to the interaction between wormlike micellar (WLM) network structures and turbulent structures (eddies).

Micelles are formed above the critical micelle concentration (c. m. c.) of a surfactant and are typically spherical and between 2 to 20 nm in size depending on its composition (Joseph et al., 2017). This is much smaller than the smallest achievable scale of turbulence with water, λ_k ~ 8.3 μm (using $\varepsilon_{avg} = P/\rho V$) at the given processing conditions: N = 60.0 rps; M_P = 0.347 kg s^{-1}, and so may be initially thought of as having no influence on the flow patterns. However, it is the transient entangle- and disentanglement of elongated, semi-flexible giant wormlike micelles (formed at much higher surfactant concentrations, with length-to-width ratio of ~ 6 – 10 and are usually ~ 5 nm in diameter (Wei et al., 2010)), that is responsible for the viscoelastic behaviour of surfactant solutions. WLMs either align or do not align in the flow direction which influences flow behaviour (Parker and Fieber, 2013).

SA and SB formulations in this study are similar to those used by Amin et al. (2015) (~ 14 wt% SLES and ~ 2 wt% CapB) in their investigation of SLES, CapB and salt mixtures. They investigated the effect of ionic strength via addition of NaCl to the molecular structure and corresponding changes in the microstructure and rheology of the SLES and CapB solutions. Thus, it is justifiable to assume that wormlike micelles may form in both SA and SB formulations in this study, more so for SB which has added NaCl, altering its viscosity by electrostatic screening (Parker and Fieber, 2013). The zero-shear viscosity can be increased up to a maximum at a given critical salt concentration beyond which results in a decrease in viscosity, this relationship is normally plotted as a 'salt-curve'. The decrease in viscosity occurs

either by shortening of the micelles or branching of the WLM network microstructures (Parker and Fieber, 2013).

There is also an existing study by Recktenwald et al. (2019) which demonstrated that a model surfactant solution with infinitesimally small elasticity and viscosity close to that of water (descriptive of SA), unexpectedly exhibited long filament lengths and lifetimes during uniaxial extensional deformation experiments e.g. Capillary Breakup Elongational Rheometer (CaBER). This phenomenon is associated with a unique banding instability e.g. formation of Elongation Induced Structures (EIS), which is analogous to Shear Induced Structures (SIS) in classical shear rheometry that manifest at a critical shear rate and is attributed to the shear-thickening behaviour observed in the hysteric regime of a surfactant flow curve. For instance, the homogenous flow between two concentric cylinders in a Couette flow splits into 'shear bands' that move at different shear rates and thus bear varying apparent viscosities and internal structures (Fardin et al., 2010; Recktenwald et al., 2019).

Ideally, evidences that support the existence of WLM e.g. via Nuclear Magnetic Resonance (NMR), Small Angle Neutron Scattering (SANS) and Cryo- Transmission electron microscopy (TEM) should be acquired (Wei et al., 2010). Similarly for proving the existence of EIS and/or SIS, techniques such as measurements of Flow Induced Birefringence (FIB) could be performed (Salipante et al., 2018). Both polymers such as PAA and surfactants are commonly used as drag reducing agents (DRA) e.g. in oil pipelines to reduce turbulence and allow for a higher flow rate at a reduced pumping power. The main difference between the two is that polymers degrade over time whereas micelles self-repair and so are referred to as "living polymers" (Arora et al., 2002; Hadri and Guillou, 2010; Mavros et al., 2011; Parker and Fieber, 2013; Rashed et al., 2016).

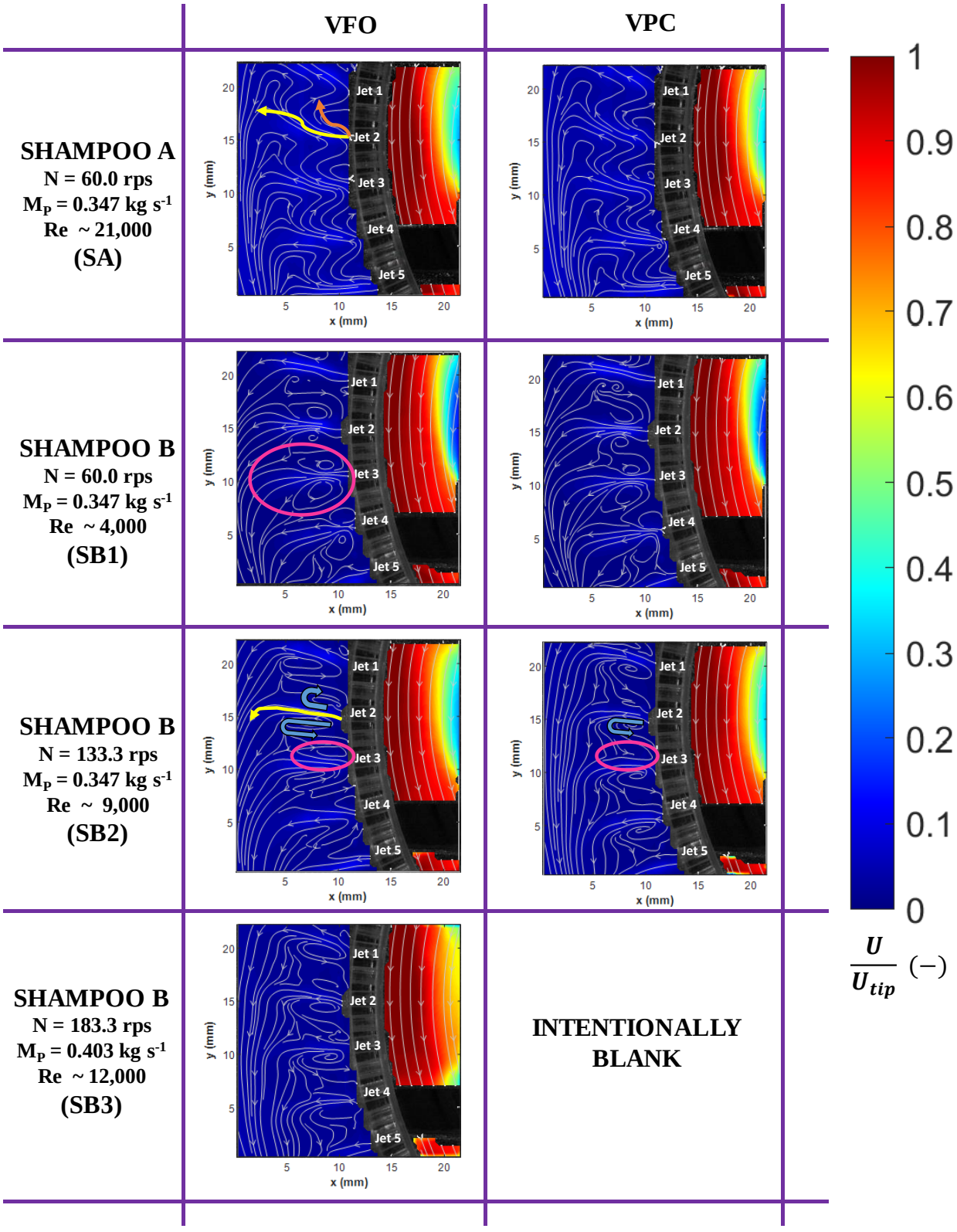

Figure 6.6: Mean velocity field plots and accompanying streamlines at VFO and VPC conditions for shampoos A and B at the indicated rotor speed, *N* and external pump flow rate, M_P

Three flow regimes were investigated for SB: low transitional (SB1) at N = 60.0 rps; M_P = 0.347 kg s^{-1} (M_T = 0.386 kg s^{-1}), high transitional (SB2) at N = 133.3 rps; M_P = 0.347 kg s^{-1} (M_T = 0.521 kg s^{-1}) and turbulent (SB3) at N = 183.3 rps; M_P = 0.403 kg s^{-1} (M_T = 0.672 kg s^{-1}). For SB1in the bulk jet region (jet 2 in Figure 6.6), it is noticeable that there are two counter-rotating recirculation loops on either side of the jet(s) (encircled magenta). This could be due to the strong shear thinning behaviour of SB (Figure 6.1a) e.g. the fast moving shear thinned fluid jets emanating from the holes interact and entrain the relatively quiescent and more viscous (less shear thinned) bulk. As a result of this, vortices (recirculation regions) on either side of the jets are formed e.g. the friction imposed by the surrounding fluid as well as the edge of the stator hole slows down the edges of the jet which curls back away from its centreline. As the distance of the jets from the stator holes increases, they spread out and lose momentum as the entrained bulk fluid slows them down. In addition, this observation could also be possibly due to the viscoelastic behaviour of SB imposed by WLM. However, as the presence of WLM in SA and SB has not been confirmed, this is speculative. The high shear region looks almost similar to that of SA but since the regime is not turbulent for SB1, they are not self-similar. Moreover, there are slower moving fluids in close proximity to the primary stator in comparison to SA. This is later discussed with the plots of the profiles of the velocity components.

For SB2 in the bulk jet region (jet 2 in Figure 6.6), the velocity field resembles that for water in Figure 6.4. This can be attributed to the shear thinning behaviour of shampoo B (Figure 6.1a). In the high shear region, the flow field is similar to that of SA since the flow is high transitional. Partially closing the valve also confines the flow inwards but in comparison to the flow field of water, the strength of the clockwise rotating secondary recirculation loop is greatly diminished (encircled magenta) and is speculated to occur due to the combined effects of the

viscoelastic and shear-thinning nature of SB. The flow field for SB3 within the bulk jet region is similar to that of SB2. In the high shear region, more fluid moves faster especially in close proximity to the primary stator (SB3 in Figure 6.6). Again, this can be attributed to the shear-thinning behaviour of SB e.g. the viscosity decreases further at increased shear rates at higher rotor speeds. There is no data collected for VPC condition to alleviate the risk of overpressurising the mixing head.

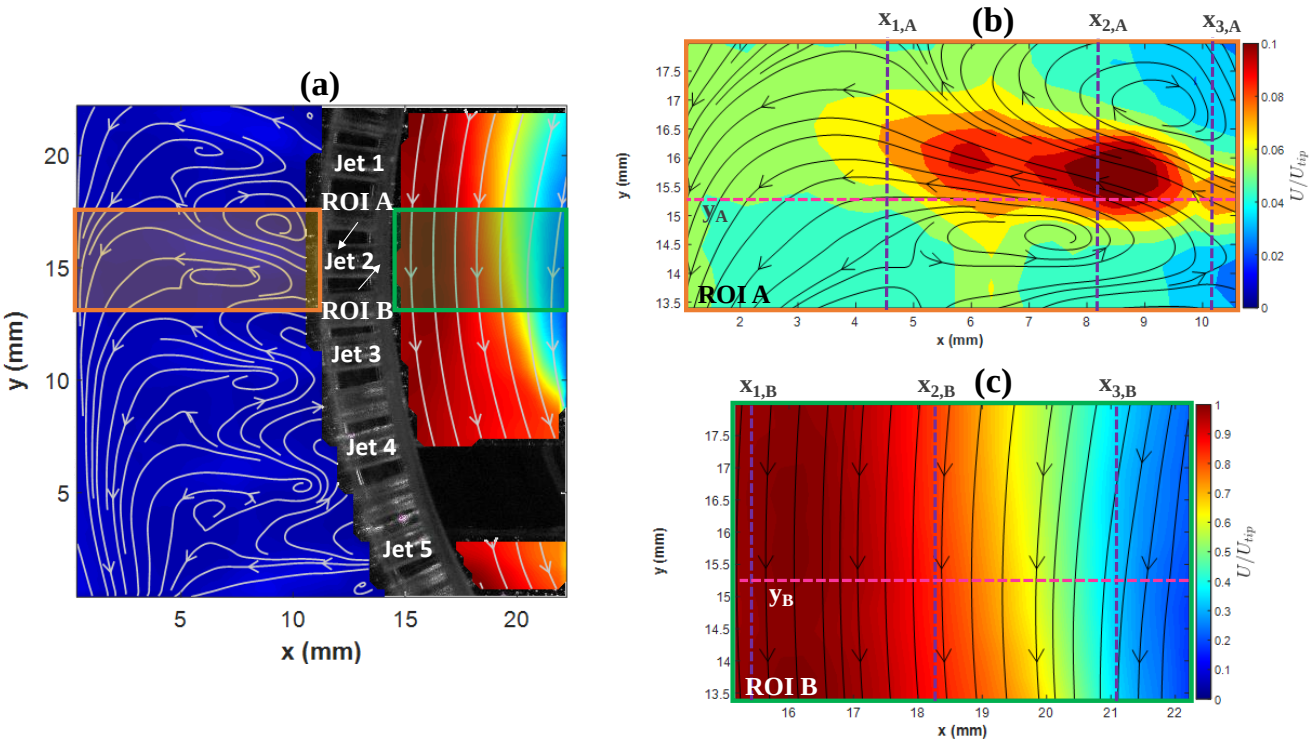

Figure 6.7: (a) Locations of ROIs A and B (b) Indications of where constant *x*- and *y*- lines are in ROI A for investigating *x*- (radial) and *y*- (tangential) velocity profiles (c) Indications of where constant *x*- and *y*- lines are in ROI B for investigating *x*- and *y*-velocity profiles. Example shown is for the VFO condition when N = 60.0 rps and M_P = 0.347 kg s^{-1} for water

Figure 6.7a highlights ROIs A and B at the second jet while Figures 6.7b and 6.7c indicate the constant *x*- and *y*- values at which mean and root mean square (RMS) velocity profiles of the radial (U) and tangential (V) components were evaluated at in ROIs A (Figures 6.8 and 6.9) and B (Figures 6.10 and 6.11) respectively. In ROI A, the three constant *x*-values of interest are: $x_{1,A}$ – near bulk, $x_{2,A}$ – jet core and $x_{3,A}$ – nearest to the stator hole. The constant *y*-value of interest is the centreline of the stator hole (y_A). In ROI B, the three corresponding *x*-

values of interest are: $x_{1,B}$ – inner wall of the secondary stator, $x_{2,B}$ – middle of the gap between the primary and secondary stator and $x_{3,B}$ – close proximity to the primary stator holes. The constant y-value of interest is also the centreline of the stator hole (y_B). It is also noteworthy that the magnitude of the normalised velocities in ROI A is about an order of magnitude lower because the jets move much slower relative to the rotor tip speed.

It is clear from Figure 6.8a that the fastest and slowest radial velocities in ROI A across all fluids can be found in the centreline ($y = y_A = 15.14$ mm) of the jet cores ($x_{2,A}$) and near the bulk ($x_{3,A}$) respectively (+ve and –ve denote direction). There are differences in radial velocity profiles for water, glycerol, SA and SB1 despite very similar measured total mass flow rates and velocities e.g. $U_{hole} = 0.67 – 0.71$ m s^{-1} (Table 6.5) at the given VFO conditions when $N =$ 60.0 rps and $M_P = 0.347$ kg s^{-1}, particularly in $x_{2,A}$ and $x_{3,A}$. The same applies for VPC conditions where $M_T = M_P$. With respect to continuity, as the fluids are incompressible and the total mass flow rates and densities do not differ significantly at the given process conditions (Table 6.3), this observation can be attributed to the jet-to-jet variations in velocity profiles. For instance, the velocity profile may differ for each respective jet but the overall integrated mass flow rate from the jet profiles should equal the total inputted mass flow rate, as demonstrated in Chapter 4.

It is also evident that the effect of partially closing the valve (closed symbols) lowers the magnitude of radial velocities (although not significantly), particularly in the jet core, confirming the findings of Espinoza et al. (2018) that for VPC conditions, the overall flow in the mixing head becomes more tangential. Figure 6.8b shows that tangential velocities in ROI A are of the same magnitude as the radial velocities but are relatively weaker e.g. closer to zero. It can also be seen that recirculation is prominent near the stator holes ($x_{3,A}$) for all fluids, where a positive kink indicates the upward fluid motion (opposite to the direction of rotor rotation).

Finally, it is clear from Figure 6.8c that across a constant *y*-value (y_A = 15.14 mm), the fastest radial velocities are found closest to the stator hole (*x* ~ 10 mm) and slowest closer to the bulk (*x* ~ 0.5 mm). The contrary is true for the tangential velocities which is as expected as the bulk moves tangentially in the direction of rotor rotation. It is also evident that as the rotor speed is increased for SB e.g. SB2 and SB3, it shear thins and behaves more like the water jets (hence similar profiles).

In terms of RMS velocities, it is shown through Figure 6.9 that irrespective of the *x*-positions at constant *y* (Figure 6.9a and 6.9b) and *y*-position at constant *x* (Figure 6.9c), the highest radial and tangential RMS velocities are associated with the profile for water (black symbols), glycerol (blue symbols) and SA (red symbols). This was expected as they are less viscous than SB and thus reach a higher state of turbulence (with prominent fluctuating velocities at higher Reynolds numbers) at a faster rate when U_{tip} is constant. For the case of glycerol, SA and SB, the Reynolds numbers at the hole exit are much lower e.g. $Re_{exit} < 2000$ (Table 6.5) which means that the turbulence in the jets is weaker.

The 'laminar length', L_{jet}, of the jets, is defined as the length beyond which the jet is considered turbulent e.g. when it begins to entrain and mix fluid (Abdel-Rahman, 2010; Kuang et al., 2015), a similar concept to entrance length in pipes due to the boundary layer. It was estimated (summarised in Table 6.5) using an empirical relationship proposed by McKenzie and Wall (1968) in Kumar et al. (1984): $\frac{L_{jet}}{d_{hole}} = \frac{1000}{Re_{exit}}$. This equation is valid for $5 < Re_{exit} < 400$ which correspond to laminar and semi-turbulent regimes and covers the Re_{exit} calculated for all fluids except for water. This approximation is justified in a sense that L_{jet} is usually determined/quantified through the images captured from flow visualisation experiments such as that by Kuang et al. (2015) and not by using an equation, which is usually empirical. In

addition, the trend of calculated values agree with research findings such as that of Kwon and Seo (2005), where the laminar length was found to decrease with increasing Re_{exit}. For instance, the jets become turbulent closer to the stator hole exit with negligible L_{jet} at $Re_{exit} > 2000$. These imply that fully developed turbulent flow is not attained outside the high shear region e.g. beyond the secondary stator, particularly in the flow out of the stator holes where viscous effects appear to be more prominent. In fact, for $Re_{exit} < 30$, the jet is considered fully laminar e.g. non-eddying and just dissipates completely into the surrounding fluid (Abdel-Rahman, 2010). It is also noteworthy that the viscosities used to calculate Re_{exit} in Table 6.5 are the infinite viscosities,μ_∞,which may not be representative of the real viscosities in the jets especially for SB which is shear thinning. The role of viscosity for SB is an essential consideration and is covered in §6.6.1. Moreover, this is a simplification of a more complex flow as the secondary stator has multiple holes which means that multiple interacting jets are generated that penetrate a moving (though much slower in comparison to U_{tip}) bulk fluid.

For ROI B, the radial and tangential velocity profiles for water, glycerol and SA overlap (Figure 6.10). Similar observations can be made for the RMS velocities (Figure 6.11), where the velocity profiles of all fluids nearly overlap as well. This implies that the flow within ROI B is approximately fully turbulent across all fluids (which makes sense as Re >> 10,000 as shown in Table 6.3) and thus are self-similar and scale with the rotor tip speed. Figure 6.10a shows that radial velocities are almost negligible ($U/U_{tip} \sim 0$) and that tangential velocities dominate in ROI B (Figure 6.10b). It is greatest near the inner wall of the secondary stator ($x_{1,B}$) ($V/U_{tip} \sim -1$) and slows down as the primary stator is approached ($x_{3,B}$) ($V/U_{tip} \sim -0.5$). This is as expected as linear velocity is greatest at the rotor blade tip and slowest nearest to its axis of rotation and in addition, jets from the primary stator interact with the predominantly tangential flow, which, in effect, cancel each other out. It is also interesting to see that, although

not to a great extent, shampoo formulations move slightly faster in ROI B. This is more significant for SB3 at ($x_{3,B}$) where more of the fluids in ROI B move closer to the rotor tip speed and is speculated to be due to its shear-thinning behaviour. At constant $y = y_B = 15.14$ mm, radial velocities are practically zero (Figure 6.10c) as the flow is, as established, predominantly tangential (greatest by the wall, $x \sim 14.5$ mm ($V/U_{tip} \sim -1$), slowest nearest to the primary stator, $x \sim 22.0$ mm ($V/U_{tip} \sim -0.1$)).

Regarding the RMS velocities in ROI B for the shampoo formulations (Figure 6.11), similar comments made with ROI A in terms of viscosity and Reynolds number apply. One interesting observation is that as the primary stator is approached e.g. from $x_{1,B}$ to $x_{3,B}$, both U_{rms} and V_{rms} profiles increasingly overlap and their magnitudes also increase. This implies that higher velocity fluctuations and thus greater degree of turbulence is found where jets interact with the flow within the primary and secondary stator gap e.g. where the most complex and chaotic flow patterns are.

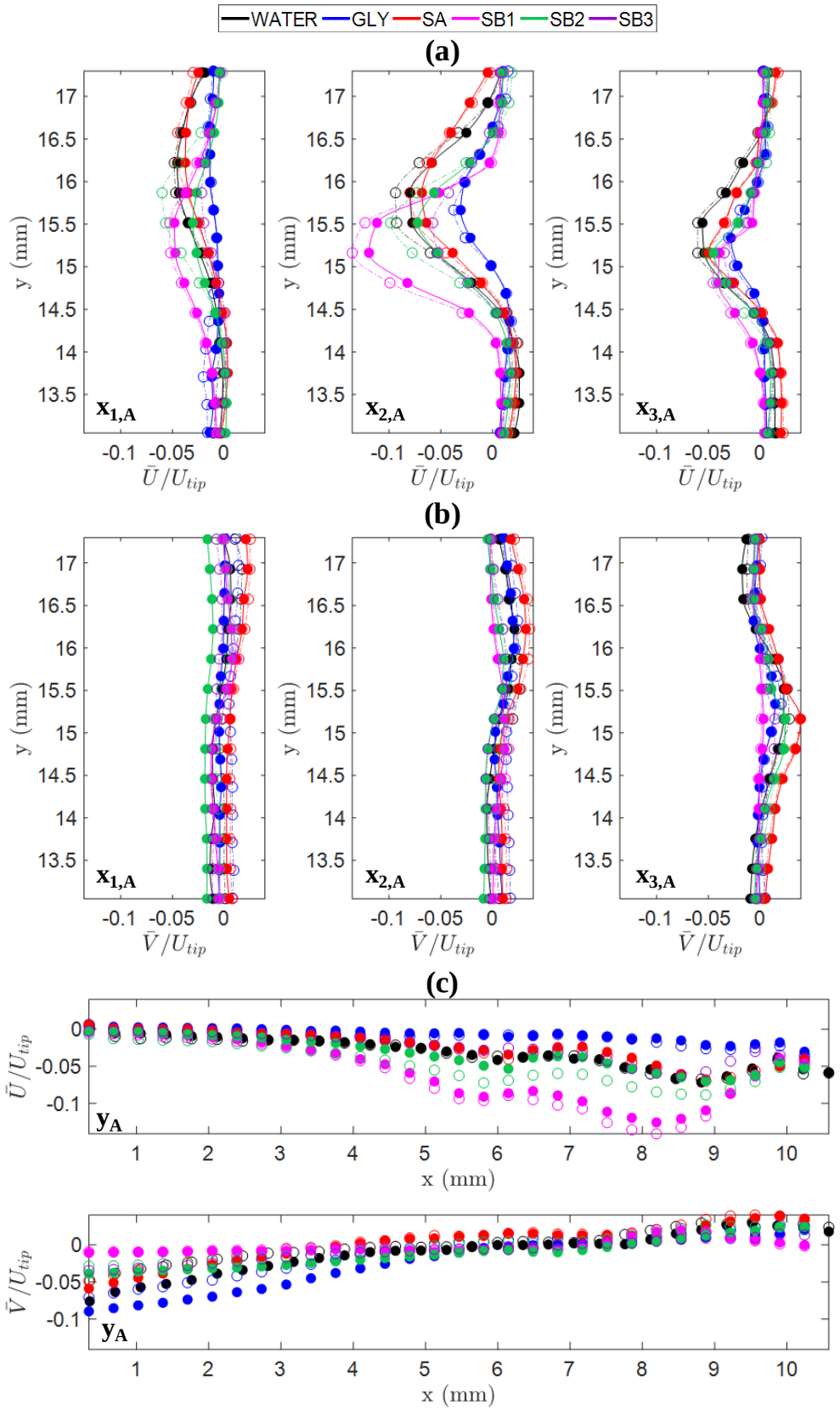

Figure 6.8: Mean velocity profiles normalised with rotor tip speed in ROI A for water, glycerol shampoos A and B (SB1, SB2 and SB3 indicate different rotor speeds and external pump flow rates): (a) *x*-velocity profiles at $x_{1,A}$ (left), $x_{2,A}$ (centre) and $x_{3,A}$ (right) (b) *y*-velocity profiles at $x_{1,A}$ (left), $x_{2,A}$ (centre) and $x_{3,A}$ (right) (c) *x*- (top) and *y*- (bottom) velocity profiles at y_A. Open and closed symbols as well as dash-dot (-.) and solid (-) (eye) guidelines denote VFO and VPC conditions

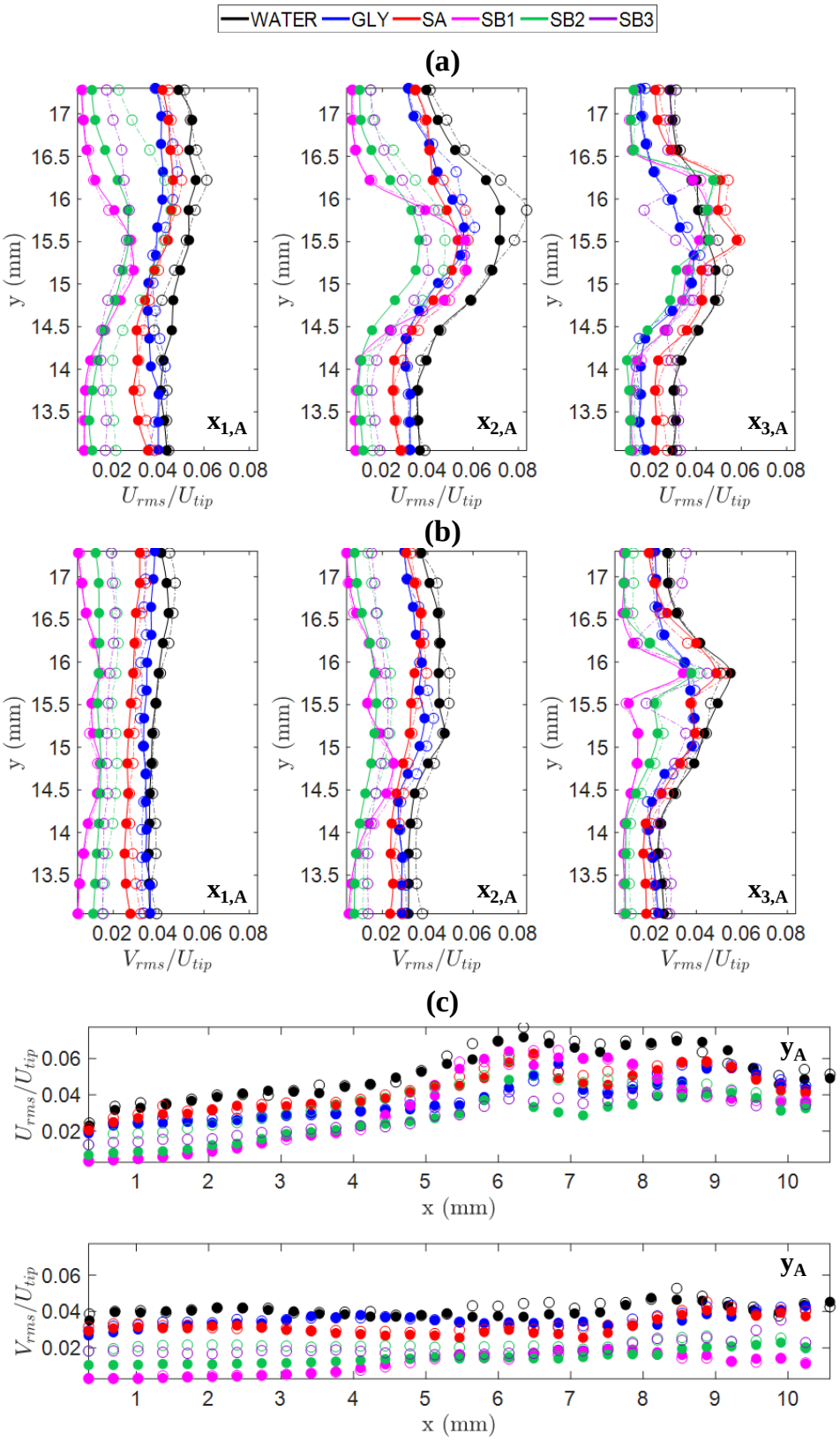

Figure 6.9: Root mean square velocity (RMS) profiles normalised with rotor tip speed in ROI A for water, glycerol, shampoos A and B (SB1, SB2 and SB3 indicate different rotor speeds and external pump flow rates): (a) *x*-velocity profiles at $x_{1,A}$ (left), $x_{2,A}$ (centre) and $x_{3,A}$ (right) (b) *y*-velocity profiles at $x_{1,A}$ (left), $x_{2,A}$ (centre) and $x_{3,A}$ (right) (c) *x*- (top) and *y*- (bottom) velocity profiles at y_A. Open and closed symbols as well as dash-dot (-.) and solid (-) (eye) guidelines denote VFO and VPC conditions

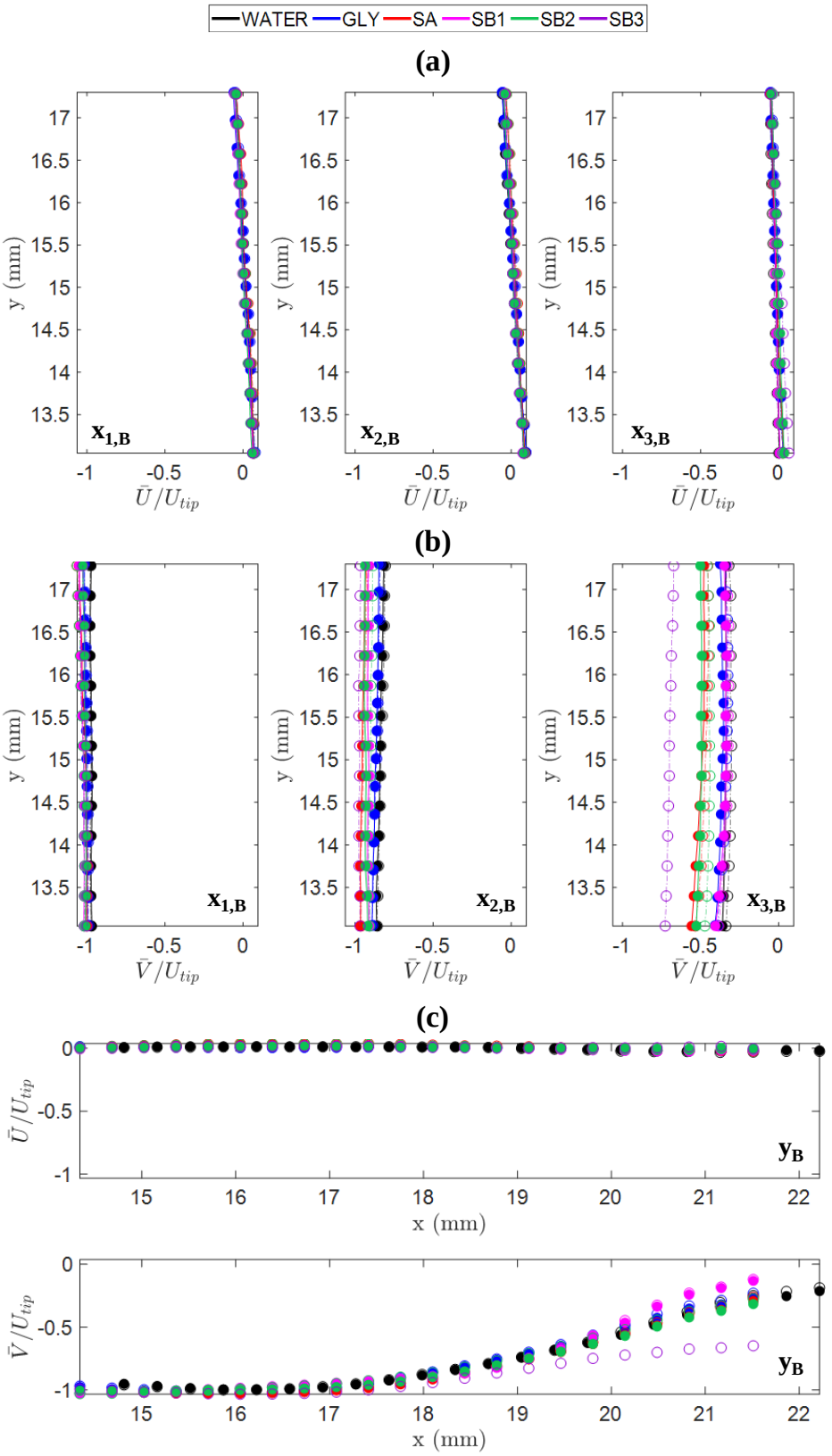

Figure 6.10: Mean velocity profiles normalised with rotor tip speed in ROI B for water, glycerol, shampoos A and B (SB1, SB2 and SB3 indicate different rotor speeds and external pump flow rates): (a) *x*-velocity profiles at $x_{1,B}$ (left), $x_{2,B}$ (centre) and $x_{3,B}$ (right) (b) *y*-velocity profiles at $x_{1,B}$ (left), $x_{2,B}$ (centre) and $x_{3,B}$ (right) (c) *x*- (top) and *y*- (bottom) velocity profiles at y_B. Open and closed symbols as well as dash-dot (-.) and solid (-) (eye) guidelines denote VFO and VPC conditions

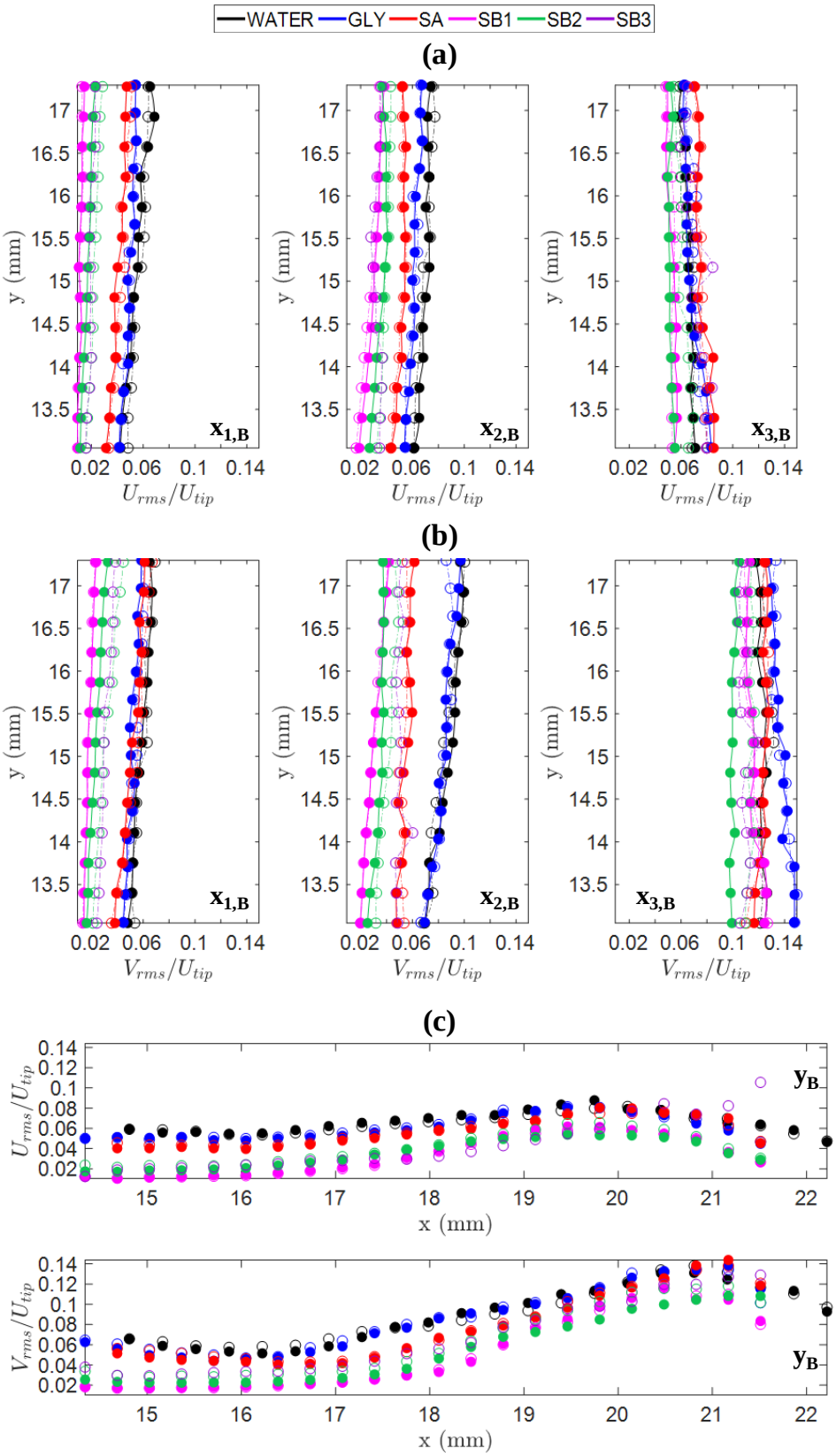

Figure 6.11: Root mean square velocity (RMS) profiles normalised with rotor tip speed in ROI B for water, glycerol, shampoos A and B (SB1, SB2 and SB3 indicate different rotor speeds and external pump flow rates): (a) *x*-velocity profiles at $x_{1,B}$ (left), $x_{2,B}$ (centre) and $x_{3,B}$ (right) (b) *y*-velocity profiles at $x_{1,B}$ (left), $x_{2,B}$ (centre) and $x_{3,B}$ (right) (c) *x*- (top) and *y*- (bottom) velocity profiles at y_B. Open and closed symbols as well as dash-dot (-.) and solid (-) (eye) guidelines denote VFO and VPC conditions

6.5 Kinetic Energy

Since droplet breakup is most likely to occur in the rotor swept volume, where the Reynolds numbers are relatively high (turbulent flow), the focus of the following sections will be on the turbulent kinetic energy (*k* or TKE) and its dissipation. However, it is also important to consider kinetic energy of the mean flow (*K* or MKE) (Hinze, 1975; Roberts and Webster, 2002), which supplies the energy that sustains turbulent fluctuations at the largest turbulent scales. It can be calculated in a similar manner to TKE in Chapter 5, where the mean of the velocity components is used instead of the mean of the fluctuating components:

$$K = \frac{3}{4}(\bar{U}^2 + \bar{V}^2) \tag{6.5}$$

The turbulent kinetic energy (*k*) is generated from the mechanical energy inputted into the fluid and manifests itself initially through the large turbulent length scales. The large eddies then transfer this energy to smaller eddies until it is eventually dissipated through the action of viscous stress at the smallest scales of turbulence (Kolmogorov length scale). This is known as the Richardson energy cascade (George, 2013; Mathieu and Scott, 2000; Tennekes and Lumley, 1972).

Through observation of Figures 6.12 to 6.14, it can be seen that for all fluids, the values of *K* (Figures 6.12a and 6.13) are generally higher than that of *k* (Figures 6.12b and 6.14), especially within the rotor swept volume. This is expected as the magnitude of mean velocities are higher than those of the fluctuating velocities. Furthermore, the rotor swept volume is also where the mechanical energy from the rotor is converted to kinetic energy and hence why *K* and *k* are greatest there.

As expected given the definition of *K*, the distribution resembles the mean velocity plots of the fluids (Figures 6.4 and 6.6). There are no discernible differences between VFO and VPC

conditions. The highest values are found in the high shear region (rotor swept volume) particularly near the inner wall of the secondary stator. This is because the linear velocity is greatest near the rotor blade tip and slowest nearest to its axis of rotation. In addition, the jets from the primary stator also interact with the fluid within the rotor swept volume, hence the presence of slower moving fluids within the vicinity of the primary stator. The lowest values are found in the bulk, which is as expected as they move much slower than the fluids within the high shear region. In contrast, the highest values of k for all fluids are found where high velocity gradients are present e.g. jets within the bulk region and within the vicinity of the jets from the primary stator which interact with the flow in the gap between the primary and secondary stators.

It is clear from Figures 6.12b and 6.14 that k is higher in water compared to glycerol and SA in the jet regions in particular; this is expected due to the local flow conditions relevant to the jets discussed above. In the rotor stator swept regions, the magnitudes are similar, since both flow regimes reflect fully developed turbulence (Table 6.3). For SB, the degree of turbulence in the jets and the rotor swept volume also increases with rotor speed e.g. by comparing SB1 (N = 60.0 rps) with SB2 (N = 133.3 rps). This could be attributed to the shear thinning behaviour of SB. Another interesting observation is that when the rotor speed is increased further e.g. SB3 (N = 183.3 rps), turbulence within the jets diminish which implies that less jetting occurs as more of the bulk fluid move tangentially. This is supported by the SB2 VPC condition as partially closing the valve seem to increase the overall tangential motion within the mixing head.

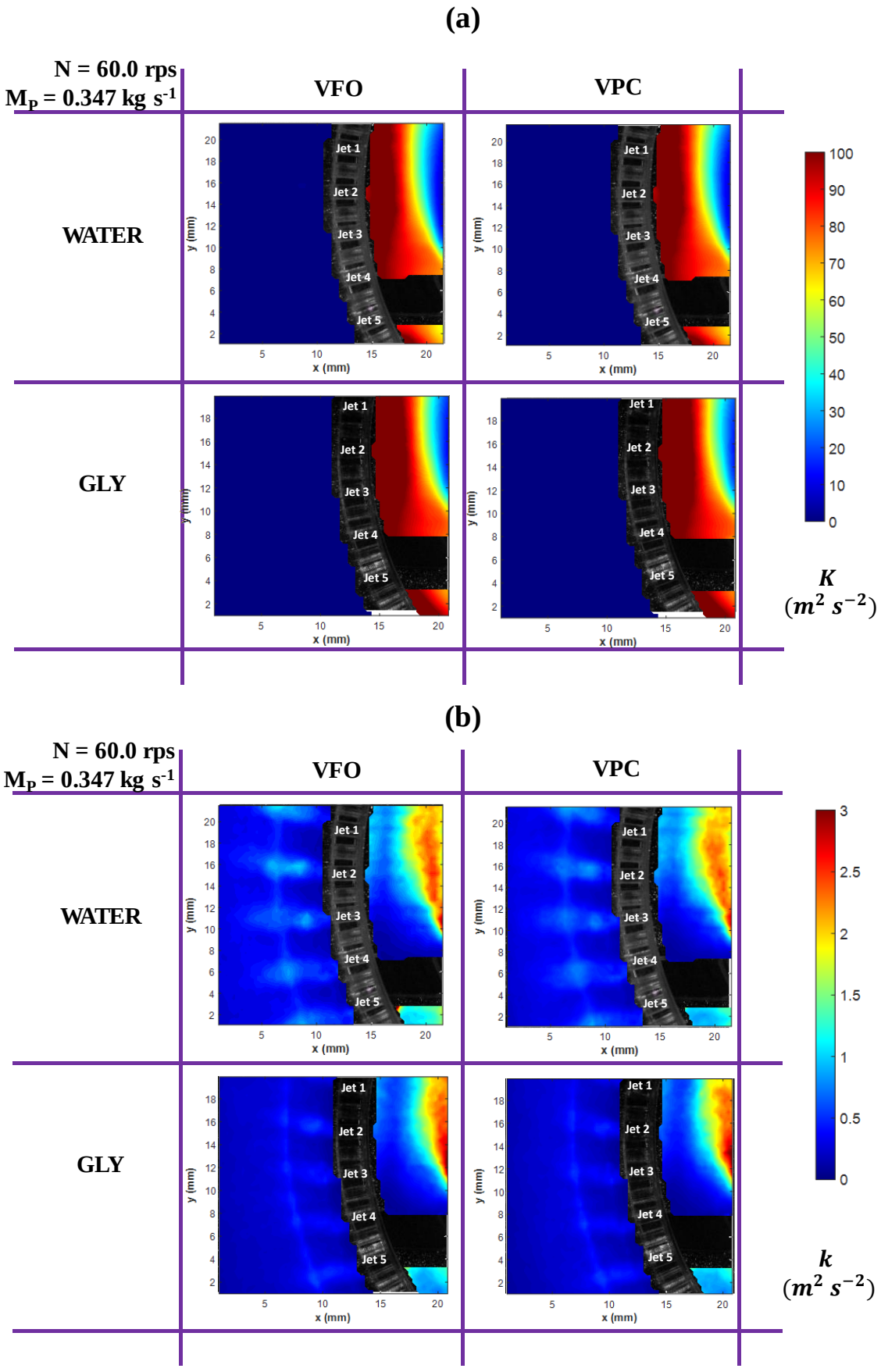

Figure 6.12: (a) Mean flow kinetic energy field plots and (b) Turbulent kinetic energy field plots at VFO and VPC conditions for water and glycerol when N = 60.0 rps and M_P = 0.347 kg s^{-1}

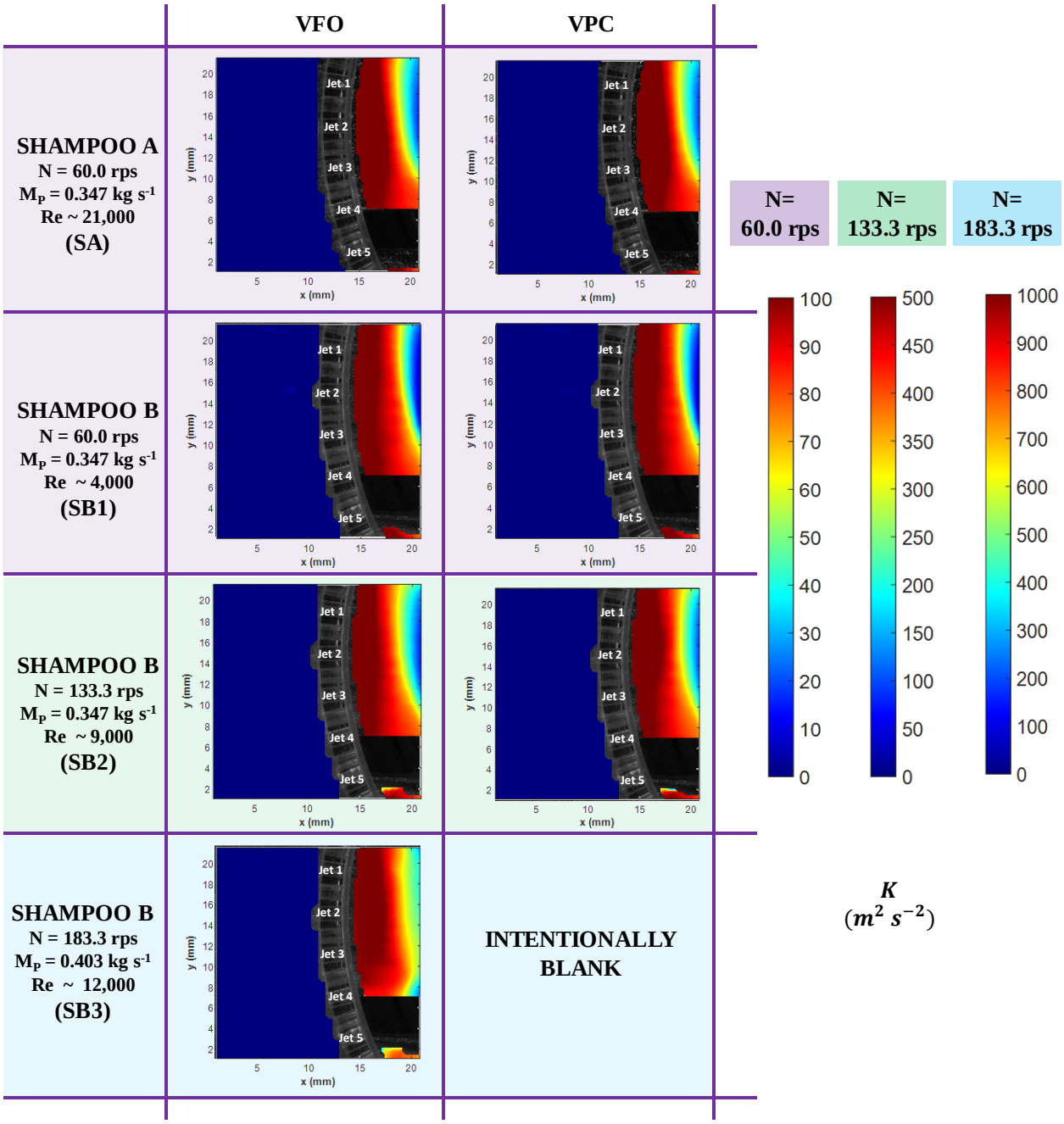

Figure 6.13: Mean flow kinetic energy field plots at VFO and VPC conditions for shampoos A and B at the indicated rotor speed, N and external pump flow rate, M_P

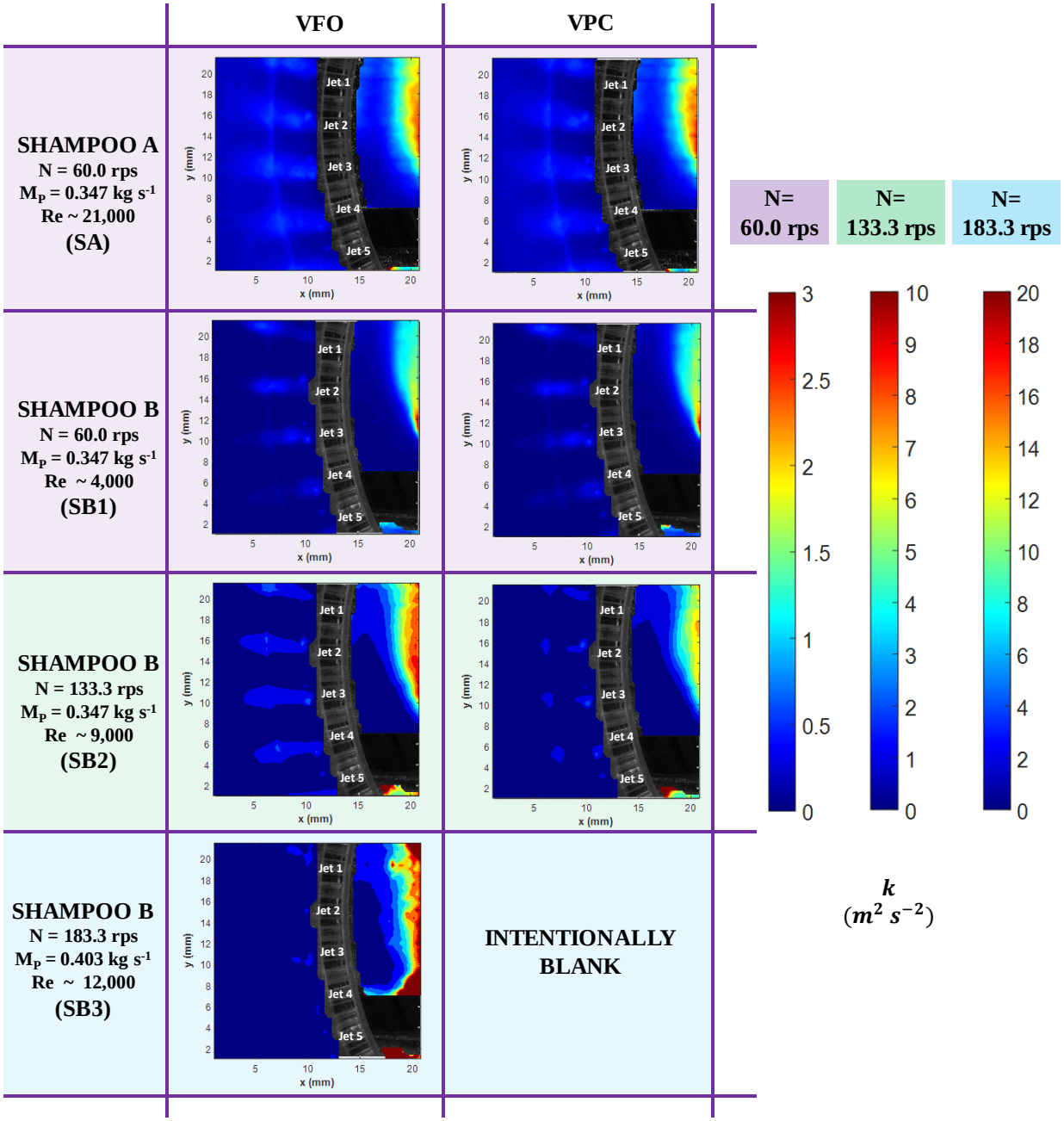

Figure 6.14: Turbulent kinetic energy field plots at VFO and VPC conditions for shampoos A and B at the indicated rotor speed, *N* and external pump flow rate, M_P

6.6 Local Specific Energy Dissipation Rate, ε

In this section, the value of kinematic viscosity for SB, υ, for the calculation of ε, was kept constant: $\upsilon = 5.97 \times 10^{-5}$ m^2 s^{-1} and was calculated using $\mu_\infty = 0.0638$ Pa s and $\rho = 1068$ kg m^{-3} from Table 6.3. The effect of using approximated apparent viscosities using Equation 6.3, is explored in §6.6.1.

It is important to note that the fluctuating velocity gradients, of which viscous dissipation of ε depends on, are associated with the small dissipative scales of the flow, whose size decreases with the fluid viscosity (Mathieu and Scott, 2000; Roberts and Webster, 2002; Tennekes and Lumley, 1972). This highlights the importance of considering the PIV resolution when estimating ε especially with the direct evaluation method which assumes that instantaneous and local gradients of fluctuating velocity can be measured at the smallest scales of turbulence (Gabelle et al., 2013), which, of course, is not true.

In the bulk jet region for both VFO and VPC conditions (Figure 6.15), the area of highest ε is within the core of the jets for both water and glycerol. However, the magnitude is greater for glycerol and the jet patterns look more confined e.g. they are shorter and more spread out. This is possibly influenced by the limited resolution of PIV. For instance, if the average Kolmogorov length (λ_k) was estimated for all fluids in a similar manner in Chapter 5 (Table 6.6), it is clear that λ_k is larger for glycerol as its viscosity is higher. It also follows that the corresponding Reynolds number is lower (Table 6.5). Thus, with respect to the effective grid resolution (Δ/λ_k), more of the smaller scales are resolved for glycerol in both bulk and high shear regions. Moreover, as the fluctuating velocity gradients are multiplied by υ to calculate ε, since $\upsilon_{GLY} > \upsilon_{WATER}$, the overall magnitude will be greater for glycerol. This analogy also applies for SA and SB. An alternative interpretation is that the higher fluid viscosity in the bulk

presents a stationary imaginary wall (see Figure 6.15 for glycerol) which confines the jets closer to the stator holes e.g. it is harder for the jet to penetrate a more viscous bulk fluid and hence greater energy is dissipated. This highlights the importance of viscous effects on the smallest scales of turbulence and thus on ε.

Table 6.6: Kolmogorov lengths (λ_k) and effective grid resolution (Δ/λ_k) at the given process conditions where $\Delta = 64$ pixels $\times$ 11.02 µm/pixel $= 705.28$ µm

Fluid (-)	**N (rps)**	**M_P (kg s^{-1})**	**M_T(kg s^{-1})**		**λ_k (µm)**		**Δ/λ_k (-)**	
			VFO	**VPC**	**VFO**	**VPC**	**VFO**	**VPC**
WATER	60.0	0.347	0.410	0.347	8.19	8.37	86.17	84.26
GLY			0.407		19.11	19.50	36.91	36.17
SA			0.391		52.33	53.15	13.48	13.27
SB1			0.386		178.83	181.29	3.94	3.89
SB2	133.3		0.521		104.13	107.96	6.77	6.53
SB3	183.3	0.403	0.672	0.403	82.52	-	8.55	-

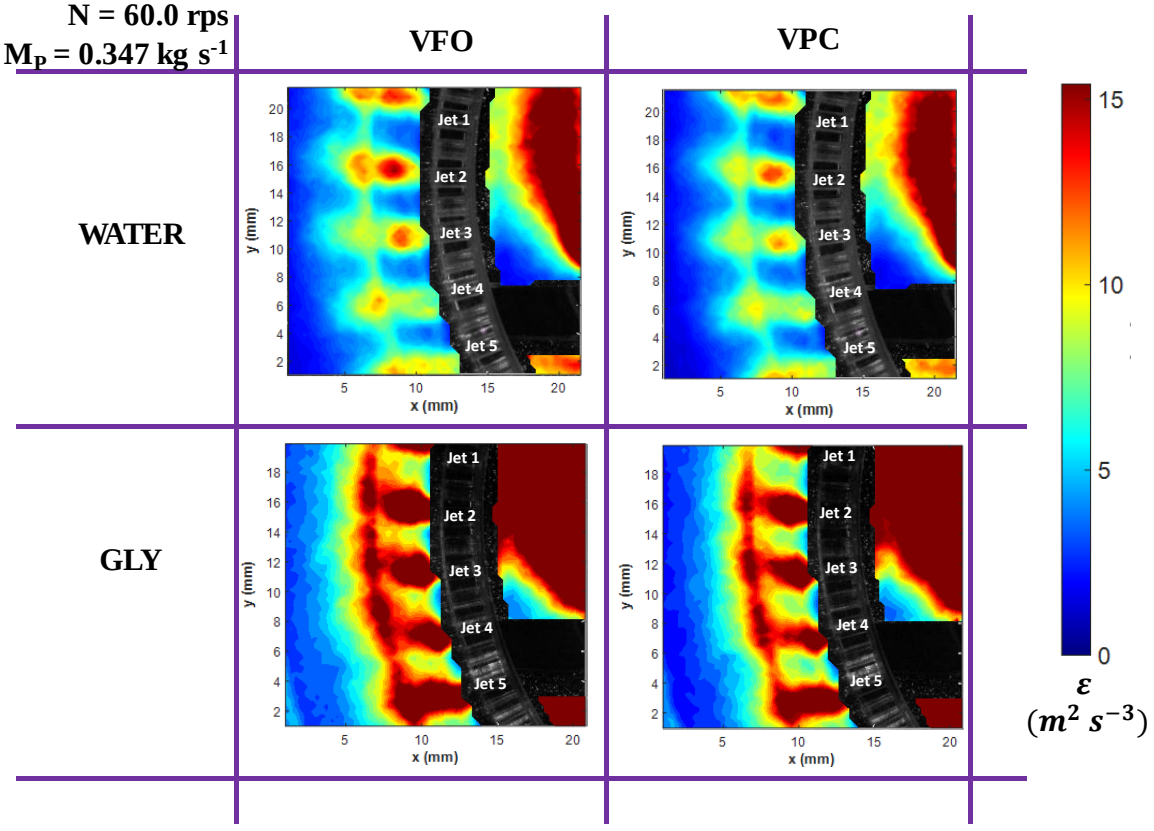

Figure 6.15: Mean turbulent kinetic energy dissipation rate field plots at VFO and VPC conditions for water and glycerol when N = 60.0 rps and M_P = 0.347 kg s^{-1}

In the high shear region, the area of highest energy dissipation for all fluids is near to the primary stator. This makes sense as the flow induced by the external pump (and also by Silverson's own pumping capability), causes disturbance into the predominantly tangential flow within the primary and secondary stator gap (induced by the rotor). This leads to the generation of higher velocity gradients and thus increased energy dissipation rates. The stronger the radial flow from the primary stator in this region becomes, the more the gap between areas of high energy dissipation along the inner wall of the secondary stator and the region within the vicinity of the primary bridges together.

Similar observations are made for VPC conditions with slight reduction in energy dissipation rate magnitude within the bulk jet region, suggesting a more uniform distribution of energy within the bulk caused by increased jet-to-jet interaction resulting from increased tangential flow of the bulk that interacts with the radial flow of the jets. Alternatively, it could be that increased tangential motion encourages the fluid to move as one body similar to solid body rotation in unbaffled stirred vessels, which often results in poor mixing and hence lower energy dissipation. Moreover, it could simply be and more probable that energy is lost as heat as the fluid residence time in the mixing head (subject to large pressure gradients) is increased when the flow is restricted, resulting in unnecessary increase in fluid temperature.

The ε distributions of SA for both VFO and VPC conditions (Figure 6.16) are very similar to those of water in Figure 6.15 with tenuous differences: in the bulk jet region, the cores of jets dissipate more energy and the fading/shedding effect around the tips of the jets appear smoothed. Similarly in the high shear region, there is a more defined and smoothed transition between the areas of high and low ε within the primary and secondary stator gap. Again, this may be attributed to the increased resolved scales for SA as its Reynolds number is

relatively lower than that of water, which means that viscous effects are more prominent at a larger λ_k (size of the smallest scales increases with decreased Reynolds number). This is why ε is higher (Equation 5.9) and there is less of the shedding effect in both ROIs A and B for SA in comparison to water. Alternatively, the possible presence of wormlike micelles in SA may be responsible for dampening the turbulence. The same analogy applies for SB1 where the locations of high ε are the same but are more localised and the shedding effect is less pronounced in both the bulk jet and high shear regions. When the rotor speed is increased e.g. SB2, similar observations are apparent but the dissipation in the bulk jets are less localised and more dissipative. For SB3, the distribution is also similar to that of SB2 within the bulk region but dissipation within the jets is relatively weaker and instead, more of the energy is dissipated near to the primary stator in the high shear region (rotor swept volume). These can be attributed to the shear thinning behaviour of SB and increase in Reynolds number.

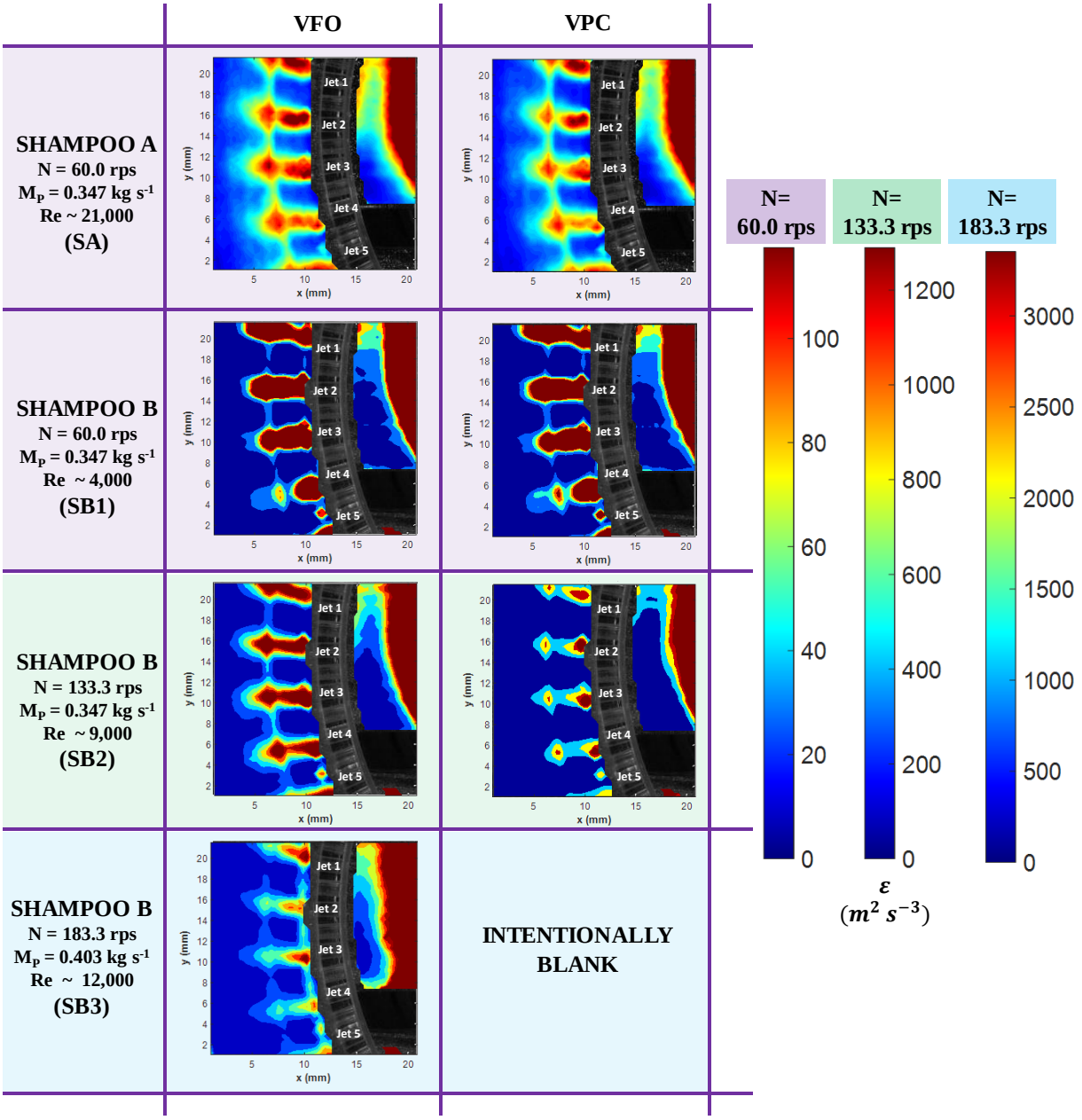

Figure 6.16: Mean turbulent kinetic energy dissipation rate field plots calculated using υ = 5.97 x 10^{-5} m^2 s^{-1} at VFO and VPC conditions for shampoos A and B at the indicated rotor speed, *N* and external pump flow rate, M_P

Profiles of turbulent kinetic energy dissipation rates, in the same locations defined in Figure 6.7 for ROIs A and B are plotted in Figures 6.17 and 6.18 respectively. Figure 6.17a shows that ε is lowest closer to the bulk ($x_{1,A}$) as the fluids move at similar velocities to the bulk hence the velocity gradients are lower, and higher in the jet core ($x_{2,A}$) and close to the stator holes ($x_{3,A}$). Water has the lowest ε in comparison to other fluids processed with the same

conditions: N = 60.0 rps and M_P = 0.347 kgs^{-1}. This was not expected as given that it has the lowest viscosity and a relatively high k (Figure 6.12b), it should have the highest ε. However, as already established, the Reynolds number for water is higher than those of the other fluids, which means that the smallest scales of turbulence are also smaller in comparison to the PIV resolution (Table 6.6). This emphasises that the measured velocity gradients suffer a greater degree of underestimation for water in comparison to other fluids. Moreover, the velocity gradients are multiplied with the respective viscosity of the fluid (Equation 5.9) which is lowest for water. This is why profiles for other fluids with higher viscosities yield higher ε.

The profiles for water, glycerol and SA are very similar, with SB1 almost overlapping as well but is slightly higher due to its higher viscosity (Equation 6.4). However, it is important to note that SB1 is in the low transitional regime. For SB2 and SB3, the viscosity used is the same as that for SB1 and thus the increase in magnitude relative to SB1 is due to the increase in measured velocity gradients with increasing rotor speed. This is assuming that most of the small scales are resolved as implied in Table 6.6. Consideration of the local viscosity for SB is also important as discussed later, as the profiles are likely to have been overestimated in shear-thinned areas. For constant $y = y_A$ = 15.14 mm (Figure 6.17b), the same trend follows in terms of absolute values between the fluids and that lowest and highest εs are found near the bulk ($x_{1,A}$) and closest to the stator hole ($x_{3,A}$), where the lowest and highest velocity gradients are respectively. The effect of partially closing the valve is only prominent for shampoo B at higher rotor speeds e.g. SB2, where the values are lower due to the increased tangential flow in the mixing head.

In ROI B, the lowest and highest values of ε are found nearest to the inner wall of the stator ($x_{1,B}$) and in close proximity to the primary stator ($x_{3,B}$) respectively (Figures 6.18a and 6.18b). The former is caused by the sudden deceleration of fluid at the inner wall of the

secondary stator while the latter is due to the interaction between the jets from the primary stator and the fluid within the primary and secondary stator gap. There are no noticeable differences between the profiles of all fluids in $x_{1,B}$ but as shampoo is subjected to higher shear rates (SB2 and SB3), it becomes more shear-thinned and so higher velocity gradients are generated. In addition, the sum of the squared gradients as per Equation 6.4 (given a relatively good effective grid resolution in Table 6.6), is then multiplied with a higher υ and thus yield higher values of ε in comparison to water and SA. This is more prominent in ($x_{2,B}$) and ($x_{3,B}$) where there are larger velocity gradients as opposed to ($x_{1,B}$), where the fluid will always move at velocities close to the rotor tip speed (lower velocity gradient).

Again, the values of ε are much lower for water because of the viscosity differences and poorer effective grid resolution (Table 6.6) e.g. more of the smaller scales are unresolved. Additionally, the differences between VFO and VPC profiles only become apparent at higher rotor speeds for shampoo. Furthermore, values of energy dissipated is consistently higher in ROI B which means that droplets are more likely to breakup there. However, as mentioned in Chapter 5, this also depends on the residence time of the droplet in this region, which is usually very short. It is also important to remember that at increased rotor speeds, Kolmogorov length scales become smaller and hence due to the limited resolution of PIV, the underestimation of ε gets worse (Kähler et al., 2012).

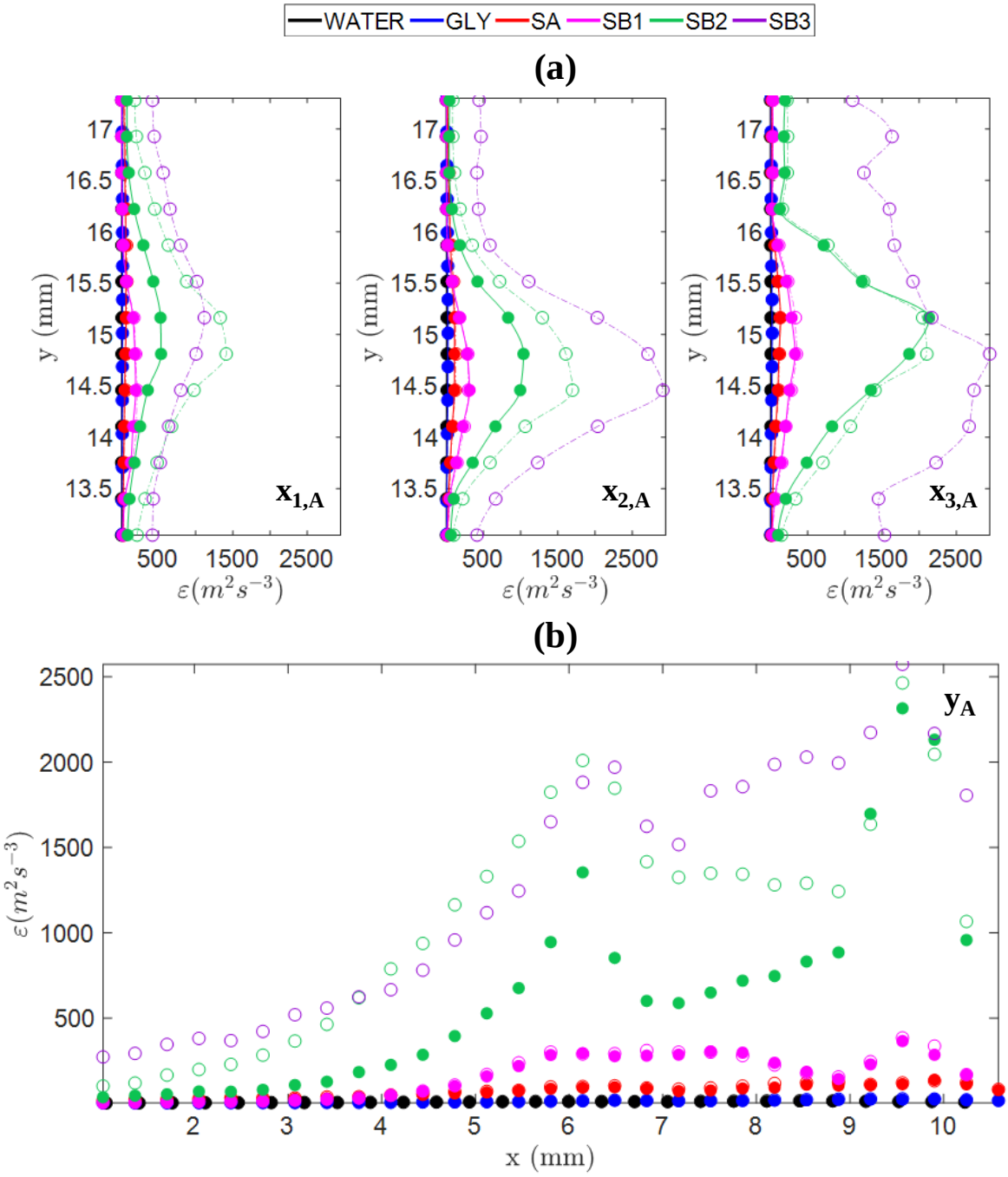

Figure 6.17: Mean local specific turbulent kinetic energy dissipation rate profiles in ROI A for water, glycerol, shampoos A and B (SB1, SB2 and SB3 indicate different rotor speeds and external pump flow rates) at (a) $x_{1,A}$ (left), $x_{2,A}$ (centre) and $x_{3,A}$ (right) and at (b) y_A. Open and closed symbols as well as dash-dot (-.) and solid (-) (eye) guidelines denote VFO and VPC conditions

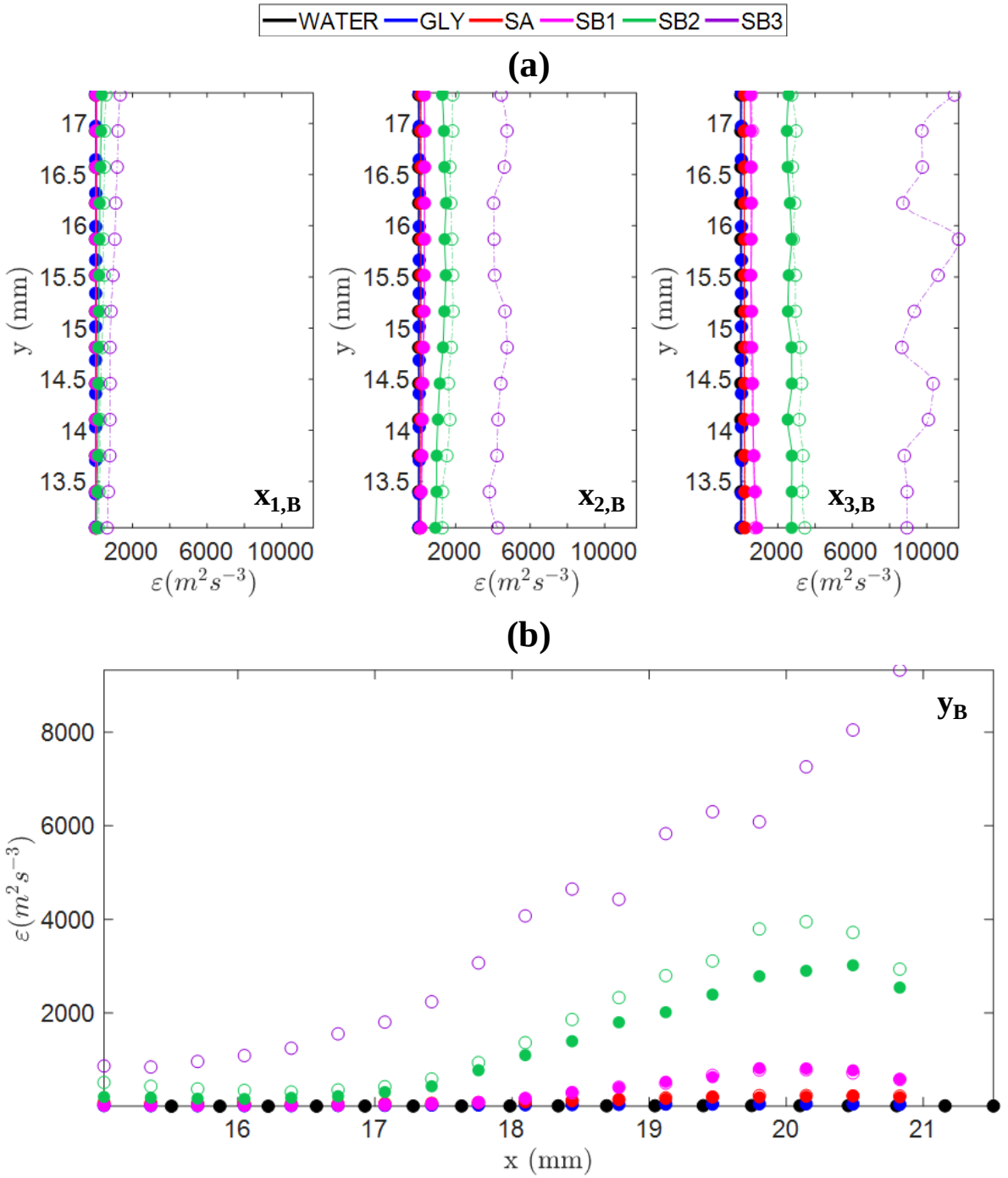

Figure 6.18: Mean local specific turbulent kinetic energy dissipation rate profiles in ROI B for water, shampoos A and B (SB1, SB2 and SB3 indicate different rotor speeds and external pump flow rates) at (a) $x_{1,B}$ (left), $x_{2,B}$ (centre) and $x_{3,B}$ (right) and at (b) y_B. Open and closed symbols as well as dash-dot (-.) and solid (-) (eye) guidelines denote VFO and VPC conditions

Contributions of the gradients in the total calculated ε (Equation 5.9) for the jet core (at $x_{2,A}$ and y_A) and middle of ROI B (at $x_{2,B}$ and y_B) are plotted in Figures 6.19 to 6.21. For ROI A (Figures 6.19a and 6.20) for all fluids, it is evident that the radial velocity (x-velocity) gradient in the y-direction $\overline{\left(\frac{\partial U''}{\partial y}\right)}$ (yellow) dominates, which is as expected as the flow out of the stator hole is predominantly radial which interacts with tangential bulk flow (flowing in the y-direction).

In contrary for ROI B (Figures 6.19b and 6.21) for all fluids, the tangential velocity (y-velocity) gradient $\overline{\left(\frac{\partial V''}{\partial x}\right)}$ (purple) dominates, which is also expected as the flow within the high shear region, which is the rotor swept area, is predominantly tangential and interacts with radial flow from the jets penetrating from the primary stator (flowing in the x-direction). It is also noteworthy that the contribution of the cross-gradient term $\overline{\left(\frac{\partial U''}{\partial y}\right)\left(\frac{\partial V''}{\partial x}\right)}$ (green) is practically negligible, as often found in similar studies (Delafosse et al., 2011; Sharp and Adrian, 2001; Wang et al., 2014). In addition, other contribution profiles (not presented) for $x_{1,A}$ and $x_{3,A}$ follow the same trend as in $x_{2,A}$. Similarly the profiles for $x_{1,B}$ and $x_{3,B}$ follow the same trend as $x_{2,B}$. Moreover, there are no significant differences between the profiles for VFO and VPC conditions and thus, the profiles for the latter are not presented.

Finally, in comparison to water and glycerol, the relative contributions of the dominating gradients are higher with the shampoo formulations.

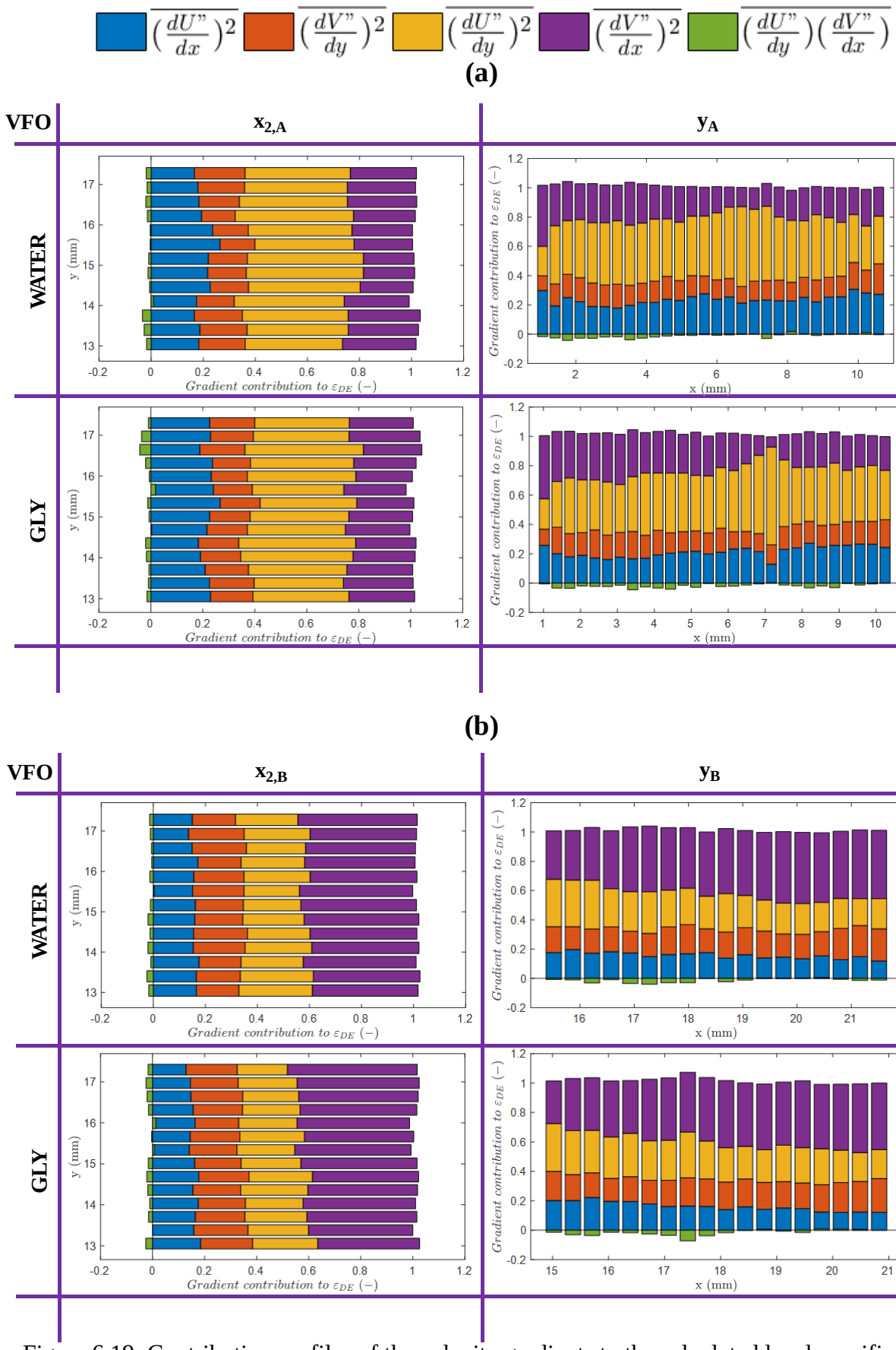

Figure 6.19: Contribution profiles of the velocity gradients to the calculated local specific turbulent kinetic energy dissipation rates in (a) ROI A at $x_{2,A}$ and y_A and (b) ROI B at $x_{2,B}$ and y_B for water and glycerol solution

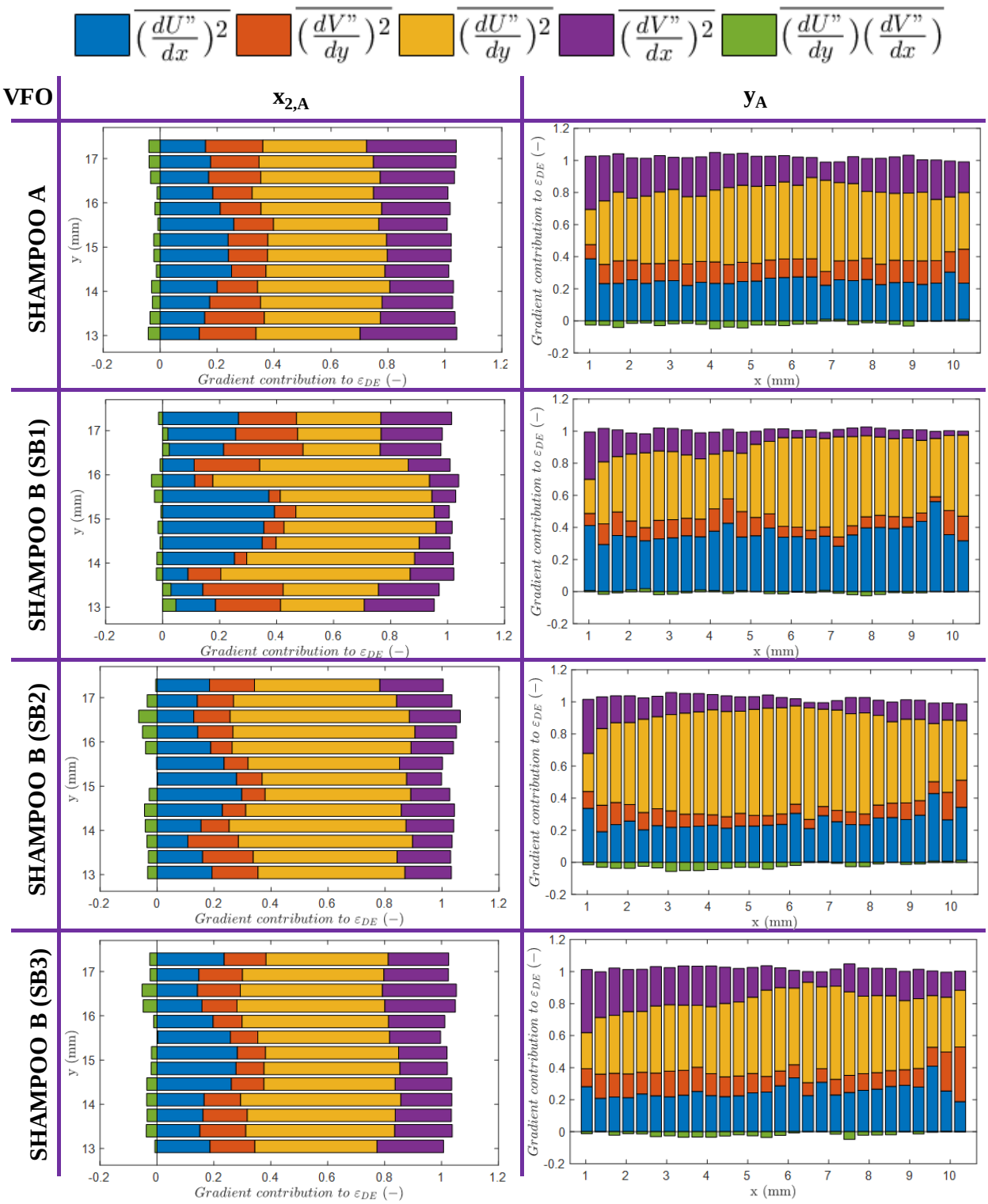

Figure 6.20: Contribution profiles of the velocity gradients to the calculated local specific turbulent kinetic energy dissipation rates in ROI A at $x_{2,A}$ and y_A for shampoo A and shampoo B (SB1, SB2 and SB3 indicate different rotor speeds and external pump flow rates)

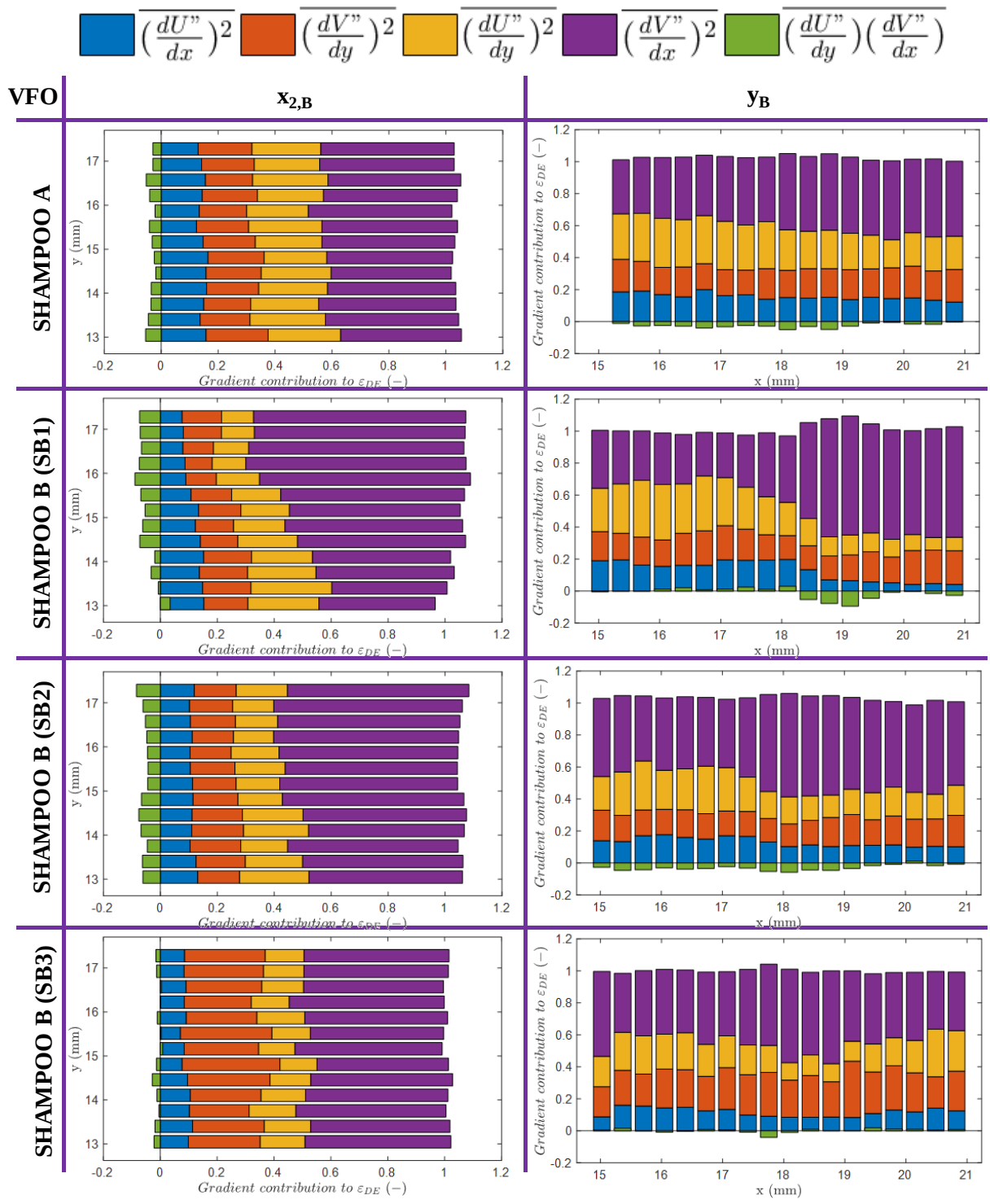

Figure 6.21: Contribution profiles of the velocity gradients to the calculated local specific turbulent kinetic energy dissipation rates in ROI B at $x_{2,B}$ and y_B for shampoo A and shampoo B (SB1, SB2 and SB3 indicate different rotor speeds and external pump flow rates)

6.6.1 Effect of Viscosity

Figure 6.22 shows the ε distribution for SB if the local kinematic viscosity, υ, was equal to $\upsilon_{constant} = 5.97 \times 10^{-5}$ m^2 s^{-1} (method 1 – left column) or approximated using Equation 6.3 (method 2 – right column). It is evident that ε has been under- and over- estimated in certain areas. This is because of the shear-thinning behaviour of SB and thus highlights the importance of taking into account local viscosities. The plots of ε using method 2, considering the limited resolution of the PIV, provides a good indication of what the actual ε distribution will look like. Treating υ as a constant is justified in a way that it is often done for similar experiments in stirred vessels through the Metzner-Otto correlation such as that by Wang et al. (2014). In addition, the trends are very similar.

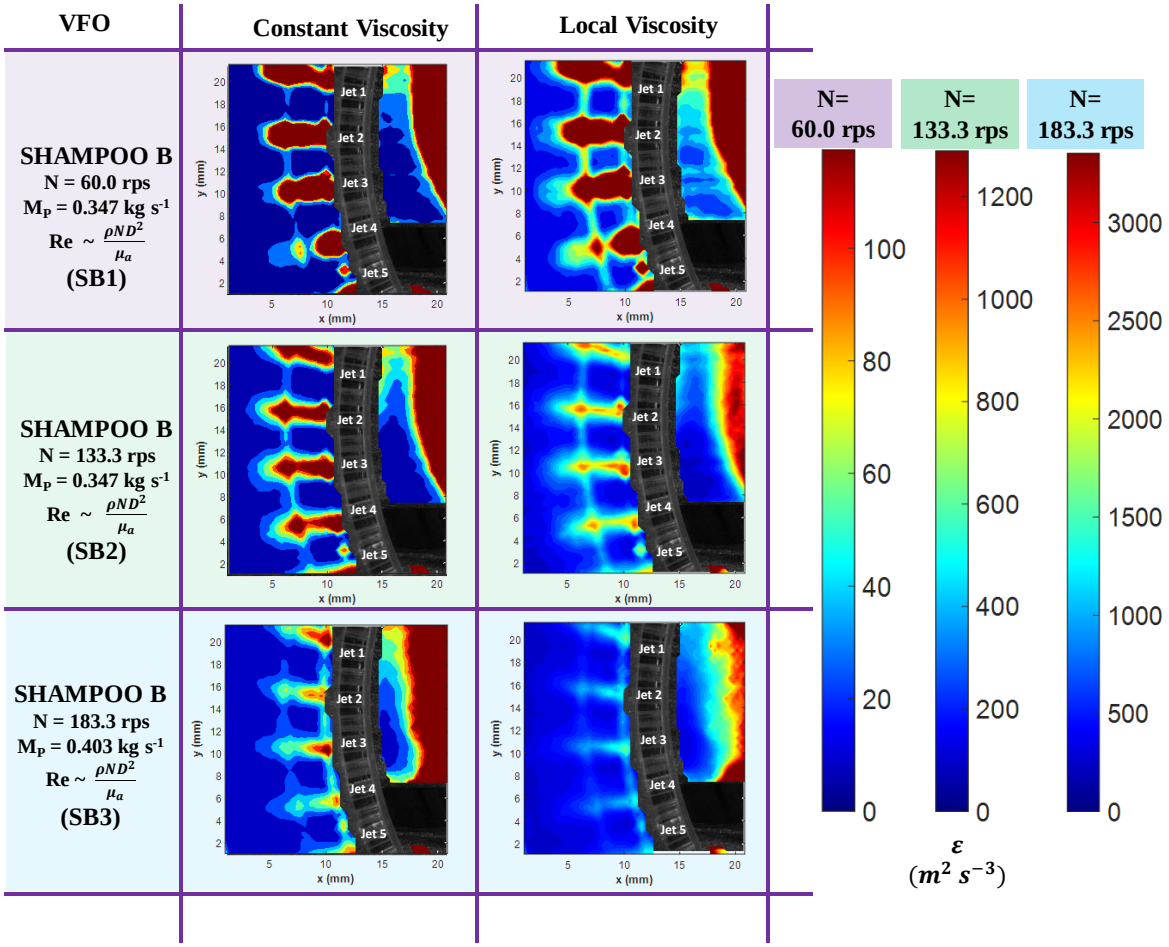

Figure 6.22: Comparison of turbulent kinetic energy dissipation rate field plots calculated using υ = 5.97 x 10^{-5} m^2 s^{-1} (left column) and estimated υ from approximated local shear rates (Equation 6.3) at VFO conditions for shampoos A and B at the indicated rotor speed, N and external pump flow rate, M_P

It can also be seen through Figure 6.22 that local viscosities were overestimated in areas where SB shear thins e.g. at the jets and close to the primary stator. In contrary, it is underestimated in stagnant regions e.g. in between the jets, the bulk and behind the rotor blade. The discrepancy between locally evaluated υ and $\upsilon_{constant}$ is greatest at low transitional regime (SB1) and least at the turbulent regime (SB3). This is because $\upsilon_{constant} = 5.97 \times 10^{-5}$ m^2 s^{-1}, is the equivalent apparent viscosity, $\mu_{apparent}$ at $\dot{\gamma} \sim 1400\ s^{-1}$ (Table 6.3), which is a relatively high shear rate and thus better approximates local viscosities in areas where shear rates are higher. However, it is noteworthy that this value is limited by the maximum achievable using the given rheometer and measuring geometry e.g. shear rates generated within the rotor swept volume are much greater than this ($\dot{\gamma}$ > 90,000 s^{-1}). From this, it can also be surmised that even at very high shear rates (SB3), shear thinning of SB inside the mixing head is still highly localised.

The two methods in which ε was calculated in $x_{2,A}$ in ROI A and $x_{2,B}$ in ROI B are compared in Figures 6.23a, where it is clear to see that ε is overestimated where local viscosities are overestimated and vice versa. For instance in $x_{2,A}$, for SB2 (green colour), the (□) symbols (method 1) is always above the (○) symbols (method 2). This is because through inspection of the corresponding υ plot in Figure 6.23b, the majority of the green symbols for SB2 is below the dashed (--) black line which represents $\upsilon = 5.97 \times 10^{-5}$ m^2 s^{-1}, which means that local viscosities have been overestimated using method 1. The same observations holds true for $x_{2,B}$. In addition, there is a more salient mismatch in viscosities in $x_{2,A}$ (Figure 6.23b) because of the presence of both fast (shear-thinned fluid in jets) and slow (bulk) moving fluids especially at low transitional regime (SB1 in magenta). In contrast, as the shear is increased (SB2), the viscosities begin to match better e.g. the fluid surrounding the jets reach a similar viscosity as the jet itself. For $x_{2,B}$, there is generally better agreement in viscosity because it is within the high shear region. However, it is often overestimated especially at higher rotor speeds (Figure

6.23a) as shear rates in this region are greater than what the rheometer is capable of generating e.g. $\dot{\gamma}$ > 90,000 s^{-1} vs. 1400 s^{-1} hence, lower viscosities are attainable in ROI B.

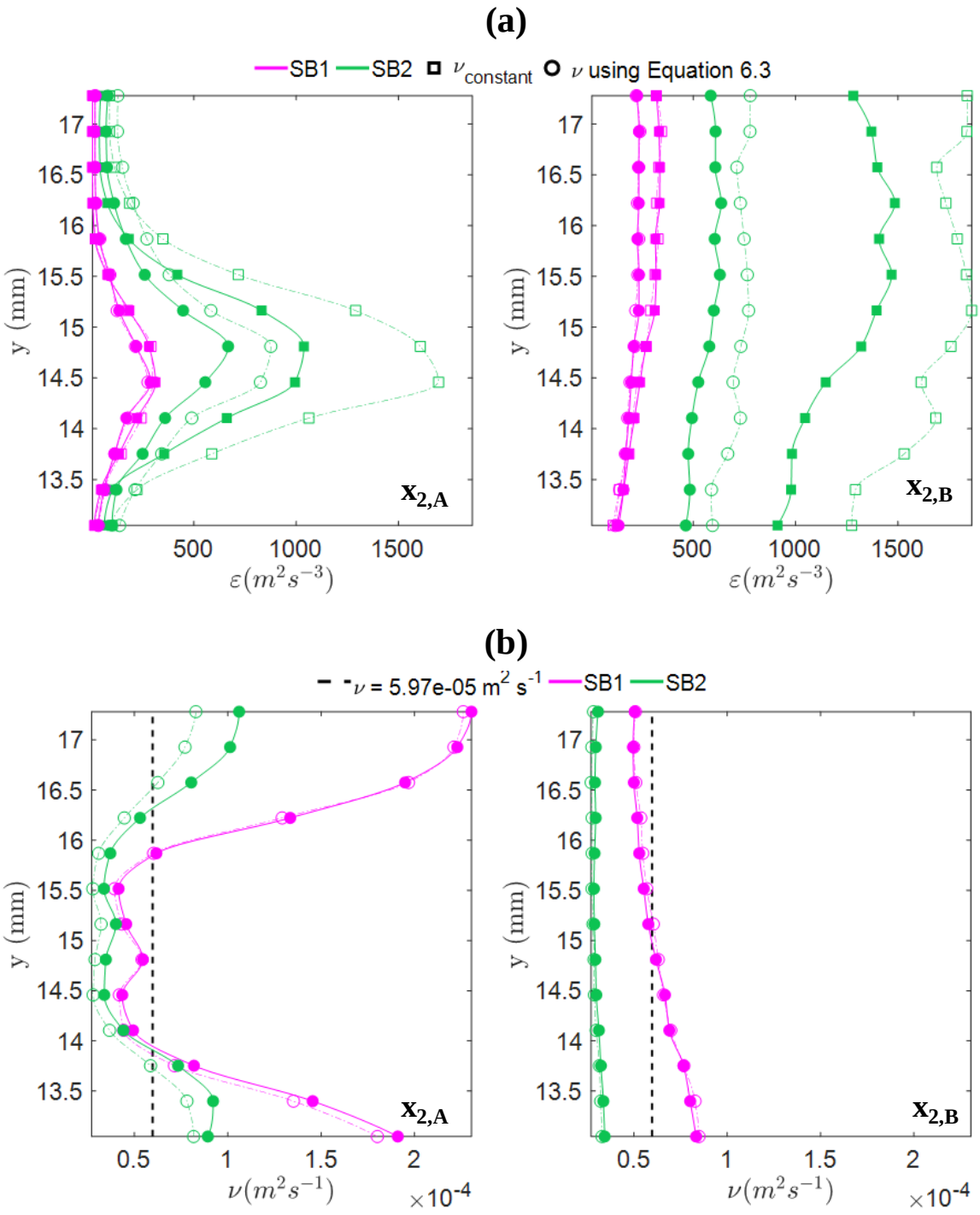

Figure 6.23: (a) Local specific turbulent kinetic energy dissipation rate profiles using $\upsilon_{constant}$ = 5.97 x 10^{-5} m^2 s^{-1} (□) and Equation 6.3 (○) for SB1 and SB2 in ROI A at $x_{2,A}$ (left) and in ROI B at $x_{2,B}$ (right) (b) Corresponding local kinematic viscosities evaluated using Equation 6.3. The black dashed (--) line represents $\upsilon_{constant}$ = 5.97 x 10^{-5} m^2 s^{-1} for comparison. Open and closed symbols as well as dash-dot (-.) and solid (-) (eye) guidelines denote VFO and VPC conditions respectively

6.7 Turbulence Intensity

Turbulence intensity, *TI*, is the ratio of the root mean square velocity to the mean flow velocity:

$$TI = \frac{U_{rms}}{\bar{U}} \tag{6.6}$$

where *TI* can be defined as component wise turbulent intensities e.g. $U_{rms}/\overline{U}$ for *x*-components and $V_{rms}/\bar{V}$ for *y*-components or as total turbulence intensity: $\sqrt{U_{rms}^2 + V_{rms}^2}/\sqrt{\overline{U} + \bar{V}}$. The latter definition is used in the discussions to follow. Turbulence is considered high if *TI* is ~ 0.05 – 0.20, medium if ~ 0.01 – 0.05 and low if < 0.01 (Chin, 2013).

Although the calculation for turbulence intensity seems straightforward (Equation 6.6), the values plotted in Figure 6.24a revealed areas where e.g. *TI* > 20, which are not possible. These are concentrated around the recirculation regions between the jets (encircled magenta), implying that *TI* in those regions are much greater than in the high shear region (rotor swept volume), which again is impossible. The underlying issue was identified as dividing relatively higher root mean square velocities with low mean e.g. near-zero velocities and roots from the uncertainty of the PIV measurement (Figure 6.24b) (Hyde, 2019). Thus, the apparent turbulence that manifests in those regions are essentially measurement of the noise.

Uncertainty is the level of doubt in a measurement and manifests as a numerical bound where the true value lies with some level of confidence as portrayed in Figure 6.25a. These values can be directly exported through the Insight 4G software which utilises the Peak Ratio (PR) uncertainty method developed by Charonko and Vlachos (2013), which incorporates a number of possible sources of error such as pixel displacement, image pre-processing and particle seeding density (Huang et al., 1997). The PR method assumes a Gaussian distribution

of the errors in pixel displacement and thus the uncertainties are expressed with an accompanying confidence level e.g. 68% and 95% for standard and expanded uncertainties respectively. It is also noteworthy that the exported values of uncertainty are scalar e.g. the magnitude of the uncertainty, as illustrated in Figure 6.25b, where $\vec{V}$ is a velocity vector and ΔV is the magnitude of uncertainty at a given confidence level. The green region is representative of the spatial bound where the head of the 'true' velocity vector may exist.

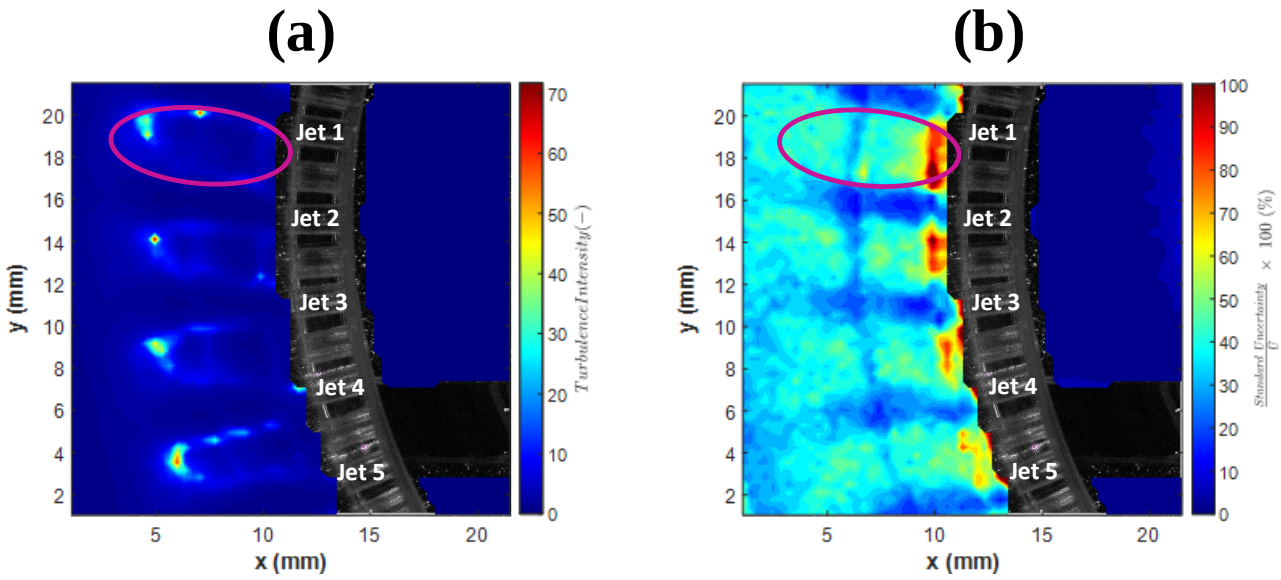

Figure 6.24: (a) Turbulence intensity plots (b) % Uncertainty plots with respect to mean velocity magnitude for water at VFO conditions before data treatment (N = 60.0 rps; M_P = 0.347 kg s^{-1})

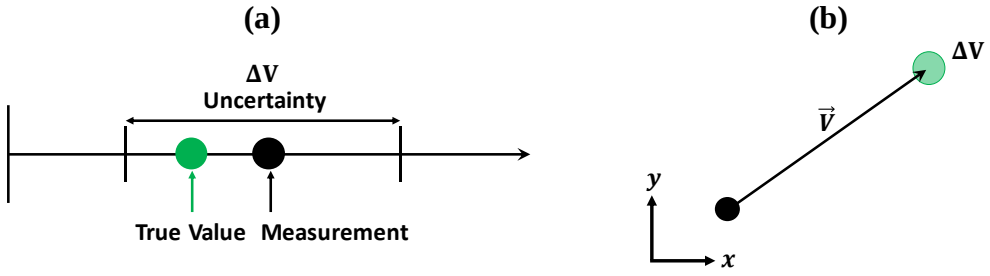

Figure 6.25: (a) Uncertainty on a number line (b) Graphical representation of the magnitude of uncertainty (enclosed in the green region)

By plotting the % of uncertainty (using standard uncertainty values with 68% confidence level) with respect to (w. r. t.) the mean velocity magnitude at each node (Figure 6.24b, it is evident that the regions of low velocities and locations of the Perspex surface imperfections (encircled magenta in Figure 6.24), are where there are high uncertainties. Unsurprisingly, these are also where the considered false areas of high *TI* are located. The reason for this is attributed to the high dynamic velocity range of the flows being studied in the mixing head e.g. velocities in the high shear region are of similar magnitude to U_{tip} whereas velocities in the bulk region are much slower. Lower uncertainties are found in the high shear region because the time interval, Δt, was evaluated with U_{tip} (Equation 3.1) and as the same Δt (and PIV resolution) is used to capture the flow phenomena in both the bulk and high shear regions (which have different characteristic velocities), the slower moving fluids in the bulk region suffer with greater uncertainties. This is evident in Figure 6.26 for water at VFO condition as an example. The same trend applies for all the other fluids and VPC conditions e.g. lower velocities have higher uncertainties and vice versa i.e. uncertainty scales with velocity. This effect seems to worsen in areas where values approach the minimum resolvable velocity (Persoons and O'Donovan, 2011).

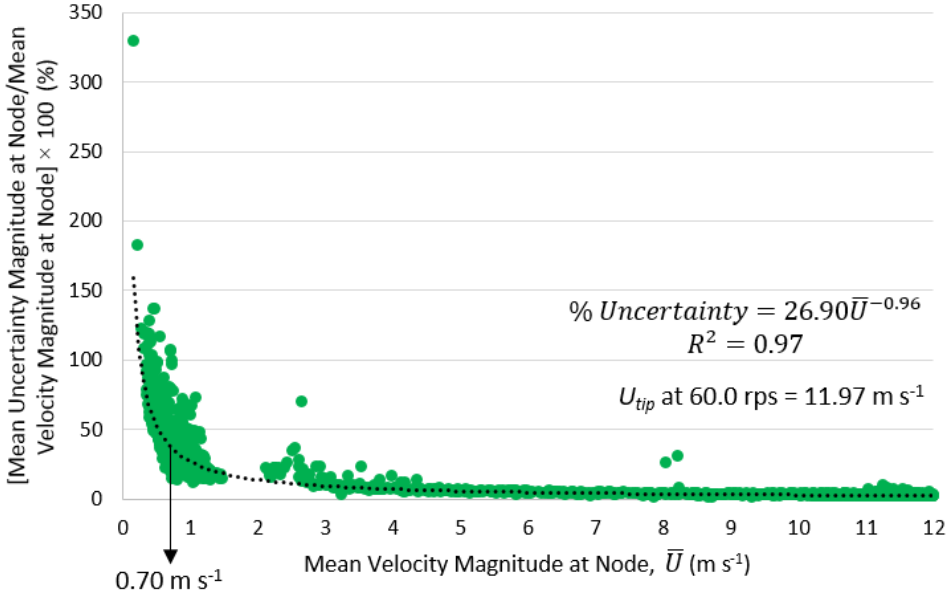

Figure 6.26: % of mean uncertainty magnitude at the node w. r. t. the mean velocity magnitude at that node versus the mean velocity magnitude at that node when N = 60.0 rps; M_P = 0.347 kg s^{-1} (VFO) for water

If a low-pass filter on the mean velocity at the node was applied e.g. < ~ 0.70 m s^{-1} (marked on Figure 6.26), which is equivalent to minimum U_{hole} in Table 6.5, the resulting velocity field and corresponding turbulence intensity, turbulent kinetic energy and energy dissipation plots, are shown in Figure 6.27. It is clear to see that more reasonable values of *TI* (between 0 and 1) are attained through this process (compare Figure 6.24a with Figure 6.27b), although values in the rotor swept volume are more credible as they are within the range of acceptable *TI* (0 – ~0.3). The effect of changing the cut-off velocity can be found in Appendix C where it is shown that increasing the cut-off velocity eliminates more data, both valid and invalid.

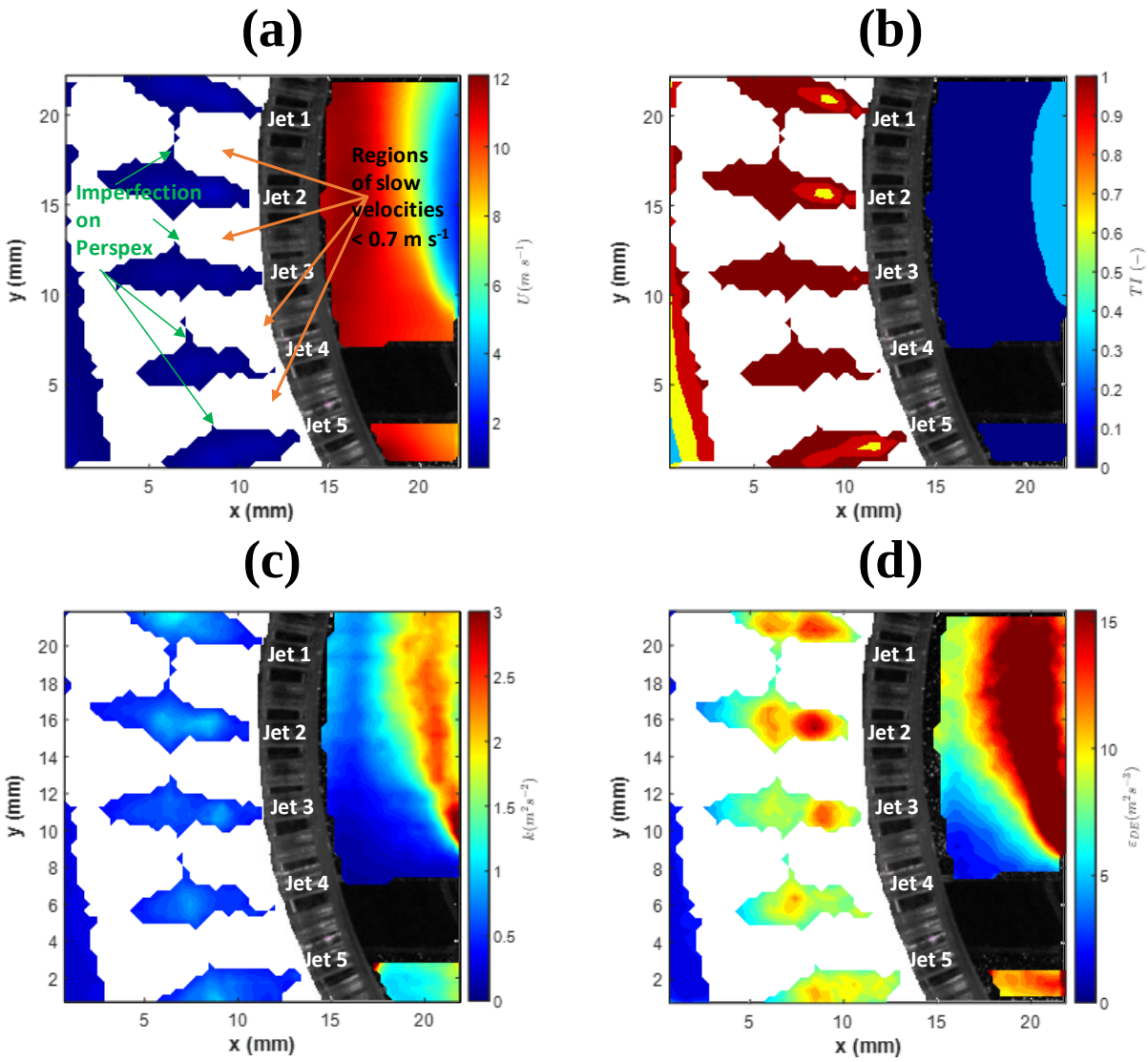

Figure 6.27: (a) Velocity plot (b) Turbulence intensity plot (c) Kinetic energy plot (d) Energy dissipation plots after applying a cut-off filter of 0.70 m s^{-1} when N = 60.0 rps; M_P = 0.347 kg s^{-1} (VFO) for water

The values of uncertainty need to be considered with respect to the other calculated turbulence properties in this study, i.e. k and ε. Due to the high dynamic range of the flow and the PIV measurement conditions chosen, as shown in Figures 6.27c and d, the areas of high k, ε and *TI* are where the velocities are high and the uncertainty is low e.g. within the jets and in the rotor swept volume in comparison to almost stagnant recirculating regions. It is recognised that the uncertainty of ~ 38% at the chosen cut-off velocity e.g. 0.70 m s^{-1} for water when N = 60.0 rps and M_P = 0.347 kg s^{-1} at VFO condition, could still be improved. An approach could be, to obtain separate data sets using optimal Δt for each respective region e.g. bulk and high shear regions (using the same PIV resolution) and then combine and plot the relevant data into a single plot, which is similar to the multi-block approach by Khan et al. (2004).

With the above considerations, and applying the same cut-off velocity of 0.70 m s^{-1}, it can be deduced from Figures 6.28 and 6.29 that in general for all fluids, the areas of high *TI* are within the jets in the bulk region (with a caveat that *TI* > 0.3 is not credible) and vicinity of the primary stator (up to ~ 0.3). These make sense as for the former, the jet from the secondary stator penetrates through the quiescent bulk, whereas for the latter, the jets from the primary stator interact with the tangentially moving fluid in a similar manner, within the primary and secondary stator gap. The relatively lower values within this gap e.g. in the middle and towards the inner wall of the secondary stator, is most likely due to the low velocity gradients behind the rotor blade as most of the fluids behind it are moving close to U_{tip}. It can also be noticed that partially closing the valve does not have much influence on *TI* distribution.

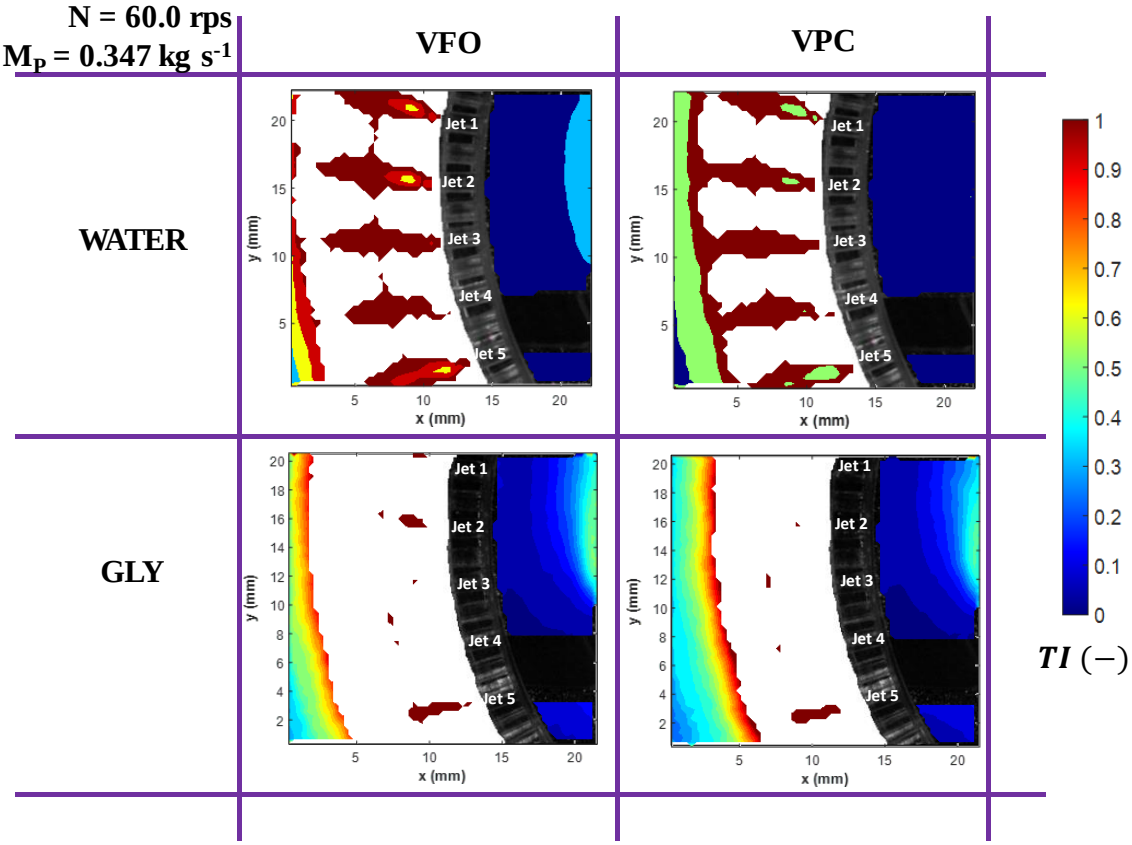

Figure 6.28: Turbulence intensity plots for water and glycerol

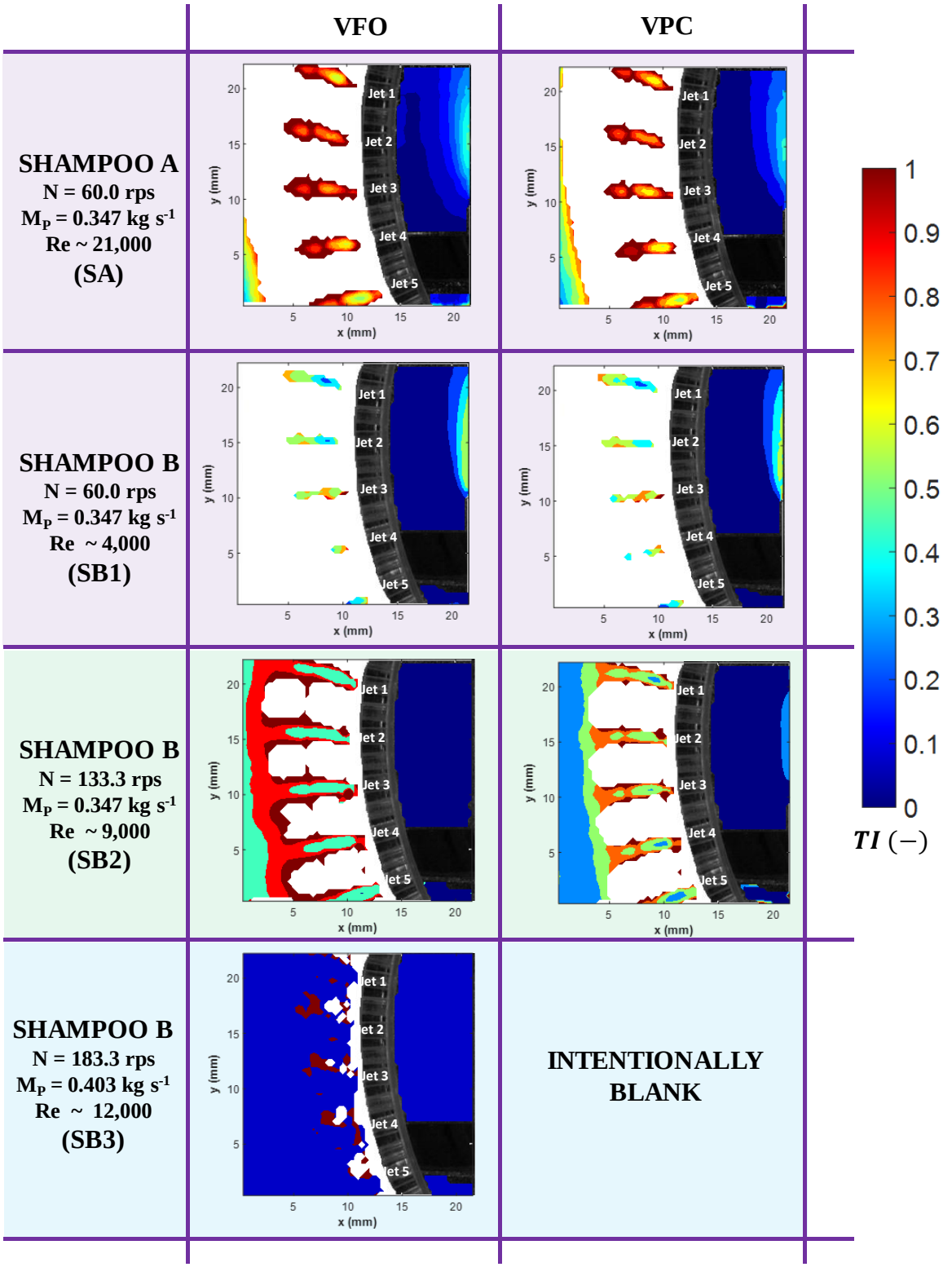

Figure 6.29: Turbulence intensity plots for the shampoo formulations

6.8 Shear Rates and Weissenberg Number

Local shear rate distributions calculated using Equation 6.1 for shampoo B are shown in Figure 6.30.

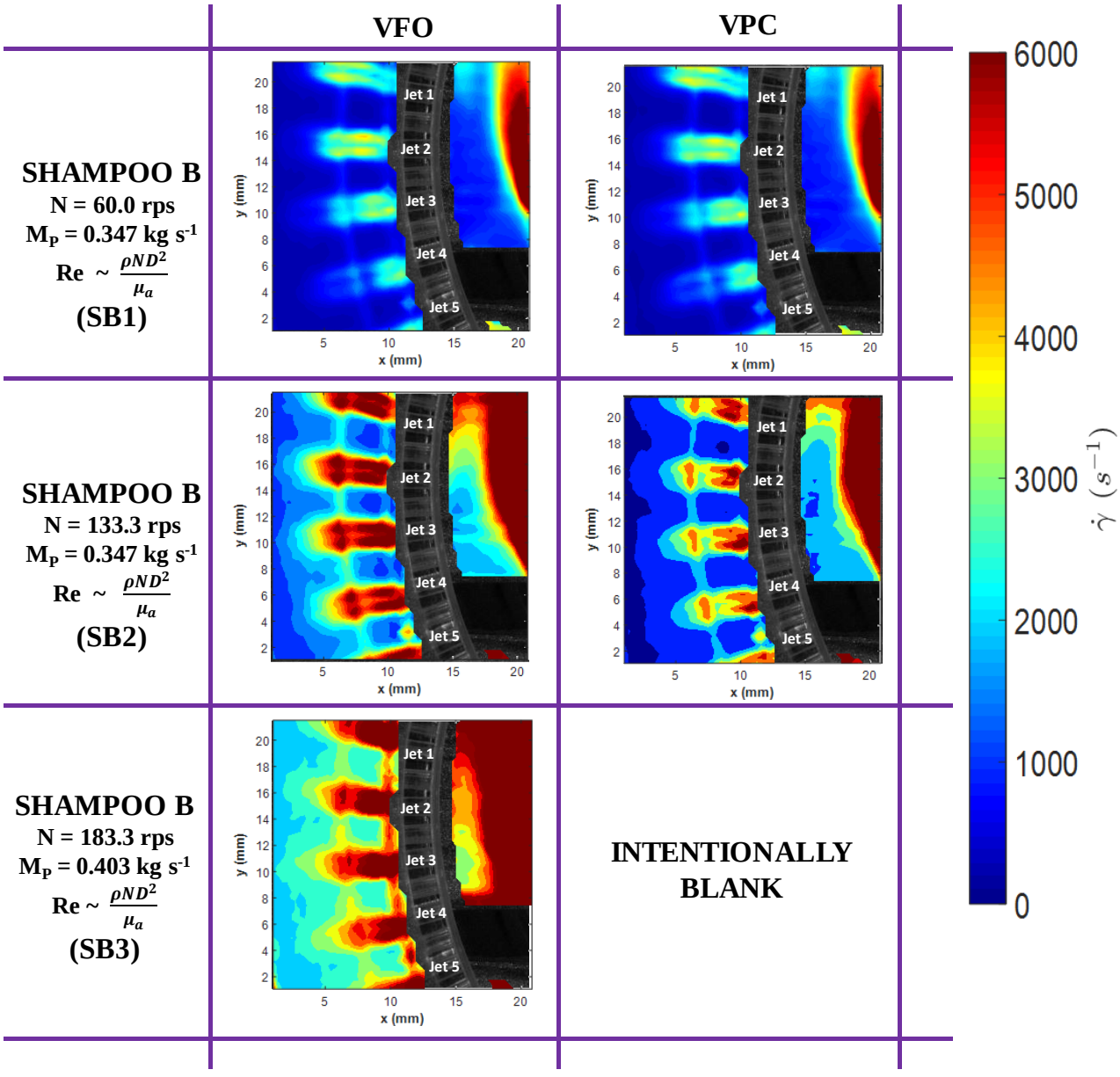

Figure 6.30: Distribution of local shear rates for shampoo B

It is not surprising to see that these distributions are very similar to the ε distribution for SB in Figure 6.22 as they are coupled through Equation 6.4 and emphasises that high deformation rates are present within the jets out of the secondary stator holes and where the jets interact with the tangential flow within the rotor swept volume.

The local shear rates are then used to evaluate local elastic effects through the calculation of the Weissenberg number:

$$Wi = \frac{elastic\ forces}{viscous\ forces} = \lambda_{RT}\dot{\gamma} \tag{6.7}$$

where λ_{RT} (Figure 6.31) is the fluid local relaxation time calculated using normal stress difference data. The resulting values were then fitted to a power law model, similar to the approach of Ozcan-Taskin (1993) and Ramsay et al. (2016):

$$\lambda_{RT} = \frac{1}{2\mu}\left(\frac{N_1}{\dot{\gamma}^2}\right) \tag{6.8}$$

$$\lambda_{RT} = a\dot{\gamma}^b \tag{6.9}$$

where *a* and *b* were evaluated as 113.33 and -2.82 respectively which are within similar values to that by Ramsay et al. (2016) (*a* ~ 87.76 to 157.36 and *b* ~ -1.81 to -1.78). It is noteworthy that only the data points that are within the acceptable axial force sensitivity of the rheometer were used. Another parameter that would have been useful to approximate was the elasticity number: *El* = *Wi*/*Re*. However, it was not attained due to the difficulty of choosing the suitable length scale to determine the local Reynolds numbers.

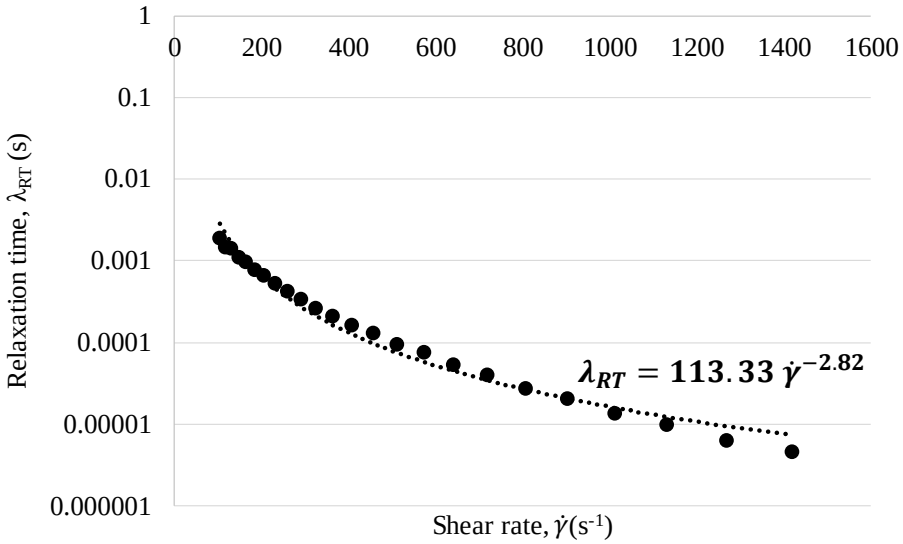

Figure 6.31: Relaxation time, λ_{RT} versus shear rate for shampoo B

According to Story et al. (2018), the critical shear rate, $\dot{\gamma}_c$ beyond which elastic effects will dominate at can be determined by estimating where the first normal stress difference N_1 vs $\dot{\gamma}$ and shear stress τ vs $\dot{\gamma}$ cross-over. Through Figure 6.1b, this was approximated as $\dot{\gamma}_c$ ~ 83.3 s^{-1}. For SB1, SB2 and SB3, for both VFO and VPC conditions, the minimum shear rates obtained using Equation 6.1 ranges from ~ 160 – 1474 s^{-1} for SB1 and SB3 respectively which implies that consideration of elastic components is important as these shear rates are above $\dot{\gamma}_c$ ~ 83.3 s^{-1}.

By comparing the local shear rate distribution in Figure 6.30, with the distribution of Weissenberg numbers in Figure 6.32, it can be seen that areas of high shear rates correspond to areas of low Weissenberg numbers and vice versa. This suggests that the elastic behaviour of the fluid dominates in the bulk where jets penetrate in ROI A and behind the rotor blade in ROI B. In contrary, it is least prominent where the fluid is shear-thinned. Areas of higher *Wi*, imply that the decrease in local velocity gradients in those locations are caused by the elastic storage within the material (Ramsay et al., 2016). Finally, it is evident that clear distinction between high (white) and low (black) areas of *Wi* is most significant at lower Reynolds number (SB1) and diminishes at higher Reynolds number (SB3) which could be indicative of dominating shear-thinning behaviour.

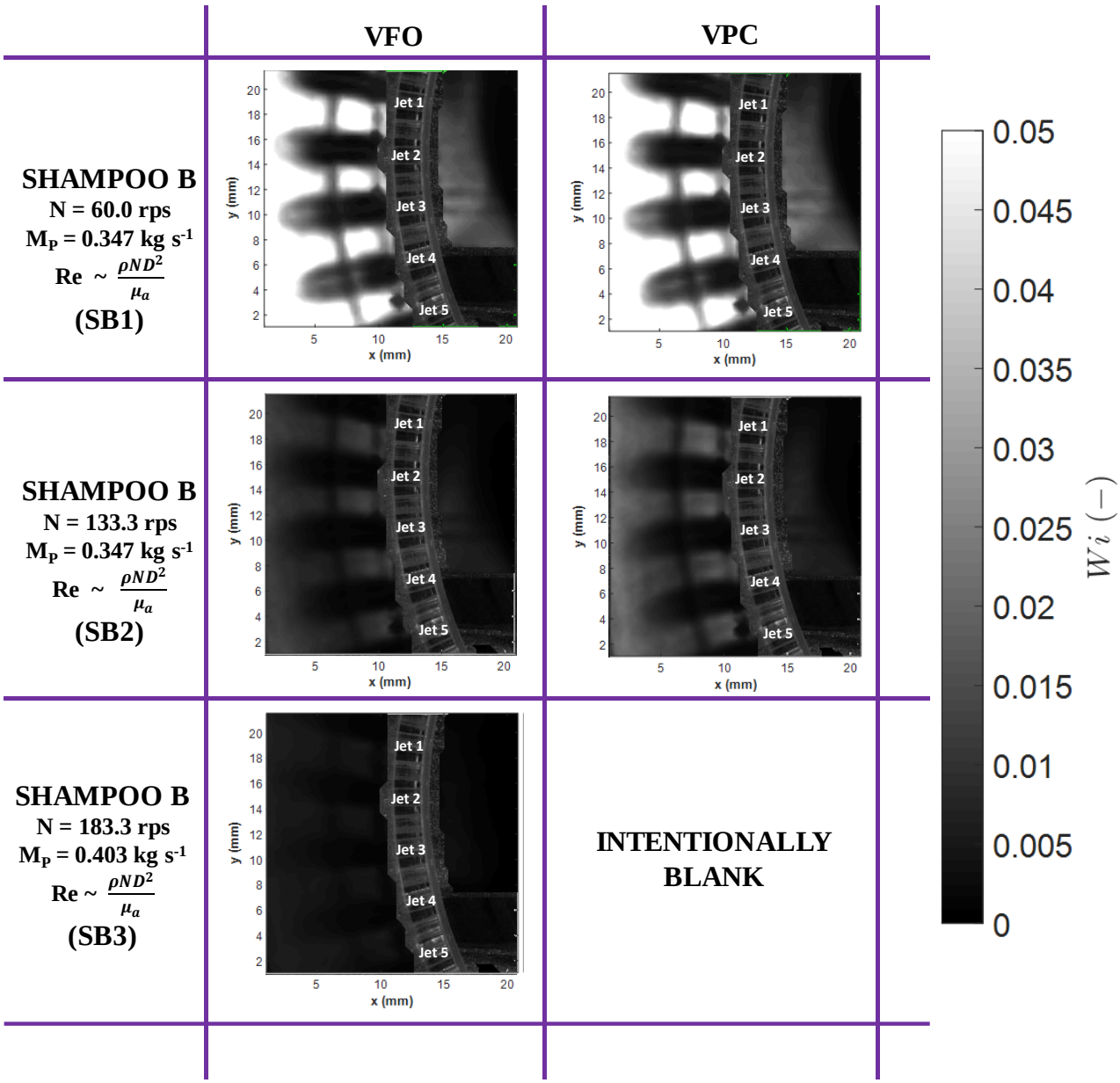

Figure 6.32: Distribution of local Weissenberg numbers for shampoo B

6.9 Conclusions

Mean velocity fields, kinetic energy and energy dissipation rate distributions as well as mean and RMS velocity and ε profiles at fixed *x*- and *y*- values at ROIs A and B were studied for a variety of case study fluids in the turbulent regime (except for SB1 and SB2 for shampoo B). These include water, glycerol and shampoos A (unsalted) and B (salted) with the latter being more representative of real consumer products.

Processing of PIV data had to be optimised for the non-Newtonian fluids (shampoo formulations) as artefacts were observed when the PIV processing settings for the Newtonian fluids (water and glycerol solution) were used. Spurious results included slow moving fluids and higher dissipation rates that persisted by the inner wall of the secondary stator. The underlying cause was identified as the particles moving faster by the inner wall of the secondary stator, beyond the allowable movement ($0.25 \times L_{IA}$) and was resolved by re-processing the images using the recursive Nyquist algorithm with 128 × 128 and 64 × 64 pixel grids for the first and second passes respectively.

The differences in flow patterns and distribution of ε in the mixing head were mainly attributed to the local flow regime e.g. Reynolds number. For instance, the shedding/dissipative effect around the jets in the bulk region (Re_{exit}) and the boundary between the area of high and low energy dissipation in the high shear region ($Re_{rotor\ swept\ volume}$) are more prominent with water as it has a lower viscosity and thus reach a higher state of turbulence at a faster rate.

The presence of surfactants (shampoos) was identified as a potential source of the displayed viscoelastic behaviours, especially for shampoo B. It was also discovered that for shear-thinning fluids like shampoo B, approximation of local viscosity through the calculation

of strain rate tensor using PIV data, yielded more representative distributions of energy dissipation rates.

In general for all fluids, areas of high ε were identified to be in the core of the jets and in close proximity to the primary stator where jets penetrating from it interact with the fluid in the gap between the primary and secondary stators. Turbulence intensity plots also support this finding although they should only be taken as qualitative indications as caution must be taken when considering the uncertainty of PIV measurements. Furthermore, partially closing the valve does not significantly alter the overall flow pattern but lowers the magnitude of energy dissipation rate especially at higher rotor speeds. This is because the overall flow in the mixing head becomes more tangential as concluded in Chapter 4. In addition, it is probable that energy is lost as heat when the fluid residence time in the mixing head is increased as the flow becomes restricted.

Finally, for SB, shear rate and Weissenberg (*Wi*) distributions were also examined. It was found that areas of high shear rates corresponded to areas of low *Wi* numbers implying that elastic effects are least significant in the shear-thinned regions e.g. within the jets in ROI A and in close proximity to the primary stator in ROI B.

Chapter 7 – Conclusions and Future Recommendations

7.1 Conclusions

In-line high shear mixers are used by industry due to the economic benefits associated with them in delivering larger continuous throughput (Qin et al., 2017). In addition, they are an integral part of many of the processes run by the sponsoring company, Unilever, especially in the manufacture of formulated emulsion products. Thus, it is vital to gain as much insight on how such mixers operate to ensure that they are run in the most efficient and cost-effective way. In this research, 2-D angle-resolved PIV was utilised to characterise the flow patterns in a pilot-scale model of an in-line Silverson 150/250 high shear mixer to contribute towards achieving this. The main conclusions from this study are outlined below in relation to the aims and objectives defined in §1.3.

1. *Assess the effects of changing process parameters such as rotor speed, externally driven flow rate and backpressure upon the flow field and pattern in the mixing head of the inline HSM for Newtonian fluids (water) (Chapter 4).*

Particular attention was given to the overall flow pattern across the whole mixing head as opposed to existing studies that focus on flow within the stator holes as well as on the effects of varying the external pump flow rate to the overall flow pattern.

The overall flow is a combination of radial and tangential flow patterns. The former is primarily provided by the external pump while the latter is induced by the rotor. The dominating flow pattern depends on the combination of external pump flow rate and rotor speed. In general, the higher the rotor speed, the more tangential the flow becomes and vice versa. Furthermore,

the addition of an outlet valve was also found to promote a more tangential flow due to restriction of the outlet flow.

Highest radial velocities were found in close proximity to the outer stator hole (where the jets are) while the highest tangential velocities were present in areas swept by the rotor blades as well as near the wall of the filled volume.

Flow rates were evaluated using *(a)* plug flow approximation and *(b)* calculating surface flow rates across all rows and fitting a function that is integrated over the effective stator thickness. The former sufficiently predicted flow rates generated by the external pump only while the latter yielded results with better accuracy and was used to calculate flow numbers that are of similar magnitude to those found in literature for a similar mixing head.

It was also found that the additional flow rate from the pump increased the flow numbers calculated for SO conditions, suggesting that it boosts the pumping action of the rotor. As the rotor speed and extent of flow restriction increase, this additional pumping is diminished and can be linked to the geometry of the outer stator. Narrower holes allow better transfer of the tangential momentum from the rotor to the surrounding fluid hence there is less pumping action as the fluid moves in the tangential direction as opposed to the radial direction.

Finally, based on the experimental study by Hall et al. (2011a), analysis of such results can be attributed to their implication on emulsification processes: a more tangential flow may be attributed to generating smaller droplet sizes due to the dominating breakup mechanism caused by fluid impingement on the stator and the role of the stator becomes more important at higher flow rates.

2. *Through the study of flow patterns, identify areas where droplet break up is likely to occur (Chapter 5).*

   and

3. *Evaluate turbulence properties such as Reynolds stresses, turbulent kinetic energy and energy dissipation rates using velocity data to determine potential governing break up mechanism(s) (Chapter 5).*

2-D PIV data were used to define turbulence characteristics and propose potential droplet break up locations and mechanisms on a 150/250 in-line Silverson high shear mixer at various processing conditions. Turbulence parameters such as Reynolds stresses, TKE and energy dissipation rates (via direct evaluation (DE) and large eddy PIV sub-grid scale (SGS) methods) were quantified and observed how they were influenced by the process parameters.

A method of quantifying the contribution of the external pump and Silverson mixer in driving the overall process flow and thus the flow inside the mixing head using pressure measurements was also discussed.

Two main regions of interest: jet region (ROI A) and high shear region (ROI B) were investigated to study how energy dissipation was influenced by the process parameters. It was found that areas of high ε are also areas of high Reynolds stresses and TKE.

In ROI A, radial flow dominates due to the emanating jets from the secondary stator (driven by the external pump) hence most of the energy is dissipated through the jet cores. As the flow becomes more tangential at higher rotor speeds, these jets become weaker and vice versa when the external pump flow rate is increased. Drops could therefore break through elongational stresses in this region. This is an important observation because most plant operators would intuitively increase the rotor speed (as it is a “high shear mixer”) to achieve

the desired droplet size. However, as discussed in Chapter 5, depending on the process application and product rheology, breakup through elongational stresses may be preferred in which case, the flow driven by the external pump is more important.

In ROI B, tangential flow dominates as it occurs within the rotor swept volume. As the flow in this region is highly turbulent, droplet break up occurs due to turbulent stresses in the inertial sub-range.

Areas of high ε or 'sweet spots' manifest due to the proposed phenomena: *(a)* fluid impaction on the inner wall of the secondary stator and *(b)* interactions between the undisturbed vortex that forms behind the rotor blade and the jets emanating from the primary stator. However, at higher rotor speeds, although the maximum value of ε increases, the number of 'sweet spots' reduces and the area of low energy dissipation behind the rotor blade extends. To alleviate this, the external pump flow rate can be increased to allow deeper jet penetration from the primary stator into the region between the primary and secondary stators. This implies that increasing the rotor speed and partially closing the valve induces solid body rotation, which in effect decreases ε.

Energy dissipation rates were found to be proportional to $N^{\sim 1.59-1.90}$ and $N^{\sim 2.42-2.84}$ using DE and SGS methods respectively at the best attained spatial resolution (~$14\lambda_K$). Both methods yielded exponents that are approaching the value of, but do not equal 3 that is well established in the literature. This is because both methods are subject to the isotropic turbulence assumption which means that since the data is from 2-D PIV, the missing z component had to be approximated, leading to the underestimation of the exponent. Moreover, both methods, especially DE, are also sensitive to the PIV resolution. For instance, as the turbulence intensifies at increasing ε, the length scales get smaller and thus more is

missed in the measurements. The effect is worse for the DE method as it does not model for length scales below the cut-off resolution.

Finally, the dependency of the energy dissipation rate with the process conditions is highly influenced by the location in the mixing head since both laminar and turbulent conditions co-exist due to the complex flow patterns in the mixing head and thus ε is not proportional to N^3 throughout the mixing head. Despite these, the evaluated exponents are within the same range in existing literature between 2.26 and 2.67 for in-line HSMs (Bourne and Studer, 1992; Hall, 2012).

4. *Assess the impact of changing fluid rheology (non-Newtonian fluids and higher viscosity Newtonian fluids) to ascertain its influence on flow patterns and turbulence and thus on potential mechanisms of droplet deformation (Chapter 6).*

Mean velocity fields, kinetic energy and energy dissipation rate distributions as well as mean and RMS velocity and ε profiles at ROIs A and B were studied for a variety of case study fluids in the turbulent regime (except for SB1 and SB2 for shampoo B). These include water, glycerol and shampoos A (unsalted) and B (salted) with the latter being more representative of real consumer products.

The differences in flow patterns and distribution of ε in the mixing head were mainly attributed to the local flow regime e.g. Reynolds number. For instance, the shedding/dissipative effect around the jets in the bulk region (Re_{exit}) and the boundary between the area of high and low energy dissipation in the high shear region ($Re_{rotor\ swept\ volume}$) are more prominent with water as it has a lower viscosity and thus reach a higher state of turbulence at a faster rate. The presence of surfactants in shampoos was also identified as a potential source of displayed viscoelastic behaviours, especially for shampoo B. In addition, shampoo B is also shear

thinning and thus, consideration of its viscosity is essential in the calculation of energy dissipation rates. Estimating local viscosities using velocity data from PIV through the calculation of the strain rate tensor seems to output more realistic results. These imply that the potential breakup mechanisms are similar but for more viscous and complex fluids, breakup via extensional stresses may be more important.

In general, for all fluids, areas of high ε were identified to be in the core of the jets and in close proximity to the primary stator where jets penetrating from it interacts with the fluid in the gap between the primary and secondary stators. It was also interesting to see that the relative contributions of the dominating gradients to ε in ROIs A and B are higher with the shampoo formulations, which may be attributed to its viscoelastic and shear thinning traits.

Partially closing the valve does not significantly alter the overall flow pattern for all fluids but lowers the magnitude of energy dissipation rate especially at higher rotor speeds. This is because the overall flow in the mixing head becomes more tangential as concluded in Chapter 4 which implies that a more uniform distribution of energy within the bulk caused by increased interaction between the tangential flow of the bulk and radial flow of the jets. Alternatively, it could be that increased tangential motion encourages the fluid to move as one body similar to solid body rotation in unbaffled stirred vessels which often results in poor mixing and hence lower energy dissipation. Moreover, it could simply be that energy is lost as heat as the fluid residence time in the mixing head is increased when the flow is restricted.

Turbulence intensities were also quantified and it was found that higher values persisted within the jets in the bulk region and close to the primary stator in the high shear region, where high velocity gradients exist.

For shampoo B, shear rate and Weissenberg (*Wi*) number distributions were also examined. It was found that areas of high shear rates corresponded to areas of low *Wi* numbers implying that elastic effects are least significant in the shear-thinned regions e.g. within the jets in ROI A and in close proximity to the primary stator in ROI B.

Finally, the importance of taking into account the uncertainty of PIV measurements, in particular with the evaluation of turbulence intensity, was also highlighted.

7.2 Implications in Practice

It is recommended, as did Hall et al. (2011a), to operate the mixer at the highest flow rate (M_T) possible. This is because at constant N, higher flow rates have the lowest energy density ($E_v = P/Q$) which means the mixer requires lower energies to achieve a desired droplet size. Doing this will increase the power drawn by the mixer but only marginally as it is dampened by the additional fluid processed. However, their experiments relied more on the pumping capability of the mixer (M_S) opposed to using the external pump to control the overall process flow rate (M_P). Thus in an industrial setup, as reflected in this work, it is recommended that if the Silverson cannot self-pump, use the external pump to help it achieve the desired throughput, M_T. Otherwise, when the Silverson mixer's pumping efficiency increases with N e.g. higher ND^3, it will be self-pumping but may still need an external pump to keep P_{inlet} slightly positive. Monitoring pressures on both the external pump and Silverson mixers is therefore vital, especially Silverson's P_{inlet}. It has to be kept slightly positive to ensure that it does not act as a pump (-ve P_{inlet}) and not shoot up that it behaves like an orifice (too high +ve P_{inlet}). The former risks the onset of cavitation, which may be good for droplet break up but not for the health of the mixer. This is also the probable reason why it is preferred in industry to have the external pump, with the help of an outlet valve, dictate the overall process flow rate.

On the other hand, the latter leads to generation of large pressure gradients by restricting the flow, which leads to unnecessary increase in outlet temperature and residence times and thus, wasted energy. The aim is to keep ΔP at or as close to zero as possible (Casugbo and Baker, 2018). This further suggests that VFO conditions are favourable over VPC conditions as similar flow patterns are achievable as long as M_T (or ΔP_T) is the same. This is also supported by the findings in this work as ε_{VFO} are consistently higher than ε_{VPC} especially at really high N. Figure 5.6 will help achieve this by providing an insight on which of the external pump or Silverson mixer drives the flow, by how much and when they crossover one another.

Other essential things to consider are: geometry of the rotor and stator, mode of operation as well as the formulation properties. For instance, most studies focus on single row stators with fewer and wider holes. Thus, although recirculation is present in the stator used in this work, which has multiple rows of narrow holes, the fluid does not re-enter the holes as is normally observed in existing studies but is instead bounced back up to the bulk by the succeeding jet. Since there are multiple rows of holes as well, jet-to-jet interactions will also occur in the *z*-direction. Moreover, the jet profile also looks very similar to the turbulent jets in sonolators or liquid whistles (Ryan et al., 2017) which is because of the additional flow provided by the external pump. In terms of the rotor, it may be an idea to increase the number of blades to increase 'sweet spots' by the stator walls.

Finally, mode of operation is also important as consideration of the design of the role of the stator and residence times are more important in single-pass emulsification. Ultimately, formulation properties will stipulate whether the flow in the mixing head is going to be laminar or turbulent and hence dictate which break up mechanisms will be most influential.

7.3 Future Recommendations

The key recommendations for future studies arising from this research are as follows:

- Increased spatial resolution is required to improve measurements and consequently get closer to the true values of the calculated properties. This can be achieved, although with great difficulty, by using higher resolution techniques such as LDA or using the multi-block approach (Khan et al., 2004) which are both labour and time intensive. The former requires the mixing head to be re-engineered e.g. installing anti-vibration mount as the technique is very sensitive to vibrations which is inherent in any motor-driven mixers. The latter will allow more zooming in but at the expense of having to use microscope optics and smaller seeding particles which can be problematic in terms of multi-scattering of the laser light. The results in this work, despite the relatively poor spatial resolution, are comparatively easier to achieve and are still highly informative.
- Experimental conditions used in this study could be modelled and the current results could be compared to computational fluid dynamic (CFD) simulation results. Moreover, 3-D PIV will also be useful to improve ε estimation using the direct evaluation method. However, this requires a major re-design of the rig to allow for stereo-PIV configurations and improved optical access.
- A more detailed study of fluids with complex rheology should be considered with particular attention to viscoelastic effects at high shear rates e.g. by performing extensional and oscillatory rheometry to understand how fluids behave when subjected to different stresses such as shear and extensional stresses. In terms of shampoo products which contain high concentrations of surfactants, studies on Shear Induced Structures (SIS) and Elongation Induced Structures (EIS) could also be pursued. The former is important between the rotor-stator gap as such observations are made in similar configurations e.g. in a Couette device

while the latter is important in the stator holes where uniaxial elongation occurs. It would be convenient if birefringence flow visualisation experiments can be conducted to reveal the existence of these phenomena and results compared to PIV measurements. In light of this, various formulations can be tested to analyse the effect of using other surfactant systems.

- If the previous point is to be achieved, it is vital to be able to take accurate PIV measurements e.g. higher spatial resolution near the inner wall of the secondary stator as well as within and through the stator holes. An approach would be to zoom in closer to the region of interest and use a suitably sized seeding particle e.g. smaller than the diameter of the stator hole and small enough to ensure that there are enough particles in the desired interrogation window size. However, limiting factors such as the quality of Perspex e.g. in terms of surface imperfections and risk of over-seeding and as previously mentioned, multi-scattering of laser light using smaller particles will present difficult challenges.
- Flow studies using different rotor and stator designs could also be done to determine the effects of geometrical factors e.g. rotor blade size, shape and number, stator hole size, shape and number as well as the rotor-stator gap size on the overall flow pattern and 'sweet spots' of high energy dissipation rates and thus potential droplet breakup mechanisms. In addition, these parameters are also essential in the pumping capability of the mixer. Moreover, the effect of changing the rotor blade position can also be explored by adjusting the time delay through the synchroniser. These investigations should also be extended to other high shear mixer manufacturers and other mixing devices since this research focused on one type of Silverson mixer only.

- Detailed flow studies in the laminar and transitional flow conditions, though less important in industry, would also be useful as geometric parameters such as the rotor-stator gap is highly likely to influence droplet break up when laminar shear dominates.
- High speed imaging of droplet breakup within regions of interest in the mixing head e.g. within the rotor swept volume and stator holes, similar to the single droplet breakup experiment conducted by Ashar et al. (2018), will be useful in identifying when, where and how droplets break inside the mixing head especially if combined with PIV results. The aim is to also determine droplet residence times in probable areas of droplet breakup and how they link to the droplet deformation and breakup time and hence understand breakage dynamics e.g. where and how the majority of final droplet sizes in a droplet size distribution (DSD) are produced. For instance, it can be used to confirm if a bimodal distribution manifests because of incomplete breakage instead of a change in breakup mechanism for emulsion systems with highly viscous dispersed phase (Hall, 2012).
- More pressure sensors should be fitted along the system pipeline so that more detailed pressure measurement analyses could be made. In this way, the influence of percentage opening of the current outlet (needle) valve or by changing it completely could also be investigated.
- In the present work, PIV was applied in a single phase system. It would also be interesting, albeit very challenging, to use PIV to investigate multiphase flows in high shear mixers. Furthermore, a future investigation may involve comparison of results with a non-optical technique such as PEPT which allows for interrogating opaque fluids.

Appendices

A: Polyacrylamide (PAA) Solution Data

The relevant data for PAA, as for the other fluids discussed in Chapter 6, are presented below. However, due to the lack of rheological data, the results were not analysed further.

A.1 Tables of Relevant Data

Table A.1: Formulation of PAA

Fluid	Composition
Polyacrylamide solution (PAA)	- 0.05 wt% Polyacrylamide (500 PPM) - 1 wt% NaCl - 40 wt% Glycerol - 58.95 wt% deionised water

Table A.2: Rheological properties of PAA

Fluid	K (Pa s^n)	n (-)	Relaxation time pre-exponential factor a (s^{b+1}) Equation 6.9	Relaxation time power law exponent b (-) Equation 6.9
PAA	0.00509	1.00	-	-

Table A.3: Reynolds number calculations for PAA in the rotor swept volume. M_T presented is for VFO conditions, for VPC conditions, $M_T = M_P$

Fluid	N (rps)	M_P (kg s^{-1})	*M_T (kg s^{-1})	μ_∞ (Pa s)	ρ (kg m^{-3})	Re = $\frac{\rho N D^2}{\mu_\infty}$ (-)	Regime (-)
PAA			0.404	0.00509	1098	52,200	Turbulent

Table A.4: Hole velocity and corresponding Reynolds numbers at the hole exit for PAA at N = 60.0 rps; M_P = 0.347 kg s^{-1}. If $M_T = M_P$, U_{hole} = 0.60 m s^{-1}

Fluid (-)	**M_T (kg s^{-1})**	**U_{hole} (m s^{-1})**	**$Re_{hole} = \frac{\rho U_{hole} D_{hole}}{\mu_\infty}$ (-)**
PAA	0.404	0.698	241

Table A.5: Kolmogorov lengths (λ_k) and effective grid resolution (Δ/λ_k) for PAA at the given process conditions where $\Delta = 64$ pixels $\times$ 11.02 µm/pixel $= 705.28$ µm

Fluid (-)	**N (rps)**	**M_P (kg s^{-1})**	**M_T(kg s^{-1})**		**λ_k (µm)**		**Δ/λ_k (-)**	
			VFO	**VPC**	**VFO**	**VPC**	**VFO**	**VPC**
PAA	60.0	0.347	0.404		26.26	26.78	26.86	26.34

A.2 Mean Flow Field

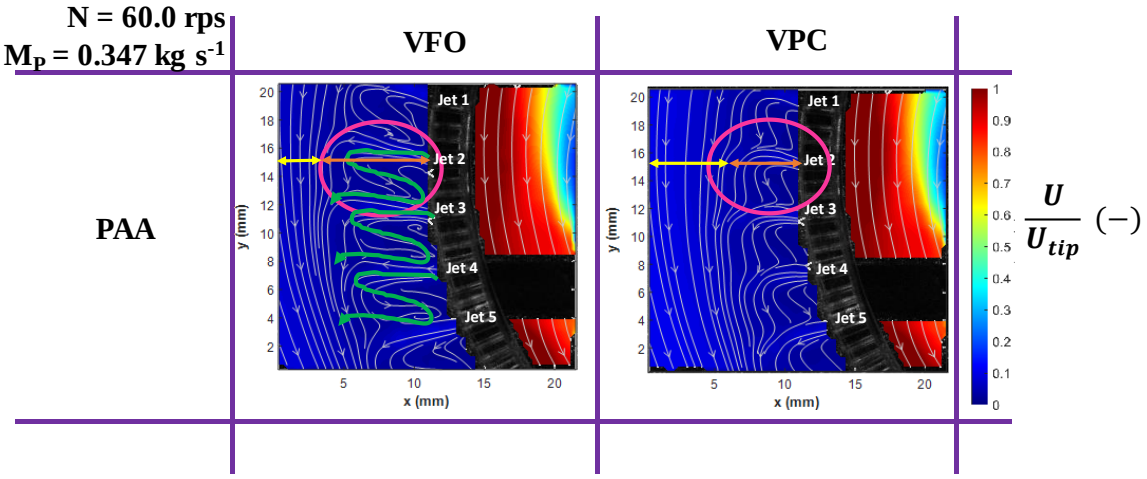

Figure A.1: Mean velocity field plots and accompanying streamlines at VFO and VPC conditions for PAA solution when N = 60.0 rps and M_P = 0.347 kg s^{-1}

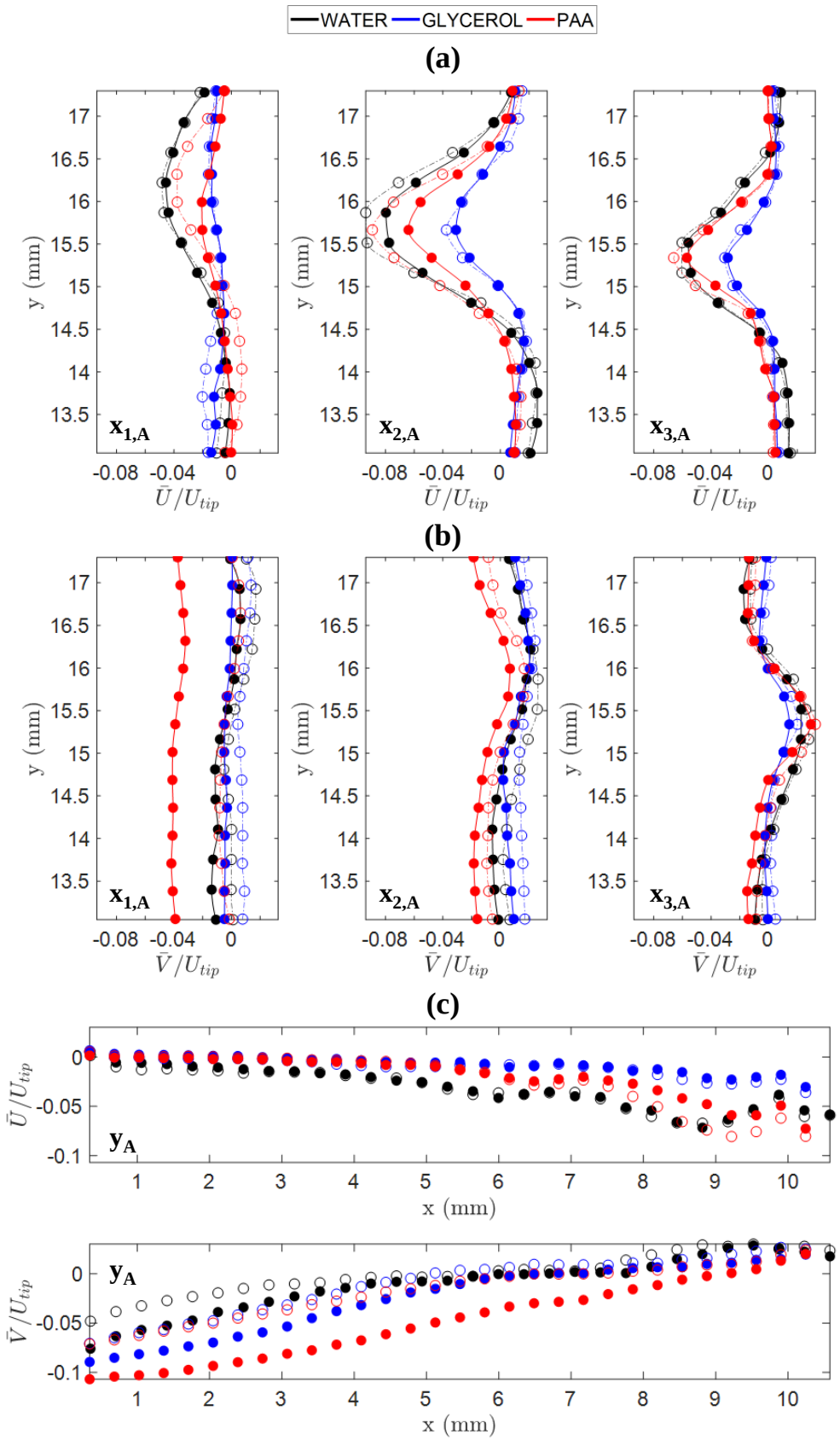

Figure A.2: : Mean velocity profiles normalised with rotor tip speed in ROI A for water, glycerol and PAA solutions: (a) *x*-velocity profiles at $x_{1,A}$ (left), $x_{2,A}$ (centre) and $x_{3,A}$ (right) (b) *y*-velocity profiles at $x_{1,A}$ (left), $x_{2,A}$ (centre) and $x_{3,A}$ (right) (c) *x*- (top) and *y*- (bottom) velocity profiles at y_A. Open and closed symbols as well as dash-dot (-.) and solid (-) (eye) guidelines denote VFO and VPC conditions

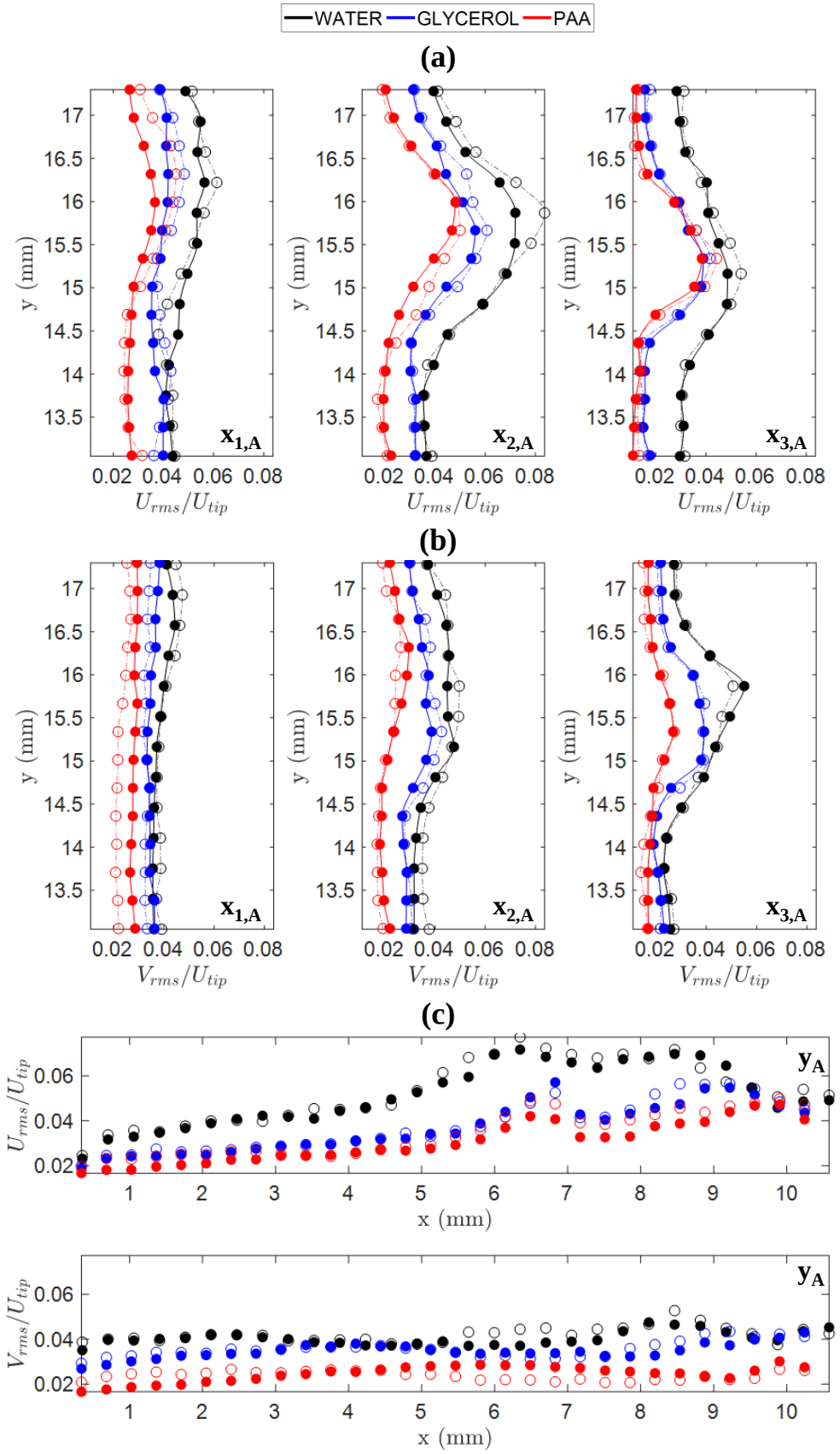

Figure A.3: Root mean square velocity (RMS) profiles normalised with rotor tip speed in ROI A for water, glycerol and PAA solutions : (a) *x*-velocity profiles at $x_{1,A}$ (left), $x_{2,A}$ (centre) and $x_{3,A}$ (right) (b) *y*-velocity profiles at $x_{1,A}$ (left), $x_{2,A}$ (centre) and $x_{3,A}$ (right) (c) *x*- (top) and *y*- (bottom) velocity profiles at y_A. Open and closed symbols as well as dash-dot (-.) and solid (-) (eye) guidelines denote VFO and VPC conditions

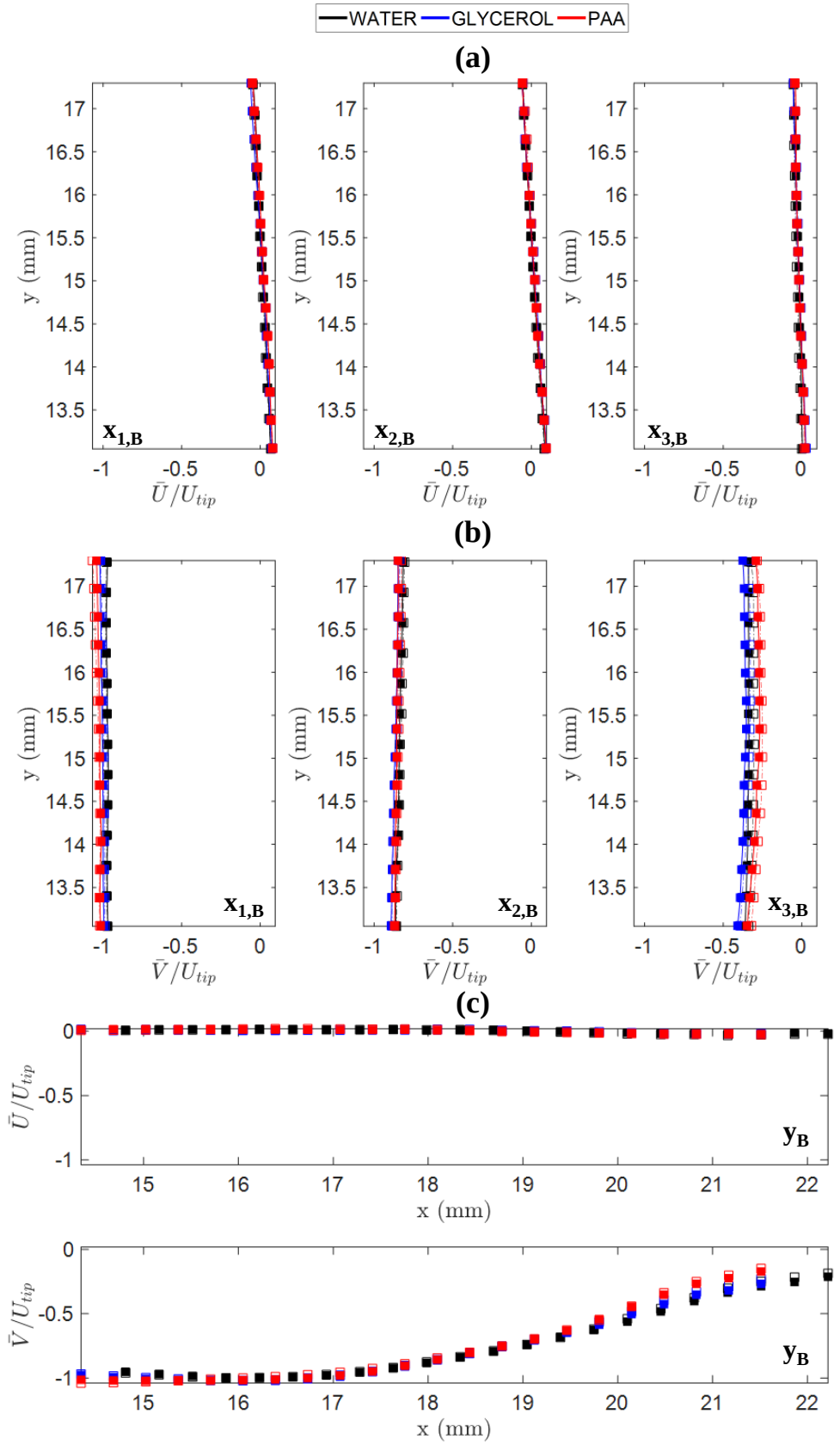

Figure A.4: Mean velocity profiles normalised with rotor tip speed in ROI B for water, glycerol and PAA solutions: (a) *x*-velocity profiles at $x_{1,B}$ (left), $x_{2,B}$ (centre) and $x_{3,B}$ (right) (b) *y*-velocity profiles at $x_{1,B}$ (left), $x_{2,B}$ (centre) and $x_{3,B}$ (right) (c) *x*- (top) and *y*- (bottom) velocity profiles at y_B. Open and closed symbols as well as dash-dot (-.) and solid (-) (eye) guidelines denote VFO and VPC conditions

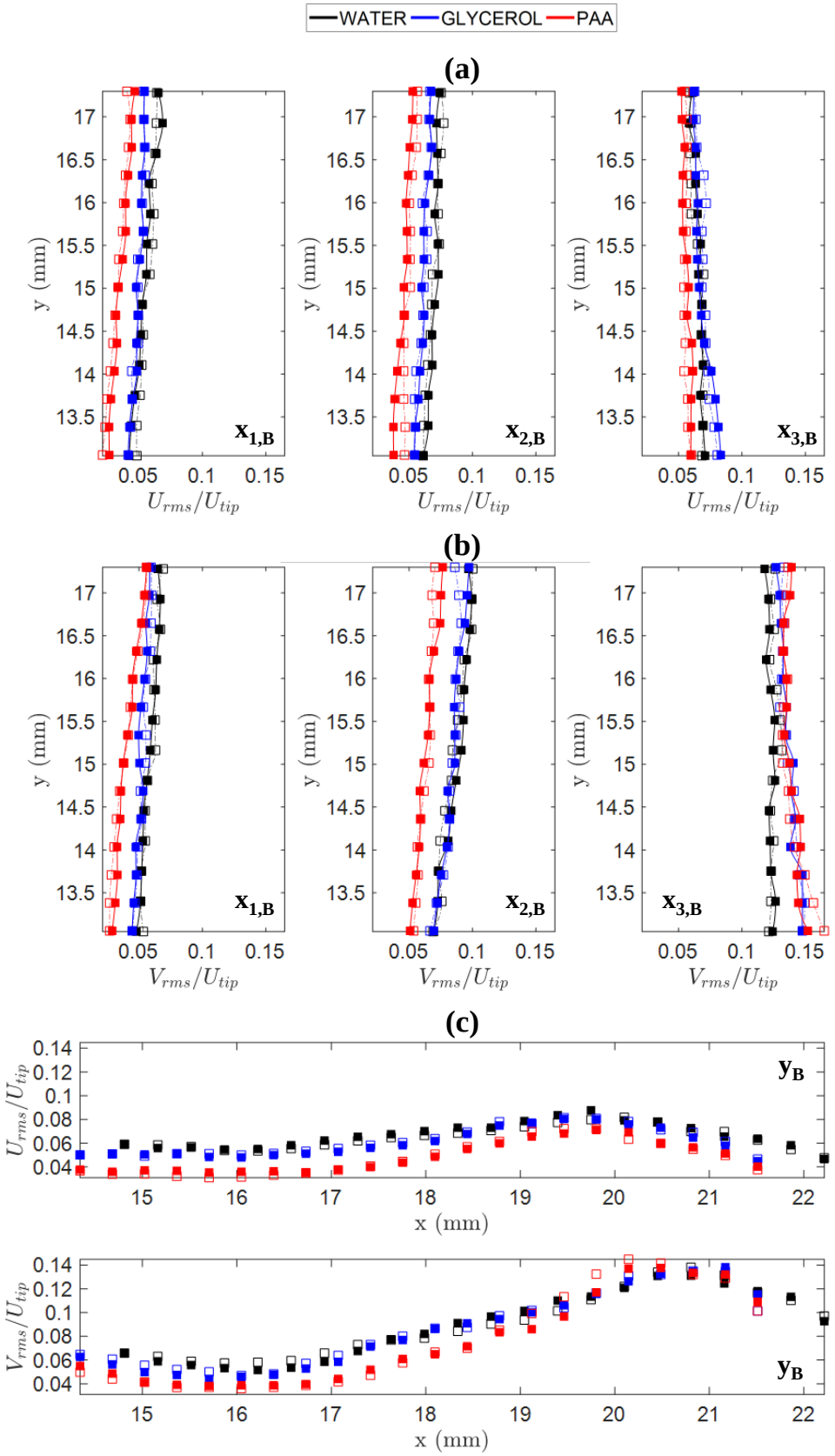

Figure A.5: Root mean square velocity (RMS) profiles normalised with rotor tip speed in ROI B for water, glycerol and PAA solutions : (a) *x*-velocity profiles at $x_{1,B}$ (left), $x_{2,B}$ (centre) and $x_{3,B}$ (right) (b) *y*-velocity profiles at $x_{1,B}$ (left), $x_{2,B}$ (centre) and $x_{3,B}$ (right) (c) *x*- (top) and *y*- (bottom) velocity profiles at y_B. Open and closed symbols as well as dash-dot (-.) and solid (-) (eye) guidelines denote VFO and VPC conditions

A.3 Kinetic Energy and Turbulent Kinetic Energy Dissipation

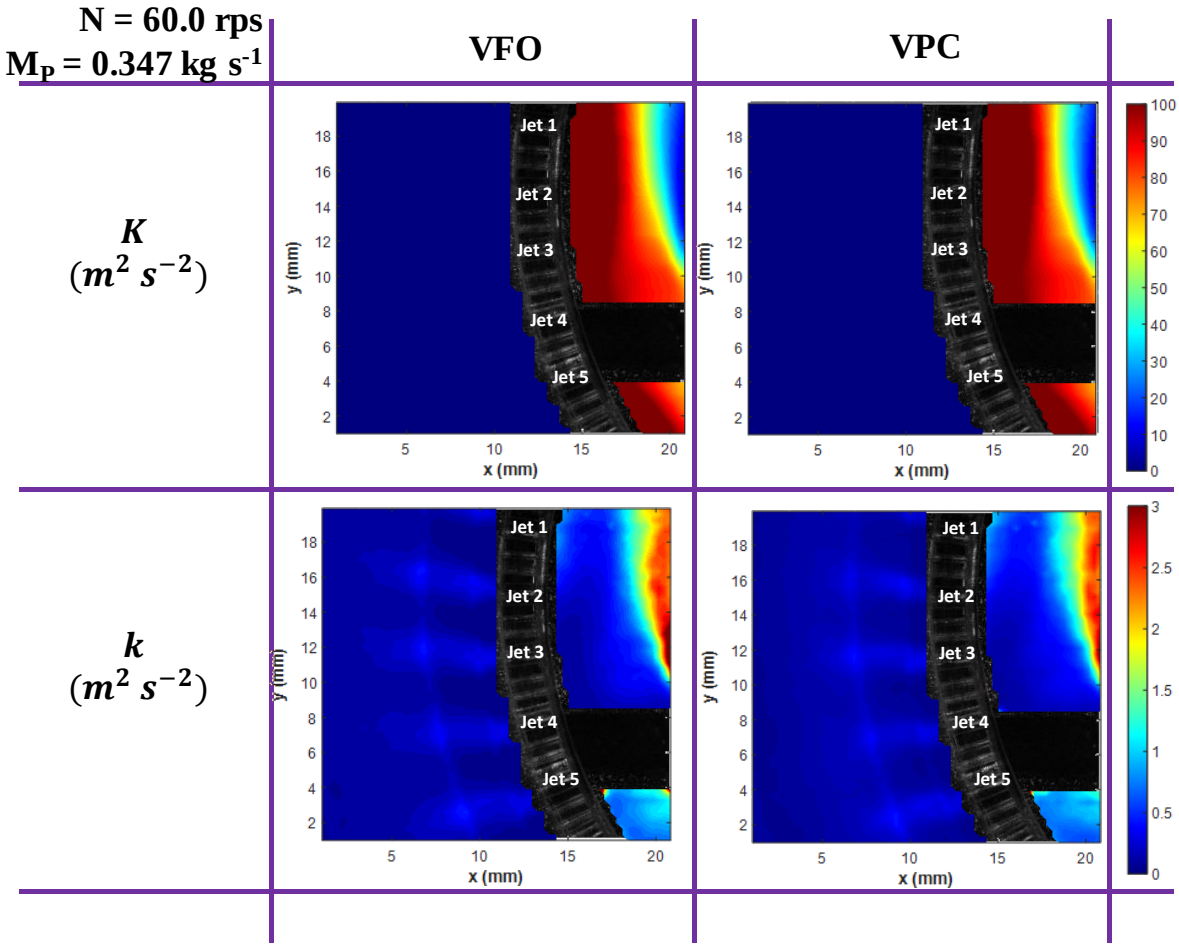

Figure A.6: Mean flow kinetic energy field plots (top) and turbulent kinetic energy field plots (bottom) at VFO and VPC conditions for PAA when N = 60.0 rps and M_P = 0.347 kg s^{-1}

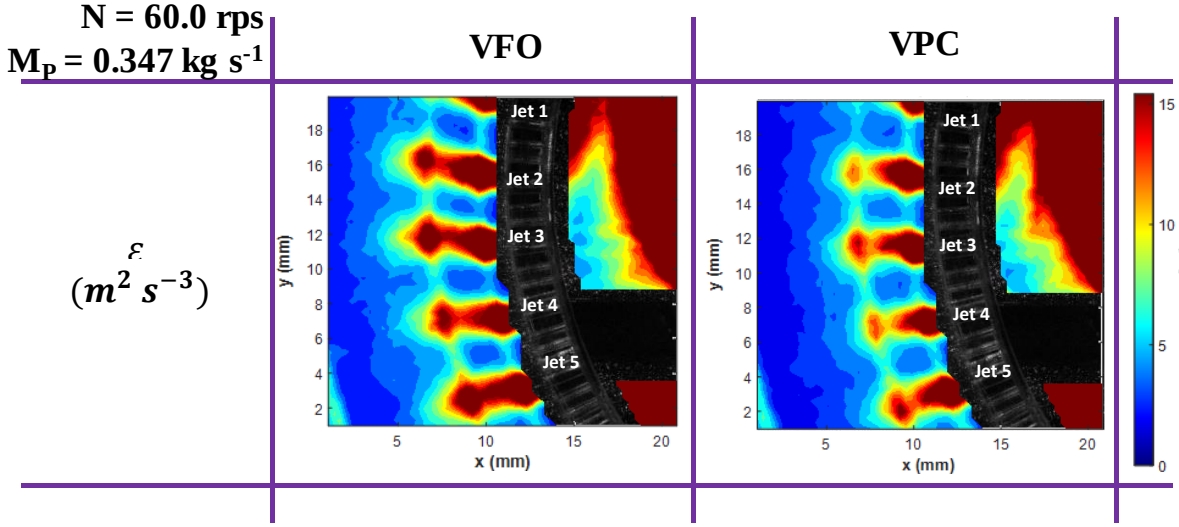

Figure A.7: Mean turbulent kinetic energy dissipation rate field plots at VFO and VPC conditions for PAA when N = 60.0 rps and M_P = 0.347 kg s^{-1}

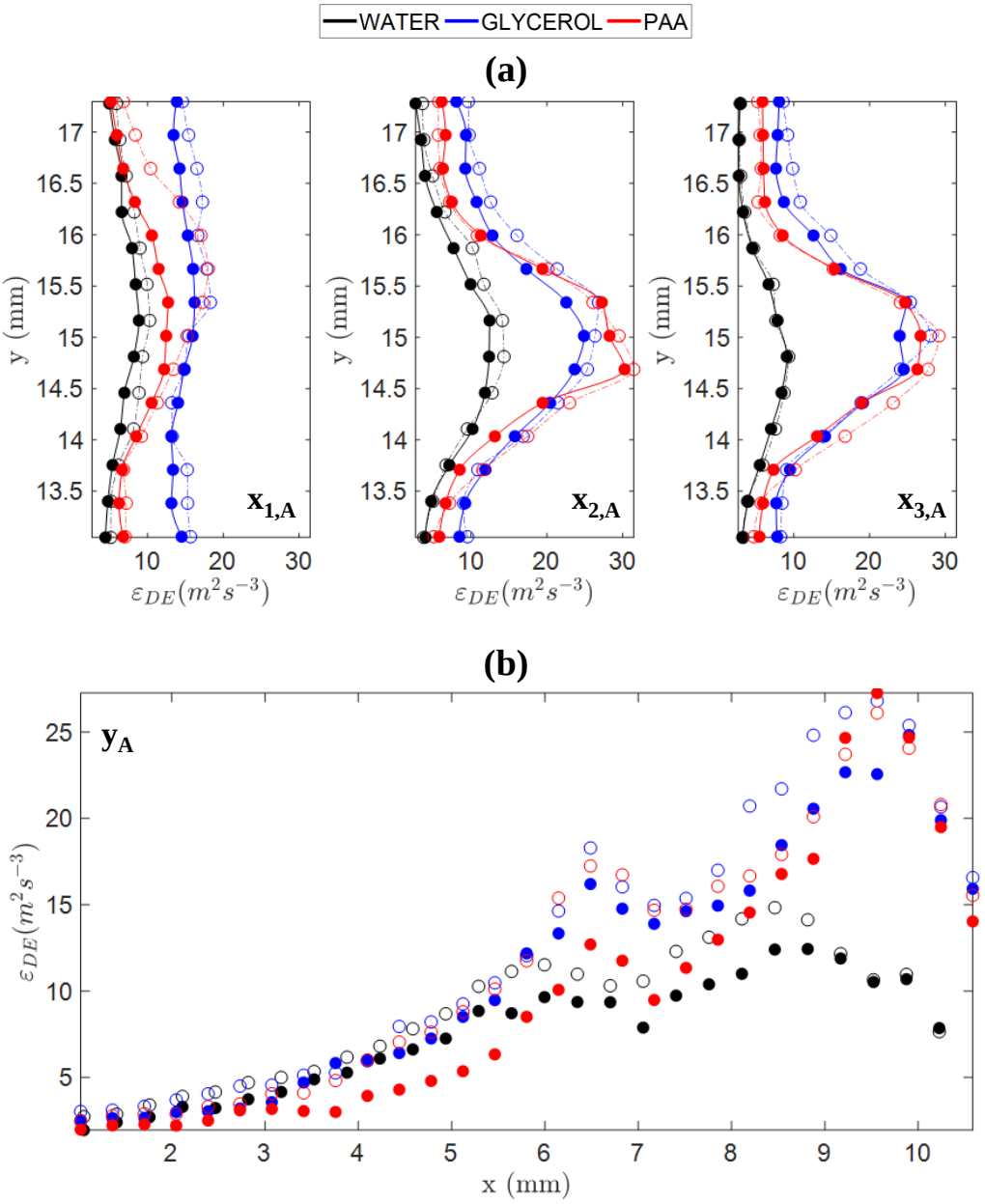

Figure A.8: Mean local specific turbulent kinetic energy dissipation rate profiles in ROI A for water, glycerol and PAA solutions at (a) $x_{1,A}$ (left), $x_{2,A}$ (centre) and $x_{3,A}$ (right) and at (b) y_A. Open and closed symbols as well as dash-dot (-.) and solid (-) (eye) guidelines denote VFO and VPC conditions

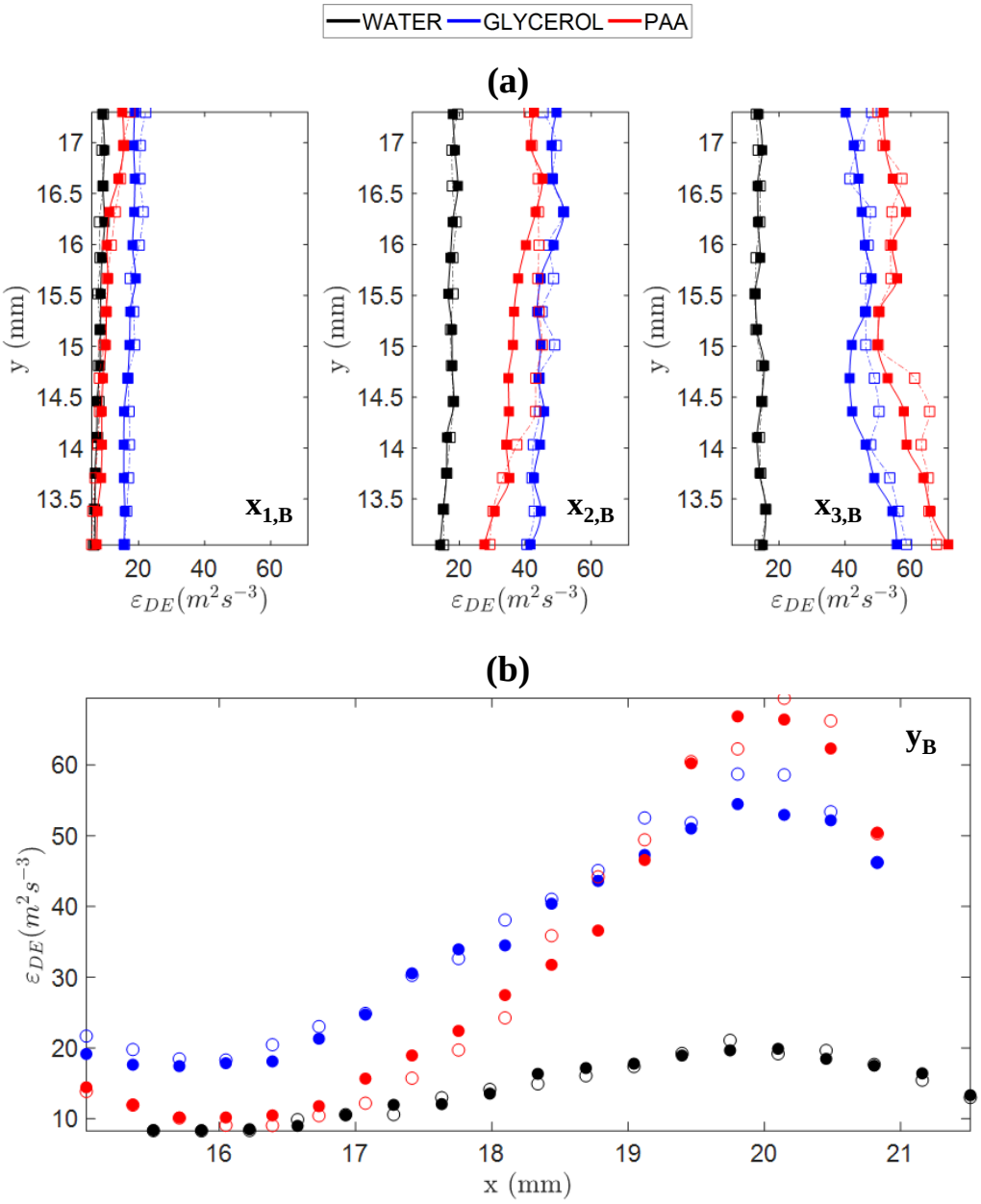

Figure A.9: Mean local specific turbulent kinetic energy dissipation rate profiles in ROI B for water, glycerol and PAA solutions at (a) $x_{1,B}$ (left), $x_{2,B}$ (centre) and $x_{3,B}$ (right) and at (b) y_B. Open and closed symbols as well as dash-dot (-.) and solid (-) (eye) guidelines denote VFO and VPC conditions

A.4 Gradient Contributions

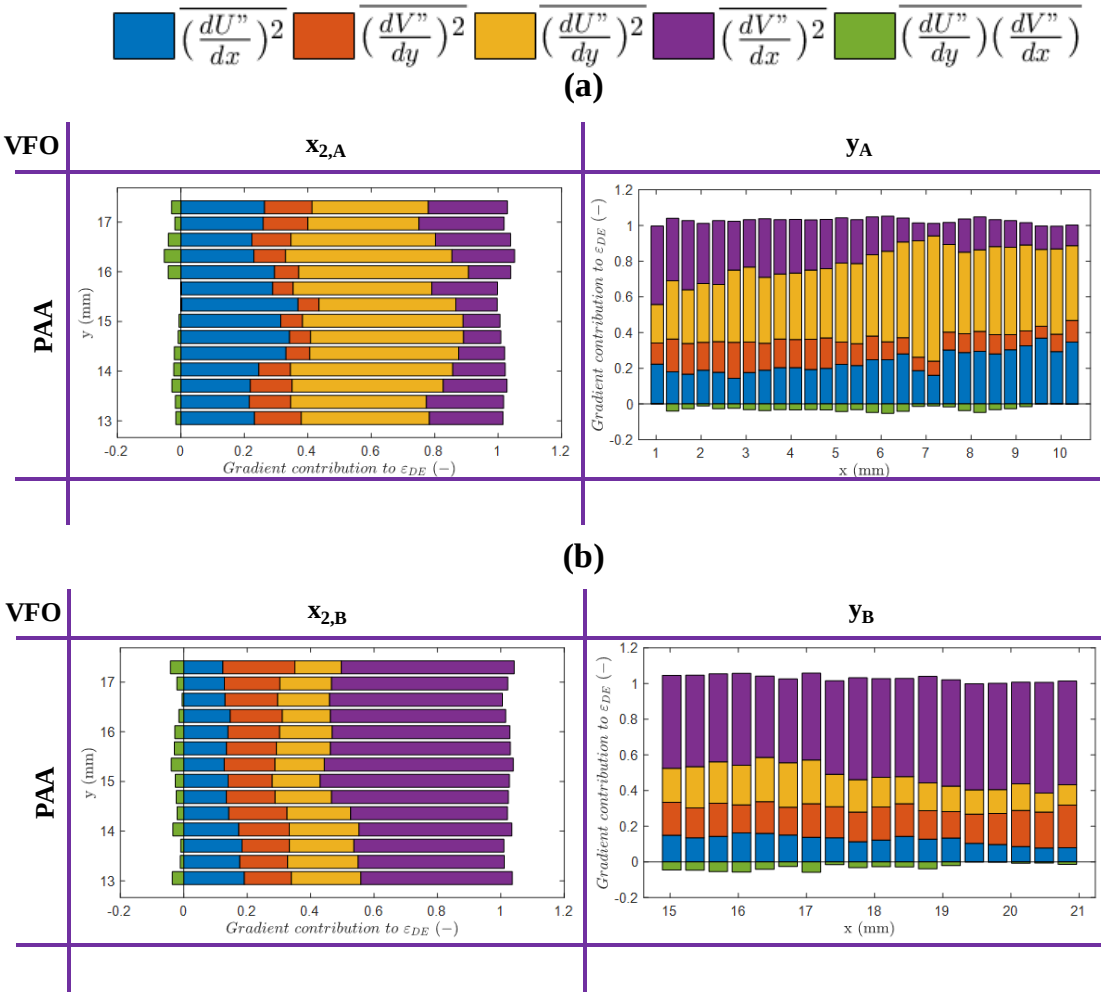

Figure A.10: Contribution profiles of the velocity gradients to the calculated local specific turbulent kinetic energy dissipation rates in (a) ROI A at $x_{2,A}$ and y_A and (b) ROI B at $x_{2,B}$ and y_B for PAA

A.5 Turbulence Intensity

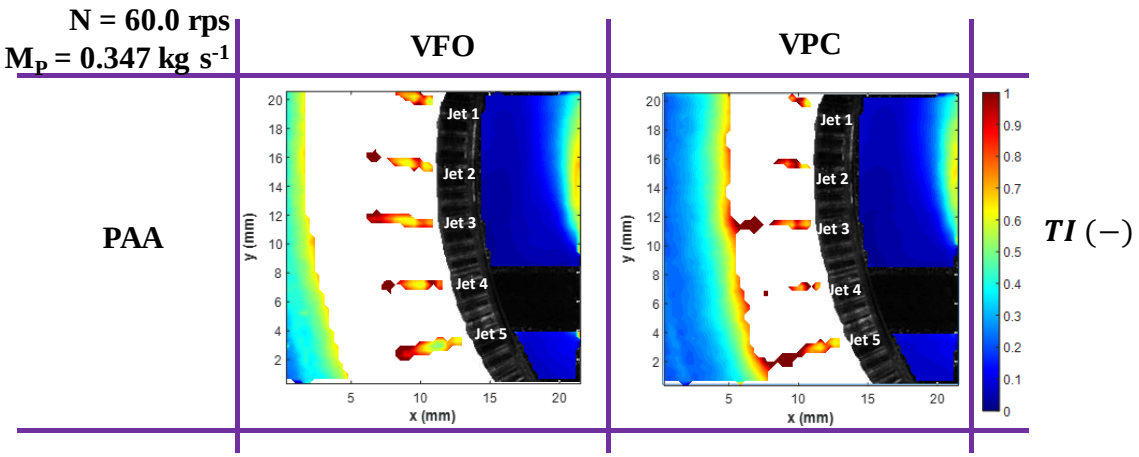

Figure A.11: Turbulence intensity plots for PAA

B: Oscillatory Rheology Data for Similar Shampoo Formulations to SB

B.1 Amplitude Sweep

Figure B.1: Amplitude sweep data for shampoo formulations with similar composition to SB with varying concentrations of NaCl (1 wt% (left) and 2 wt% (right)). Data source is from an Embedding Manufacturing Development into Formulation Research (EMFormR*) project internal report

G' – elastic modulus (Pa)
G'' – viscous modulus (Pa)
δ° – phase angle (degree)
η^* – complex viscosity (Pa s)

*Collaborative project between Johnson Matthey (JM), Unilever (UL), ITS Ltd., University of Birmingham (UoB) and University of Manchester (UoM) EPSRC Reference: EP/L505778/1

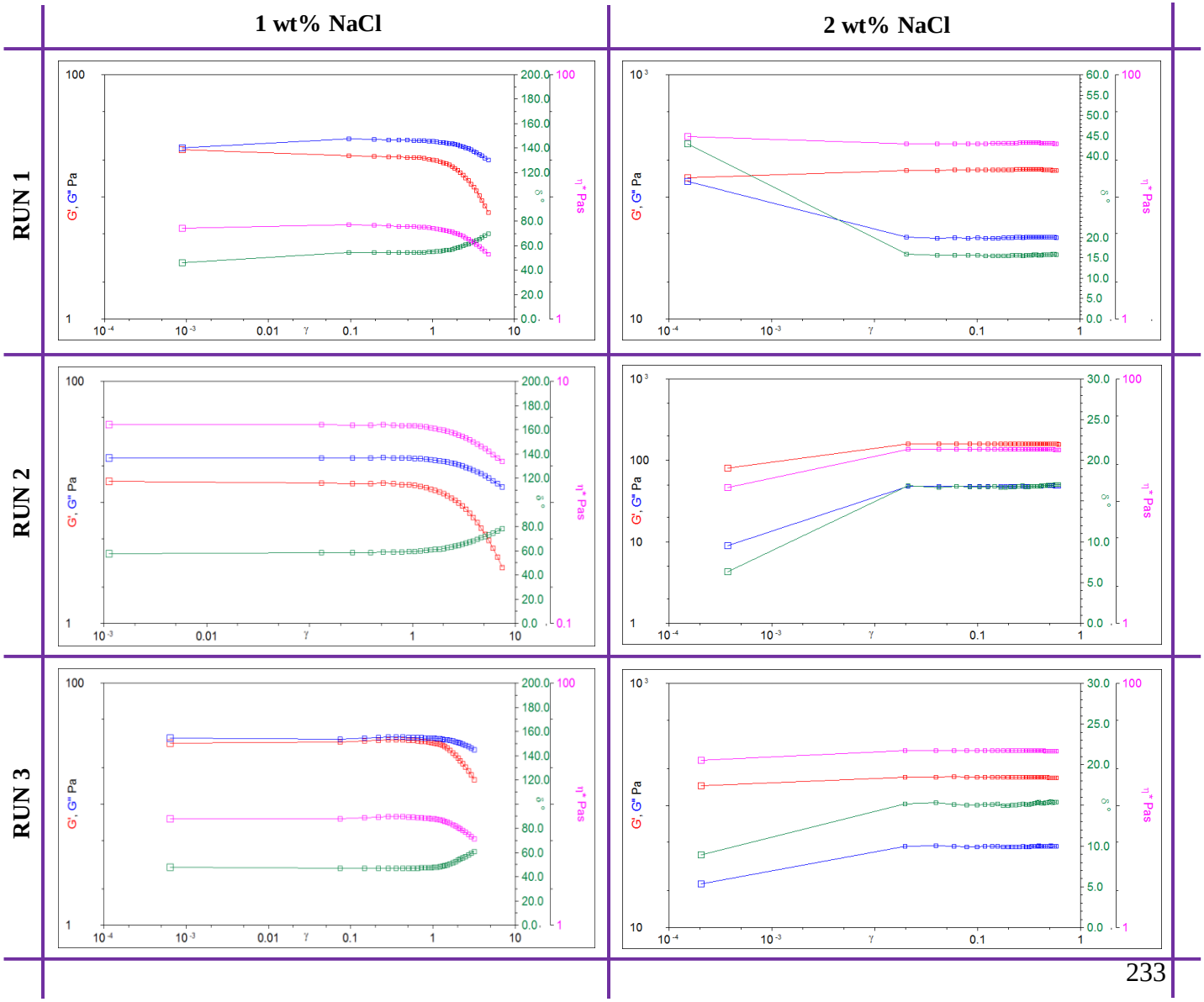

B.2 Frequency Sweep

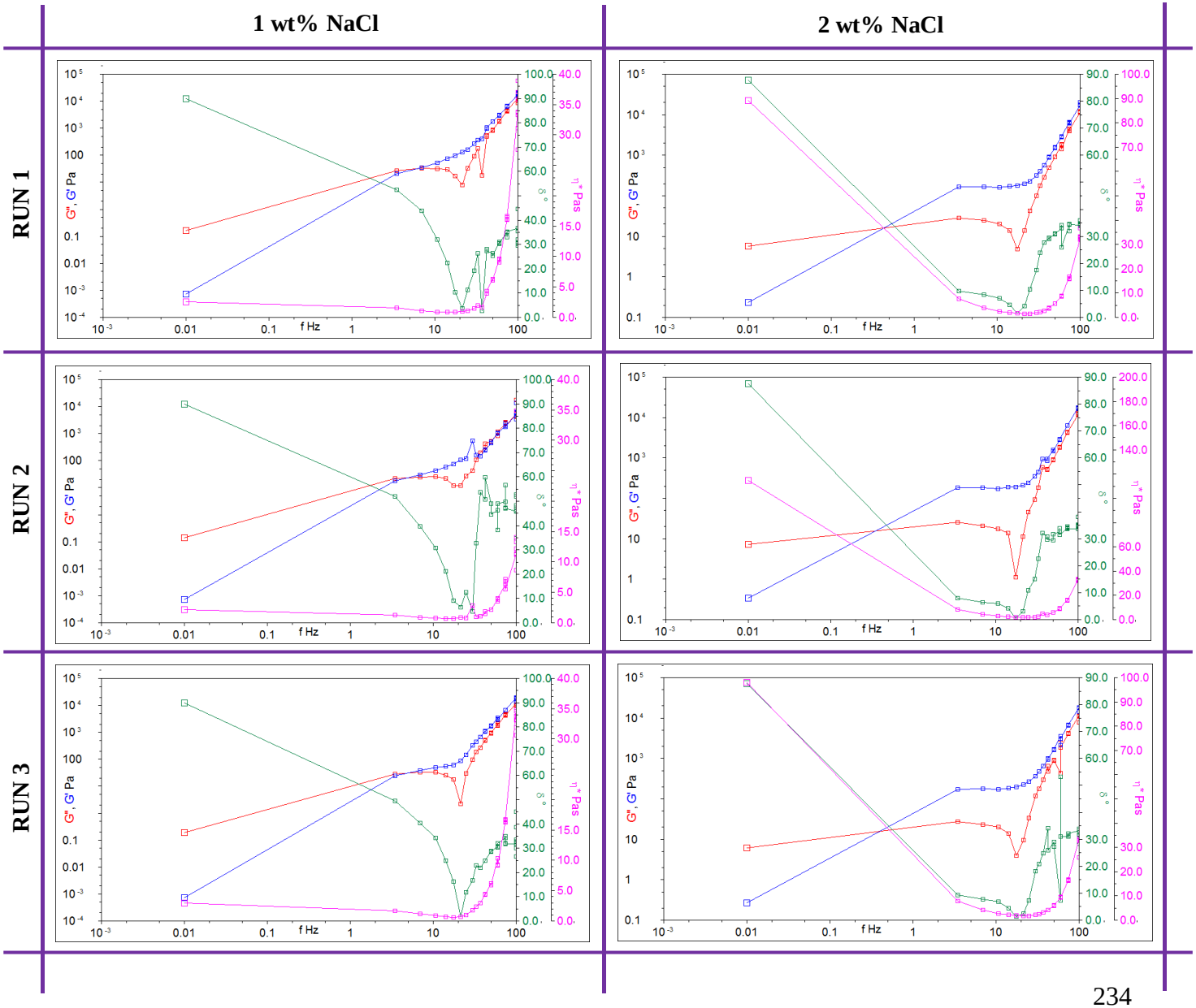

Figure B.2: Frequency sweep data for shampoo formulations with similar composition to SB with varying concentrations of NaCl (1 wt% (left) and 2 wt% (right)). Data source is from an Embedding Manufacturing Development into Formulation Research (EMFormR*) project internal report

G' – elastic modulus (Pa)
G'' – viscous modulus (Pa)
δ° – phase angle (degree)
η^{*} – complex viscosity (Pa s)

*Collaborative project between Johnson Matthey (JM), Unilever (UL), ITS Ltd., University of Birmingham (UoB) and University of Manchester (UoM) EPSRC Reference: EP/L505778/1

C: Investigation of Cut-Off Velocity

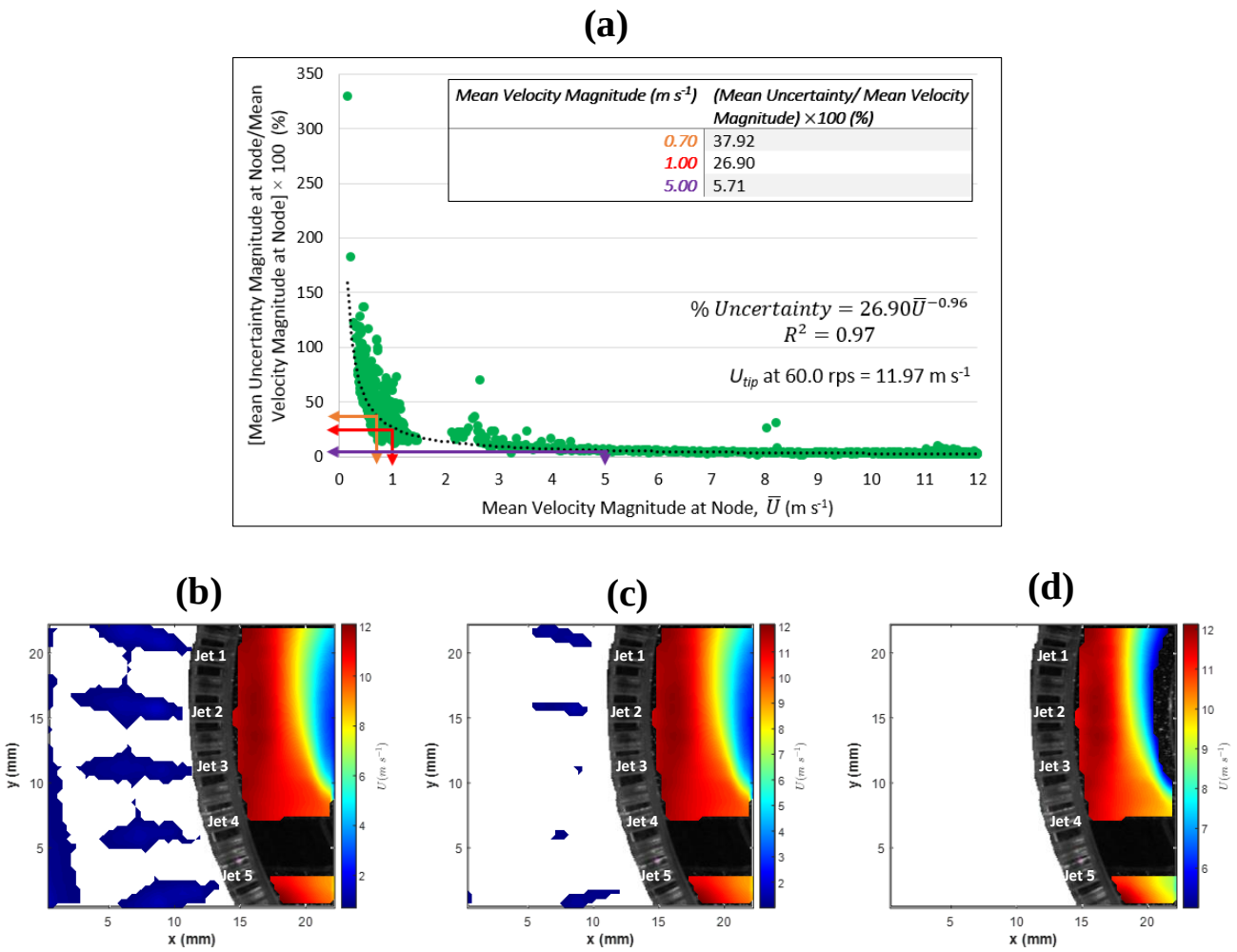

Figure C.1: (a) % of mean uncertainty magnitude at the node w. r. t. the mean velocity magnitude at that node versus the mean velocity magnitude at that node when N = 60.0 rps; M_P = 0.347 kg s^{-1} (VFO) for water and the corresponding velocity plots when cut-off velocities have been applied: (b) 0.70 m s^{-1}, (c) 1.00 m s^{-1}, (d) 5.00 m s^{-1}

References

Abdel-Rahman, A. (2010) A Review of Effects of Initial and Boundary Conditions on Turbulent Jets. **WSEAS Transactions on Fluid Mechanics**, 5.

Abu-Jdayil, B., Mohameed, H.A., Sa'id, M., et al. (2004) Rheological Characterization of Hair Shampoo in the Presence of Dead Sea Salt. **International Journal of Cosmetic Science**, 26 : 19-29.

Adrian, R.J. (1986) Image shifting technique to resolve directional ambiguity in double-pulsed velocity. **Appl Opt**, 25: (21): 3855-3858.

Adrian, R.J. and Westerweel, J. (2011) **Particle Image Velocimetry**. New York, USA: Cambridge University Press.

Ahmed, J., Ptaszek, P. and Basu, S. (2017) "6.1.1.1 Extensional Flow in Food Industry". **Advances in Food Rheology and its Applications**. Elsevier.

Ahmed, U., Michael, V., Hou, R., et al. (2018) An energy transport based evolving rheology in high-shear rotor–stator mixers. **Chemical Engineering Research and Design**, 133: 398-406.

Alberini, F. (2013) **Blending of non-Newtonian Fluids in Static Mixers: Assessment via Optical Methods**. PhD, University of Birmingham.

Alberini, F., Liu, L., Stitt, E.H., et al. (2017) Comparison between 3-D-PTV and 2-D-PIV for determination of hydrodynamics of complex fluids in a stirred vessel. **Chemical Engineering Science**, 171: 189-203.

Amin, S., Blake, S., Kennel, R.C., et al. (2015) Revealing New Structural Insights from Surfactant Micelles through DLS, Microrheology and Raman Spectroscopy. **Materials**, 8: (6): 3754-3766.

Ancey, C. (2005) **Notebook: Introduction to Fluid Rheology** [online]. http://lhe.epfl.ch/cours/doctorat/cours-DEA.pdf [Accessed 4 May 2015]

Anton-Paar (2019) **Basics of Rheology** [online]. https://wiki.anton-paar.com/en/basics-of-rheology/ [Accessed 23 August 2019]

Armenante, P.M. (2008) **Special Topics - Modules in Pharmaceutical Engineering ChE 702: Liquid Mixing Fundamentals** [online]. https://pharmahub.org/resources/295/download/NJIT_Module-Liquid_Mixing_Fundamentals-Armenante.ppt [Accessed 27 August 2019]

Arora, K., Sureshkumar, R., Scheiner, M.P., et al. (2002) Surfactant-induced effects on turbulent swirling flows. **Rheologica Acta**, 41: (1): 25-34.

Ashar, M., Arlov, D., Carlsson, F., et al. (2018) Single droplet breakup in a rotor-stator mixer. **Chemical Engineering Science**, 181: 186-198.

Atiemo-Obeng, V.A. and Calabrese, R.V. (2004) "Rotor-stator mixing devices". In Paul, E.L., Atiemo-Obeng, Victor A., Kresta, Suzanne M. (Ed.) **Handbook of Industrial Mixing**. John Wiley & Sons, Inc. pp. 479-505.

Atkins, M.D. (2016) "Chapter 5 - Velocity Field Measurement Using Particle Image Velocimetry (PIV)". In Kim, T.;Lu, T.J. & Song, S.J. (Eds.) **Application of Thermo-Fluidic Measurement Techniques**. Butterworth-Heinemann 125-166.

Aubin, J., Le Sauze, N., Bertrand, J., et al. (2004) PIV measurements of flow in an aerated tank stirred by a down- and an up-pumping axial flow impeller. **Experimental Thermal and Fluid Science**, 28: (5): 447-456.

Baker, M.R. (1993) Droplet breakup using in-line mixers located in recirculation loops around batch vessels. **Chemical Engineering Science**, 48: (22): 3829-3833.

Bakshi, U.A. and Godse, A.P. (2007) **Basic Electrical and Electronics Engineering**. Pune, India: Technical Publications Pune.

Baldi, S., Ducci, A. and Yianneskis, M. (2004) Determination of Dissipation Rate in Stirred Vessels Through Direct Measurement of Fluctuating Velocity Gradients. **Chemical Engineering & Technology**, 27: (3): 275-281.

Baldi, S. and Yianneskis, M. (2003) On the Direct Measurement of Turbulence Energy Dissipation in Stirred Vessels with PIV. **Industrial & Engineering Chemistry Research**, 42: (26): 7006-7016.

Bematek (2019) **Introduction to Colloid Mills** [online]. https://www.bematek.com/docs/colloidal-mills/BR-32-003A_Intro%20to%20Colloid%20Mills%20(7-19-16).pdf [Accessed 20 August 2019]

Bhushan, B. (2013) **Introduction to Tribology**. 2nd Edition.New York: John Wiley & Sons Ltd.

Bonn, D., Rodts, S., Groenink, M., et al. (2008) Some Applications of Magnetic Resonance Imaging in Fluid Mechanics: Complex Flows and Complex Fluids. **Annual Review of Fluid Mechanics**, 40: (1): 209-233.

Bourne, J.R. and Studer, M. (1992) Fast reactions in rotor-stator mixers of different size. **Chemical Engineering and Processing: Process Intensification**, 31: (5): 285-296.

Brown, D.A.R., Jones, P.N., Middleton, J.C., et al. (2004) "Experimental Methods". In Paul, E.L., Atiemo-Obeng, Victor A., Kresta, Suzanne M. (Ed.) **Handbook of Industrial Mixing**. John Wiley & Sons Inc. pp. 145-256.

Calabrese, R., Francis, M., Kevala, K., et al. (2002) Fluid dynamics and emulsification in high shear mixers. **Proceedings of the 3rd World Congress on Emulsions**.

Calabrese, R.V., Chang, T.P.K. and Dang, P.T. (1986) Drop breakup in turbulent stirred-tank contactors. Part I: Effect of dispersed-phase viscosity. **AIChE Journal**, 32: (4): 657-666.

Calabrese, R.V., Francis, M.K., Mishra, V.P., et al. (2000) "Chapter 19 - Measurement and Analysis of Drop Size in a Batch Rotor-Stator Mixer". In van den Akker, H.E.A. & Derksen, J.J. (Eds.) **10th European Conference on Mixing**. Amsterdam, Elsevier Science 149-156.

Carrillo De Hert, S. and Rodgers, T.L. (2017) Continuous, recycle and batch emulsification kinetics using a high-shear mixer. **Chemical Engineering Science**, 167: 265-277.

Casugbo, C. and Baker, M.R. (2018) Pumping capacity of inline dynamic mixers and its effect on process flow control. **Chemical Engineering Research and Design**, 132: 982-988.

Chan, C.W., Seville, J., Fan, X., et al. (2009) Solid particle motion in a standpipe as observed by Positron Emission Particle Tracking. **Powder Technology**, 194: (1): 58-66.

Chang, Q. (2016) "Chapter 11 - Emulsion, Foam, and Gel". In Chang, Q. (Ed.) **Colloid and Interface Chemistry for Water Quality Control**. Academic Press 227-245.

Charonko, J.J. and Vlachos, P.P. (2013) Estimation of uncertainty bounds for individual particle image velocimetry measurements from cross-correlation peak ratio. **Measurement Science and Technology**, 24: (6): 065301.

Chhabra, R. and Shankar, V. (2018) "3.2 The Nature of Fluid Flow". **Coulson and Richardson's Chemical Engineering, Volume 1A - Fluid Flow - Fundamentals and Applications (7th Edition)**. Elsevier.

Chhabra, R.P. and Richardson, J.F. (1999) "Chapter 1 - Non-Newtonian fluid behaviour". In Chhabra, R.P. & Richardson, J.F. (Eds.) **Non-Newtonian Flow in the Process Industries**. Oxford, Butterworth-Heinemann 1-36.

Chin, C.S. (2013) **Computer-Aided Control Systems Design: Practical Applications using MATLAB and Simulink**. Boca Raton, Florida: CRC Press.

Chiti, F., Bakalis, S., Bujalski, W., et al. (2011) Using positron emission particle tracking (PEPT) to study the turbulent flow in a baffled vessel agitated by a Rushton turbine: Improving data treatment and validation. **Chemical Engineering Research & Design - CHEM ENG RES DES**, 89: 1947-1960.

Cooke, M., Rodgers, T.L. and Kowalski, A.J. (2012) Power consumption characteristics of an in-line silverson high shear mixer. **AIChE Journal**, 58: (6): 1683-1692.

D'Errico, J. (2005) **Surface fitting using gridfit** [online]. https://uk.mathworks.com/matlabcentral/fileexchange/8998-surface-fitting-using-gridfit MATLAB Central File Exchange [Accessed 29 October 2017]

Dalgleish, D., G. (2001) "Food Emulsions". In Sjoblom, J. (Ed.) **Encyclopedic Handbook of Emulsion Technology**. CRC Press 207-232.

Dantec Dynamics (2019a) **Measurement Principles of LDA** [online]. https://www.dantecdynamics.com/measurement-principles-of-lda [Accessed 26 August 2019]

Dantec Dynamics (2019b) **Measurement Principles of PIV** [online]. https://www.dantecdynamics.com/measurement-principles-of-piv [Accessed 21 August 2019]

Dantec Dynamics (2019c) **Seeding Materials** [online]. https://www.dantecdynamics.com/seeding-materials [Accessed 26 July 2019]

Davies, J.T. (1985) Drop sizes of emulsions related to turbulent energy dissipation rates. **Chemical Engineering Science**, 40: (5): 839-842.

Davies, J.T. (1987) A Physical Interpretation of Drop Sizes in Homogenisers and Agitated Tanks, Including the Dispersion of Viscous Oils. **Chemical Engineering Science**, 42: (7): 1671-1676.

Delafosse, A., Collignon, M.-L., Crine, M., et al. (2011) Estimation of the turbulent kinetic energy dissipation rate from 2D-PIV measurements in a vessel stirred by an axial Mixel TTP impeller. **Chemical Engineering Science**, 66: 1728-1737.

Dubey, D., Malviya, R. and Sharma, P.K. (2014) Evaluation of Marketed Shampoo (Synthetic and Natural) for Their Hair Cleansing, Dirt Dispersion, Wetting Time, Solid Content and Foaming Capacity Properties. **Global Journal of Pharmacology**, 8: (4): 490 - 493.

Earle, R.L. (1983) "Chapter 11 - Size Reduction". In Earle, R.L. (Ed.) **Unit Operations in Food Processing (Second Edition)**. Amsterdam, Pergamon 159-165.

Espinoza, C.J.U., Simmons, M.J.H., Alberini, F., et al. (2018) Flow studies in an in-line Silverson 150/250 high shear mixer using PIV. **Chemical Engineering Research and Design**, 132: 989-1004.

Fardin, M.A., Lopez, D., Croso, J., et al. (2010) Elastic Turbulence in Shear Banding Wormlike Micelles. **Physical Review Letters**, 104: (17): 178303.

Fishwick, R., Winterbottom, M., Parker, D., et al. (2005) The Use of Positron Emission Particle Tracking in the Study of Multiphase Stirred Tank Reactor Hydrodynamics. **The Canadian Journal of Chemical Engineering**, 83: (1): 97-103.

Free, M.L. (2008) "Chapter 1 - Introduction to Surfactants". In Biresaw, G. & Mital, K.L. (Eds.) **Surfactants in Tribology**. CRC Press.

Fryer, P., Pyle, D.L. and Rielly, C.D. (1996) **Chemical Engineering for the Food Industry**. Boston, MA, USA: Springer.

Gabelle, J.-C., Morchain, J., Anne-Archard, D., et al. (2013) Experimental determination of the shear rate in a stirred tank with a non-newtonian fluid: Carbopol. **AIChE Journal**, 59: (6): 2251-2266.

Gabriele, A., Nienow, A.W. and Simmons, M.J.H. (2009) Use of angle resolved PIV to estimate local specific energy dissipation rates for up- and down-pumping pitched blade agitators in a stirred tank. **Chemical Engineering Science**, 64: 126-143.

Garti, N. and Lutz, R. (2006) "Double Emulsions". In Somasundaran, P. (Ed.) **Encyclopedia of Surface and Colloid Science**. 2nd ed. Boca Raton, Taylor & Francis.

George, W.K. (2013) **Lectures in Turbulence for the 21st Century** [online]. https://www.uio.no/studier/emner/matnat/math/MEK4300/v13/undervisningsmateriale/tb_16january2013.pdf [Accessed

Gingras, J.-P., Tanguy, P., Mariotti, S., et al. (2005) Effect of Process Parameters on Bitumen Emulsions. **Chemical Engineering and Processing: Process Intensification**, 44: 979-986.

Govender, I., Morrison, A.J., Mainza, A., et al. (2010) Using positron emission particle tracking (PEPT) to investigate industrial systems. **XXV International Mineral Processing Congress 2010, IMPC 2010**, 4.

Gubitosa, J., Rizzi, V., Fini, P., et al. (2019) Hair Care Cosmetics: From Traditional Shampoo to Solid Clay and Herbal Shampoo, A Review. **Cosmetics**, 6.

Hadri, F. and Guillou, S. (2010) DRAG REDUCTION BY SURFACTANT IN CLOSED TURBULENT FLOW. **International Journal of Engineering Science and Technology**, 2: 6876 - 6879.

Håkansson, A. (2018) Rotor-Stator Mixers: From Batch to Continuous Mode of Operation—A Review. **Processes**, 6: (4): 32.

Håkansson, A., Andersson, R., Mortensen, H.-H., et al. (2017a) Experimental investigations of turbulent fragmenting stresses in a rotor-stator mixer. Part 2. Probability distributions of instantaneous stresses. **Chemical Engineering Science**, 171: 638-649.

Håkansson, A., Arlov, D., Carlsson, F., et al. (2017b) Hydrodynamic difference between inline and batch operation of a rotor-stator mixer head - A CFD approach. **The Canadian Journal of Chemical Engineering**, 95: (4): 806-816.

Håkansson, A. and Innings, F. (2017) The dissipation rate of turbulent kinetic energy and its relation to pumping power in inline rotor-stator mixers. **Chemical Engineering and Processing**, 115: 46-55.

Håkansson, A., Mortensen, H.H., Andersson, R., et al. (2017c) Experimental investigations of turbulent fragmenting stresses in a rotor-stator mixer. Part 1. Estimation of turbulent stresses and comparison to breakup visualizations. **Chemical Engineering Science**, 171: 625-637.

Hall, S. (2012) **Scale-up of emulsification in in-line rotor-stator mixers**. PhD Thesis, University of Birmingham, UK.

Hall, S., Cooke, M., El-Hamouz, A., et al. (2011a) Droplet break-up by in-line Silverson rotor–stator mixer. **Chemical Engineering Science**, 66: 2068-2079.

Hall, S., Cooke, M., Pacek, A.W., et al. (2011b) Scaling up of silverson rotor–stator mixers. **The Canadian Journal of Chemical Engineering**, 89: (5): 1040-1050.

Hemrajani, R.R. and Tatterson, G.B. (2004) "Mechanically stirred vessels". In Paul, E.L., Atiemo-Obeng, Victor A., Kresta, Suzanne M. (Ed.) **Handbook of Industrial Mixing**. John Wiley & Sons, Inc. 345-390.

Herrera, M.L. (2012) **Analytical Techniques for Studying the Physical Properties of Lipid Emulsions**. New York: Springer.

Hinze, J.O. (1955) Fundamentals of the hydrodynamic mechanism of splitting in dispersion processes. **AIChE Journal**, 1: (3): 289-295.

Hinze, J.O. (1975) **Turbulence**. 2nd edition.New York: McGraw-Hill.

Hoque, M.M., Sathe, M.J., Mitra, S., et al. (2015) Comparison of specific energy dissipation rate calculation methodologies utilising 2D PIV velocity measurement. **Chemical Engineering Science**, 137: 752-767.

Horiba (2014) **A Guide to Particle Size Analysis** [online]. https://www.horiba.com/fileadmin/uploads/Scientific/eMag/PSA/Guidebook/pdf/PSA_Guidebook.pdf [Accessed 4 May 2015]

Huang, H., Dabiri, D. and Gharib, M. (1997) On errors of digital particle image velocimetry. **Measurement Science and Technology**, 8: (12): 1427-1440.

Hyde, M. (2015) **Personal Communication**.

Hyde, M. (2019) **Personal Communication**.

IKA (2019) [online]. https://www.ikaprocess.com/en [Accessed 20 August 2019]

Ingram, A., Hausard, M., Fan, X., et al. (2007) **Portable Positron Emission Particle Tracking (PEPT) for Industrial Use** [online]. https://dc.engconfintl.org/cgi/viewcontent.cgi?article=1110&context=fluidization_xii Vancouver, Canada [Accessed 10 September 2019 2019]

Inolex (2019) **Formulating Clear Conditioning Shampoo** [online]. https://caliscc.org/images/downloads/1_Formulating-Clear-Conditioning-Shampoos-Judy-Zhuang-Inolex.pdf [Accessed 12 September 2019]

Intelligent Laser Applications (2019) **PIV Synchroniser** [online]. https://www.velocimetry.net/downloads/PIVSynchroniser.pdf [Accessed 21 August 2019]

James, J., Cooke, M., Kowalski, A., et al. (2017a) Scale-up of batch rotor-stator mixers. Part 2—Mixing and emulsification. **Chemical Engineering Research and Design**, 124: 321-329.

James, J., Cooke, M., Trinh, L., et al. (2017b) Scale-up of batch rotor–stator mixers. Part 1—Power constants. **Chemical Engineering Research and Design**, 124: 313-320.

Jasińska, M., Bałdyga, J., Cooke, M., et al. (2013) Application of test reactions to study micromixing in the rotor-stator mixer (test reactions for rotor-stator mixer). **Applied Thermal Engineering**, 57: 172-179.

Jasińska, M., Bałdyga, J., Cooke, M., et al. (2015) Specific features of power characteristics of in-line rotor–stator mixers. **Chemical Engineering and Processing**, 91: 43-56.

Jones, J.R. and Bridgwater, J. (1998) A case study of particle mixing in a ploughshare mixer using Positron Emission Particle Tracking. **International Journal of Mineral Processing**, 53: (1): 29-38.

Joseph, M., Trinh, H.M. and Mitra, A.K. (2017) "Chapter 7 - Peptide and Protein-Based Therapeutic Agents⁎". In Mitra, A.K.;Cholkar, K. & Mandal, A. (Eds.) **Emerging Nanotechnologies for Diagnostics, Drug Delivery and Medical Devices**. Boston, Elsevier 145-167.

Kähler, C.J., Scharnowski, S. and Cierpka, C. (2012) On the resolution limit of digital particle image velocimetry. **Experiments in Fluids**, 52: (6): 1629-1639.

Karbstein, H. and Schubert, H. (1995) Developments in the continuous mechanical production of oil-in-water macro-emulsions. **Chemical Engineering and Processing: Process Intensification**, 34: (3): 205-211.

Khan, F.R. (2005) **Investigation of turbulent flows and instabilities in a stirred vessel using particle image velocimetry**. PhD Thesis, Loughborough University.

Khan, F.R., Rielly, C.D. and Hargrave, G.K. (2004) A Multi-Block Approach to Obtain Angle-Resolved PIV Measurements of the Mean Flow and Turbulence Fields in a Stirred Vessel. **Chemical Engineering & Technology**, 27: (3): 264-269.

Khan, M.K. (2015) "1.5 Classification of Flows". **Fluid Mechanics and Machinery**. Oxford University Press.

Kim, J.W. (2015) **Comparison between particle image velocimetry data and computational fluid dynamics simulations for an in-line slot and tooth rotor-stator mixer**. MSc Thesis, University of Maryland, College Park, MD, USA.

Kolmogorov, A.N. (1949) On the breakage of drops in a turbulent flow. **Dokaldy Akademii Nauk Uzbekskoi SSSR**, (66): 825-828 (Originally in Russian. Reprinted and translated in Selected Works of A.N. Kolmogorov, Volume 821: Mathematics and Mechanics, Tikhomirov, V.M. (Ed.), 1991, pp. 1339-1343.

Kowalski, A.J. (2009) An expression for the power consumption of in-line rotor-stator devices. **Chemical Engineering and Processing: Process Intensification**, 48: (1): 581-585.

Kowalski, A.J., Cooke, M. and Hall, S. (2011) Expression for turbulent power draw of an in-line Silverson high shear mixer. **Chemical Engineering Science**, 66: (3): 241-249.

Kuang, J., Wang, X.L., Lu, T., et al. (2015) Role of Laminar Length of Round Jet Impinging on Metal Foams. **Journal of Thermophysics and Heat Transfer**, 30: 1-8.

Kumar, K.R., Rankin, G.W. and Shidhar, K. (1984) Laminar length of a non-Newtonian fluid jet. **Journal of Non-Newtonian Fluid Mechanics**, 15: (1): 13-27.

Kutz, M. (2013) "44.4.3.2 Oscillatory Mode". **Handbook of Measurement in Science and Engineering, Volume 2**. John Wiley & Sons.

Kwon, S.J. and Seo, I.W. (2005) Reynolds number effects on the behavior of a non-buoyant round jet. **Experiments in Fluids**, 38: (6): 801-812.

Langford, S., Wiggins, C., Tenpenny, D., et al. (2016) Positron Emission Particle Tracking (PEPT) for Fluid Flow Measurements. **Nuclear Engineering and Design**, 302: 81-89.

Laurén, S. (2019) **Surface and interfacial tension - What is it and how to measure it? (White Paper)** [online]. https://www.atascientific.com.au/wp-content/uploads/2017/02/surface-and-interfacial-tension-what-is-it-and-how-to-measure-it.pdf Biolin Scientific [Accessed 6 August 2019]

Laurent, B.F.C. and Cleary, P.W. (2012) Comparative study by PEPT and DEM for flow and mixing in a ploughshare mixer. **Powder Technology**, 228: 171-186.

Lee, J.H.W. and Chu, V.H. (2003) "Turbulent Jets". **Turbulent Jets and Plumes: A Lagrangian Approach**. Boston, MA, Springer US 21-54.

Leng, D.E. and Calabrese, R.V. (2004) "Immiscible Liquid–Liquid Systems". In Paul, E.L.;Atiemo-Obeng, V.A. & Kresta, S.M. (Eds.) **Handbook of Industrial Mixing**. 639-753.

Lim, W.L., Chew, Y.T., Chew, T.C., et al. (1994) Particle image velocimetry in the investigation of flow past artificial heart valves. **Annals of Biomedical Engineering**, 22: (3): 307-318.

Liu, L. and Barigou, M. (2013) Numerical modelling of velocity field and phase distribution in dense monodisperse solid–liquid suspensions under different regimes of agitation: CFD and PEPT experiments. **Chemical Engineering Science**, 101: 837-850.

Lowe, H.C. (1979) "Flow in Ducts". **Fluid Mechanics: Theory, worked examples and problems**. London, Macmillan Education UK 156-188.

Mac Namara, C., Gabriele, A., Amador, C., et al. (2012) Dynamics of textile motion in a front-loading domestic washing machine. **Chemical Engineering Science**, 75: 14-27.

Malkin, A.Y. and Isayev, A.I. (2006) **Rheology: Concepts, Methods & Applications**. Toronto: ChemTec Publishing.

Malvern (2012) **A Basic Guide to Particle Characterisation** [online]. http://golik.co.il/Data/ABasicGuidtoParticleCharacterization(2)_1962085150.pdf [Accessed 4 May 2015]

Marigo, M., Davies, M., Leadbeater, T., et al. (2013) Application of Positron Emission Particle Tracking (PEPT) to validate a Discrete Element Method (DEM) model of granular flow and mixing in the Turbula mixer. **International Journal of Pharmaceutics**, 446: (1): 46-58.

Martin, J. and McCutcheon, S. (1999) **Hydrodynamics and Transport for Water Quality Modeling**. Boca Raton: CRC Press, Inc.

Mathieu, J. and Scott, J. (2000) **An Introduction to Turbulent Flow**. Cambridge: Cambridge University Press.

Mavros, P., Ricard, A., Xuereb, C., et al. (2011) A study of the effect of drag-reducing surfactants on flow patterns in stirred vessels. **Chemical Engineering Research and Design**, 89: (1): 94-106.

McClements, D.J. (2005) **Food Emulsions: Principles, Practices and Techniques**. Boca Raton, USA: CRC Press.

McKinley, G.H. and Sridhar, T. (2002) FILAMENT-STRETCHING RHEOMETRY OF COMPLEX FLUIDS. **Annual Review of Fluid Mechanics**, 34: (1): 375-415.

Metzner, A.B. and Otto, R.E. (1957) Agitation of non-Newtonian fluids. **AIChE Journal**, 3: (1): 3-10.

Middleman, S. (1998) **An introduction to fluid dynamics : principles of analysis and design**. New York: Wiley.

Mihailova, O. (2016) **Characterisation of Flow, Mixing and Changeover in SMX Static Mixers**. EngD, University of Birmingham.

Mihailova, O., Lim, V., McCarthy, M.J., et al. (2015) Laminar mixing in a SMX static mixer evaluated by positron emission particle tracking (PEPT) and magnetic resonance imaging (MRI). **Chemical Engineering Science**, 137: 1014-1023.

Mihailova, O., O'Sullivan, D., Ingram, A., et al. (2016) Velocity field characterization of Newtonian and non-Newtonian fluids in SMX mixers using PEPT. **Chemical Engineering Research and Design**, 108.

Minnick, B.A., Kim, J.W., Ko, D.I., et al. (2018) Flow and power characteristics of an axial discharge rotor-stator mixer. **Chemical Engineering Research and Design**, 136: 477-490.

Mitsui, T. (1997) **New Cosmetic Science**. Amsterdam, Netherlands: Elsevier Science B. V.

Mortensen, H.H., Calabrese, R.V., Innings, F., et al. (2011) Characteristics of batch rotor–stator mixer performance elucidated by shaft torque and angle resolved PIV measurements. **The Canadian Journal of Chemical Engineering**, 89: (5): 1076-1095.

Mortensen, H.H., Innings, F. and Håkansson, A. (2017) The effect of stator design on flowrate and velocity fields in a rotor-stator mixer—An experimental investigation. **Chemical Engineering Research and Design**, 121: 245-254.

Mortensen, H.H., Innings, F. and Håkansson, A. (2018) Local levels of dissipation rate of turbulent kinetic energy in a rotor–stator mixer with different stator slot widths—An experimental investigation. **Chemical Engineering Research and Design**, 130: 52-62.

Müller, C.R., Davidson, J.F., Dennis, J.S., et al. (2007) A Study of the Motion and Eruption of a Bubble at the Surface of a Two-Dimensional Fluidized Bed Using Particle Image Velocimetry (PIV). **Industrial & Engineering Chemistry Research**, 46: (5): 1642-1652.

Nienow, A.W., Harnby, N. and Edwards, M.F. (1997) "Chapter 1 - Introduction to Mixing Problems". In Harnby, N.;Edwards, M.F. & Nienow, A.W. (Eds.) **Mixing in the Process Industries**. Oxford, Butterworth-Heinemann 1-24.

Osswald, T. and Rudolph, N. (2015) "6. Rheometry". **Polymer Rheology - Fundamentals and Applications**. Hanser Publishers.

Osswald, T.A. and Menges, G. (2012) "5.1.1 Continuum Mechanics". **Material Science of Polymers for Engineers (3rd Edition)**. Hanser Publishers.

Ozcan-Taskin, N.G. (1993) **On the effects of viscoelasticity in stirred tanks**. PhD Thesis, University of Birmingham.

Pacek, A.W., Hall, S., Cooke, M., et al. (2013) "Emulsification in Rotor–Stator Mixers". In Tadros, T.F. (Ed.) **Emulsion Formation and Stability**. 127-167.

Padron, G.A. (2001) **Measurement and comparison of power draw in batch rotor-stator mixers**. MSc Thesis, University of Maryland, College Park, MD, USA.

Parker, A. and Fieber, W. (2013) Viscoelasticity of anionic wormlike micelles: effects of ionic strength and small hydrophobic molecules. **Soft Matter**, 9: (4): 1203-1213.

Parker, D.J. and Fan, X. (2008) Positron emission particle tracking—Application and labelling techniques. **Particuology**, 6: (1): 16-23.

Parker, D.J., Forster, R.N., Fowles, P., et al. (2002) Positron emission particle tracking using the new Birmingham positron camera. **Nuclear Instruments and Methods in Physics Research Section A: Accelerators, Spectrometers, Detectors and Associated Equipment**, 477: (1): 540-545.

Paul, E.L., Atiemo-Obeng, V.A. and Kresta, S.M. (2004) **Handbook of Industrial Mixing: Science and Practice**. New Jersey: John Wiley & Sons, Inc.

Persoons, T. and O'Donovan, T.S. (2011) High Dynamic Velocity Range Particle Image Velocimetry Using Multiple Pulse Separation Imaging. **Sensors**, 11: (1): 1-18.

Peters, D.C. (1997) "Chapter 14 - Dynamics of Emulsification". In Harnby, N.;Edwards, M.F. & Nienow, A.W. (Eds.) **Mixing in the Process Industries**. Oxford, Butterworth-Heinemann 294-321.

Phan-Thien, N. (2002) **Understanding Viscoelasticity: Basics of Rheology**. Springer.

Pope, S.B. (2000) **Turbulent Flows**. Cambridge: Cambridge University Press.

Qin, H., Xu, Q., Li, W., et al. (2017) Effect of stator geometry on the emulsification and extraction in the inline single-row blade-screen high shear mixer. **Industrial & Engineering Chemistry Research**, 56: (33): 9376-9388.

Raffel, M., Willert, C., Wereley, S., et al. (2007) **Particle Image Velocimetry: A Practical Guide**. Berlin: Springer.

Rafiee, M., Bakalis, S., Fryer, P., et al. (2011) Study of laminar mixing in kenics static mixer by using Positron Emission Particle Tracking (PEPT). **Procedia Food Science**, 1.

Rafiee, M., Simmons, M., Ingram, A., et al. (2013) Development of positron emission particle tracking for studying laminar mixing in Kenics static mixer. **Chemical Engineering Research and Design**, 91: 2106–2113.

Ramsay, J., Simmons, M.J.H., Ingram, A., et al. (2016) "Mixing of Newtonian and viscoelastic fluids using "butterfly" impellers".

Rao, M.A. (2007) **Rheology of Fluid and Semisolid Foods: Principles and Applications**. New York USA: Springer US.

Rashed, M.K., Salleh, M.A.M. and Ismail, M.H.S. (2016) Investigating the effects of surfactants on drag reduction performance of diesel fuel in a rotating disk apparatus. **Journal of Purity, Utility Reaction and Environment**, 5: (1): 18-30.

Recktenwald, S.M., Haward, S.J., Shen, A.Q., et al. (2019) Heterogeneous flow inside threads of low viscosity fluids leads to anomalous long filament lifetimes. **Scientific Reports**, 9: (1): 7110.

Reynolds, O. (1883) XXIX. An experimental investigation of the circumstances which determine whether the motion of water shall be direct or sinuous, and of the law of resistance in parallel channels. **Philosophical Transactions of the Royal Society of London**, 174: 935-982.

Roberts, P.J.W. and Webster, D.R. (2002) "Chapter 2: Turbulent Diffusion". In Shen, H.H.;Cheng, A.H.-D.;Wang, K.-H.;Teng, M.H. & Liu, C.C.K. (Eds.) **Environmental fluid mechanics : theories and applications**. USA, American Society of Civil Engineers.

Rodgers, T.L. and Cooke, M. (2012) Rotor–stator devices: The role of shear and the stator. **Chemical Engineering Research and Design**, 90: 323-327.

Rounds, R.S. (2005) "Rheology of Liquid Detergents". In Lai, K.-Y. (Ed.) **Liquid Detergents**. Boca Raton, CRC Press 73 - 112.

Rueger, P.E. and Calabrese, R.V. (2013a) Dispersion of water into oil in a rotor–stator mixer. Part 1: Drop breakup in dilute systems. **Chemical Engineering Research and Design**, 91: 2122-2133.

Rueger, P.E. and Calabrese, R.V. (2013b) Dispersion of water into oil in a rotor–stator mixer. Part 2: Effect of phase fraction. **Chemical Engineering Research and Design**, 91: 2134-2141.

Ryan, D.J., Simmons, M.J.H. and Baker, M.R. (2017) Determination of the flow field inside a Sonolator liquid whistle using PIV and CFD. **Chemical Engineering Science**, 163: 123-136.

Saarenrinne, P., Piirto, M. and Eloranta, H. (2001) Experiences of turbulence measurement with PIV. **Measurement Science and Technology**, 12: 1904-1910.

Saito, Y., Fan, X., Ingram, A., et al. (2011) A new approach to high-shear mixer granulation using positron emission particle tracking. **Chemical Engineering Science**, 66: (4): 563-569.

Salager, J.-L. (2002) **Surfactants: Types and Uses** [online]. http://www.nanoparticles.org/pdf/Salager-E300A.pdf [Accessed 18 February 2015]

Salipante, P.F., Meek, S.E. and Hudson, S.D. (2018) Flow fluctuations in wormlike micelle fluids. **Soft Matter**, 14: (44): 9020-9035.

Schramm, L.L. (2006) "Preparation, Inhibition, and Destruction of Dispersions". **Emulsions, Foams, and Suspensions**. Wiley-VCH Verlag GmbH & Co. KGaA 201-221.

Segur, J.B. and Oberstar, H.E. (1951) Viscosity of Glycerol and Its Aqueous Solutions. **Industrial & Engineering Chemistry**, 43: (9): 2117-2120.

Sharp, K.V. and Adrian, R.J. (2001) PIV study of small-scale flow structure around a Rushton turbine. **AIChE Journal**, 47: (4): 766-778.

Shaw, D. (1992) **Introduction to Colloid and Surface Chemistry**. 4th.Great Britain: Elsevier Science Ltd.

Sheng, J., Meng, H. and Fox, R.O. (2000) A large eddy PIV method for turbulence dissipation rate estimation. **Chemical Engineering Science**, 55: 4423-4434.

Shi, J., Xu, S., Qin, H., et al. (2013) Single-pass emulsification processes in two different inline high shear mixers. **Industrial & Engineering Chemistry Research**, 52: (40): 14463-14471.

Shinnar, R. (1961) On the Behaviour of Liquid Dispersions in Mixing Vessels. **Journal of Fluid Mechanics**, 10: (02): 259-275.

Silverson (2016) "Installation, Operating & Maintenance Manual (UHS-074-150/250MS)". Chesham, United Kingdom.

Silverson (2019) [online]. https://www.silverson.co.uk/en/ [Accessed 20 August 2019]

Simmons, M.J.H. (2012) "2LMS: Liquid Mixing in Industrial Systems [Lecture Notes]". United Kingdom, University of Birmingham.

Smagorinsky, J. (1963) General circulation experiments with the primitive equations. **Monthly Weather Review**, 91: 99-164.

Sparks, T. (1993) **Operational characteristics of rotor/stator mixers**. MPhil Thesis, Cranfield University, UK.

Sparks, T. (1996) **Fluid mixing in rotor/stator mixers**. PhD Thesis, Cranfield University, UK.

Stein, M., Ding, Y.L., Seville, J.P.K., et al. (2000) Solids motion in bubbling gas fluidised beds. **Chemical Engineering Science**, 55: (22): 5291-5300.

Story, A., Jaworski, Z., Simmons, M.J., et al. (2018) Comparative PIV and LDA studies of Newtonian and non-Newtonian flows in an agitated tank. **Chemical Papers**, 72: (3): 593-602.

Szalai, E.S., Alvarez, M.M. and Muzzio, F.J. (2004) "Laminar Mixing: A Dynamical Systems Approach". In Paul, E.L., Atiemo-Obeng, Victor A., Kresta, Suzanne M. (Ed.) **Handbook of Industrial Mixing: Science and Practice**. New Jersey, USA, John Wiley & Sons, Inc. pp. 89-143.

Tadros, T.F. (2009) "Emulsion Science and Technology: A General Introduction". **Emulsion Science and Technology**. Wiley-VCH Verlag GmbH & Co. KGaA 1-56.

Teledyne Dalsa (2019) **CCD vs CMOS** [online]. https://www.teledynedalsa.com/en/learn/knowledge-center/ccd-vs-cmos/ [Accessed 21 August 2019]

Tennekes, H. and Lumley, J.L. (1972) **A first course in turbulence**. MIT Press.

Thapar, N. (2004) **Liquid-liquid dispersions from in-line rotor-stator mixers**. PhD Thesis, Cranfield University, UK.

TSI (2017) **Insight 4G^{TM} Global Image, Acquisition, Analysis & Display Software - User's Guide: P/N 6004904, Revision E, March 2017**. USA: TSI Inc.

University of Birmingham (2019) **Positron Emission Particle Tracking (PEPT) Overview** [online]. https://www.birmingham.ac.uk/research/activity/physics/particle-nuclear/positron-imaging-centre/positron-emission-particle-tracking-pept/pept-overview.aspx [Accessed 26 August 2019]

Utomo, A.T. (2009) **Flow patterns and energy dissipation rates in batch rotor-stator mixers**. PhD Thesis, The University of Birmingham.

Utomo, A.T., Baker, M. and Pacek, A.W. (2008) Flow pattern, periodicity and energy dissipation in a batch rotor–stator mixer. **Chemical Engineering Research and Design**, 86: 1397-1409.

Utomo, A.T., Baker, M. and Pacek, A.W. (2009) The effect of stator geometry on the flow pattern and energy dissipation rate in a rotor–stator mixer. **Chemical Engineering Research and Design**, 87: 533-542.

Van de Velden, M., Baeyens, J. and Smolders, K. (2007) Solids mixing in the riser of a circulating fluidized bed. **Chemical Engineering Science**, 62: (8): 2139-2153.

Walstra, P. (1983) "Formation of Emulsions". In Becher, P. (Ed.) **Encyclopedia of Emulsion Technology**. New York, Marcel Dekker Inc. pp. 57-127.

Walstra, P. (2005) "Chapter 8 - Emulsions". In Lyklema, J. (Ed.) **Fundamentals of Interface and Colloid Science**. Academic Press 1-94.

Walstra, P. and Smulders, P.E.A. (1998) "Emulsion Formation". In Binks, B.P. (Ed.) **Modern Aspects of Emulsion Science**. Cambridge, UK, The Royal Society of Chemistry.

Wang, X., Feng, X., Yang, C., et al. (2014) Energy Dissipation Rates of Newtonian and Non-Newtonian Fluids in a Stirred Vessel. **Chemical Engineering & Technology**, 37: (9): 1575-1582.

Wei, J., Kawaguchi, Y., Yu, B., et al. (2010) Microstructures and rheology of micellar surfactant solution by Brownian dynamics simulation. **Nonlinear Dynamics**, 61: (3): 503-515.

Weiss, J. (2008) **Emulsion Processing - Homogenization** [online]. http://people.umass.edu/mcclemen/FoodEmulsions2008/Presentations%28PDF%29/%285%29Emulsion_Formation.pdf [Accessed 19 February 2015]

Westerweel, J. (1997) Fundamentals of digital particle image velocimetry. **Measurement Science and Technology**, 8: (12): 1379.

Westerweel, J., Elsinga, G.E. and Adrian, R.J. (2013) Particle Image Velocimetry for Complex and Turbulent Flows. **Annual Review of Fluid Mechanics**, 45: (1): 409-436.

Wu, H. and Patterson, G.K. (1989) Laser-Doppler measurements of turbulent-flow parameters in a stirred mixer. **Chemical Engineering Science**, 44: (10): 2207-2221.

Xu, D. and Chen, J. (2013) Accurate estimate of turbulent dissipation rate using PIV data. **Experimental Thermal and Fluid Science**, 44: 662-672.

Xu, S., Cheng, Q., Li, W., et al. (2013a) LDA measurements and CFD simulations of an in-line high shear mixer with ultrafine teeth. **AIChE Journal**, 60: (3): 1143-1155.

Xu, S., Shi, J., Cheng, Q., et al. (2013b) Residence time distributions of in-line high shear mixers with ultrafine teeth. **Chemical Engineering Science**, 87: 111-121.

Zhang, C., Gu, J., Qin, H., et al. (2017) CFD analysis of flow pattern and power consumption for viscous fluids in in-line high shear mixers. **Chemical Engineering Research and Design**, 117: 190-204.

Zhang, J., Xu, S. and Li, W. (2012) High shear mixers: A review of typical applications and studies on power draw, flow pattern, energy dissipation and transfer properties. **Chemical Engineering and Processing**, 57-58: 25-41.

Zhang, Z. (2010) **LDA Application Methods: Laser Doppler Anemometry for Fluid Dynamics**. Berlin, Heidelberg: Springer Berlin Heidelberg.

Zhou, G. and Kresta, S.M. (1998) Correlation of mean drop size and minimum drop size with the turbulence energy dissipation and the flow in an agitated tank. **Chemical Engineering Science**, 53: (11): 2063-2079.